Université de Montréal
Université catholique de Louvain

Using Experiment and First-Principles to Explore the Stability of Solid Electrolytes for All-Solid-State Lithium Batteries

By
Yasmine Benabed

Département de chimie, Faculté des arts et sciences

Département de chimie, Secteur des sciences et technologies

A dissertation submitted in partial fulfilment of the requirements for the degree of

Doctor of Philosophy

(Chemistry)

January 2023

Université de Montréal

Département de chimie, Faculté des arts et sciences

Université catholique de Louvain

Département de chimie, Secteur des sciences et technologies

This dissertation entitled

Using Experiment and First-Principles to Explore the Stability of Solid Electrolytes for All-Solid-State Lithium Batteries

Presented by

Yasmine Benabed

Has been evaluated by a jury composed of the following people:

Richard Martel
President of the jury

Mickaël Dollé
Advisor

Geoffroy Hautier
Co-advisor

Gian-Marco Rignanese
Co-advisor

Alexandru Vlad
Member of the jury

Ali Seifitokaldani
External examiner

Matthias Ernzerhof
Member of the thesis support committee

Jean-François Gohy
Member of the thesis support committee

Résumé

Les batteries aux ions lithium (BIL) sont considérées comme la technologie la plus prometteuse en matière de stockage d'énergie. Elles possèdent les plus hautes densités d'énergie connues, permettant la miniaturisation constante des appareils électroniques commercialisés. La recherche dans le domaine des BIL s'est plus récemment tournée vers leur implémentation dans les véhicules électriques, qui nécessitera de plus hautes densités d'énergie et de puissance[1]. Une manière concrète d'augmenter la densité d'énergie d'une BIL est d'en augmenter le voltage de cellule. Pour se faire, la nouvelle génération de batteries sera composée de matériaux d'électrode positive à haut potentiel (tel que $LiMn_{1.5}Ni_{0.5}O_4$ avec un potentiel de 4.7 V vs. Li^+ /Li) et de lithium métallique en électrode négative. Néanmoins, l'introduction de ces matériaux d'électrode positive à haut potentiel est limitée par la stabilité électrochimique de l'électrolyte liquide conventionnel, composé d'un sel de lithium et de solvants organiques (typiquement $LiPF_6$ + EC/DEC), qui s'oxyde autour de 4.2 V vs. Li^+/Li[2,3]. L'utilisation du lithium métallique comme électrode négative est entravée par la nature liquide de l'électrolyte conventionnel, qui n'offre pas assez de résistance mécanique pour empêcher la formation de dendrites de lithium, causant à terme le court-circuit de la batterie. De tels courts-circuits présentent un risque d'incendie car les électrolytes liquides sont composés de solvants organiques inflammables à basse température, posant un sérieux problème de sécurité.

Les électrolytes solides, de type céramique ou polymères, sont développés en alternative aux électrolytes liquides. Ils ne contiennent aucun solvant inflammable et sont stables à haute température. Ils constituent l'élément clé d'une nouvelle génération de batteries au lithium dite batteries au lithium tout-solide. Ces dernières sont développées pour répondre à des attentes élevées en termes de sécurité, de stabilité et de haute densité d'énergie. Les électrolytes solides doivent satisfaire un certain nombre d'exigences avant de pouvoir être commercialisés, notamment posséder une conductivité ionique élevée, une large fenêtre de stabilité électrochimique et une conductivité électronique négligeable. Ces propriétés constituent les critères les plus importants à prendre en compte pour la sélection de matériaux d'électrolytes solides. Cependant, on remarque dans la littérature que la majorité des études se concentre sur la conductivité ionique des électrolytes solides, reléguant au second plan l'exploration de leurs

[1] George E. Blomgren 2017 *J. Electrochem. Soc.* **164** A5019
[2] M. Doeff *et al.* Batteries for Sustainability. Springer, New York, **2012**.
[3] A. Guéguen *et al.* 2016 *J. Electrochem. Soc.* **163** A1095

stabilité électrochimique et conductivité électronique. La fenêtre de stabilité électrochimique a longtemps été annoncée comme étant très large chez les électrolytes solides céramiques (au moins de 0 à 5 V vs. Li^+/Li). Néanmoins, des études plus récentes tendent à démontrer que la valeur de cette fenêtre dépend grandement de la méthode électrochimique utilisée pour la mesurer, et qu'elle est de surcroit souvent surestimée. Dans ce contexte, le premier objectif de cette thèse a été de développer une méthode pertinente pour déterminer la fenêtre de stabilité des électrolytes solides avec précision. Cette méthode a été optimisée et validée sur des électrolytes solides céramiques phare comme $Li_{1.5}Al_{0.5}Ge_{1.5}(PO_4)_3$, $Li_{1.3}Al_{0.3}Ti_{1.7}(PO_4)_3$ et $Li_7La_3Zr_2O_{12}$. Quant à la conductivité électronique, elle est rarement étudiée dans les électrolytes solides, qui sont considérés comme isolants électroniques compte tenu de leur large bande interdite. Cela dit, de récentes études à ce sujet prouvent que malgré leur bande interdite, les électrolytes solides peuvent générer de la conductivité électronique par le biais de défauts, et que celle-ci, même faible, peut éventuellement mettre l'électrolyte en échec. Pour cette raison, le second objectif de ce projet de thèse a été d'explorer la formation de défauts dans les électrolytes solides afin de déterminer leur effet sur la génération de conductivité électronique. Pour avoir une vision d'ensemble, les premiers-principes ont été utilisés pour étudier six électrolytes solides largement utilisés notamment $LiGe_2(PO_4)_3$, $LiTi_2(PO_4)_3$, $Li_7La_3Zr_2O_{12}$, et Li_3PS_4.

Mots-clés : Électrolytes solides, Fenêtre de stabilité électrochimique, PITT, Produits de décomposition, Conductivité électronique, Défauts, Limites de dopabilité.

Abstract

Lithium-ion batteries (LIBs) are considered the most promising energy storage technology. LIBs electrode materials have the highest known energy densities, allowing the constant miniaturization of commercial electronic devices. Research in the field of LIBs has more recently turned to their implementation in electric vehicles, which will require higher energy and power densities[4]. A concrete way to increase the energy density of LIBs is to increase the cell voltage. To do so, the new generation of batteries will be composed of high potential positive electrode materials (such as $LiMn_{1.5}Ni_{0.5}O_4$ with a potential of 4.7 V vs. Li^+/Li) and metallic lithium in the negative electrode. Nevertheless, the introduction of these high potential positive electrode materials is limited by the electrochemical stability of conventional liquid electrolytes, composed of a lithium salt and organic solvents ($LiPF_6$ + EC/DEC), which gets oxidized around 4.2 V vs. Li^+/Li[5,6]. The use of metallic lithium as the negative electrode is also hindered by the liquid nature of the conventional electrolyte, which does not offer enough mechanical resistance to prevent the formation of lithium dendrites, ultimately causing a short-circuit of the battery. Such short-circuits are likely to lead to thermal runaway because liquid electrolytes are composed of organic solvents that are flammable at low temperature, posing a serious safety issue.

Solid electrolytes, based on ceramics or polymers, are developed as an alternative to liquid electrolytes. They contain no flammable solvents and are stable at high temperatures. They are the key element of a new generation of lithium batteries called all-solid-state lithium batteries. These are developed to meet high expectations in terms of safety, stability and high energy density. Solid electrolytes must satisfy a number of requirements before they can be commercialized, including possessing a high ionic conductivity, a wide electrochemical stability window and negligible electronic conductivity. These properties are the most important criteria to consider when selecting solid electrolyte materials. However, the majority of studies found in the literature focuses on the ionic conductivity of solid electrolytes, overshadowing the exploration of their electrochemical stability and electronic conductivity. The electrochemical stability window has long been reported to be very wide in ceramic solid electrolytes (at least from 0 to 5 V vs. Li^+/Li). Nevertheless, more recent studies tend to show that the value of this window depends greatly on the electrochemical method used to measure it, and that it is often overestimated. In this context, the first objective of this thesis was to develop a relevant method to determine the stability window of solid electrolytes with precision. This method was optimized and validated on flagship ceramic solid electrolytes such as $Li_{1.5}Al_{0.5}Ge_{1.5}(PO_4)_3$, $Li_{1.3}Al_{0.3}Ti_{1.7}(PO_4)_3$ and $Li_7La_3Zr_2O_{12}$. As for the

[4] George E. Blomgren 2017 *J. Electrochem. Soc.* **164** A5019
[5] M. Doeff *et al.* Batteries for Sustainability. Springer, New York, **2012**.
[6] A. Guéguen *et al.* 2016 *J. Electrochem. Soc.* **163** A1095

electronic conductivity, it is scarcely studied in solid electrolytes, which are considered as electronic insulators given their wide band gaps. That being said, more recent studies on this subject proved that despite their band gap, solid electrolytes can generate electronic conductivity through defects, and that electronic conductivity, even if it is weak, can eventually cause the failure of the electrolyte. For this reason, the second objective of this thesis project was to explore the formation of defects in solid electrolytes in order to determine their effect on the generation of electronic conductivity. To get a better overview, first-principles were used to investigate six widely used ceramic solid electrolytes, including $LiGe_2(PO_4)_3$, $LiTi_2(PO_4)_3$, $Li_7La_3Zr_2O_{12}$, and Li_3PS_4.

Keywords: Solid electrolytes, Electrochemical stability window, PITT, Decomposition products, Electronic conductivity, Defects, Dopability limits.

Table of Contents

List of tables

List of figures

List of abbreviations

AC	alternative current circuit
AIMD	*ab initio* molecular dynamics
Al:LLZO	$Li_{6.25}Al_{0.25}La_3Zr_2O_{12}$
ALD	atomic layer deposition
ASR	area-specific resistance
ASSLB	all-solid-state lithium battery
BET	Brunauer-Emmett-Teller
BG	band gap
BIL	*batterie aux ions lithium*
BLTS	*batterie au lithium tout solide*
BYD	build your dreams
CATL	contemporary amperex technology limited
CBM	conduction band minimum
CÉCI	*consortium des équipements de calcul intensif*
CPE	constant phase element
CV	cyclic voltammetry
CVD	chemical vapor deposition
DC	direct current circuit
DEC	diethyl carbonate
DFT	density functional theory
DL	dopability limit
DMC	dimethyl carbonate
EC	ethylene carbonate
EDS	energy-dispersive X-ray spectroscopy
EELS	electron energy loss spectroscopy
EIS	electrochemical impedance spectroscopy
ESW	electrochemical stability window
FAST	field assisted sintering technique
FEG	field emission gun
FIB	focused ion beam
FNRS	*fond national de la recherche scientifique*
FWHM	full width at half maximum
GGA	generalized gradient approximation
GITT	galvanostatic intermittent titration technique

GPPD	grand potential phase diagram
HF	Hartree-Fock
HFP	hexafluoropropylene
HSE	Heyd-Scuseria-Ernzerhof
IBE	ion beam etching
LAGP	$Li_{1.5}Al_{0.5}Ge_{1.5}(PO_4)_3$
LATP	$Li_{1.3}Al_{0.3}Ti_{1.7}(PO_4)_3$
LE	liquid electrolyte
LED	light-emitting diode
LGP	$LiGe_2(PO_4)_3$
LGPS	$Li_{10}Ge(PS_6)_2$
LIB	lithium-ion battery
LIPON	lithium phosphorous oxynitride
LISICON	lithium super ionic conductor
LiTFSI	lithium bis(trifluoromethanesulfonyl)-imide
LLTO	$Li_{3x}La_{2/3-x}TiO_3$
LLZO	$Li_7La_3Zr_2O_{12}$
LSV	linear sweep voltammetry
LTP	$LiTi_2(PO_4)_3$
LZP	$LiZr_2(PO_4)_3$
MAS	magic-angle spinning
MGI	materials genome initiative
MP/mp	materials project
MSD	mean-squared displacement
NASICON	natrium super ionic conductor
Nb:LLZO	$Li_{6.5}La_3Zr_{1.5}Nb_{0.5}O_{12}$
NCA	$LiNi_{0.8}Co_{0.15}Al_{0.05}O_2$
NEB	nudged-elastic-band
NiMH	nickel metal hydride
NMC	$LiNi_xMn_yCo_zO_2$
NMR	nuclear magnetic resonance
NSERC	natural sciences and engineering research council of Canada
OCP	open-circuit potential
PAN	polyacrylonitrile
PAW	projector augmented wave
PBE	Perdew-Burke-Ernzerhof
PC	propylene carbonate

PEO	polyethylene oxide
PITT	potentiostatic intermittent titration technique
PMMA	polymethyl methacrylate
ppm	parts per million
PSW	phase stability window
pV	pseudo-Voigt
PVA-CN	cyanoethyl polyvinyl alcohol
PVDF	polyvinylidene fluoride
PXRD	powder X-ray diffraction
PyCDT	python charged defect toolkit
rpm	round per minute
RT	room temperature
RTIL	room temperature ionic liquids
SAED	selected area electron diffraction
SDD	silicon drift detector
SE	solid electrolyte
SEI	solid electrolyte interphase
SEM	scanning electron microscopy
SHE	standard hydrogen electrode
SPEX	high-energy ball milling
SPS	spark plasma sintering
SS	stainless steel
SSW	stoichiometry stability window
STEM	scanning transmission electron microscopy
SVI	stepwise voltage increase
Ta:LLZO	$Li_{6.4}La_3Zr_{1.4}Ta_{0.6}O_{12}$
TEM	transmission electron microscopy
VASP	Vienna *ab initio* simulation package
VBM	valence band maximum
vs.	versus
XPS	X-ray photoelectron spectroscopy
xPTHF	polytetrahydrofuran
XRD	X-ray diffraction

To our beloved Khira,

your girls miss you like the Sahara misses the rain.

Acknowledgments

Finding the right words to properly express my immense gratitude to all the people who have supported me during my Ph.D. is no easy task. Trying to do so in a non-scientific and eloquent manner has proven to be even more difficult, after the many months spent writing my thesis using short, direct, and factual sentences. Now, at the finish line, I am taking a long deep breath to reflect and thank the many individuals without whom this thesis could not be published in the shape and form that is before you.

My list of acknowledgements easily begins with one particular person, who was not only my Ph.D. advisor at Université de Montréal, but also a mediator, a manager, a career agent, a father-like figure and an academic mentor, professor Mickaël Dollé. If I was asked to describe him, I would say that Mickaël is the embodiment of *The Big Bang Theory's* Sheldon Cooper and *The Office's* Michael Scott. No words could properly express the debt I owe for his help. His scientific vision, work ethics and dedication to research will shape you as a scientist, but it is his empathy, humanity, and compassion towards his students that will leave a permanent impression on you as a person. I thank him for not just opening the doors for me, but for kicking them down in the pursuit of my success, like it was his own. Thank you for always keeping an eye on me. I extend my sincere gratitude to professor Geoffroy Hautier, my advisor from Université catholique de Louvain, now Dartmouth College. His invaluable teaching and scientific rigor through the years played a crucial part in my academic journey. I am particularly grateful to him for introducing me to the field of computational chemistry and for always encouraging me to trust myself. Finally, though I have had less time with professor Gian-Marco Rignanese as an advisor, he has my profound appreciation for ensuring that I overcame all the final obstacles to complete my Ph.D. at UCL. His kindness and availability came at a time when it was most needed.

To the members of my jury: professor Richard Martel, professor Alexandru Vlad and professor Ali Seifitokaldani, I thank them for taking the time to evaluate this manuscript and providing me with feedback. To the remaining members of my advisory committee: professor Jean-François Gohy and professor Matthias Ernzerhof, I am grateful to them for providing me with guidance and valuable insights throughout my Ph.D.

On a day to day basis, I could not have undertaken this journey without the LCES research group, the circumstantial family that one adopts through the highs and lows of a Ph.D. To my fellow *Crazy Batteries* whatsapp group members, I will remember fondly our time spent in the laboratory from early mornings to late hours where corridors were plunged into darkness. I shall

start by thanking Steeve, the man with a thousand middle fingers, the caffeine-doped nuclear reactor of our group. Steeve was a major source of support for this thesis that *"sounded complicated"* from the start and I cannot thank him enough for his endless energy and advice, even when they often started with *#@!?*%&&.* I could not have done it without him. I would like to recognize the support of Elsa, who often reminded me that *"this year was our year,"* along with Marc and Cedric. To Erica and Nora, whose kindness and pet-sitting services have saved me on numerous occasions. To the very entertaining organized chaos that are Manon, Léa and Caroline, who to this day has not sold any of us into living in Longueuil. I thank Claire, David, Joseph, Julien, Gabrielle, Arnaud, Paul and Denis for always turning lunch breaks into lively social debates. Maxime, Adrien, Gaël, Vincent and Philippe left our lab before I reached the finish line, but I cherish the time we spent together and thank them for teaching me two life lessons: 1) Only laughter can help you survive a Ph.D., and 2) *Pétanque* is so much more than just a game. I will also remember the energy of Pejman, Nina, Laurence, and the quirky humor of Olivier and Dorian. Lastly, I would like to extend my sincere thanks to Fadwa, Arnaud and Dan (may he rest in peace) for sharing the struggles of conference organization together. I couldn't have managed any of it without them.

I am extremely grateful to the MODL research group. Especially to George, for his precious guidance, and to Sergy, Aurélie, Francesco, David, Vishank and Benoit who religiously bestowed upon me the art and virtue of playing *Whist*. I would also like to extend my sincere thanks to Guillaume and Giuliana for their unwavering good energy, as well as Martha, Diana, Sadia, Jean-Michel and especially Vinciane, for their help and kindness throughout the years.

To my friends, who have been the cornerstones of my personal life. I cannot express my appreciation enough for the great care they provided me with. To my mama bear, Celia, I thank her for being the best improvised therapist and reminding me that I am "*only human, and that it's ok."* Over the last five years, her care and patience have been priceless. To Fatiha, for always helping me take a deep breath when needed, whether that be in the form of a wild party or a quiet evening in. To my friends: Marilou, Nazim, Sarah, Walid and Rabah, I couldn't have done without all the laughs and the lovely company. I would like to thank Victor for his patience and support throughout this crucial year. To my childhood friend, Cindy, and our therapeutic 3-hour long video chats over the past years. I thank her for always letting me share my unfiltered thoughts. To Christophe, Kevin, Adrien and Djalal, who always knew when to show up for me.

My time in Belgium each year would not have been the same without the Tebache, my cross-Atlantic foster family. To Myriam, Karim, Benjamin and their lovely parents, Rania and

Messaoud, I thank them profoundly for their kindness and generosity. I would also like to thank Benoît and Guillaume, my friends from Brussels, my dance buddies who have always made my memories of Brussels warmer and brighter. To my friends and family in Paris, I thank them for always welcoming me, often with little to no notice, and for taking care of me in their own special Parisian way. Lastly, thank you to my friend, Kien, for sending me photographs of his never-ending travels and keeping me company virtually while I ran my experiments.

We are nearing the end now. When it comes to my family, I shall start by thanking my dear mother, Naïma. I am deeply indebted (literally and figuratively) to her for supporting me through my years of education, and for lifting me up, often with the encouraging refrain: "*Finish this Ph.D. already, it's time to earn a real salary!".* To my free-minded father, Nasser, who always meant well when he insisted on sending me all the articles on ''*this new revolutionary battery''* he found on randommagazine.bs and for encouraging me with his French proverbs, like this one: *"Eh bien...des chercheurs qui cherchent on en trouve, mais des chercheurs qui trouvent, on en cherche*!". To my sister Lydia, for laughing at all my little Ph.D. setbacks and always making up for it with a batch of her love-filled, gluten-free matcha cookies. To my cousin Seddik, I am grateful for his random but well-timed *"Mimine, how are you?"* texts which always came when I needed to vent. I am thankful for the tenderness of my aunt Selma, uncle Khelil, and cousin Salah. To my grandparents, Rachid and Khira (may she rest in peace), who always showed me how proud they were, even when they often asked me: *"But haven't you finished school yet?!"*. Finally, to my dog, Tyla the cutest, who took her supervisor role very seriously and made sure I finished writing my thesis (almost) on time.

1. GENERAL INTRODUCTION

The excessive consumption of fossil fuels, speculation around oil prices and ever-increasing emission of greenhouse gases compel us to question the foundations on which our society has evolved since the industrial revolution. It stimulates us to reconsider our overall energy consumption and to start looking for alternative energy sources, based on renewable and clean energy. For instance, finding an alternative energy source to cover the domestic needs in electricity and heating and to power transportations will reduce the greenhouse emissions by 46% [1]. Several countries pursued the nuclear energy route to cover the domestic needs in electricity and heating but came short in finding safe and lasting options to store the subsequent nuclear waste. They also faced on several occasions the disastrous consequences of nuclear-related incidents [2], calling for the necessity of a cleaner and safer option to produce energy.

Among renewable energy sources, solar, wind and hydroelectric energies are the most prominent options because of how abundant and versatile they are. However, they remain unreliable if used alone because their intensity is variable in time and diffuse in space [3]. A robust solution is to couple these energy sources to an intermediate energy storage system, which stores electrical energy in the form of chemical energy before converting it back into electrical energy when needed, like secondary batteries and supercapacitors. Alleviating the greenhouse gases emissions from transportations will also require switching from combustion engines to a ‘’greener’’ alternative like secondary batteries. They are considered the most promising option for the world-scale democratization of electrified transportation [4]. Moreover, the secondary battery asserted itself as the most promising device to meet the energy needs of an increasingly mobile and technology-oriented society. In fact, it already plays a crucial role in today’s technology as they are implemented in most of the portable, computing, telecommunication, entertainment devices, and more recently in electric and hybrid vehicles, used in modern society.

1.1 – The basics of a secondary battery

The three main components of a battery are the positive electrode, the negative electrode and the electrolyte. The two electrodes are connected externally through an electrical conduction system and internally through the ion conducting electrolyte as shown in **Figure 1.1**. Each electrode has a chemical potential that depends on its band structure and is related to its Gibbs free energy. The positive electrode has the highest potential and the negative electrode has the lowest potential. The difference of potential between the positive and negative electrodes defines the potential (or voltage) of the electrochemical cell. During the discharge of a battery, the electrons released from the oxidation reaction at the negative electrode spontaneously travel to feed a reduction reaction at the positive electrode. This transfer of negative charges is accompanied by a simultaneous transfer of positive charges through the electrolyte [5] as indicated in **Figure 1.1**. In a secondary battery, referred to as ''rechargeable battery'', the redox reaction occurring during the discharge is reversible. This means that a current can be applied to force the electrons in the opposite direction, pushing the opposite redox reactions to happen.

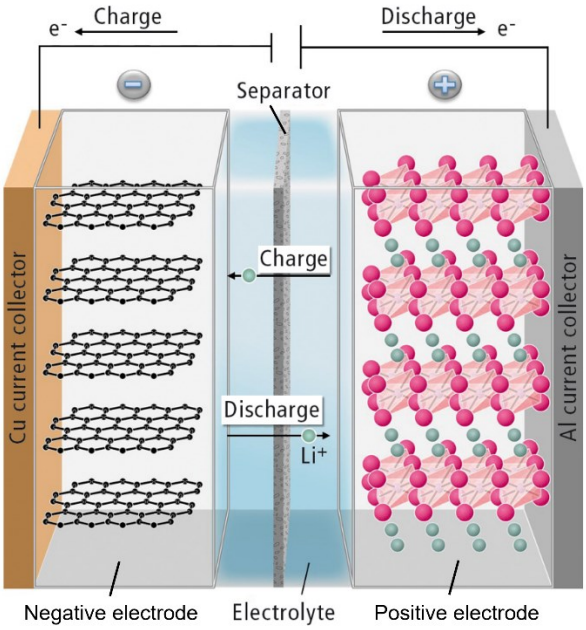

Figure 1.1 - Schematic representation of the functional principle of a lithium-ion battery. In this representation: the positive electrode is $LiCoO_2$ and the negative electrode is graphite [6].

1.1.1 – Performance metrics

Several key metrics help assess the performance of batteries. The energy density is usually considered the first feature to be sought after but power density, long term stability, safety, production cost and recyclability are also important parameters to consider [7].

1.1.1.1 – Energy density

The energy density is global metric used to compare systems with one another. It is the amount of energy that can be stored in a given system, it is often normalized by the system's mass and is referred to as the gravimetric (or specific) energy density, in $W.h.kg^{-1}$ [8]. It can also be normalized by the system's volume and is referred to as the volumetric energy density, in $W.h.L^{-1}$. The energy density (E_d) is derived from the coulombic capacity of a system (C) and its average voltage (V):

$$E_d = \int V(C)dC \qquad \text{Eq. 1.1}$$

The higher the energy density of a system, the greater the amount of energy it can store. In a battery, the energy density can be increased by increasing the capacity of its active materials and/or the cell voltage:

1.1.1.1.1 – Capacity

The capacity, expressed in A.h, is the total amount of electrical energy generated from electrochemical reactions and stored by a system. It corresponds to the number of electrons transferred between the negative and positive electrodes after the redox reactions occur. The capacity can be normalized by the mass of the system and referred to as the specific capacity, expressed in $A.h.g^{-1}$. In a battery, the actors involved in the redox reactions are the positive and negative electrode materials, they are the components responsible for generating the electrical energy. The theoretical specific capacity C of these materials is calculated from their molecular weight (M), the number of electrons involved in the redox reaction (n_e) and the Faraday constant (F), using the following relation:

$$C = \frac{n_e F}{M} \qquad \text{Eq. 1.2}$$

1.1.1.1.2 – Cell voltage

The cell voltage, expressed in V, is the difference of potential between the positive and negative electrode. The energy density of a battery can be enhanced by increasing its cell voltage. For example: if the cell voltage of a battery is increased from 4.2 V to 5 V, the energy density would increase by 20% (considering the capacity of both electrode materials remains the same). However, the reduction potential of the negative electrode material needs to be higher than the reduction potential of the electrolyte while the oxidation potential of the positive electrode material needs to be lower than the oxidation potential of the electrolyte, as illustrated in **Figure 1.2**. Otherwise, the electrolyte will be reduced and/or oxidized before the negative and positive electrode materials. The difference between the oxidation and reduction potentials of the electrolyte is referred to as the electrochemical stability window (ESW) and the cell voltage needs inevitably to be comprised within it. For this reason, intense efforts are invested into developing high-voltage positive electrode materials and low-voltage negative electrode materials but also electrolytes with wide electrochemical stability windows.

In order to efficiently estimate the energy density of a battery, all active and inactive components of the battery must be taken into account. The electrochemically inactive components are referred to as ‘’deadweight’’ and need to be minimized to increase the energy density of a battery [9].

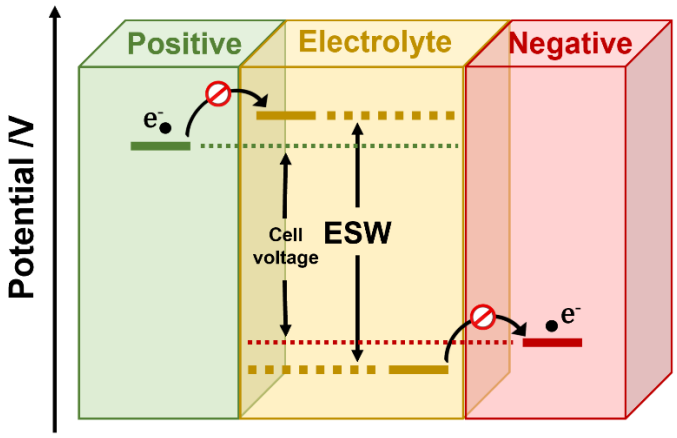

Figure 1.2 - Schematic representation of the cell voltage in a battery and the adequate electrochemical stability window of the electrolyte.

1.1.1.2 – Power

The power measures how fast a battery can deliver energy. It's the time rate of energy transferred from/to the system per volume unit (power density), given in $W.L^{-1}$, or per mass unit (specific power), expressed in $W.kg^{-1}$ [10]. The implementation of electric vehicles will require fast charging/discharging batteries, this need for higher currents will lead to the degradation of both electrodes, to the loss of energy in the form of heat and to the formation of lithium dendrites [11]. Therefore, electrode materials will need to have stable structures and fast redox kinetics with low activation energy barriers in order to withstand fast cycling rates [9].

1.1.1.3 – Cycling life

The cycling life is the ability of a battery to carry charging and discharging cycles without suffer from substantial performance loss. The cycling life depends on the long-term stability between the different components of a battery, such as the stability between positive electrode and electrolyte or negative electrode and electrolyte [9]. The cycling life also depends on the ability of the system to maintain its mechanical integrity as the volume and temperature change during cycling. The minimum cycling life that manufacturers expect from a battery is around 1000 cycles, equivalent to 3 years of daily use, but are actively working to increase it to 3000 cycles [9].

1.1.1.4 – Safety, cost and recyclability

Thermal runaway, mechanical failure, short circuit and toxic leakage are all considered safety hazards and can be triggered by the constant increase in energy and power density. The performance and reliability of a battery will depend on the risk of these hazards happening. The cost in $/kW.h of energy storage capacity is a key parameter that will decide on the commercialization potential of a technology. For example, the target cost for any energy storage technology is 100 $/kW.h to be cost-competitive in the field of transportation [12]. Finally, the recyclability is the ability of a battery to be reprocessed, and its materials extracted and reused, to generate minimum waste. The recyclability of a battery is tightly linked to the environmental impact and cost of its recycling process.

1.1.2 – A brief history of the battery

The first battery was prototyped in 1800 when Alessandro Volta stacked disc electrodes of copper and zinc, each time separated by a cloth soaked in brine acting as the electrolyte (**Figure**

1.3A). Experimenting on the Volta's ''voltaic pile'' cell, Humphry Davy was able to establish a link between electric current and chemical reactions, followed by Michael Faraday who discovered electromagnetism, erecting the foundations of modern electrochemistry [13]. Since then, several battery prototypes have emerged, in particular the Daniell cell in 1836, consisting of two compartments of zinc and copper connected by a salt bridge (**Figure 1.3B**) [14]. In 1866, the French engineer Georges-Lionel Leclanché disclosed his battery based on zinc and manganese oxide rods as negative and positive electrodes, immersed in an aqueous ammonium chloride solution as the electrolyte. This cell was redesigned to give the alkaline battery in 1930 [15].

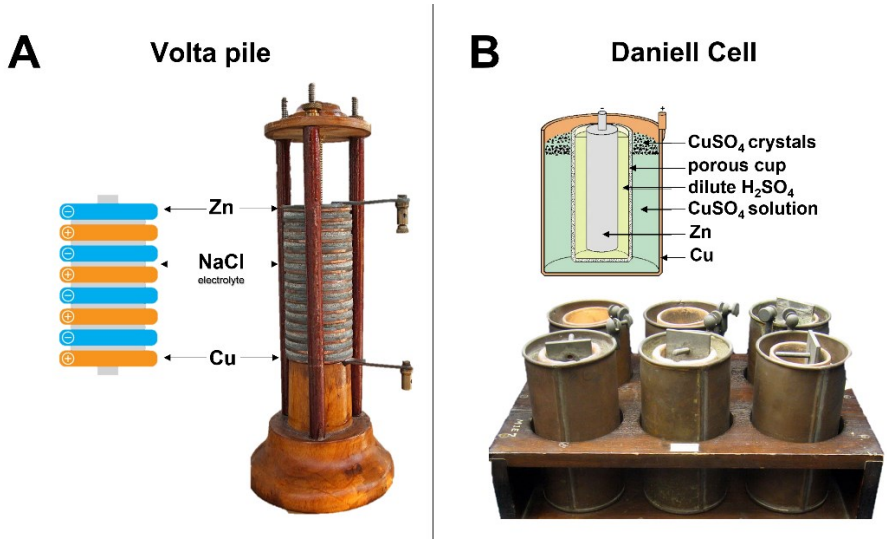

Figure 1.3 - Picture and corresponding schematic representation of A) the Volta pile and B) the Daniell cell.

Soon after, two other groundbreaking discoveries were made when Gaston Planté and Waldemar Jungner respectively invented the lead–acid and nickel-cadmium rechargeable batteries (**Figure 1.4**). The lead-acid battery operates through the oxidation of metallic lead at the positive electrode and the reduction of lead dioxide PbO_2 at the negative electrode [16]. The lead-acid battery was the first rechargeable battery to reach the market with a gravimetric energy density of 120 $W.h.kg^{-1}$, it was effectively used in several industrial applications and is still used in combustion engine vehicles to this day. The nickel-cadmium was further improved and led to the nickel metal hydride (NiMH) battery with a gravimetric energy density of 80 $W.h.kg^{-1}$. It operates following the reversible insertion of a proton into a NiO(OH) positive electrode, followed by the oxidation of a MH_x negative electrode (**Figure 1.4**). NiMH batteries are extensively used in the automobile industry (Toyota, Honda, Ford and General Motors), they have much longer cycling life than lead-acid batteries but suffer from low gravimetric energy density [17]. In order to improve

the performances of the NiMH battery, several insertion ions have been tested to replace the proton, which offered high ionic conductivity but was limited to aqueous media. All the studies converged to what seemed to be the most promising candidate, the lithium ion.

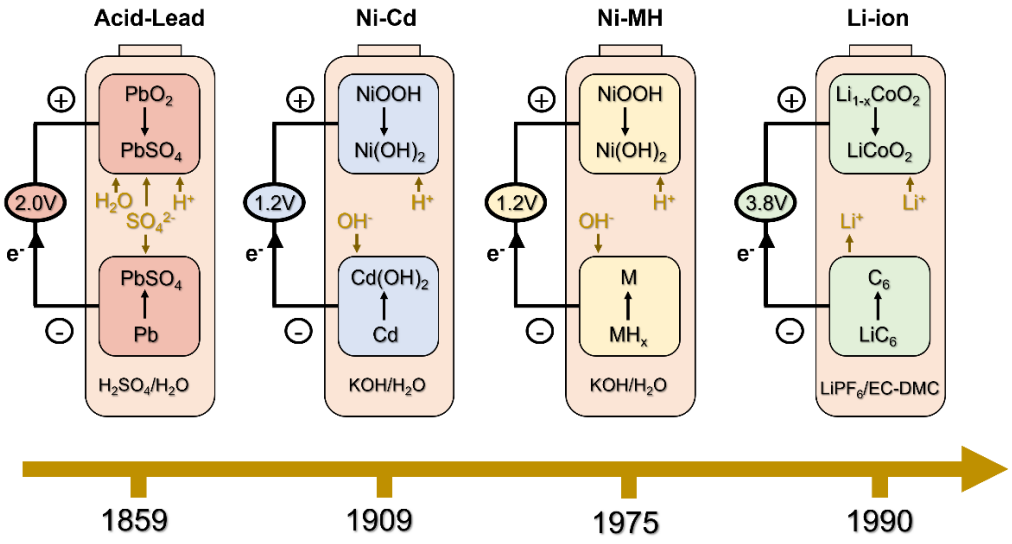

Figure 1.4 - Evolution of the battery chemistry over the years, from acid-lead to Li-ion [8].

1.2 – The lithium-ion battery

The first rechargeable lithium-ion battery was patented by Whittingham *et al.* in 1977 and was first commercialized by Sony in 1991 [18, 19]. It now occupies an unprecedented place in the consumer market. All considered, lithium-ion batteries have outperformed all other energy storage technologies such as Pb-acid, Ni−Cd, and Ni−MH batteries and have proven to be an efficient energy storage technology [20]. State-of-the-art LIBs have the highest volumetric and gravimetric energy densities found on the market (100-265 $Wh.kg^{-1}$ and 250-670 $Wh.L^{-1}$) as shown in the Ragone plot of **Figure 1.5A** [21]. LIB cells deliver more than 3.6 V, three times higher than Ni-Cd or Ni-MH batteries and have low self-discharge rates (1.5-2% per month). Commercialized lithium-ion batteries are generally composed of an insertion material as the negative electrode, a lamellar metal oxide based on lithium as the positive electrode and an inorganic lithium salt dissolved in organic solvents as the electrolyte. When a Li-ion battery is cycled, the lithium ion swings between the negative and positive electrodes, referred to as the “rocking chair” mechanism [22]. The revolutionary role played by Li-ion batteries in the modern world was acknowledged in 2019 when the Royal Swedish Academy of Sciences has decided to award the Nobel prize in chemistry to J. Goodenough, S. Whittingham and A. Yoshino, three pioneers in the development of today’s Li-ion battery (**Figure 1.5B**).

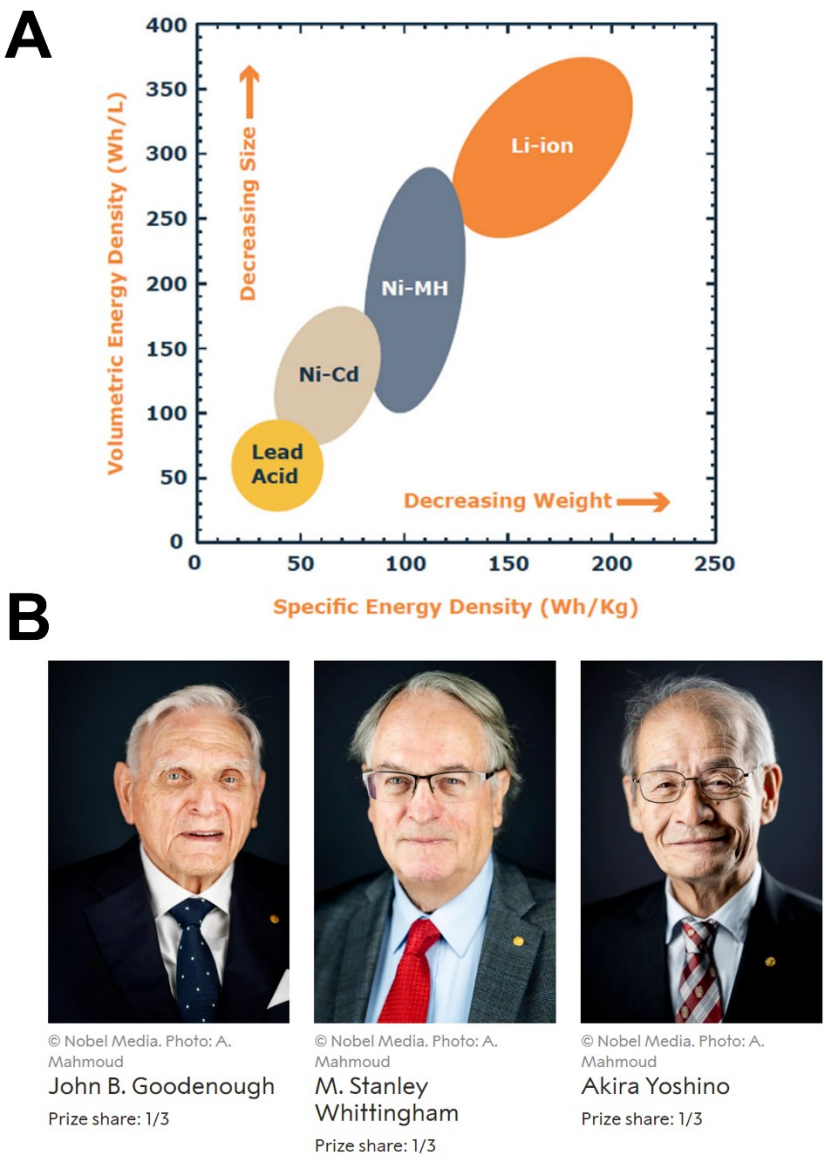

Figure 1.5 - A) Ragone plot comparing different battery technologies in terms of volumetric and gravimetric energy densities, placing the Li-ion batteries at the top of the performance list [23]. B) 2019 Nobel prize laureates J. Goodenough (USA), S. Whittingham (UK) and A. Yoshino (Japan) for their pioneering contribution to the development of Li-ion batteries [24].

The increasing demand for powerful and reliable energy storage sources in the medical and military fields, together with the explosion of the consumer portable electronic market, have triggered a relentless quest to improve the Li-ion battery, focusing on its main components: the positive electrode, the negative electrode and the electrolyte.

1.2.1 – The positive electrode

Stanley Whittingham first investigated chalcogenides as potential positive electrode materials for Li-ion batteries in 1977 [18, 25]. The Li_xTiS_2 (0<x<1) material stood out given its great structural stability and was soon after commercialized by EXXON® (**Figure 1.6A**) [26, 27]. Lamellar oxide V_2O_5 followed as the next promising positive electrode material [28, 29]. Studies focused on the lithiated ω-$Li_xV_2O_5$ and hydrated $H_yV_2O_5$●$0.4H_2O$●C phases as they displayed the most promising properties [30-32]. Research extended to other lamellar oxides and was marked by the discovery of $LiCoO_2$ in 1980 by Goodenough *et al.* (**Figure 1.6B**) [33]. Ten years later, the $LiCoO_2$ positive electrode material was commercialized by SONY® in the first Li-ion battery [19]. $LiCoO_2$-based batteries are still commercialized to this day. However, $LiCoO_2$ capacity of 130 $mA.h.g^{-1}$, its low life cycle and the limited cobalt resources, make $LiCoO_2$ an unreliable positive electrode material for future generations of batteries. For this reason, research turned to other lamellar oxides such as NiO_2 and its more stable substituted version $LiNi_{0.7}Co_{0.3}O_2$ [34]. The latter displayed excellent properties and was commercialized by SAFT® [35]. A similar phase of composition $LiNi_{0.8}Co_{0.15}Al_{0.05}O_2$ (NCA) was also commercialized by Panasonic® and Tesla®, with an excellent capacity of 185 $mA.h.g^{-1}$ and a good cyclability (**Figure 1.6C**) [36]. In the 1990s, a switch was operated from lamellar to spinel oxides with the discovery of $LiMn_2O_4$ material (**Figure 1.6D**), preferred to cobalt-based materials for its reduced impact on the environment and its lower price [37]. Analogous compound $LiMnO_2$, synthesized by Bruce and Delmas, also displayed promising properties but suffered from structural instability during cycling [38-40]. In order to solve this issue, Yoshio, Liu *et al.* introduced cobalt and nickel into the $LiMnO_2$ structure, resulting in the successful synthesis of $LiNi_{0.5}Mn_{0.5}O_2$, $LiNi_{0.8}Mn_{0.1}Co_{0.1}O_2$ (NMC811) and $LiNi_{0.33}Mn_{0.33}Co_{0.33}O_2$ (NMC111), with capacities exceeding 150 $mA.h.g^{-1}$ and an operating voltage of 3.7 V vs. Li^+/Li [41, 42]. NMC positive electrode materials were commercialized by LG® and are nowadays implemented in electric vehicles, along with NCA materials. In parallel, researchers started looking for iron-based materials as a more affordable and abundant alternative to cobalt and nickel. This initiative led to the discovery of $LiFePO_4$ by Padhi *et al.* in 1997 (**Figure 1.6E**) [43]. This olivine type compound has a promising theoretical capacity of 170 $mA.h.g^{-1}$ and good cyclability but suffered from low intrinsic electronic conductivity. The problem persisted until Ravet *et al.* patented the process of coating $LiFePO_4$ with carbon, significantly improving its conductivity [44]. $LiFePO_4$ has attracted increasing interest given its abundant, affordable and non-toxic elements. $LiFePO_4$-based batteries are now commercialized by several companies, including BlueSolutions®, Build Your Dreams® (BYD) and Contemporary Amperex Technology Limited® (CATL).

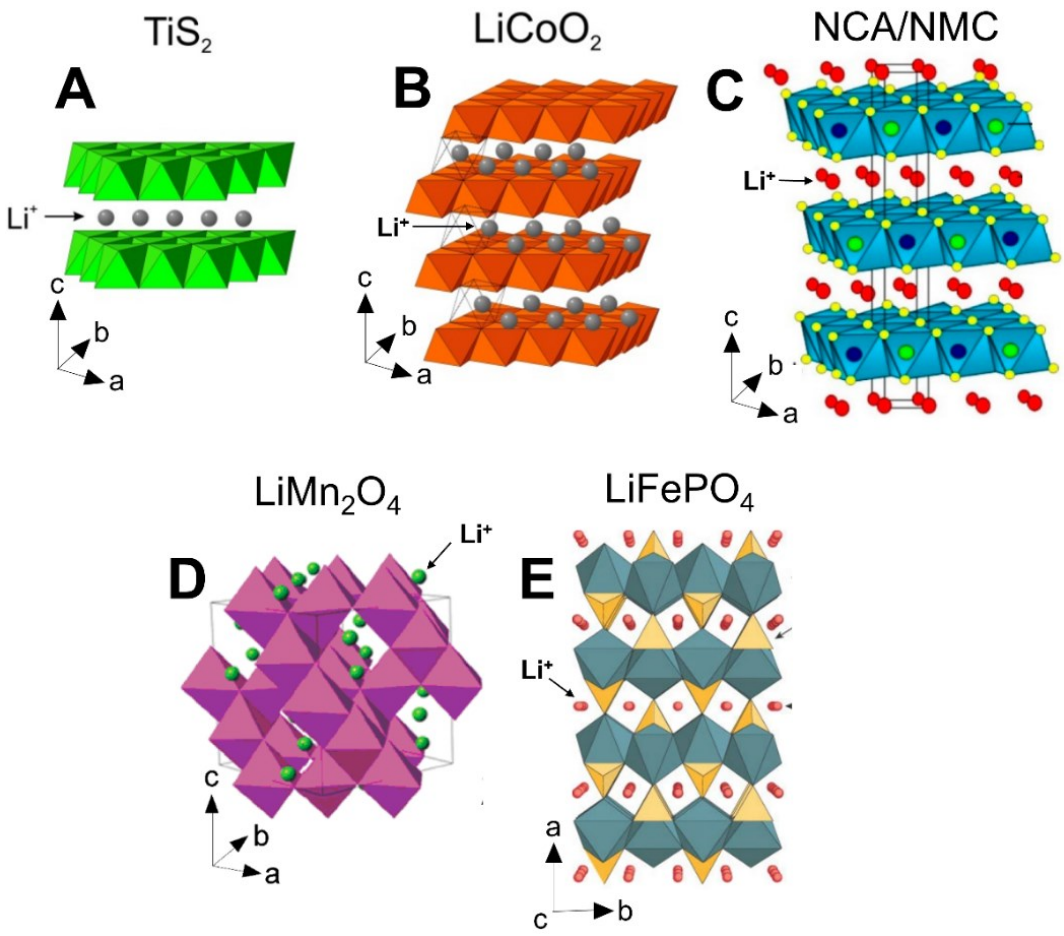

Figure 1.6 - Crystal structure of different positive electrode materials : A) TiS_2 [45], B) layered-type $LiCoO_2$ [45], C) layered-type $LiNi_xCo_yAl_zO_2$ (NCA) and $LiNi_xMn_yCo_zO_2$ (NMC) [46], D) spinel-type $LiMn_2O_4$ [47] and E) olivine-type $LiFePO_4$ [48].

1.2.2 – The negative electrode

Li-based batteries use two types of negative electrodes: metallic lithium electrodes, where lithium is stripped and plated on the surface of the electrode (Li-metal batteries), and lithium-based active materials where Li ions are inserted or intercalated following a rocking chair mechanism (Li-ion batteries). Metallic lithium is the most sought-after negative electrode material because of its high electropositivity (-3.04 V vs. SHE) and its low molar mass (6.94 $g.mol^{-1}$), resulting in one of the highest energy densities available (3862 $mA.h.g^{-1}$) [49, 50]. Using lithium metal as the negative electrode instead of other negative electrode active materials could increase the energy density of Li-ion batteries by 70% compared to other negative electrode materials. However, its low potential of 0 V vs. Li^+/Li makes conventional liquid electrolytes unstable against it,

systematically forming a passivation layer at the lithium metal/electrolyte interface. Moreover, as the cycling progresses, this passivation layer fractures due to an irregular deposition of lithium on the surface, giving rise to the formation of dendrites [51]. The dendrites keep growing due to the low transference number of liquid electrolytes. As they develop, these dendrites reach the positive electrode to form a bridge between the two electrodes, causing the battery to short-circuit.

Graphite (C_6) was also investigated as a negative electrode material (**Figure 1.7A**); it has a relatively low reduction potential (between 0.5 V and 2.1 V vs. Li^+/Li) and a good specific capacity of 372 $mA.h.g^{-1}$ when fully lithiated [52, 53]. Graphite material is the most commercialized negative electrode on the market today. Nevertheless, conventional electrolytes are not stable at LiC_6 potential neither. They break down to form a protective passivation layer that allows the C_6 negative electrode to keep functioning. In 1986, the company Matsushita® introduced lithium metal alloys (Li_xM) as an alternative to metallic lithium or graphite [54]. Li_xSi in particular showed a remarkable capacity of 4200 $mA.h.g^{-1}$ but suffered from a large volume expansion (300%) that invariably caused the electrode to collapse [55]. In 1997, Fuji® introduced the STALION technology with tin oxides (SnO_x) and intermetallic (Sn_xSb, Sn_xAg_y) materials (**Figure 1.7B**) [56]. No commercialization was pursued given the restricted availability and high price of Sn and Ag elements. The search for stable negative electrode materials was more recently marked by the discovery and commercialization of insertion spinel-type material $Li_4Ti_5O_{12}$ (**Figure 1.7C**), with an operational potential of 1.5 V vs. Li^+/Li and an excellent cyclability [57]. It is commercialized as a negative electrode material.

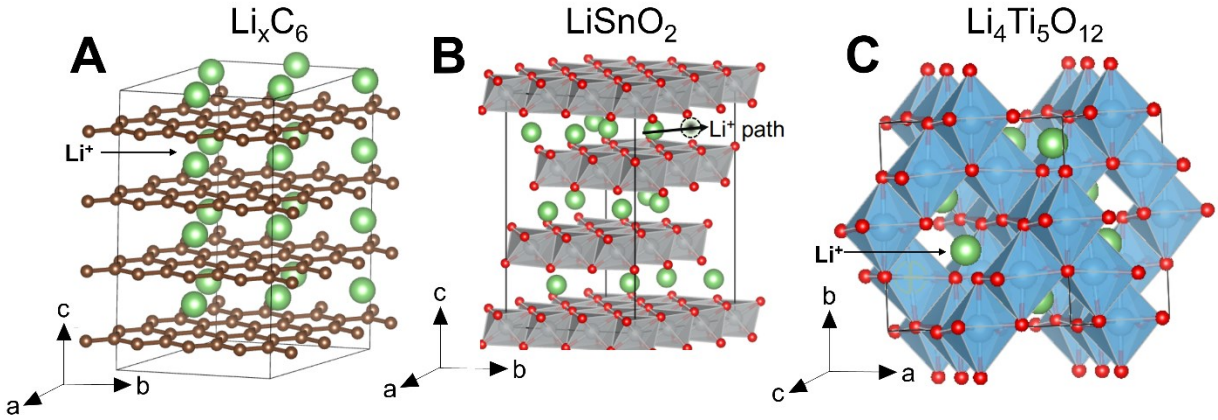

Figure 1.7 - Crystal structure of different negative electrode materials : A) lithiated graphite Li_xC_6 [58], B) STALION $LiSnO_2$ materials [59] and C) spinel-type $Li_4Ti_5O_{12}$ [60].

Positive and negative electrode materials were thoroughly explored over the past decades, they come from different structural families, they exhibit very diverse conduction mechanisms,

operating potentials and theoretical capacities. **Figure 1.8** gathers most of the positive and negative electrode materials considered for Li-based batteries. In the figure, a significant difference in capacity is observed between Li metal and the other negative electrode materials, justifying the efforts to implement Li metal as the negative electrode in Li-ion batteries.

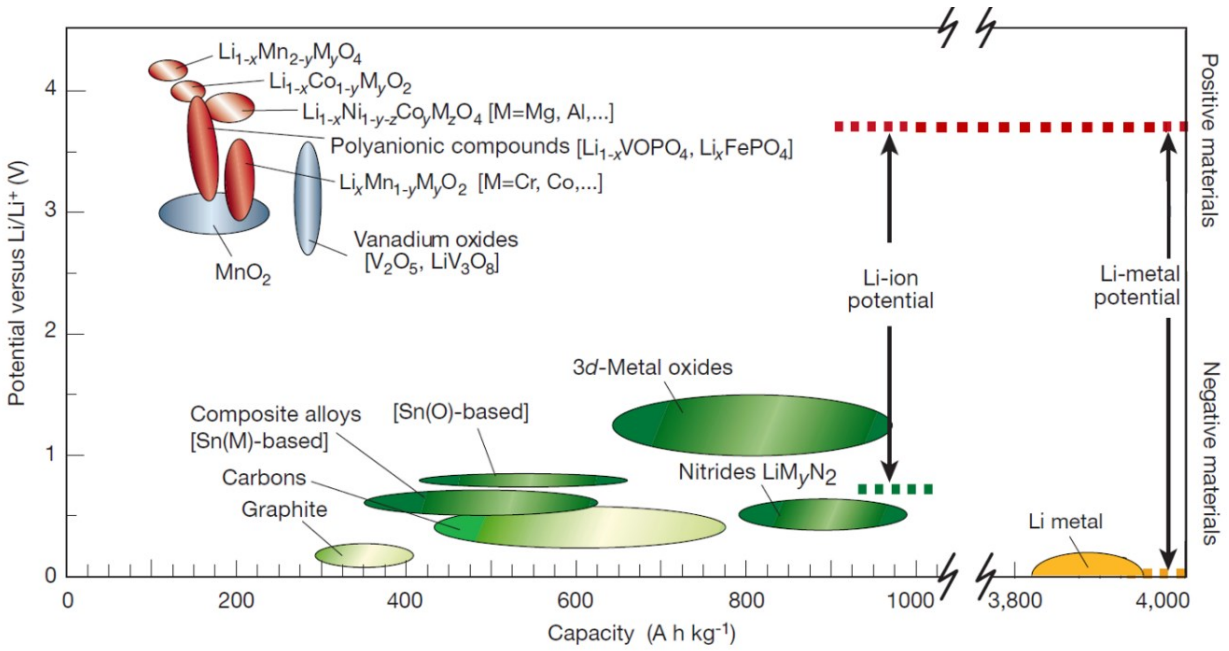

Figure 1.8 - Potential as a function of the capacity for different positive and negative electrode materials of interest for Li-based batteries [48].

1.2.3 – The electrolyte

The first electrolytes considered for Li-ion batteries consisted of inorganic lithium salts dissolved in organic solvents like carbonates. Their low viscosity allows adequate diffusion of lithium and their window of stability generally extends from 1 to 4.3 V vs. Li^+/Li [61-65]. $LiClO_4$ in propylene carbonate (PC) was the first electrolyte to be tested in a battery but was not considered a viable option given the toxicity of $LiClO_4$ and its limited diffusion of lithium ions in addition to the exfoliating effect of PC on graphite negative electrodes [66]. It quickly gave way to $LiPF_6$ lithium salt dissolved in linear and cyclic carbonates-based solvents such as diethyl carbonate (DEC), dimethyl carbonate (DMC) and ethylene carbonate (EC), introduced by Yamaki *et al*. [66]. This electrolyte shows an excellent ionic conductivity of 10^{-2} $S.cm^{-1}$ and is used in most lithium-ion batteries commercialized today. However, carbonated organic solvents are extremely flammable with low temperature flash points (<60 °C), causing the $LiPF_6$ salt to decompose and produce LiF, POF_3 and HF gases in contact with moisture [67]. As an alternative, researchers developed a

vinylidene fluoride/hexafluoropropylene (PVDF/HFP) copolymer membrane impregnated with liquid electrolyte, the prototype led to the commercialization of the PLiON© technology by Bellcore® Laboratories in 1996 [68]. It is currently marketed under license in several storage systems but was not considered suitable to electric vehicles. Research has more recently focused on room temperature ionic liquids (RTIL) to replace conventional liquid electrolytes [69-71]. They have better thermal stability, but their high viscosity significantly reduces the conductivity of lithium ions. Imidazole and pyrrolidium based ionic liquids were found to be the most promising candidates but were neither stable nor affordable enough to enter the market [72]. The gelation of the conventional liquid electrolyte ($LiPF_6$/EC-DMC) in a polymer matrix, like poly(acrylonitrile) (PAN) or poly methyl methacrylate (PMMA), were also investigated [73].

Despite many efforts put into finding alternative solvents/salts combinations, the standard $LiPF_6$ in carbonate-based organic solvents (EC, DEC, DMC) liquid electrolyte remains the state-of-the-art in conventional Li-ion batteries. However, as mentioned above, these organic solvents are highly flammable, leading to a significant risk of thermal runaway, and their decomposition products at higher potentials include toxic gas HF [66]. In addition, the limited electrochemical stability window of carbonate-based organic liquid electrolytes [61, 64, 74, 75] (1-4.3 V) narrows the choice of positive and negative electrodes in LIBs [76-78]. For instance, liquid electrolytes react against lithium metal to form a passivation layer, referred to as a solid electrolyte interphase (SEI), stable in time that allows the battery to keep functioning. However, stripping/plating Li metal (negative electrode) with carbonate-based organic liquid electrolytes induce the inherent growth of lithium dendrites within the electrode material. With no physical barrier to stop their growth, these dendrites puncture the separator and cause a short-circuit, an overpressure and eventually the death of the battery. The formation of dendrites is also triggered by the liquid electrolytes' low transference number ($t_+ < 0.3$-0.5, to be defined later in the manuscript) [79]. On the other hand, high potential positive electrode materials, such as $LiNi_{0.5}Mn_{1.5}O_4$[80], $LiNi_{0.8}Co_{0.15}Al_{0.05}O_2$ [81] and $LiNi_xMn_yCo_zO_2$ [82, 83], require the use of an electrolyte stable in the range of their operation potentials, i.e., with a wide enough electrochemical stability window. In this context, considerable effort was made to replace the flammable and reactive conventional liquid electrolyte with a safer and more thermally stable ceramic or polymer solid electrolyte (SE) [49, 84-86].

1.3 – Solid electrolytes

Ionic conductivity in solids was first observed by Faraday, through his work on Ag_2S and PbF_2, followed by Nernst on ZrO_2 and other oxides but only at high temperature [87]. In 1967, Na^+ and Ag^+ conductivity was observed in Na-doped β-Alumina ($Na_{1+x}Al_{11}O_{17+x/2}$) and $RbAg_4I_5$, making

them the first room-temperature solid super-ionic conductors [88, 89]. Super-ionic conductors have distinct crystal structures that allow them to conduct ions at 10^{-3} S.cm^{-1} at RT. The ionic conductivity in such solids can originate from: 1) a phase transition that triggers the mobility of ions through the creation of Frenkel pairs, like it's the case for AgI [87], 2) the presence of layers and tunnels in the structure that allow 1D, 2D or 3D transport pathways for ions, as seen in β-alumina and $Na_{1+x}Zr_2P_{3-x}Si_xO_{12}$ NASICON materials [90, 91], 3) a heavy doped and disordered structure that allows high concentrations of charge carriers, as often seen in fluorite structured materials such as $RbBiF_4$, Y-doped CeO_2 and rare-earth-doped CaF_2 [92, 93], 4) the presence of mobile protons as seen in HUO_2PO_4-$4H_2O$, materials with high proton mobilities are included in a separate class, owing to their distinctive transport mechanisms [87, 94]. Solid ionic conductors are extraordinarily diverse and include all sorts of materials. They are currently studied for several applications, including fuel cells and sensors, but mostly as solid electrolytes for batteries.

Operating a battery require the solid electrolyte to have 1) a high ionic conductivity at room temperature (>10^{-3} S.cm^{-1}), to efficiently transport Li ions, 2) a high transference number ($t_+ \rightarrow 1$) with only lithium ions diffusing through an immobile framework, to prevent concentration gradients in the cell and sustain higher current densities, allowing shorter charging times, 3) a wide electrochemical stability window, to enable the use of metallic lithium as the negative electrode and high-potential positive electrodes, 4) a negligible electronic conductivity (<10^{-12} S.cm^{-1}), to prevent self-discharge and short-circuits [95], 5) a good thermal stability, to ensure safety in case of overheating, 6) a good chemical stability against electrode materials, especially against metallic lithium and the positive electrode materials of interest, also a good chemical stability against air/moisture, to facilitate and reduce the costs related to handling and processing, 7) mechanical strength, to prevent the formation of lithium dendrites while maintaining mechanical integrity following the volume expansion of the electrodes, and 8) a low impact on the environment, ideally using abundant and affordable elements.

The solid electrolyte is processed with the positive and negative electrodes to form a new generation of batteries, the all-solid-state battery (ASSLB) [96-98]. ASSLBs have attracted growing interest over the past decade, being the subject of an increasing number of publications each year (**Figure 1.9A**), mostly because they could enable the use of metallic lithium as the negative electrode. The latter would significantly increase the gravimetric and volumetric energy densities of the battery (at the cost of considerable processing challenges), making it ever more performant for modern applications (**Figure 1.9B**). Several families of solid electrolytes were investigated through the decades, they are divided into two major groups, organic polymers and inorganic ceramics.

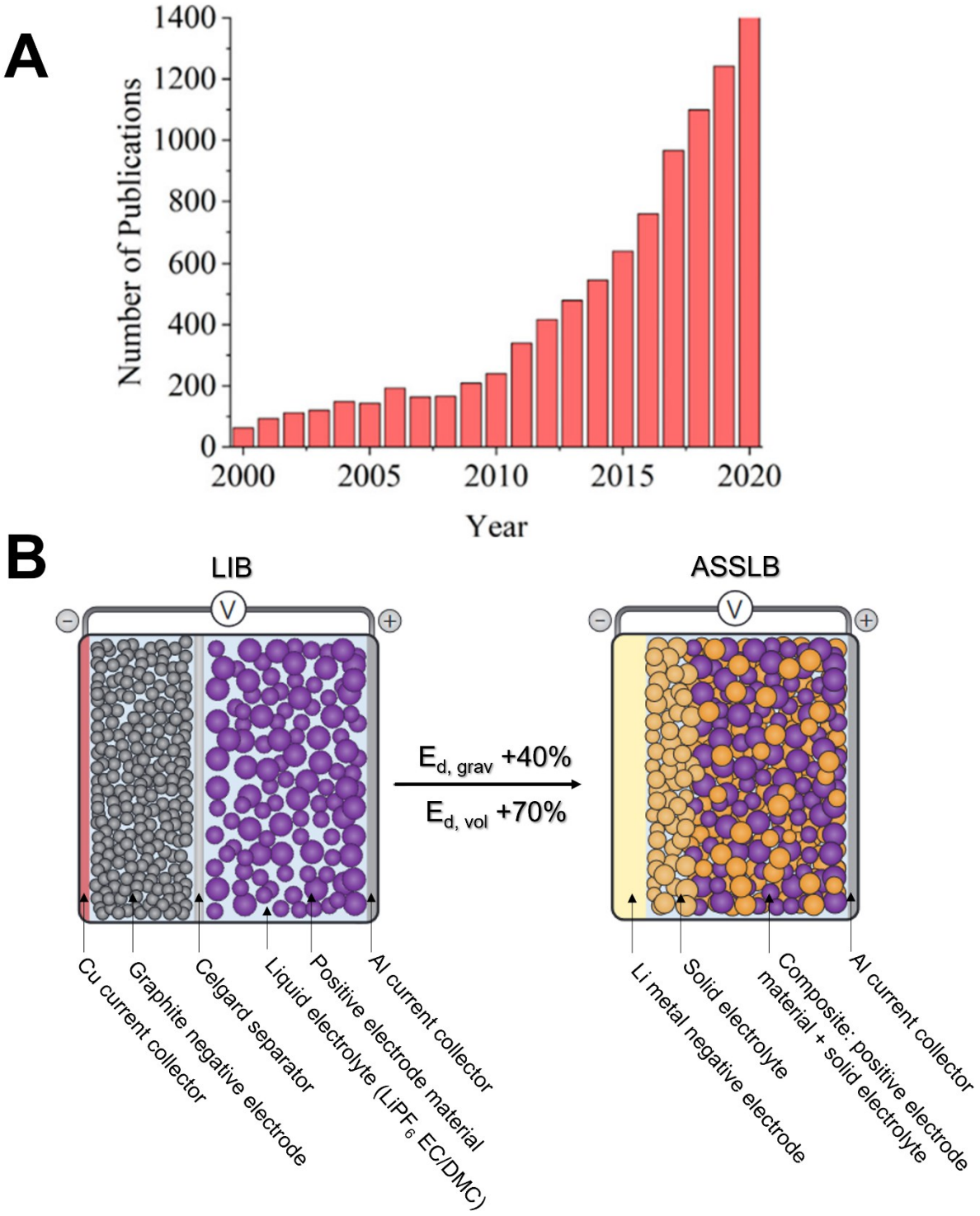

Figure 1.9 - A) Number of published papers on solid-state lithium metal batteries from 2000 to 2020 [99]. B) Architectures for the conventional lithium-ion and all-solid-state batteries. The volumetric and gravimetric energy densities are represented by $E_{d,vol}$ and $E_{d,grav}$, respectively. With a lithium-metal negative electrode, which has a theoretical energy density of 3700 $mA.g^{-1}$, ASSLB can achieve a significant gain in energy density [7].

1.3.1 – Organic polymer solid electrolytes

Ion conducting polymers are typically prepared by dissolving monovalent ion salts in polyethers. In typical Li-ion conducting polymers, Li^+ cations are solvated by the O^{2-} anions of the polyether to form ionic pairs, high mobility of the Li ions requires an amorphous polymer framework [87]. Polymer solid electrolytes have attracted considerable attention because they feature low elastic moduli, making them flexible and adaptable to volume expansion during cycling, also providing them with a good interfacial contact against electrode materials [100]. Polymer-based SEs have also demonstrated the best results against lithium metal, especially polyethylene oxide (PEO) with lithium bis(trifluoromethanesulfonyl)-imide salt (LiTFSI) [101]. Fenton and Wright first discovered that PEO was an ionic conductor [102, 103]. Armand *et al.* later suggested it could be used, combined with a lithium salt, as a solid electrolyte in electrochemical devices [104]. PEO polymer has a good chemical compatibility with electrodes, a reasonable electrochemical stability and strong dissociation capacity for lithium salts. ASSLBs using PEO-LiTFSI as the electrolyte, metallic lithium as the negative electrode and $LiFePO_4$ as the positive electrode are currently commercialized by Blue Solutions® [105].

Nevertheless, PEO-LiTFSI has limited thermal stability and limited stability toward high potentials (it reacts at 3.8 V vs. Li^+/Li). Furthermore, PEO-LiTFSI only achieves a full-potential ionic conductivity in its amorphous state, above the melting temperature (T_m) and needs to operate at rather high temperatures (> 60 °C). At its melting point, PEO becomes liquid and starts creeping, losing all mechanical strength. Additionally, its low transference number ($t_+ \approx 0.2$), due to its highly mobile counter-ions, and low-rate capability hinder the possibility of fast charging and the access to high energy-density batteries [106-110]. To optimize the ionic conductivity and mechanical strength of PEO at RT, researchers have explored many strategies such as grafting [111], copolymerization [112], blending [113], adding plasticizers [114], adding inorganic and nanosized fillers [115]…etc. Several polymers have been investigated to replace PEO, like polyvinylidene fluoride (PVDF) [116, 117], polyacrylonitrile (PAN) [118], cyanoethyl polyvinyl alcohol (PVA-CN) [119, 120], polytetrahydrofuran (xPTHF) [121], etc … Nonetheless, an upper limit of 10^{-4} $S.cm^{-1}$ at RT has been reached so far for polymer electrolytes, often followed by a significant reduction in mechanical properties [122, 123]. To compensate for polymers' low ionic conductivity at RT, researchers suggested to take advantage of the high ionic conductivity (>10^{-4} $S.cm^{-1}$ at RT) and thermal stability of ceramic solid electrolytes combined with polymers' excellent deformability and wetting properties to develop hybrid composite SEs [124, 125]. However, the relevance of hybrid composite solid electrolytes is still a subject of heated debate.

Given the scope of this manuscript and for the sake of conciseness, we will not consider polymer, amorphous, gel or hybrid SEs in greater detail. Instead, we will focus on the exploration of inorganic ceramic solid electrolytes.

1.3.2 – Inorganic ceramic solid electrolytes

Ceramic solid electrolytes are considered a promising alternative based on the following accounts: 1) they can exhibit high ionic conductivity (>10^{-3} S.cm^{-1}) at RT, while polymer electrolytes need higher temperatures to become super ionic conductors, 2) they have high elastic moduli and could act as a mechanical barrier on the growth of dendrites, 3) their rigid nature can prevent parasitic cross-overs of redox reactants between the positive electrode and the negative electrode and prevent redox shuttle phenomena, avoiding capacity fade and short-circuit [126], 4) they should allow the design of high voltage bipolar stacked batteries as illustrated in **Figure 1.10A**, effectively decreasing the dead space between single cells as it enables the use of thinner or no current collector and bypass the separator since SEs act as the electrolyte but also as a separator (**Figure 1.10B**), 5) they possess greater transference numbers than liquid and polymer electrolytes because the only charge carriers are lithium cations, therefore, they could give access to higher current densities and faster charging than conventional LIBs [7]. 6) they could operate at low and high temperatures, from –50 to 200 °C or higher, at which conventional liquid electrolytes would freeze or decompose [127]. 7) some of them show promising electrochemical stability against lithium metal at 0 V vs. Li^+/Li or at high potentials, up to 5 V vs. Li^+/Li, enabling the use of high-potential positive electrode materials and lithium metal as the negative electrode, increasing the energy density in a battery by 25% if we consider a very thin and dense SE layer [128-131].

Given their potential application in ASSLBs, inorganic ceramic-based SEs have been developing very rapidly, they divide in different families depending on their elemental composition and crystal structure, some are oxide-based and others sulfur-based:

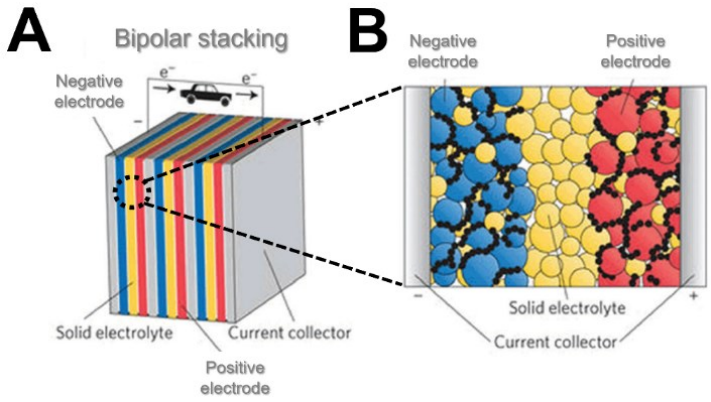

Figure 1.10 - A) Bipolar stacking configuration possible with ASSLBs, where the electrode materials are coated on the two sides of the current collector, reducing the weight and volume of the battery package. B) Schematic representation of a graphite-based ASSLB [49].

1.3.2.1 – NASICON-type ionic conductors

NAtrium Super Ionic CONductor (NASICON) solid electrolytes were first synthesized by Goodenough *et al.* in 1976 [91]. The crystal structure belongs to the rhombohedral *R-3C* space group, based on the general formula $Na_{1+x}Zr_2P_{3-x}Si_xO_{12}$ ($0<x<3$), Na^+ ions, located in interstitial sites, are mobile along the c-axis and can be replaced by Li ions. Numerous studies have been conducted on Li-analogues to NASICON-type conductors with the general formula of $LiM_2(PO_4)_3$ (M= Ge, Zr, Ti, Al, …) as illustrated in **Figure 1.11A** [132], mainly $LiTi_2(PO_4)_3$ (LTP), $LiGe_2(PO_4)_3$ (LGP) and $LiZr_2(PO_4)_3$ (LZP). The NASICON structural frame hosts 3D interconnected channels for Li diffusion [133]. Increasing their ionic conductivity was possible through a partial substitution of M in the initial structure to give $Li_{1+x}M_xX_{2-x}(PO_4)_3$ [134, 135]. Indeed, the ionic conductivity of the LTP, LGP and LZP has been considerably enhanced by substituting Ti^{4+}, Ge^{4+} and Zr^{4+} with Sc^{3+}, Al^{3+}, Y^{3+}, Ga^{3+}, Fe^{3+}, Lu^{3+}, In^{3+}, La^{3+} and Cr^{3+}, or by substituting P^{5+} with Si^{4+} [136-138]. More specifically, Al^{3+} substitution has been demonstrated to be the most effective, leading to the syntheses of $Li_{1.3}Al_{0.3}Ti_{1.7}(PO_4)_3$ (LATP) and $Li_{1.5}Al_{0.5}Ge_{1.5}(PO_4)_3$ (LAGP) [139]. LATP and LAGP were widely investigated for their ionic conductivities up to 1.09 10^{-3} $S.cm^{-1}$ and 5.08 10^{-3} $S.cm^{-1}$ at RT respectively [140, 141]. LATP and LAGP are reported to be stable against air/moisture [142, 143], and to have wide electrochemical windows (up to 6 V vs. Li^+/Li) but to react against lithium metal due to the reduction of Ti^{4+} to Ti^{3+} and Ge^{4+} to Ge^{3+} as a compensation to the Li insertion [128, 129, 144-149]. These reactions become notably exothermic above 250 °C [150]. A Cr-doped version of LAGP, $Li_{1.5}Al_{0.4}Cr_{0.1}Ge_{1.5}(PO_4)_3$, displayed an ionic conductivity of 6.65 10^{-3} $S.cm^{-1}$ at RT, the highest reported for NASICON-type SEs, and a stated ESW ranging from 0 to 7 V vs. Li^+/Li [151].

1.3.2.2 – Garnet-type ionic conductors

The garnet structure crystallizes in a face-centered cubic system (*Ia-3d* space group), with the general formula $A_3B_2X_3O_{12}$ (A = Ca, Mg, Y, La or Ln; B = Al, Fe, Ga, Ge, Mn, Ni, V; X = Si, Ge, Al). Garnets are also found in the less common and less conducting tetragonal system (*I41/acd* space group). The most interesting garnets investigated in electrochemistry are the Li-rich garnets, where Li is introduced in excess [152]. Thangadurai *et al.* first reported Li-rich garnets $Li_5La_3M_2O_{12}$ (M= Nb, Ta) capable of conducting lithium ions [153]. La and M sites can be partly substituted by lithium to give Li-rich garnet-type solid electrolytes such as $Li_7A_xLa_yM_zO_{12}$ (A = Mg, Ca, Sr, Ba and M = Zr, Sn, Ta) phases [154-161]. Thangadurai *et al.* divide garnet-type Li-rich ion conductors into four categories, according to the number of lithium added to the initial garnet-structure: 1) Li_3-phases like $Li_3Ln_3Te_2O_{12}$ (Ln = Y, Pr, Nd, Sm–Lu) and $Li_{3+x}Nd_3Te_{2-x}Sb_xO_{12}$ (x = 0.05–1.5), 2) Li_5-phases with the general formula $Li_5La_3M_2O_{12}$ (M = Nb, Ta, Sb), 3) Li_6-phases such as $Li_6ALa_2M_2O_{12}$ (A = Mg, Ca, Sr, Ba; M = Nb, Ta) and 4) Li_7-phases including $Li_7La_3M_2O_{12}$ (M = Zr, Sn) [162]. Li_3-phases structures are characterized with a low ionic conductivity at RT (10^{-7} – 10^{-8} S.cm^{-1}) [163, 164] suggesting that increasing the amount of lithium to $Li_{5,6,7}$-phases should increase the ionic conductivity. Li_5-phases were the first Li-rich garnet-type phases to be discovered with an excess Li incorporated. Ionic conductivities were therefore increased for garnets to 10^{-5} – 10^{-7} S.cm^{-1} at RT. Li_6-phases were successfully synthesized substituting the trivalent La^{3+} with divalent ions such as Mg, Ca or Sr, which resulted in an increased ionic conductivity to 10^{-4} – 10^{-6} S.cm^{-1} at RT. The first Li_7-rich garnet-type SE was the cubic phase $Li_7La_3Zr_2O_{12}$ (LLZO), synthesized by Murugan *et al.* (**Figure 1.11B**) and characterized by a high ionic conductivity at RT of 2.44 10^{-4} S.cm^{-1} [159]. Synthesized at lower sintering temperatures, $Li_7La_3Zr_2O_{12}$ was reported to form a less conductive tetragonal polymorph [160]. Nevertheless, Al-doping during synthesis at lower temperatures was proven to stabilize $Li_7La_3Zr_2O_{12}$ in its cubic phase [165, 166]. Partially substituting Zr^{4+} by Ta^{5+} or Te^{6+} in $Li_7La_3Zr_2O_{12}$ to give $Li_{6.4}La_3Zr_{1.4}Ta_{0.6}O_{12}$ and $Li_{6.5}La_3Zr_{1.75}Te_{0.25}O_{12}$ was reported to significantly increase ionic conductivity to 1–1.6 10^{-3} S.cm^{-1} at RT [167, 168]. LLZO was reported to be electrochemically stable against lithium metal [130, 159, 169], but this conclusion was more recently challenged by others [170-173]. Initial studies on LLZO found it to be stable up to 5 and 9 V vs. Li^+/Li [130, 174], but it was more recently reported to react early at high potentials according to F. Han *et al.* (4 V vs. Li^+/Li) [175], making LLZO's stability at low and high potentials a subject of controversy. LLZO-type structures are also limited by their sensitivity to ambient air, more specifically by their reactions with adsorbed H_2O or CO_2, leading to the formation of highly resistive Li_2CO_3 [176].

1.3.2.3 – Perovskite-type ionic conductors

Perovskite-type SEs were initially reported by Takahashi *et al.* in 1971 [177]. The crystal structure of perovskites belongs to cubic *Pnma* space group, with the general formula ABO_3 (A = La, Sr, Ca and B = Al, Ti). Li^+ can be introduced in the perovskite structure on the A site to become an ionic conductor, creating the $Li_{3x}La_{2/3-x}TiO_3$ (LLTO) structure (**Figure 1.11C**) [131]. The ionic conductivity is particularly temperature-dependent in this material given that a crossover from 2D to 3D diffusion pathways is observed at 200 K [178, 179]. The ionic conductivity also relies on the concentrations of both Li ions and vacancies on the A site. Vacancy-doped structure $Li_{0.33}La_{0.56}\square_{0.11}TiO_3$ displayed the highest ionic conductivity reported in perovskite-type SEs (1.4 10^{-3} $S.cm^{-1}$ observed at RT) [180]. Doping the A site in the formula $Li_{0.5}M_{0.5}TiO_3$ with metal ions (M = Sm, Nd, Pr, and La) also allows improving the ionic conductivity. For instance, $Li_{0.34}La_{0.56}TiO_3$ displayed a bulk ionic conductivity of 10^{-3} $S.cm^{-1}$ at RT [180, 181]. LLTO and its doped versions are characterized by a high bulk conductivity, excellent thermal stability (>1300 °C) and stability in air/moisture [182-184]. However, LLTO-type structures suffer from high grain boundary resistance, significantly affecting the total conductivities in polycrystalline ceramic samples. LLTO electrochemical stability window is reported to stretch to high potentials (up to 8 V vs. Li^+/Li) but to react early at low potentials, due to the reduction of Ti^{4+} ions to Ti^{3+} (1.8 – 1.5 V vs. Li^+/Li), and being chemically unstable against lithium metal [131, 169, 185, 186]. The family of anti-perovskites, with the general formula Li_3OX (X = Cl, Br), was also investigated as solid electrolytes [187-189]. Li_3OCl, Li_3OBr, $Li_3OCl_{0.5}Br_{0.5}$ and $Li_3OCl_{0.2}Br_{0.8}$ anti-perovskite materials were reported to have conductivities as high as 8.5 10^{-4} and 1.94 10^{-3} $S.cm^{-1}$ at RT [190]. Anti-perovskite SEs are characterized by low melting points and minimal grain boundary resistance but are still in the early stages of development as to be applied in ASSLBs [191].

1.3.2.4 – Borates and phosphate-type ionic conductors

Borates and phosphates like $Li_2B_4O_7$, Li_3PO_4, $Li_4P_2O_7$ and $LiPO_3$ were widely investigated for their good manufacturing reproducibility and wide electrochemical stability but suffer from very low ionic conductivity (10^{-7}–10^{-6} $S.cm^{-1}$ at RT) [192]. For instance, the ionic conductivity of $LiPO_3$ is around 10^{-8} $S.cm^{-1}$ at RT but can be increased by doping, it is the case for $(LiI)_{0.3}(LiPO_3)_{0.7}$ which displays an ionic conductivity of 10^{-6} $S.cm^{-1}$ [193]. Li_3PO_4 sparked a lot of interest for applications in thin film all-solid-state batteries [194]. N-doped Li_3PO_4 was first synthesized in thin films at Oak Ridge National lab to give lithium phosphorous oxynitride $Li_{3+x}PO_{4-y}N_z$ (LIPON) depicted in **Figure 1.11D**. They used several deposition methods, such as metal–organic chemical vapor deposition

(CVD), atomic layer deposition (ALD) or magnetron sputtering, to deposit a thin layer of Li_3PO_4 under an N_2 atmosphere [195]. LIPON thin films have a rather low ionic conductivity as compared to other oxide-based solid electrolytes (2.3 10^{-6} $S.cm^{-1}$ at RT) [196, 197] but display a wide electrochemical stability window (0 to 5 V vs. Li^+/Li) [198]. Additionally, LiPON thin films have the advantage of forming good interfacial contact with electrodes but on the other hand suffer from poor mechanical properties. LIPON thin film is the only ceramic SE currently used in a commercialized ASSLB (microbattery), first developed by Bates *et al.* in 1992 [199].

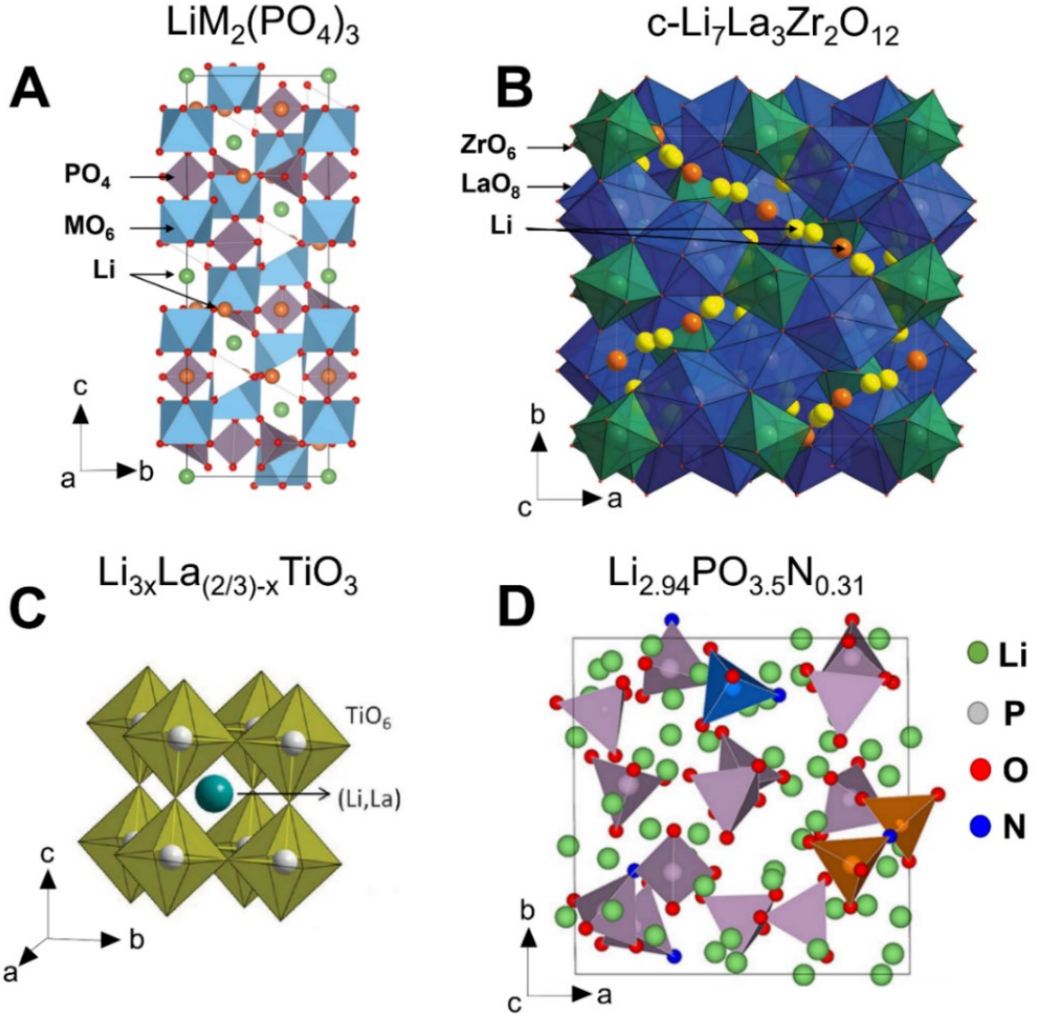

Figure 1.11 - Crystal structure of different oxide-based solid electrolytes : A) NASICON-type $LiM_2(PO_4)_3$ (M = Ti, Ge, Zr) [200], B) garnet-type cubic-phase $Li_7La_3Zr_2O_{12}$ [201], C) perovskite-type $Li_{3x}La_{(2/3)-x}TiO_3$ [162] and D) N-doped Li_3PO_4 ($Li_{3+x}PO_{4-y}N_z$ or LiPON) [202]. Different colors of the same element indicate different crystallographic sites (e.g., green and orange Li in $LiM_2(PO_4)_3$).

1.3.2.5 – Thio-LISICON-type ionic conductors

Thio-LISICON solid electrolytes were introduced by Kanno *et al.* [203, 204] when they substituted the oxygen atoms in the initial γ-Li_3PO_4 LISICON structure with S^{2-} anions. The LISICON initial phase has an ionic conductivity around 10^{-7} S.cm^{-1} at RT as the lack of lithium disorder in the structure prevents a significant ionic diffusion [205]. Nevertheless, because of its high polarizability, large ionic radius and low electronegativity, S^{2-} interacts less with lithium ions, facilitating the Li-ion diffusion through an original 3D framework structure and therefore increasing the ionic conductivity [206]. The thio-LISICON ionic conductor family includes several phases derived from the general formula $Li_xA_{1-y}B_yS_4$ (A = Si, Ge and B = P, Al, Zn, Ga, Sb) such as Li_3PS_4, Li_4SiS_4, Li_4SnS_4, Li_2SiS_3 and $Li_4P_2S_6$, with ionic conductivities ranging from 10^{-7} to 10^{-3} S.cm^{-1} [203, 207]. The highest conductivity recorded for thio-LISICONs is reported for $Li_{10}Ge(PS_6)_2$ (LGPS) with an ionic conductivity of 1.2 10^{-2} S.cm^{-1} (**Figure 1.12A**) [203, 206], which is comparable to the conductivity of liquid electrolytes currently used in LIBs.

However, thio-LISICONs are known to suffer from a limited electrochemical stability window and a problematic stability against metallic lithium due to the reactivity of germanium. Studies focused on substituting Ge^{4+} with Sn^{4+} but the resulting $Li_{10}Sn(PS_6)_2$ material displayed lower ionic conductivity [208, 209]. Krauskopf *et al.* investigated $Li_{10}Sn(PS_6)_2$ and proved that increasing the amount of Sn^{4+} in $Li_{10}Ge_{1-x}Sn_x(PS_6)_2$ leads to a smaller bottleneck along the diffusion channels, causing a stronger interaction between Li^+ and S^{2-}, consequently increasing the energy activation barrier to the lithium diffusion [210]. The thio-LISICON $Li_{11}Si_2PS_{12}$ was investigated using NMR and displayed a remarkable conductivity of 2 10^{-2} S.cm^{-1} at RT but which was only achievable under high pressure [211]. Kato *et al.* discovered the two materials $Li_{9.54}Si_{1.74}P_{1.44}S_{11.7}Cl_{0.3}$ and $Li_{9.6}P_3S_{12}$ and reported an ionic conductivity of 2.5 10^{-2} and 1.2 10^{-3} S.cm^{-1} at RT respectively [212]. They determined the electrochemical stability window of $Li_{9.6}P_3S_{12}$ to range from 0 to 5 V vs. Li^+/Li, a value that has yet to be confirmed. Thiophosphate LISICON materials demonstrate the best ionic conductivities, they have the advantage of being malleable and exhibit a low grain boundary resistance. This makes them easy to process into composites with electrode materials at low temperatures [213], a valuable asset given that processing solid electrolytes in ASSLBs is one of the biggest challenges met today. However, they suffer from poor chemical and electrochemical stability [175, 214]. They decompose in contact with air to give neurotoxic H_2S gas, making them challenging to process and prone to safety hazards.

1.3.2.6 – Argyrodite-type ionic conductors

The family of argyrodites was first introduced by Deiseroth *et al.* [215], they are derived from the $Li_2S–P_2S_5$ phase diagram and described by the formula $Li_{12-x}MA_{4-x}X_x$ (with M = Si, Ge, Sn, P, As; A = O, S, Se, Te and X = Cl, Br, I; $0 \leq x \leq 2$) [214]. Argyrodites come in both crystalline and amorphous phases. The ionic conductivity of the amorphous phases varies depending on the synthesis, including the ratio of both Li_2S and P_2S_5 precursors. Among them, the glass–ceramic $Li_7P_3S_{11}$ ($70Li_2S–30P_2S_5$) synthesized by melt process and heat treatment displays the highest ionic conductivity in the family (1.7 10^{-2} $S.cm^{-1}$) [216]. It was justified by the high amount of Li_2S in the amorphous matrix, the absence of grain boundaries in $Li_7P_3S_{11}$ crystals [217] and the presence of a 1D conduction path along the c-axis that allows a fast diffusion of Li ions.

The substitution of sulfur with halides in argyrodites was proven to increase their ionic conductivity. For example, the addition of halides in the parent phase Li_7PS_6 to form Li_6PS_5X (X = Cl, Br, I) phases [215], shown in **Figure 1.12B**, increases the ionic conductivity to 10^{-3} $S.cm^{-1}$ [214]. Studies showed that the substitution of sulfur with a halogen creates disordered Li vacancies to ensure charge compensation, increasing the local Li-ion diffusivity, especially in Li_6PS_5Cl and Li_6PS_5Br [218]. Argyrodites have generally limited electrochemical stability and are very sensitive to moisture, making their processing and synthesis strenuous, but remain one the most promising families of SEs for commercial applications [219-222].

1.3.2.7 – Hydride-type ionic conductors

Hydrides are regarded as reliable solid electrolytes due to their high stability against lithium metal, high mechanical strength and excellent flexibility, leading to low grain boundary resistance. Hydride compounds with high ionic conductivity are derived from the general formula Li_xAH_y (A = B, N, Al), they were first discovered by Matsuo *et al*. when they investigated the $LiBH_4$ compound (**Figure 1.12C**) and proved that it could be a super-ionic conductor in the *P6₃mc* phase [223]. The most promising hydrides explored are the borohydrides, based on $[BH_4]^-$ or $[B_nH_n]^{2-}$ anionic moieties [224]. $LiBH_4$, $Li_2B_{12}H_{12}$ and $Li_2B_{10}H_{10}$ were all the subject of great interest because of expected and observed high ionic conductivities around 10^{-3} $S.cm^{-1}$ at RT, exceeding 10^{-1} $S.cm^{-1}$ at higher temperatures (>100 °C) [223, 225, 226]. The electrochemical stability window of $LiBH_4$ ranged from 0 to 5 V vs. Li^+/Li when assessed using cyclic voltammetry (CV) but has yet to be confirmed [227, 228]. Experiments exposing $LiBH_4$ to $LiFePO_4$ and $LiCoO_2$ positive electrode materials concluded on $LiBH_4$ instability at their interfaces. On the other hand, $LiBH_4$ is proved to

be stable against metallic lithium through the formation of a stable solid electrolyte interphase (SEI) at the interface [228].

Although other hydrides like $LiNH_2$, Li_3AlH_6, and Li_2NH generally exhibit lower ionic conductivities than borohydrides, Matsuo *et al.* developed two hybrid compounds $Li(BH_4)_{0.25}(NH_2)_{0.75}$ and $Li(BH_4)_{0.5}(NH_2)_{0.5}$ which exhibited promising ionic conductivities around 10^{-4} S cm^{-1} at RT, higher than those of both parent $LiBH_4$ and $LiNH_2$ hydrides [229].

Tang *et al.* first explored carba-*closo*-borohydrides $LiCB_9H_{10}$, $LiCB_{11}H_{12}$ and $NaCB_{11}H_{12}$ materials as a new class of solid electrolytes and observed ionic conductivities as high as 1.5 10^{-1} S.cm^{-1} at 130 °C [230]. However, these materials are hard to stabilize and suffer from low ionic conductivity at RT [230]. Hybrid hydride-sulfide systems were also investigated; the two materials $67(0.75Li_2S{\cdot}0.25P_2S_5){\cdot}33LiBH_4$ and $90LiBH_4{\cdot}10P_2S_5$ were successfully synthesized by mechanochemical method and exhibited excellent conductivities of 10^{-3} S.cm^{-1} at RT, attributed to a reduced electrostatic interaction between anions and lithium cations caused by the $S^{2-}/[BH_4]^-$ random distribution [231-233].

1.3.2.8 – Halide-type ionic conductors

Halides superionic conductors are derived from the general formula of Li_3MX_6 (M = trivalent rare earth metal, X = F, Cl, Br, I). Halides were interesting to explore as solid electrolytes because they are characterized by a weak coulombic interaction between large halogen atoms and lithium ions, ensuring a good diffusion of lithium atoms. Halide anions (especially for F^- and Cl^-) were also expected to have high electrochemical redox potentials [234-236]. Liu *et al.* investigated the material $Li_3Y(BrCl)_3$ (**Figure 1.12D**) and estimated its ionic conductivity to reach 7.2 10^{-3} S.cm^{-1} after hot pressing, although this value was proved to be strongly dependent on the synthesis and testing conditions [237, 238]. Fluoride-based halides display the widest electrochemical stability windows but demonstrate the lowest ionic conductivities at RT, which limits their use as solid electrolytes [236]. In general, all halides are reported to suffer from poor air and moisture stability [236].

More recent studies investigated hybrid halide-hydride systems. For instance, Maekawa *et al.* synthesized $Li_4(BH_4)_3I$ and $Li(BH_4)_{0.7}Br_{0.2}Cl_{0.1}$ hybrid materials with a fair ionic conductivity of 10^{-5} S.cm^{-1} at RT [239]. These halide-hydride systems were also coupled to argyrodites in order to improve their ionic conductivity at RT; $Li(BH_4)_{0.75}I_{0.25}{\cdot}(0.75Li_2S{\cdot}0.25P_2S_5)$ was the first material of this kind introduced by Kharbachi *et al.* with a great ionic conductivity averaging 10^{-3} S.cm^{-1} at RT and an apparent wide electrochemical stability window ranging from 0 to 5 V vs. Li^+/Li [240].

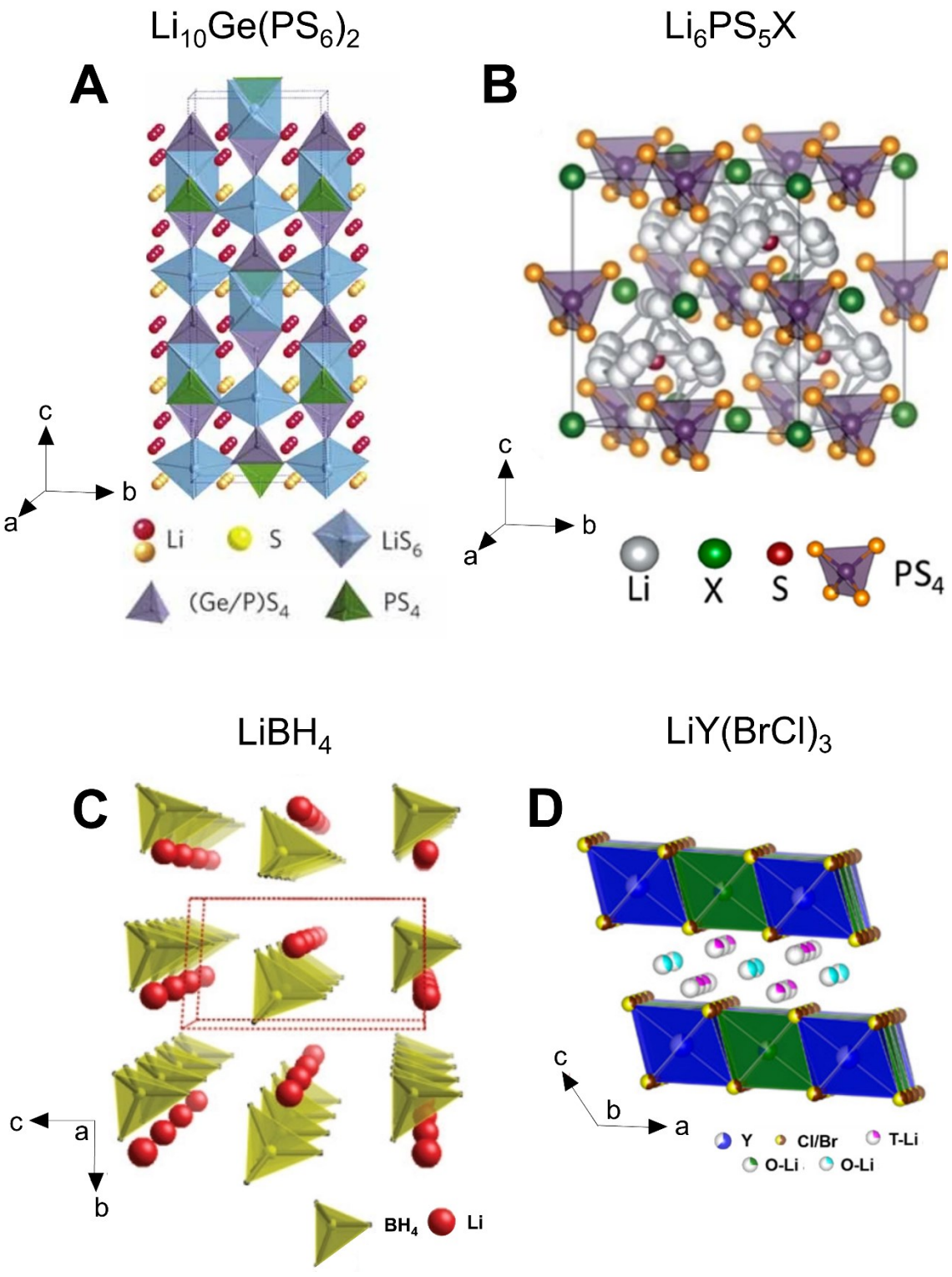

Figure 1.12 - Crystal structure of sulfur, hydride and halide solid electrolytes : A) LISICON-type $Li_{10}Ge(PS_6)_2$ [206], B) argyrodite-type Li_6PS_5X (X = Cl, Br, I, F) [241], C) hydride-type borohydride $LiBH_4$ [242] and D) halide-type $LiY(BrCl)_3$ [243]. Different colors of the same element indicate different crystallographic sites (e.g., red and orange Li atoms in $Li_{10}Ge(PS_6)_2$).

1.4 – Properties of solid electrolytes

All the different families of inorganic ceramic solid electrolytes investigated showed both advantages and drawbacks with regards to two types of properties: 1) intrinsic properties, which characterize an inherent feature of the solid electrolyte, regardless of its environment, and 2) extrinsic properties, which are the properties of the solid electrolyte when processed in a system (e.g., in an ASSLB). For a long time, the focus was put on optimizing the intrinsic properties of SEs, essentially increasing the ionic conductivity, but researchers have more recently acknowledged the equal importance of extrinsic properties in the development of ASSLBs.

1.4.1 – Intrinsic properties

1.4.1.1 – Bulk ionic conductivity

The ionic conductivity in a solid electrolyte is related to its crystal structure, which is usually composed of a face-sharing polyhedral frame supporting a network of mobile elements. The presence of a 3D network structure is favored over 1D and 2D frameworks because it allows the fast conduction of mobile species through continuous and interconnected networks, this structural trait is characteristic of most super-ionic conductors such as NASICON, perovskite and LISICON-type SEs [244, 245]. The ionic conductivity is possible when vacancies are distributed within the polyhedral framework, creating conduction channels to allow the mobile ions to hop from a vacancy to another with low migration barriers [210]. Ionic diffusion mechanisms also happen through Schottky interstitials, and interstitial-antisite exchanges, by continuously displacing the mobile ion to the next available site [246]. Both mechanisms are illustrated in **Figure 1.13A**. Therefore, the concentration and distribution of defects in a crystal structure will determine the diffusion types and pathways. More specifically, the ionic conductivity (σ_{ionic}) in solids is governed by the concentration of mobile ion carriers (n), the activation energy (E_a) and the mobility of mobile ion carriers (μ) following equations 1.3 and 1.4:

$$\sigma_{ionic} = n.q.\mu \quad \text{Eq. 1.3} \qquad \textit{with} \qquad \mu \propto e^{\frac{-E_a}{k_B T}} \quad \text{Eq. 1.4}$$

where q is the charge of the mobile ions, k_B is the Boltzmann constant and T is the temperature. Equations 1.3 and 1.4 show that low activation energies and high concentration of mobile ion carriers (vacancies and/or interstitials) are necessary to score a high ionic conductivity. Moreover, to yield high ionic conductivity, the conduction channels need to be neither too narrow, because it

would create a restrictive bottleneck with a very high activation energy, nor too wide, because it would decrease the polarizing effect of the anions on the mobile cation and impair its motion [247].

Strategies to increase the ionic conductivity in SEs include 1) doping the materials with aliovalent elements to increase the concentration of defects: higher-valence cations, to form cation vacancies and anion interstitials, and lower-valence cations, to form cations interstitials and anion vacancies [49, 248], 2) using materials with a highly polarizable anion in the sublattice, such as S^{2-} and halogen anions, that create softer bonds with the mobile cation, lowering the activation barrier and encouraging the cation mobility [249]. For these reasons, the best ionic conductivities at RT are reported for doped and sulfide-type solid electrolytes. The ionic conductivities for all the different SEs are reported in **Figure 1.13B** to illustrate this fact. For instance, doping NASICON-type materials by partially substituting Ti^{4+} in $LiTi_2(PO_4)_3$ or Ge^{4+} in $LiGe_2(PO_4)_3$ with Sc^{3+}, Fe^{3+}, La^{3+} and especially Al^{3+} effectively increased the bottleneck size in the structure, increasing significantly their ionic conductivities from 10^{-8} to $10^{-4}/10^{-3}$ S.cm^{-1} at RT [139-141, 250]. One of the best oxide Li-ion conductors is the doped perovskite-type material $Li_{0.33}La_{0.56}\square_{0.11}TiO_3$ with an ionic conductivity of 1.4 10^{-3} S.cm^{-1} [180]. In addition, argyrodites and thio-LISICON are better ionic conductors than oxide-based solid electrolytes thanks to the presence of large and highly polarizable S^{2-} anions, the best examples being $Li_{10}Ge(PS_6)_2$ (σ = 1.2 10^{-2} S.cm^{-1} at RT) [203, 206] and $Li_7P_3S_{11}$ (σ = 1.7 10^{-2} S.cm^{-1} at RT) [216]. Higher ionic conductivities are also obtained from the joint contribution of doping and the presence of a halogen anion sublattice, like it is the case for anti-perovskite-type material $Li_3OCl_{0.2}Br_{0.8}$ (σ = 1.94 10^{-3} S.cm^{-1} at RT) [190].

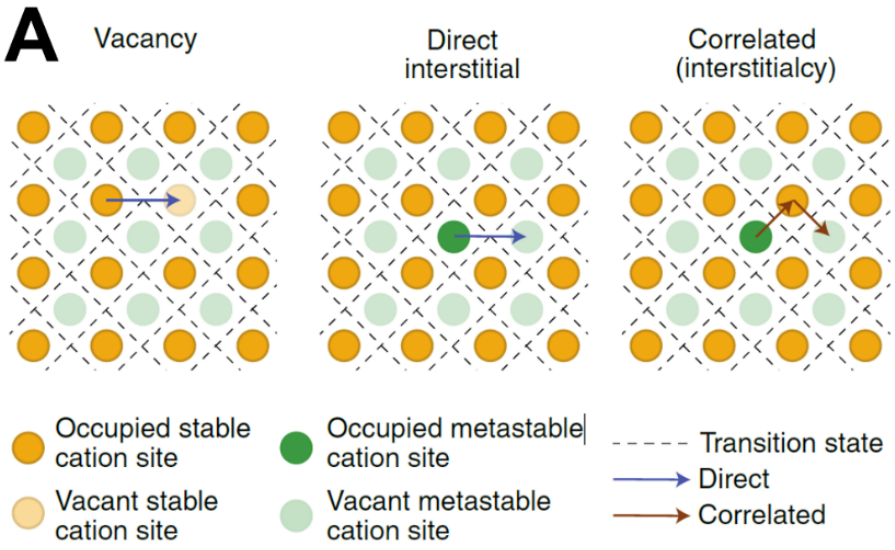

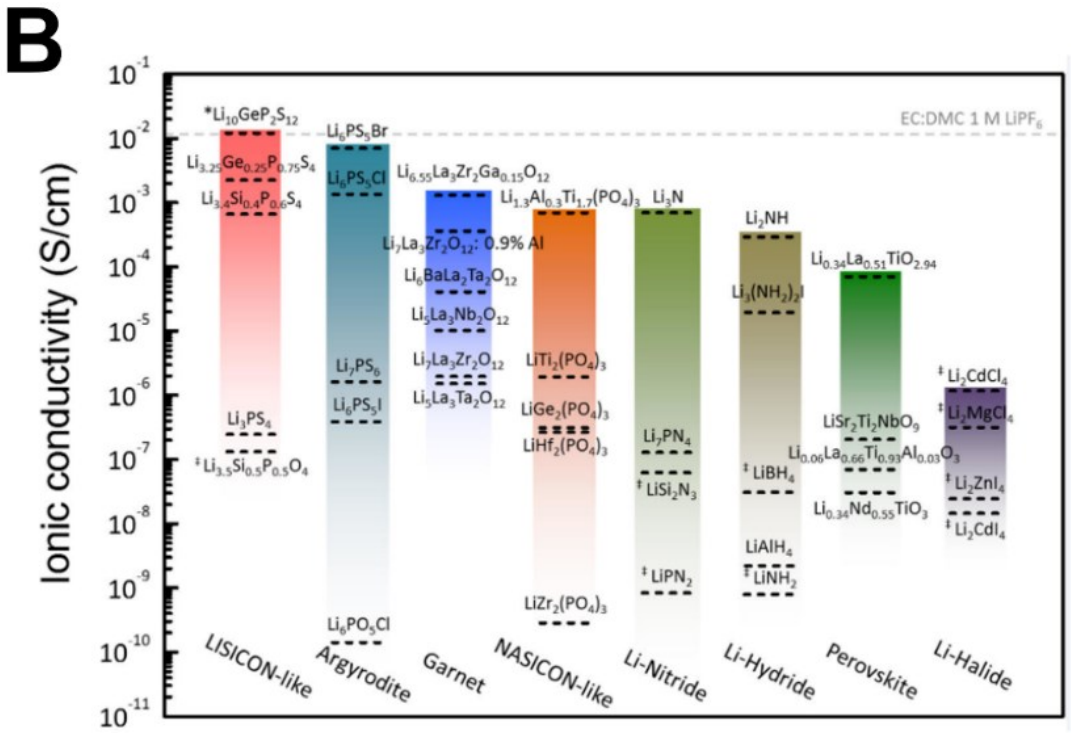

Figure 1.13 - A) Common lithium migration mechanisms: vacancy, direct interstitial and correlated (interstitialcy) involving a single site (blue arrow) or multiple sites (red arrow) [127]. B) Reported total ionic conductivity for several solid electrolytes at RT [134].

1.4.1.2 – Stability against air

The stability of solid electrolytes against ambient air is crucial given the fact that air-stable materials would significantly lower the manufacturing cost compared to air-sensitive ones. Processing air-sensitive materials at an industrial level requires the use of clean and dry rooms, which is possible at the cost of heavy investments. Sulfide-based LISICONs and argyrodites have the highest ionic conductivities, but they are hygroscopic and require to be handled in inert atmospheres, otherwise the hydrolysis of sulfides with air moisture generates toxic H_2S gas [251]. The most stable sulfide-based material against air and moisture is the $75Li_2S–25P_2S_5$ glass-ceramic. The addition of metals into $Li_2S–P_2S_5$ systems such as Bi, Sn, Fe or Zn proved to increase the stability of sulfides against air via an H_2S absorption mechanism [252]. Hydrides display the same instability against ambient air. For example, $LiBH_4$ generates flammable H_2 gas when exposed to moisture, making the material too dangerous for large-scale production [253]. Encapsulating $LiBH_4$ in a SiO_2 matrix stabilizes it against ambient moisture and helped increase its ionic conductivity to 10^{-4} $S.cm^{-1}$ at RT [254]. Although sulfide and hydride-based materials are the most problematic regarding the stability against air/moisture, some oxide-based

materials also display a subtle yet existing instability against moisture and CO_2. It's the case for garnet and perovskite-type materials such as $Li_xLa_3M_2O_{12}$ (M = Zr, Sn, Nb and Ta) and $Li_2SrTa_2O_7$. More specifically, $Li_7La_3Zr_2O_{12}$ is reported to form LiOH and resistive Li_2CO_3 at the surface when exposed to moisture and CO_2, hindering its ionic conductivity. Nevertheless, none of these decomposition products represent any health or environmental hazard, unlike H_2S produced in sulfur-based SEs. On the other side, NASICON-type materials are reported to be stable against air and moisture [143, 255-257].

1.4.1.3 – Electrochemical stability window

The electrochemical stability window (ESW) is the potential range within which the solid electrolyte is neither reduced nor oxidized. A narrow electrochemical window is a critical problem to overcome because it is the main limitation to the cell voltage, as previously mentioned in section 1.1.1.2 [258]. The reduction potential of a solid electrolyte is often determined by the reduction potentials of the cationic elements composing the SE. For example, the oxide-based SEs LLTO, LATP and LAGP have their reduction potential when Ge^{4+} and Ti^{4+} are reduced to Ti^{3+} and Ge^{2+} respectively [147, 186]. On the other end, the oxidation potential of a solid electrolyte is usually set by the anion framework, typically limited by the anion with the lowest ionization potential following the order $N^{3-} < P^{3-} < H^- << S^{2-} < I^- < O^{2-} < Br^- < Cl^- << F^-$ [259]. Above elemental considerations, the specific structure and bonding characteristics will also influence the ESW. For example, P atoms will be easier to reduce if they are weakly bonded to sulfur atoms compared to strongly bonding O atoms, as portrayed by the increased stability of Li_3PO_4 compared to Li_3PS_4 [259]. For this reason, sulfide-type solid electrolytes are known to have much narrower ESWs than their oxide-type counterparts. The ESW can be improved in solid electrolytes by creating stronger interactions between the atoms within the structure. For example, the stability of sulfide-based SEs LGPS was improved by partially substituting Li^+ with Ba^{2+} to form $Li_{9.4}Ba_{0.3}GeP_2S_{12}$. The strong interaction between Ba^{2+} and S^{2-} anions in the sublattice led to an enhanced stability [260]. However, such substitutions will most of the time hinder the ionic conductivity.

The stability window of solid electrolytes is traditionally characterized by CV, where the current is reported as a function of a sweeping voltage. CV curves provide us with information on the chemical reactions happening and on the material's cycling reversibility. However, these experiments may not reflect the concrete situation of a battery for two reasons: first, the ESW is overestimated when a conventional planar Li/SE/Inert blocking electrode cell configuration is used, in which the contact area between the SE and the inert blocking electrode is limited, resulting

in small redox current signals and even slower kinetics of the electrolyte's decomposition reaction. For example, LGPS's ESW was reported to be of 0 - 5 V vs. Li^+/Li using CV in a planar cell configuration at a 1 $mV.s^{-1}$ scan rate [206]. However, the use of a Li/LGPS/LGPS+C composite cell configuration concluded on a much narrower window of 1.7 - 2.1 V vs. Li^+/Li [175]. The same was observed for LLZO [175]: LLZO's stability window was initially assessed using a planar configuration Li/LLZO/Pt and was reported to range from 0 to 5 V vs. Li^+/Li as seen in **Figure 1.14A** [206]. However, in a composite configuration Li/LLZO/ LLZO+C, the apparent oxidation of LLZO was observed as early as 4.0 V (**Figure 1.14B**). The same was observed for LIPON solid electrolyte [261]. More details regarding the ESW will be given in chapters 3 and 4. Second, the electrochemical stability window is usually overestimated when fast rate CV is used to probe the solid electrolyte. It is too fast to detect the sluggish decomposition reactions happening. The voltage sweeping causes a constant perturbation of the system, which never reaches equilibrium. Done this way, the observed stability might be due to kinetic limitations of the redox reaction rather than its real thermodynamic stability. Most decomposition products at high voltages are electronically insulating and/or are only formed at large overpotentials (especially when gas is produced). Therefore, fast rate CV does not allow enough time for these reactions to happen, giving way to an apparent stability [262].

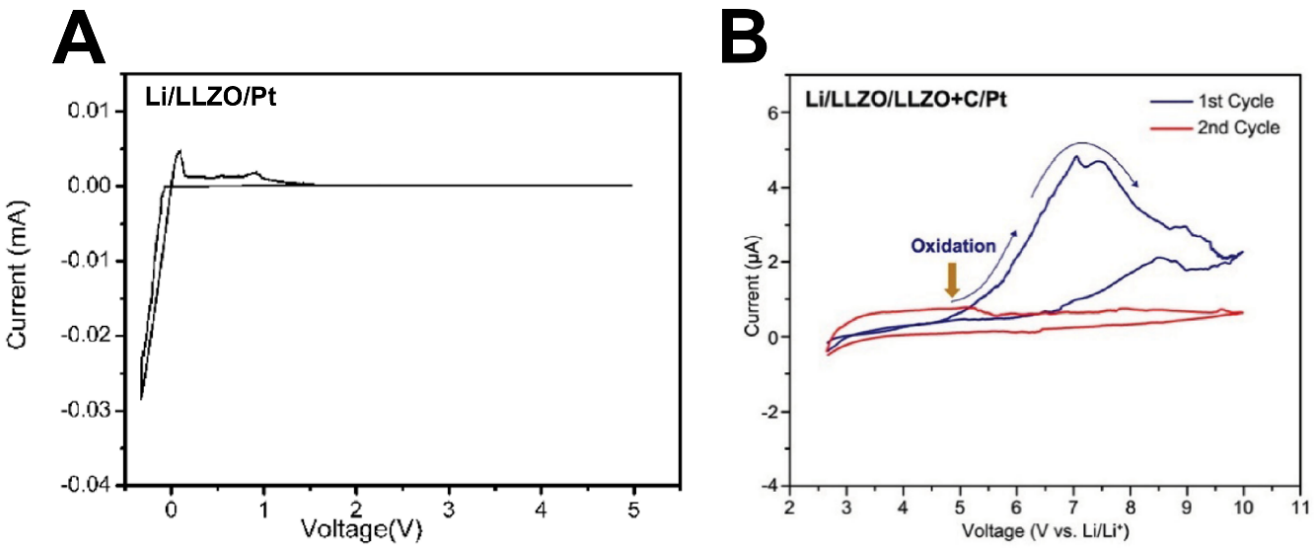

Figure 1.14 - Comparison of two ESWs assessed for LLZO using cyclic voltammetry on A) a planar configuration Li/LLZO/Pt between −0.3 and 5 V at a scanning rate of 0.1 $mV.s^{-1}$ [263] and B) a composite configuration Li/LLZO/LLZO+C/Pt between 2.6 and 10.0 V at a scanning rate of 0.01 $mV.s^{-1}$ [175].

1.4.1.4 – Electronic conductivity

A very characteristic issue in solid-state super-ionic conductors is the occurrence of electronic conduction. However, even though preferentially very small, it is never zero due to diffusive motion of the ions [87]. Electronic conductivity must be negligible, if not inexistent, in solid electrolytes. Even very small electronic conductivities can lead to perceptible self-discharge and cause parasitic chemical reactions within the battery [262]. The electronic conductivity in solid electrolytes must not exceed 10^{-6} S.cm^{-1} at any temperature [264]. Ideally, it should be around 10^{-12} S.cm^{-1} or remain at least four orders of magnitude smaller than the ionic conductivity [95]. Here, we define the ionic conductivity to be the value calculated exclusively from the concerted diffusion of mobile Li^+ ions through the structure. Not to be confused with the conductivity of other ions in the structure (nor the ones that originate from defects).

Electronic conductivity occurs intrinsically, by drift of free charge carriers, and extrinsically, brought by impurities and defects. Charge carriers, and therefore electronic conductivity, are generated by thermal excitation of electrons to current-carrying states. The electronic conductivity is deduced from the charge carrier concentrations and their mobility [265]:

$$\sigma_e = e(n\mu_e + p\mu_h) \qquad \text{Eq. 1.5}$$

where σ_e is the electronic conductivity, e is the elementary charge, n and p are the charge carrier concentrations of electrons and holes respectively. μ_e and μ_h are the mobilities of electrons and holes respectively. The mobility is related to the carrier effective mass [266]:

$$\mu = \frac{e}{m*}\bar{\tau} \qquad \text{Eq. 1.6}$$

where m^* is the effective mass of the material and $\bar{\tau}$ the scattering time.

The electronic conductivity is determined experimentally in solid electrolytes via DC polarization measurements, using cells in a symmetric configuration with ion blocking Au electrodes.

The ionic conductivity in solid electrolytes was extensively investigated in order to achieve liquid electrolyte-like ionic conductivity. In the process, other properties such as the electronic conductivity were considered of secondary importance. However, studies recently established a link between electronic conductivity in solid electrolytes and the formation of lithium dendrites in ASSLBs, proving that the plating of Li in SEs was proportional to the increase of their electronic conductivity [267]. In the context of this study, the electronic conductivity was measured for LLZO and Li_2S-P_2S_5 to be 5.5 10^{-8} and 2.2 10^{-9} S.cm^{-1} respectively. These values are far above the ideal threshold of 10^{-12} S.cm^{-1}. Moreover, another study showed that the electronic conductivity of LLZO increased from 1.2 10^{-7} to 1.1 10^{-6} S.cm^{-1} after LLZO is reduced [268], proving that electronic

conductivity can be an electrochemically activated process (in which case an extrinsic dimension could be considered for the electronic conductivity). These studies highlight the importance of a negligible electronic conductivity in SEs and of identifying the sources for high electronic conductivity. More details regarding the electronic conductivity in solid electrolytes will be provided in chapter 5.

1.4.1.5 – Mechanical properties

The mechanical properties of solid electrolytes are defined by three metrics: 1) the elasticity, related to the atomic bonding of the material, corresponds to the elastic deformation of the material under applied stress and is derived from its Young modulus, 2) the plasticity, related to the hardness of a material, depends on the microstructure, the phase composition and the Young modulus of the material. It describes its resistance and rigidity to non-elastic deformations and is derived from the shear modulus of the material. 3) the fracture toughness, which describes the ability of a material to resist crack growth, depends on the volume, porosity and existing defects in the material [269].

An isotropic distribution of mechanical properties along all directions is desired for SEs [270]. Rhombohedral R3c phases, such as NASICONs, possess anisotropy mechanical properties while materials with higher symmetry (e. g., cubic like garnets and perovskites) possess more isotropic mechanical properties [271]. Typically, inorganic ceramics exhibit a higher hardness than that of organic polymers. Among ceramic solid electrolytes, sulfide-based SEs such as LISICONs and argyrodites have much smaller Young moduli than oxide-based SEs (<40 GPa for sulfides vs. >100 GPa for oxides), giving them the advantage over oxides of being more compliant to deformation [272-276]. A low Young modulus allows the ceramics to be processed more easily, with low sintering temperatures. The ability of processing materials at low temperatures is a crucial property in SEs because it circumvents the reactivity and decomposition issues encountered at high temperatures. SEs with high Young moduli were advertised as the solution to prevent the formation of dendrites at the interface with metallic lithium [277, 278]. However, dendrites were later reported to form between the cracks at the surface of SEs regardless of their Young moduli [279]. On the other side, oxide-based materials exhibit higher fracture toughness values than sulfur-based materials (around 0.1 $MPa.m^{1/2}$ for argyrodites vs. ≈ 1 $MPa.m^{1/2}$ for oxides) [272, 273, 275], making them more resistant to crack growth. It is worth mentioning that even oxide-based SEs appear rather brittle compared to metals with fracture toughness ranging from 20 to 100 $MPa.m^{1/2}$ [280].

1.4.2 – Extrinsic properties

To ensure the concerted electronic and ionic transfers through a battery, sufficient contact and cohesion are required between the solid electrolyte and the electrodes. This prerequisite is easily fulfilled with conventional electrolytes because their liquid nature provides a perfect wetting of the electrodes. In ASSLBs, the electrode materials need to be processed with the solid electrolyte into very dense composite electrodes in order to ensure sufficient contact between the two. To ensure the electronic insulation, ideally a thin and dense solid electrolyte layer should be placed between the two composite electrodes, with a large area in order to obtain a low internal resistance. The abilities of solid electrolytes to be processed in ASSLBs are referred to as extrinsic properties. **Figure 1.15** summarizes the extrinsic properties that solid electrolytes need to possess in order to be processed in ASSLBs. The figure demonstrates that extrinsic properties in solid electrolytes are mostly related to interfaces, including interfaces within the solid electrolyte layer and interfaces between the SE and the composite electrodes. These extrinsic properties are detailed in the following sections.

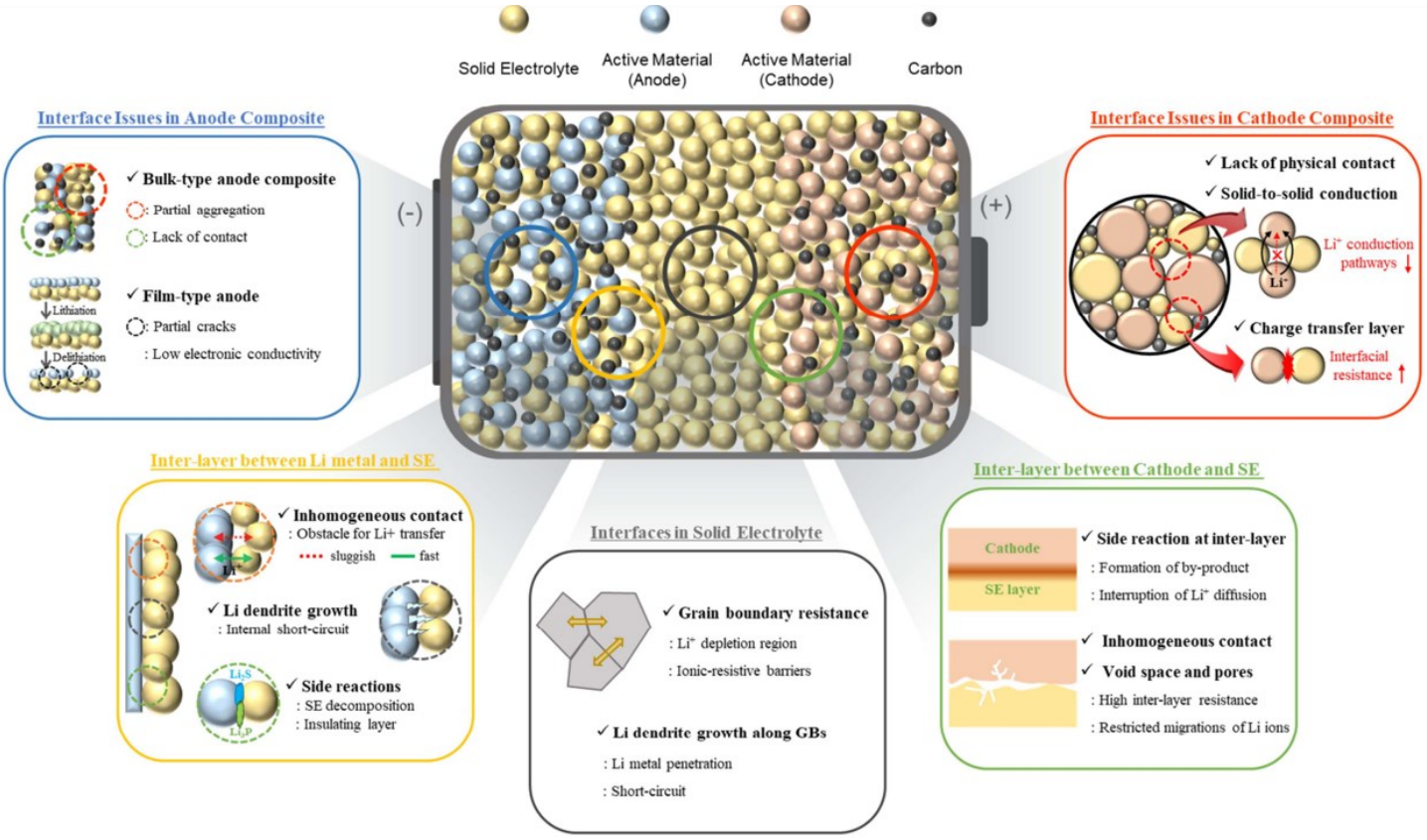

Figure 1.15 - Schematic illustration and brief summary of the extrinsic properties to take into account in order to implement solid electrolytes in all-solid-state batteries [126].

1.4.2.1 – Chemical stability against positive and negative electrodes

The behavior of solid electrolytes at their interface with electrode materials often present major deviations from their behavior in the bulk materials. The formation of hardly characterizable decomposition products at the interface, often ionic insulators and/or electronic conductors, hinder the performance of solid electrolytes. Stabilizing these interfaces is crucial to the development of solid electrolytes and establishing viable SE/electrode material combinations for all-solid-state batteries. The term ‘’interface’’ refers to the area of contact between the solid electrolyte and electrode material phases. On the other hand, ‘’interphase’’ refers to the new phase that is formed at the interface due to chemical and electrochemical reactions [127].

1.4.2.1.1 – SE/negative electrode material

The introduction of Li metal as the negative electrode in ASSLBs is considered possible thanks to solid electrolytes. However, overwhelming evidence showed that most relevant solid electrolytes are not thermodynamically stable against metallic lithium. Perovskite LLTO and NASICON LATP solid electrolytes were proven to react in contact with metallic lithium, with the reduction of Ti^{4+} by Li metal [281, 282]. NASICON-type materials LAGP and LZP are not stable against Li metal neither [283-285]. Recent studies shed light on the instability of garnet Al, Ta, Nb and W doped-LLZO against lithium metal at high temperature, as seen on **Figure 1.16A** [170]. Ma *et al.* used aberration corrected scanning transmission electron microscopy to observe the phase transition of a thin layer of cubic-LLZO into tetragonal-LLZO at the interface with Li metal [286]. LiPON was also reported to be reduced by Li metal to from Li_3P, Li_3N, and Li_2O decomposition products that act as a passivation layer [261]. Sulfide-type solid electrolytes are also known to be unstable against Li metal. Argyrodite Li_2S-P_2S_5 and LISICON-type LGPS solid electrolytes react in direct contact with Li metal to form a highly resistive interphase. The decomposition of LGPS at the interface with Li metal into Li_3P, Li_2S and Li–Ge alloys was observed using *in situ* X-ray photoelectron spectroscopy (XPS) combined with time-resolved electrochemical measurements by Wenzel *et al.* [287].

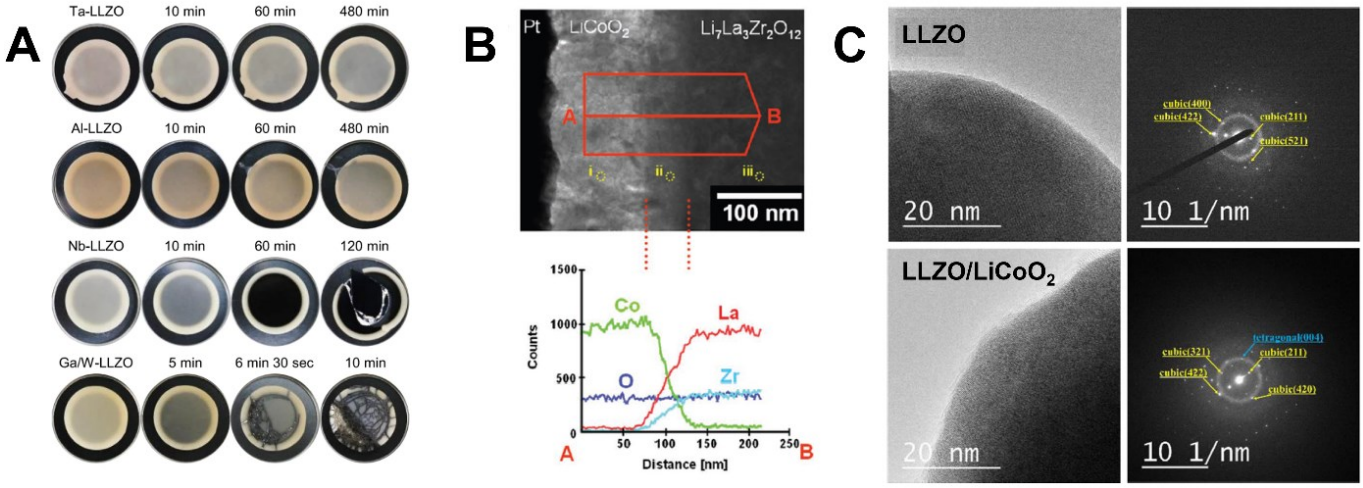

Figure 1.16 - A) Optical images of Ta, Al, Nb and Ga/W-doped LLZO pellets in contact with Li metal at 200 °C over time after assembly under a cold-isostatic pressure of 250 MPa [170]. B) TEM cross-section image and the corresponding EDS line profile of an LLZO/ $LiCoO_2$ thin-film interface, an intermediate layer of ≈50 nm thickness of La_2CoO_4 was formed due to mutual diffusion [288]. C) Comparison of two TEM cross-section images of pristine LLZO and LLZO/$LiCoO_2$ powders and their corresponding electron diffraction patterns. The electron diffraction pattern of the garnet surface in LLZO/$LiCoO_2$ is assigned to tetragonal-LLZO [289].

Solid electrolytes that are ‘’pseudo-stable’’ against lithium include LiPON, Li_3PS_4 and Li_4PS_4I due to kinetic stabilization. The decomposition products at the interface Li_2O, Li_2S, Li_3P, Li_3N and LiI, which are all electronically insulating and thermodynamically stable against metallic Li, have no thermodynamic driving force to form deeper in the bulk. The resulting reducing interphase stabilizes the solid electrolyte [49], the same phenomenon is not observed when the decomposition products are mixed conductors, like it’s the case for LATP and LLTO.

1.4.2.1.2 – SE/positive electrode material

The use of high potential positive electrodes will require stable interfaces between positive electrode materials and solid electrolytes. Oxide-based solid electrolytes tend to be more thermodynamically stable against positive electrode materials than sulfide-based SEs [290]. The exception being LLZO, which instability against positive electrode materials like $LiCoO_2$, NMC and NCA was reported [288, 291]. Kim *et al.* observed the formation of La_2CoO_4 at the interface (**Figure 1.16B**) while Park *et al.* noticed the formation of tetragonal-LLZO (**Figure 1.16C**) [288, 289]. Side reactions were also observed between LiPON and $LiCoO_2$, where an ultrathin layer of nitrogen-containing species NO^{2-} and NO^{3-} was formed when LiPON was sputtered onto $LiCoO_2$,

but the interphase is considered stable and therefore not detrimental to the battery's operation [292].

Sulfur-based solid electrolytes are almost all thermodynamically unstable against oxide-based positive electrode materials. When sulfur-based SEs are in contact with oxide-based positive electrode materials, a space-charge layer is formed in the interface. This space-charge layer is created because Li ions in SEs are strongly attracted to highly electronegative oxygen atoms in the oxide-based positive electrode materials, leading to the depletion of Li ions in the solid electrolyte layer at the interface [293]. Particularly, LISICON-type solid electrolyte LGPS was reported to be chemically unstable with most of the relevant positive electrode materials such as $LiCoO_2$, $LiMn_2O_4$ and $LiFePO_4$ [259, 294]. Hydride SEs have high reducing capability and reduce most positive electrode materials. The combination of $LiBH_4$ and $LiCoO_2$ was investigated and the formation of $LiBO_2$, Li_2O, Co_3O_4 and CoO(OH) decomposition products was observed [295]

To solve the interfacial instability, addition of buffer layers and surface modifications have been reported on the solid electrolyte and the positive electrode material. Coating of stable oxide-type materials such as $LiNbO_3$, Li_2SiO_3, Li_3PO_4, $Li_4Ti_5O_{12}$, Al_2O_3, $BaTiO_3$ and Li_2O-ZrO_2 surface is a popular approach for preventing side reactions and for stabilizing sulfur and oxide-based solid electrolytes alike with oxide positive materials [206, 294, 296-303]. For example, Sakuda *et al.* used Li_2SiO_3 coating on the surface of $LiCoO_2$ to successfully stabilize its interface with Li_2S–P_2S_5 material [294].

1.4.2.2 – Grain boundary ionic conductivity

The grain boundary conductivity is specific to ceramic solid-state materials. The grain boundary is the interface between two grains, or crystallites, in a polycrystalline material, they are considered 2D defects in the crystal structure. In heterogeneous systems such as ceramic SEs, the contribution of the interfaces is significant to the total conductivity of the material. In fact, because the percolation of mobile Li-ions is interrupted by the distortions created by the misalignment of grains [304], the grain boundary resistivity hinders the total ionic conductivity of many SEs as it is often several orders of magnitude greater than the bulk resistivity [305].

In general, SEs powders need to be processed into high-aspect-ratio membranes or pellets, regardless of the synthesis method used [127]. High densification is necessary to percolate the grains and can be achieved through a combination of high temperature sintering and pressing [306]. Many factors will influence the grain boundary ionic conductivity, among them the

grain and particle sizes, the bulk density, the sintering time and temperature, the pressure applied. In general, larger grain size, smaller particle size, smaller grain boundaries and high bulk density lead to higher ionic conductivities, although better conductivities were obtained for LLZO, $LiNbO_3$, $Li_4Ti_5O_{12}$, ZrO_2, CeO_2 and TiO_2 when their grain size reached the nano scale [307-312]. This phenomenon is justified by a lower impurity segregation (impurities act to block Li-ion conduction) on the grain boundaries of nanocrystalline materials [309].

Thanks to their high machinability and softness, sulfide-based and borohydride solid electrolytes have a grain boundary resistivity that can be easily reduced by cold-pressing, allowing a high total ionic conductivity at RT [313]. On the other hand, oxide-based solid electrolytes suffer from high grain boundary resistivity. Based on the Schottky barrier model, the grain boundary resistivity has been attributed to the creation of a space charge layer between the grains and the Li^+ depletion at the grain boundary [314, 315]. Garnet-type LLZO is the oxide-based solid electrolyte with the lowest grain boundary resistivity thanks to its three-dimensional lithium paths connecting the grains [316]. Strategies were explored to decrease the grain boundary resistivity in solid electrolytes, especially in oxide-based SEs. The explored routes mainly gravitate around high temperature sintering, such as the use of spark plasma sintering (SPS), which enables a precise control of the microstructure [317-319]. Adding excess Li during sintering was suggested to compensate for the depletion of Li^+ at the grain boundaries of LLTO solid electrolyte and decrease the grain boundary resistivity [320]. Filling the grain boundaries with additives such as amorphous silica or sintering agents yielded positive outcomes for LLTO, LAGP and LATP [320-322].

1.4.2.3 – Resistance at the interface

The interfacial resistance between the solid electrolyte and the electrodes is a property that needs to be optimized before a large-scale commercialization of ASSLBs is possible. Poor interfaces obstruct the large-scale transfer of ions in a battery and significantly hinder its cycling performance. This resistance is due to an insufficient contact area between the SE and the electrodes in ASSLBs, unlike conventional Li-ion batteries, where a perfect wetting of the electrodes by the liquid electrolyte is observed. Like for grain boundary resistivity, the interface resistivity problem mainly occurs in rigid oxide-based SEs, while soft and deformable sulfide or hydride-type SEs avoid it. Many strategies were explored to decrease the interfacial resistance on oxide-based solid electrolytes: 1) applying external pressure on the ASSLB to enforce intimate contact [323], 2) co-sintering the electrode material and the solid electrolyte or soldering them

together to provide an intimate contact [319, 324-326], 3) dry or wet polishing the surface of the solid electrolyte to remove impurities and ensure a perfectly flat surface [327, 328], as demonstrated with LAGP in **Figure 1.17A,** 4) depositing Li, Si, Al, In, Au or Nb metal layers between the lithium negative electrode and the solid electrolyte (e.g., Al-coated LLZO in **Figure 1.17B** and **C**) [289, 329-333], similar results were achieved with oxide compounds such as Li_3PO_4 [334], ZnO [335], ZrO_2 [336], Li_3BO_3 [337], $LiNbO_3$ [338], $BaTiO_3$ [339], TaO_3 [340], $LiAlO_2$ [341], Li_2CO_3 [342], Al_2O_3 [343], amorphous C [344] and polyethylene oxide-based polymer interlayers [148, 345, 346], 5) melting the solid electrolyte on the electrode material or vice versa to increase the wetting [347, 348], 6) building 3D structured components to increase the contact between the electrolyte and electrodes [349], 7) using sacrificial polymer matrix to embed interspersed solid electrolyte and positive electrode particles [350] and 8) growing solid electrolyte and electrode particles in the same orientation to decrease the lattice mismatch between the two and facilitate the migration on Li ions [351].

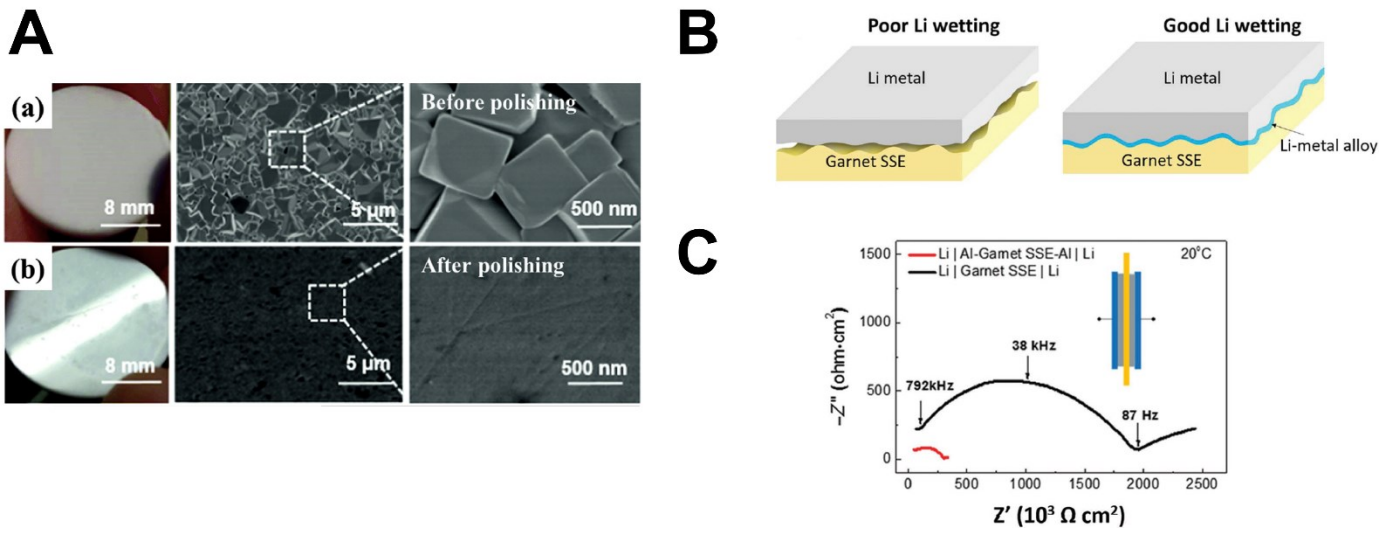

Figure 1.17 - A) Photograph and SEM images of LAGP pellets showing the surface and microstructure (a) before and (b) after polishing [352]. B) Schematic representation of a solid electrolyte and metallic lithium interface with and without Al-coating [329]. C) EIS measurements of a Li/LLZO/Li and Li/Al-LLZO-Al/Li interface at RT, R_{int} decreased from 950 to 75 $\Omega.cm^{-2}$ [329].

1.4.2.4 – Mechanical integrity during cycling

Solid electrolytes are rigid materials and run the risk of mechanical fracture, delamination and a loss of physical contact following the volume change of electrodes upon cycling [353-357]. Indeed, reversible insertion of lithium ions in and out of the electrodes' active materials causes a volume expansion and contraction of the electrodes. The SE particles cannot sufficiently suppress this volume change, and the continuous mechanical stress during cycling generates cracks that propagate in the solid electrolyte as illustrated in **Figure 1.18A** [353, 355]. Such phenomenon was even observed with ductile solid electrolytes like argyrodite-type material $75Li_2S{\cdot}25P_2S_5$ after cycling (**Figure 1.18B**). Another important mechanical issue with all solid electrolytes is the growth of lithium dendrites along the grain boundaries despite the high young and shear moduli of solid electrolytes, as seen many times through optical and electronic microscope observations, including for LLZO and LIPON SEs, displayed in **Figure 1.18C** [358]. Solid electrolytes were initially expected to be immune to this dendrite-induced failure by virtue of their mechanical strength, but recent studies have demonstrated the ability of metallic Li to penetrate into even sintered solid electrolytes [359]. Ceramic solid electrolytes all suffer from mechanical failure and loss of physical contact upon cycling, the development of effective strategies to alleviate this issue is imperative in the engineering of ASSLBs.

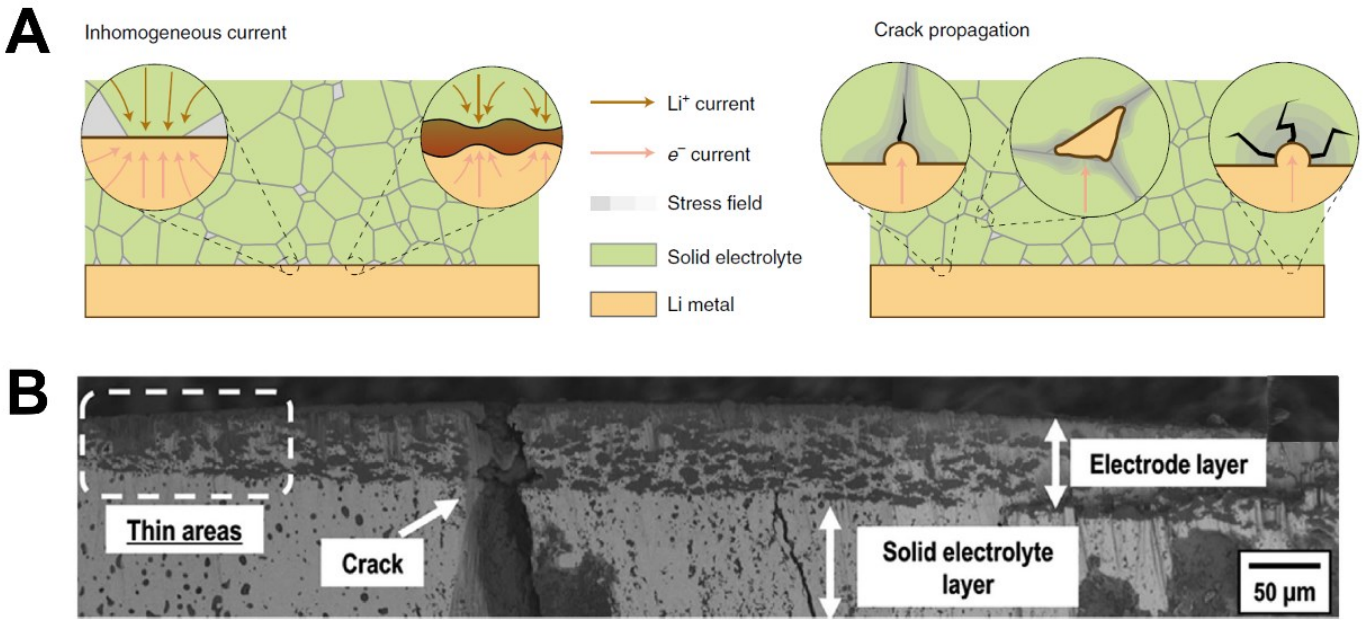

C

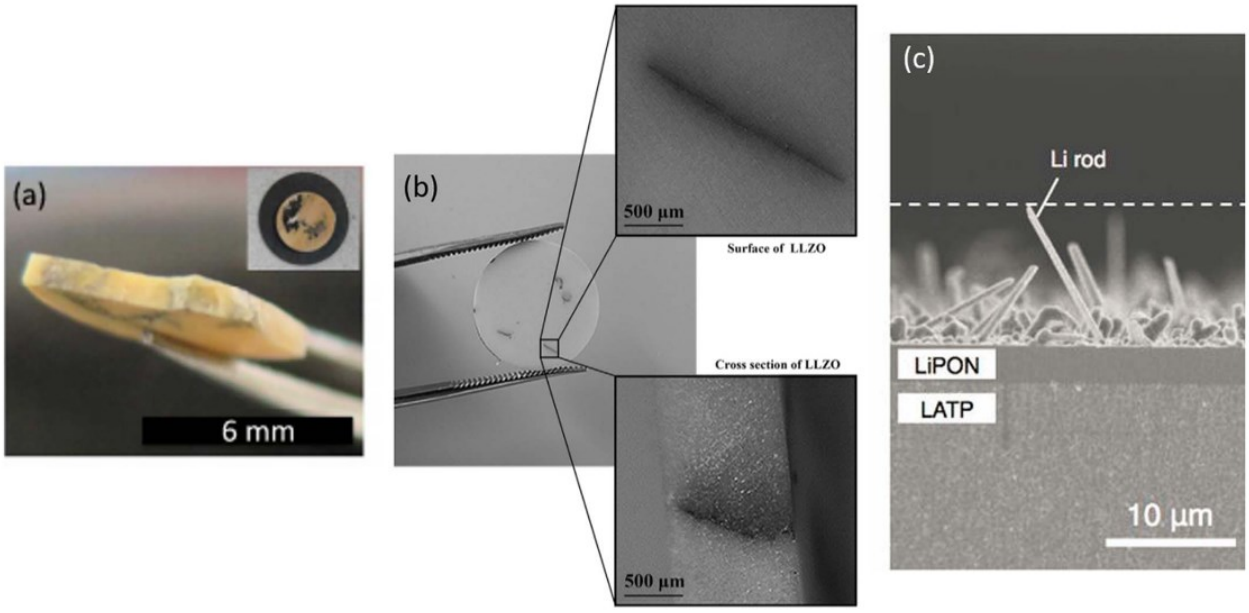

Figure 1.18 - A) Schematic representation of an inhomogeneous Li deposition on the SE surface: imperfect contact and interphase formation (brown) cause current hotspots (left). The preferential Li deposition in grain boundaries and within grains creates localized stress resulting in cracks (right) [127]. B) Cross-sectional SEM micrograph of a graphite/$75Li_2S{\cdot}25P_2S_5$ interface after cycling. The SE particles cannot suppress the volume change in graphite, and the continuous mechanical stress during cycles results in the generation of partial cracks in SE particles [360]. C) Reports of Li metal transverse dendrite grown in SEs: (a) Ga-doped LLZO cycled with Li metal [361], (b) Al-doped LLZO samples after symmetric Li plating [348] and (c) cross section SEM image of Li metal microstructure at a LiPON-Li interface showing the formation of dendrites [362].

The exploration of these intrinsic and extrinsic properties has been at the heart of the development of ASSLBs for several decades. Despite impressive advancements, none of the reported SEs can meet all the requirements to be implemented in ASSLBs. **Figure 1.19A** compares different SE families with regard to general aspects that are redox stability, ion selectivity, electronic and ionic resistances, device integration, processing cost, mechanical strength, thermal and chemical stability. The figure shows that none of the solid electrolyte families covers the entire radar plot. These specific criteria are not all fulfilled at once because intrinsic properties such as a high ionic conductivity, a chemical and electrochemical stability against high-potential positive electrode materials and metallic lithium negative electrode and chemical stability against air/moisture/CO_2 cannot all be found in one unique SE. In addition to these essential materials properties, ASSLBs also face many further challenges largely associated with solid-solid

interfaces, such as the lack of contact at the electrolyte/ electrodes interface and the mechanical failures following the electrodes' volume expansion upon cycling. As a result, no ASSLB has managed to reach the performances of a commercialized conventional Li-ion battery, as highlighted in **Figure 1.19B**.

The study of solid electrolytes is tedious because the characterization of the solid-solid interface is complicated. Interfaces are concealed within the SE and the electrodes or between the SE's grains. Therefore, characterizing short-range interactions, atomistic mechanisms and diffusion phenomena at the interface is complex and delicate. In addition, reactions often occur on a small fraction of the surface and can hardly be observed or characterized experimentally, making the results reported on the matter controversial because difficult to reproduce. Understandably, it is rather difficult to address all these challenges using only the conventional experimental trial-and-error approach. Computational modeling intervenes in this context as a key element, it complements experiments by simulating localized phenomena at the atomistic level and providing valuable understanding of the underlying mechanisms occurring in ASSLBs.

A

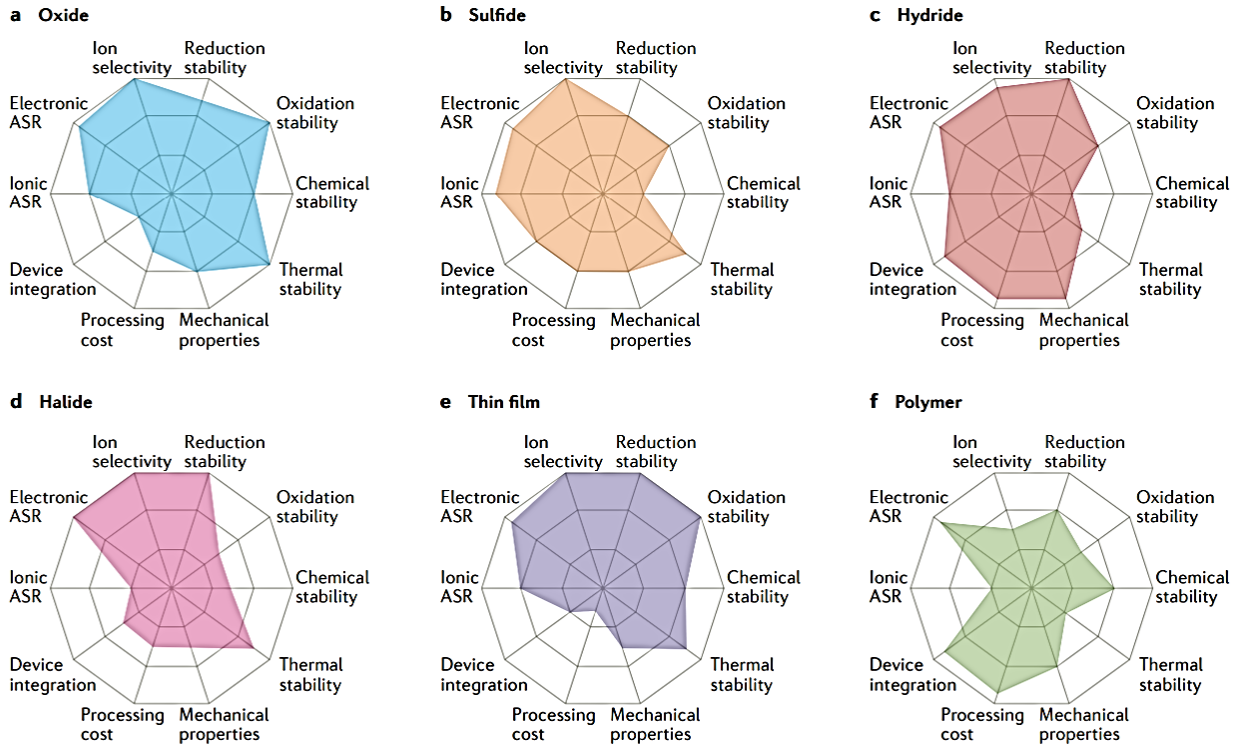

B

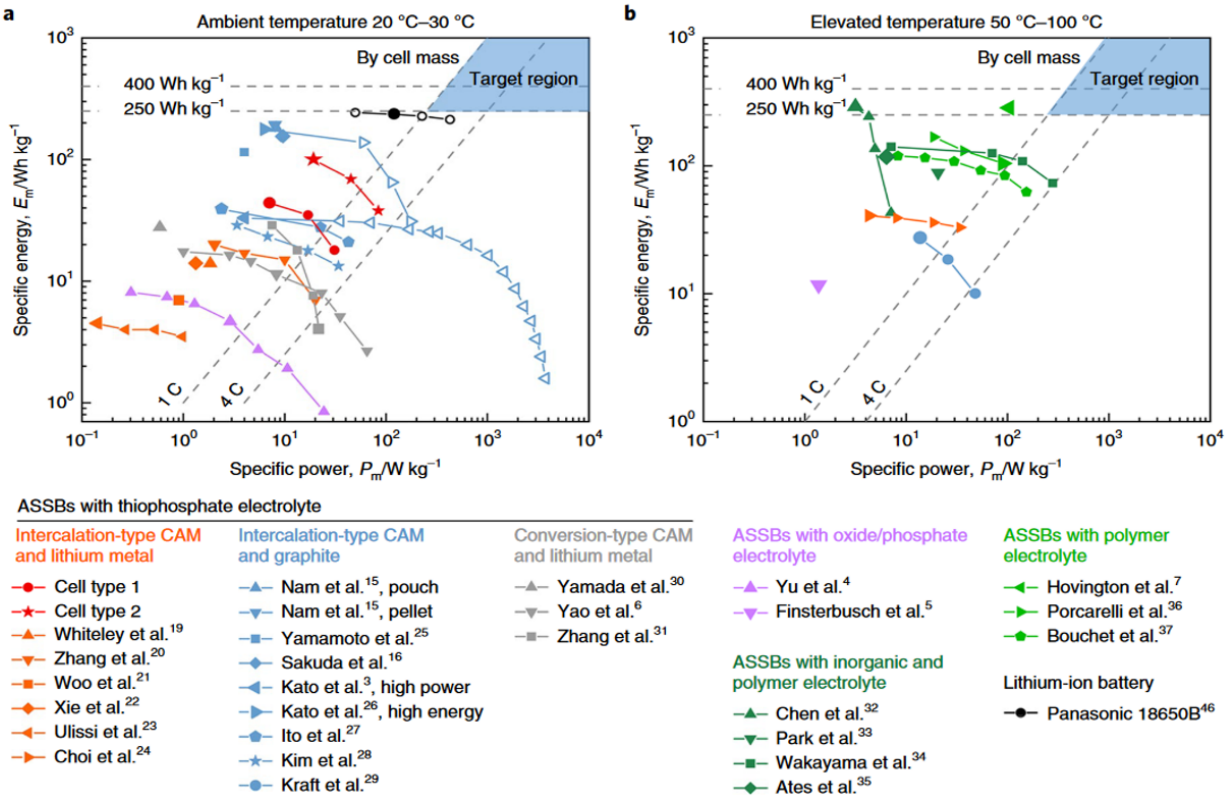

Figure 1.19 - A) Radar plots of performance properties of different solid electrolyte families: a) oxides, b) sulfides, c) hydrides, d) halides, e) thin-films like LIPON and f) polymer solid electrolytes. ASR stands for area-specific resistance. B) Ragone plots for ASSLBs cycled at a) room temperature (20–30 °C) and b) higher temperatures (50–100 °C). Dashed lines indicate targets for specific energy and C-rate. The specific energy and power are normalized to the cell mass. Filled symbols indicate data of cells that were charged and discharged at equal current density. Empty symbols indicate cycling data in which the rate test was only applied to discharge, whereas charging was carried out at lower current [363].

1.5 – First-principles for all-solid-state lithium batteries

First-principles computations are based on the fundamentals of quantum mechanics. One of the most widely used approach relies on density functional theory (DFT). DFT calculations deal with the ground states of the electrons in a system. The wavefunctions of the electrons are determined by solving the Schrödinger equation in many-body quantum mechanics resorting to various approximations [364]. First-principles calculations have become the most reliable approach to model the atomic scale. Computational modeling based on DFT calculations has been developed to compute the energies of SEs structures and obtain fundamental understanding

of their properties at an impressively large scale [365]. Comprehensive materials databases were created to gather and redistribute all these computed data, encouraged by the materials genome initiative (MGI) [366]. Such databases were built to systematically produce, organize and share data to supply computational tools that will screen, optimize and predict materials at very large scale and rate [367-369]. One of the most developed databases is the Materials Project®, launched by researchers from the Massachusetts institute of technology and further developed in the Lawrence Berkeley National Laboratory [370], it provides thermodynamic data and quantities that can be used to compute several properties of solid electrolytes.

Computational modeling has proved to be extremely useful not only at anticipating and resolving all the challenges faced with SEs mentioned in the previous sections, but also in predicting and designing new materials with great potential application in ASSLBs.

1.5.1 – Ionic diffusion in solid electrolytes

1.5.1.1 – Simulating and understanding ionic conductivity

A high ionic conductivity is a single property that only a handful of candidates possess among solid materials, understanding the fast Li^+ diffusion mechanisms in super-ionic conductors like LGPS or LLTO is important in order to screen and design for novel solid electrolytes. Ionic diffusion in materials can be studied using the nudged-elastic-band (NEB) method [371]. The NEB method is used to compute the transition state and activation energy needed for a mobile ion to migrate along a predetermined path, from one equilibrium site to another via vacancies and interstitial sites. To run a NEB calculation, it is necessary to provide as input data the initial and final migration sites as well as an initial migration path. In general, NEB calculations are suited to study materials with well-defined hopping sites and migration pathways [247, 372]. When the initial migration path cannot be guessed, the use of *ab initio* molecular dynamics (AIMD) is preferred to NEB. In AIMD, the atomic forces from first-principles methods are used to propagate the atoms in the system according to the laws of classical mechanics [372]. These simulations are performed to directly observe migration mechanisms of all ions in real-time, allowing to identify the precise diffusion mechanisms and migration pathways without having to assume diffusion pathways [373]. However, they require heavy computational power, with each step, of the tens of thousands necessary to converge the simulation, being a separate DFT calculation. The first diffusional feature extracted from AIMD simulations is the mean-squared displacement (MSD) of a mobile ion (e.g., Li^+) expressed in equation 1.7 [374]:

$$MSD_{\sigma}^{Li}(t) = \frac{1}{N_{Li}} \sum_{i,j}^{N_{Li}} \langle [\boldsymbol{R}_i(t'+t) - \boldsymbol{R}_i(t')][\boldsymbol{R}_j(t'+t) - \boldsymbol{R}_j(t')] \rangle \quad \text{Eq. 1.7}$$

with N_{Li} is the number of Li ions in the system, t is the time, $\boldsymbol{R}_i$ is the position of the ith Li ion, $\boldsymbol{R}_j$ is the position of the jth counter-ion and the brackets <…> represent the average over many starting times t' [375, 376]. The MSD is the distance traveled by an ion in a certain period of time. The collective diffusion coefficient $D^{Li}{}_{\sigma}$ of the mobile ion Li is quantified by fitting Einstein's relation 1.8:

$$D_{\sigma}^{Li} = \lim_{t \to \infty} \frac{MSD_{\sigma}^{Li}(t)}{2dt} \quad \text{Eq. 1.8}$$

d is the system's dimension (d=3 for 3D materials). The ionic conductivity (σ_{ionic}) is derived from the collective diffusion coefficient using a corrected Nernst-Einstein relation 1.9 [377]:

$$\sigma_{ionic}(t) = \frac{N_{Li} Z^2 e^2}{V k_B T} D_{\sigma}^{Li} \quad \text{Eq. 1.9} \qquad \text{and} \qquad \sigma_{ionic} = A e^{-\frac{E_A}{k_B T}} \quad \text{Eq. 1.10}$$

where N_{Li} is the number of Li ions in the system, e is the elementary charge of an electron, Z is the charge of the mobile Li ion, V is the volume of the cell, k_B is the Boltzmann constant and T the temperature. The activation energy of Li diffusion E_A can be derived from the ionic conductivity following Arrhenius's equation 1.10, where A is a constant related to the attempt frequency [374].

The ionic conductivity and activation energy computed for solid electrolytes using AIMD are in excellent agreement with the experimentally measured ionic conductivity for many solid electrolytes such as LATP, LLZO and LGPS (1.4 10^{-2} S.cm^{-1} calculated vs. 1.2 10^{-2} S.cm^{-1} measured at RT) [378, 379]. AIMD also allowed the first observation of the 3D conduction mechanism of Li^+ ions in LGPS, later confirmed by neutron diffraction [378, 380], and the first observation of a concerted migration of Li^+ ions in the material (multiple Li ions hopping to the nearest sites) [381]. The concerted migration of Li^+ is illustrated in **Figure 1.20A**, and was proven using NEB to decrease the activation energy barrier in solid electrolytes, as exemplified with LATP in **Figure 1.20B.** The concerted migration was later confirmed as a diffusion mechanism in several other materials such as LLZO, $LiZnPS_4$, $Na_{10}SnP_2S_{12}$, and $LiTaSiO_5$ [373, 382-384].

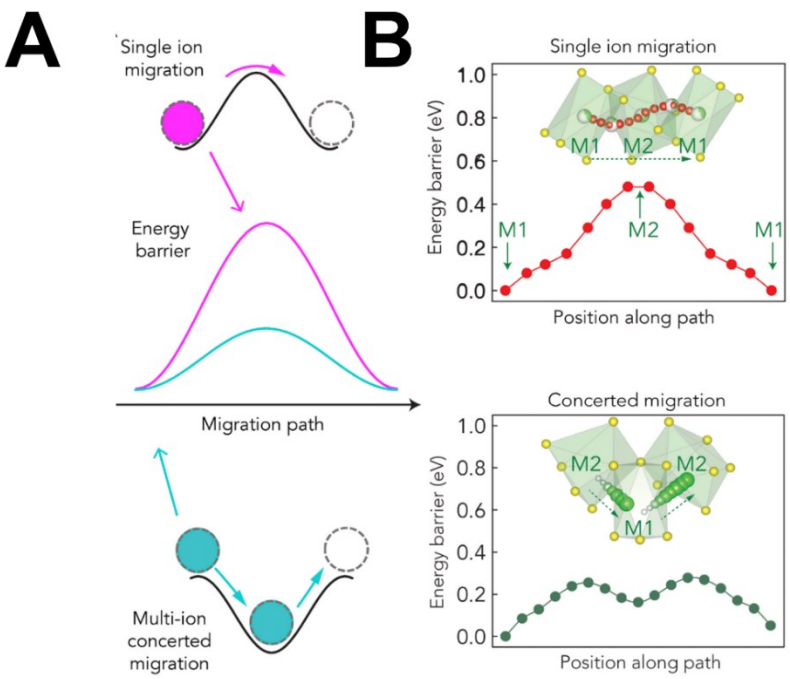

Figure 1.20 - A) Diffusion mechanisms and their corresponding energy profiles for single-ion migration (pink) and a multiple-ion concerted migration (blue) in SEs [385]. (B) Comparison between the energy barrier of a single Li+ migration (upper) and a concerted migration (lower) in LATP solid electrolyte, calculated using NEB [385].

1.5.1.2 – Screening for novel super-ionic conductors

First-principles computations using NEB and AIMD on solid electrolytes enabled the distinction of structural features associated with good ionic conductivity: 1) polarizable anions like S^{2-} that allowed Li ions to migrate with a lower activation energy, 2) a body-centered cubic anion sublattice, 3) the presence of medium-sized open and interconnected diffusion channels and 4) a high mobile Li-ion carrier concentration (defects and disordered phases) [247]. Richards *et al.* used these sought-after properties as criteria to screen materials, on the lookout for undiscovered super-ionic conductors. They singled out a new potential super-ionic conductor $Li_{1+2x}Zn_{1-x}PS_4$ ($0<x<0.75$) with a computed ionic conductivity of 10^{-2} $S.cm^{-1}$ at RT [382]. These materials were later successfully synthesized and displayed a good ionic conductivity ranging from 10^{-4} to 10^{-3} $S.cm^{-1}$ ($0.5<x<0.8$) [386, 387]. First-principles calculations also allow the design of new super-ionic conductors by modifying an initial structure for it to meet the requirements for high ionic conductivity. He *et al.* successfully did so by designing the super-ionic conductor $Li_{1.25}Ta_{0.75}Zr_{0.25}SiO_5$ with an ionic conductivity of 10^{-3} $S.cm^{-1}$ at RT from the initial $LiTaSiO_5$ structure [373]. The material was later synthesized and tested experimentally with an ionic

conductivity of 2.97 10^{-5} S.cm^{-1} at RT, two orders of magnitude higher than the pristine $LiTaSiO_5$ [388]. Another example is the one of thio-LISICON $Li_{10}Sn(PS_6)_2$, modeled by substituting Sn for Ge in the LGPS structure [379]. The AIMD simulated ionic conductivity was of 6 10^{-3} S.cm^{-1} at RT, this material was later synthesized experimentally with a concordant ionic conductivity of 7 10^{-3} S.cm^{-1} [389]. The simulated thio-LISICON $Li_{10}Si(PS_6)_2$ was also predicted to have an excellent ionic conductivity of 2.3 10^{-2} S.cm^{-1} at RT and inspired the synthesis of the Cl-doped version $Li_{9.54}Si_{1.74}P_{1.44}S_{11.7}Cl_{0.3}$, with an outstanding measured ionic conductivity of 2.5 10^{-2} S.cm^{-1} [379, 390]. These examples of super-ionic conductors, modeled based on simple structural prerequisites with experimentally confirmed excellent ionic conductivity, show the span of the predictive power of first-principles computations.

1.5.2 – Electrochemical stability window

The elaboration of computational databases like the Materials Project® made available DFT computed energies of hundreds of thousands of inorganic structures, allowing the construction of entire phase diagrams. Moreover, first-principles enabled the construction of phase diagrams open to one element. Such phase diagrams represent phase equilibria in an isothermal, isobaric system that is open to an element [391]. To keep an element open means that the chemical potential of this element (μ) can be changed. This type of phase diagram, referred to as grand potential phase diagram (GPPD), simulates external conditions depending on the element kept open. For example, a GPPD that is open with respect to μ_{Li} simulates the phase equilibria under an applied potential vs. Li$^+$/Li via equation 1.11:

$$\boldsymbol{V = -\frac{\mu_{Li} - \mu^{\circ}_{Li}}{e}} \qquad \text{Eq. 1.11}$$

Where V is the applied potential vs. Li$^+$/Li, μ_{Li} is the chemical potential of lithium, μ°_{Li} is the standard computed energy for lithium metal and e is the elementary electron charge. More details regarding the GPPD are given in chapters 2 and 3.

Using the GPPD, is it possible to predict the thermodynamic stability of solid electrolytes as a function of an applied potential vs. Li$^+$/Li, translating to their thermodynamic electrochemical stability windows. **Figure 1.21** displays the GPPD computed for LLZO. The $(Li)_{open}$-La-Zr-O phase diagram is kept open to lithium. The thermodynamic electrochemical stability window was computed for LLZO to be ranging from μ_{Li} = -0.05 eV to μ_{Li} = -2.91 eV, which corresponds to the range of μ_{Li} within which LLZO is a stable phase of the phase diagram. To illustrate this concept, four examples are presented: μ_{Li} = 0 eV corresponding to Li metal (**Figure 1.21A**), μ_{Li} = -0.06 eV

which is right in LLZO's ESW (**Figure 1.21B**), μ_{Li} = -1.23 eV which is deep in LLZO's ESW (**Figure 1.21C**) and μ_{Li} = -3.20 eV which is outside of LLZO's ESW (**Figure 1.21D**). In the figure, we see that LLZO appears as a stable phase in the La-Zr-O diagram when -2.91 < μ_{Li}< -0.05 eV.

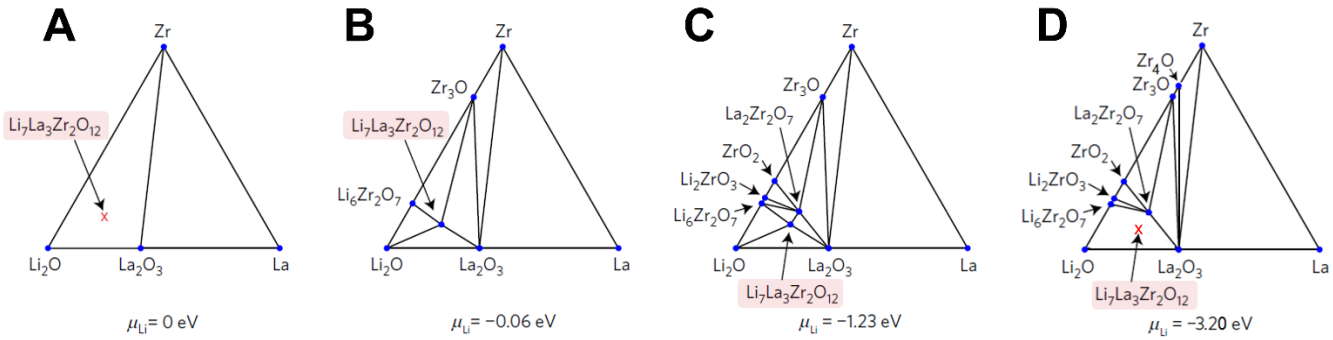

Figure 1.21 - GPPD of the Li-La-Zr-O system, open to Li, showing the phase equilibria of LLZO at different Li chemical potentials (normalized by the chemical potential of Li metal): A) μ_{Li} = 0 eV corresponding to Li metal, B) μ_{Li} = -0.06 eV, C) μ_{Li} = -1.23 eV and D) μ_{Li} = -3.20 eV. The thermodynamic ESW of LLZO ranges from -0.05 to -2.91 eV, within which LLZO is a stable phase of the diagram (B and C). Outside this window, LLZO is not reported on the GPPD as a stable phase (A and D) [332].

As mentioned in section 1.4.1.3, the ESW of solid electrolytes was hitherto severely overestimated using CV and planar cell configurations. Measured this way, most ESWs of solid electrolytes ranged from 0 to 5 or 6 V vs. Li^+/Li. On the other hand, thermodynamic ESWs computed using the GPPD were much narrower than the experimentally measured ones [175, 259, 392-394]. The significant discrepancy between theoretical and experimental values of ESWs put several research groups on track to figure out that inappropriate experimental setup and characterization technique were the origin of overestimated experimental ESWs. For example, the thermodynamic ESW of LGPS was computed to be [1.71 V - 2.42 V] vs. Li^+/Li (**Figure 1.22A**), far less than the [-0.5 - 5] V vs. Li^+/Li range first announced experimentally by Kamaya *et al.* using CV and a Li/$Li_{10}GeP_2S_{12}$/Au planar cell configuration [175, 206, 392]. Han *et al.* later determined LGPS's electrochemical stability window using a composite cell configuration (Li/LGPS/LGPS+C) and found it to be [1.7 V– 2.1 V] vs. Li^+/Li (**Figure 1.22B**), in better agreement with first-principles predictions [175].

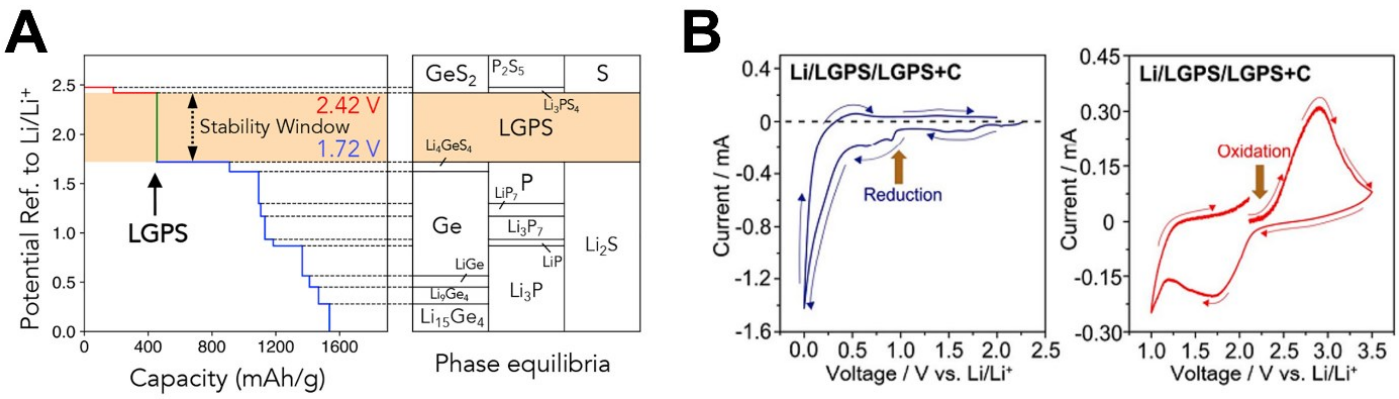

Figure 1.22 - Comparison of the electrochemical stability window of LGPS assessed using A) first-principles, reported to be ranging from 1.72 to 2.14 V vs. Li^+/Li (corrected to 2.42 V according to Nolan *et al*. [365]) with the corresponding phase equilibria and B) cyclic voltammetry, on a Li/LGPS/LGPS+C composite cell, indicating the reduction (1.7 V) and oxidation (2.1 V) peaks in the anodic and cathodic scans, respectively [175].

GPPD calculations also allowed to determine the decomposition products following the oxidation or reduction of the solid electrolyte. Many of them were successfully computed by Zhu *et al.* and are gathered in **Table 1.1** [392]. For example, the decomposition products of LGPS were predicted to be Li_4GeS_4, P and Li_2S upon Ge^{4+} reduction and Li_3PS_4, S and GeS_2 upon S^{2-} oxidation [175, 392], both confirmed by XPS [175, 395]. The reduction of P^{5+} in LiPON and Li_6PS_5Cl was first reported from first-principles calculations and were later confirmed by *in situ* XPS analyses [259, 261, 392, 396].

Table 1.1 - Computed thermodynamic electrochemical stability windows and corresponding phase equilibria at the redox potentials of various SEs, using the GPPD method [392].

	reduction potential (V)	phase equilibria at the reduction potential	oxidation potential (V)	phase equilibria at the oxidation potential
Li_2S	-	Li_2S (stable at 0 V)	2.01	S
LGPS	1.71	P, Li_4GeS_4, Li_2S	2.14	Li_3PS_4, GeS_2, S
$Li_{3.25}Ge_{0.25}P_{0.75}S_4$	1.71	P, Li_4GeS_4, Li_2S	2.14	Li_3PS_4, GeS_2, S
Li_3PS_4	1.71	P, Li_2S	2.31	S, P_2S_5
Li_4GeS_4	1.62	Li_2S, Ge	2.14	GeS_2, S
$Li_7P_3S_{11}$	2.28	Li_3PS_4, P_4S_9	2.31	S, P_2S_5
Li_6PS_5Cl	1.71	P, Li_2S, LiCl	2.01	Li_3PS_4, LiCl, S
$Li_7P_2S_8I$	1.71	P, Li_2S, LiI	2.31	LiI, S, P_2S_5
LiPON	0.68	Li_3P, $LiPN_2$, Li_2O	2.63	P_3N_5, $Li_4P_2O_7$, N_2
LLZO	0.05	Zr_3O, La_2O_3, Li_2O	2.91	Li_2O_2, La_2O_3, $Li_6Zr_2O_7$
LLTO	1.75	$Li_4Ti_5O_{12}$, $Li_{7/6}Ti_{11/6}O_4$, $La_2Ti_2O_7$	3.71	O_2, TiO_2, $La_2Ti_2O_7$
LATP	2.17	P, $LiTiPO_5$, $AlPO_4$, Li_3PO_4	4.21	O_2, $LiTi_2(PO_4)_3$, $Li_4P_2O_7$, $AlPO_4$
LAGP	2.70	Ge, GeO_2, $Li_4P_2O_7$, $AlPO_4$	4.27	O_2, $Ge_5O(PO_4)_6$, $Li_4P_2O_7$, $AlPO_4$
LISICON	1.44	Zn, Li_4GeO_4	3.39	Li_2ZnGeO_4, Li_2GeO_3,O_2

Wide ESWs for LATP, LAGP and LLZO were also reported using CV and planar cell configurations, with oxidation potentials all exceeding 6 V vs. Li^+/Li, and are significantly higher than their computed oxidation potentials of 4.21, 4.27 and 2.91 V vs. Li^+/Li respectively [392, 394]. However, as for LGPS, an optimized experimental setup allowed to determine much narrower experimental ESWs for these materials and confirmed their decomposition into O_2 upon oxidation, as predicted by first-principles calculations. More details on this subject are given in chapters 3 and 4.

High-throughput studies on the electrochemical stability windows of materials also came up with design principles for wide ESWs materials. For example, it was observed that increasing the Li content in the composition of a SE lowers its oxidation potential [397]. It was also observed that the reduction of a SE was mostly due to the reduction of its non-Li cation. First-principles calculations also show that nitrides are the materials with the lowest reduction potentials and are the most stable against metallic lithium [397]. These rational design principles for wide ESWs materials can be used as criteria to filter the search for, or design, novel solid electrolytes.

1.5.3 – Solid electrolyte/electrode interface stability

The availability of computational materials databases and the possibility to easily construct entire phase diagrams enabled large-scale thermodynamic computations on materials stability, including the thermodynamic equilibrium and the reaction energy between two materials [259, 393, 398]. This reaction energy is computed by constructing a phase diagram comprising all the elements present in these two materials (that are available in the database). If the two materials are not stable against each other, their reaction energy will be <0 eV and they will decompose to form the most stable phases of the phase diagram. These computations simulate the reactivity/stability of two materials when they are mixed or at their interface when they are put in contact. They can also be combined with a GPPD to simulate the reaction between two materials when a potential is applied, which best describes the situation in a cycling battery. As previously mentioned in section 4.2.1, most solid electrolytes are not thermodynamically stable against positive and negative electrode materials. The characterization of the interface between them being extremely difficult, computing the reaction energies and thermodynamic equilibria at the SE/electrode interface can play a crucial role in understanding the behavior of solid electrolytes within ASSLBs.

First-principles thermodynamic stability computations ran by Zhu *et al*. predicted the instability of LiPON against metallic lithium, which decomposes to form more stable phases Li_3N,

Li_3P and Li_2O, way before it was observed experimentally through *in situ* XPS analyses [261, 392]. First-principles simulations also predicted c-LLZO's instability against lithium metal to form less conductive t-LLZO phase at the interface [172]. LiPON's instability against $LiCoO_2$ positive electrode material was anticipated using first-principles and later observed by *in situ* scanning transmission electron microscopy (STEM), electron energy loss spectroscopy (EELS) and XPS analyses, where Co_3O_4, Li_2O, Li_2O_2, Li_3PO_4 and $LiNO_2$ decomposition products were confirmed [399-401]. Also predicted was the instability between many solid electrolytes and positive electrode materials, including Li_3PS_4 and $LiCoO_2$ to form Co_9S_8, Li_2S and more stable sulfate/phosphate phases Li_2SO_4 and Li_3PO_4 [393]. Cobalt sulfides and phosphates were indeed observed experimentally using energy-dispersive X-ray spectroscopy (EDS) analyses [402]. This same first-principles study predicted that Li_3PS_4 was even more reactive against delithiated $Li_{0.5}CoO_2$ or when a high potential of 5 V vs. Li^+/Li was applied. The same behavior was also predicted for similar sulfide-based solid electrolytes such as Li_6PS_5Cl and LGPS, which was successfully observed experimentally [396, 403-405]. In agreement with experimental findings, first-principles computations established that sulfide-based solid electrolytes were predominantly unstable against positive electrode materials. Miara *et al.* also predicted interfacial reactivity between LATP or LLZO solid electrolytes and high-potential spinel-type positive electrode materials ($Li_2NiMn_3O_8$, $Li_2FeMn_3O_8$, $LiCoMnO_4$) at high temperature, which is relevant given that such temperatures will be necessary to process these materials in ASSLBs [406]. Richards *et al.* computed the ESW of solid electrolytes (**Figure 1.23A**) and their chemical stability against several positive electrode materials (**Figure 1.23B**), they showed that most solid electrolytes were unstable against positive electrode materials with the exception of Li_3PO_4 [259].

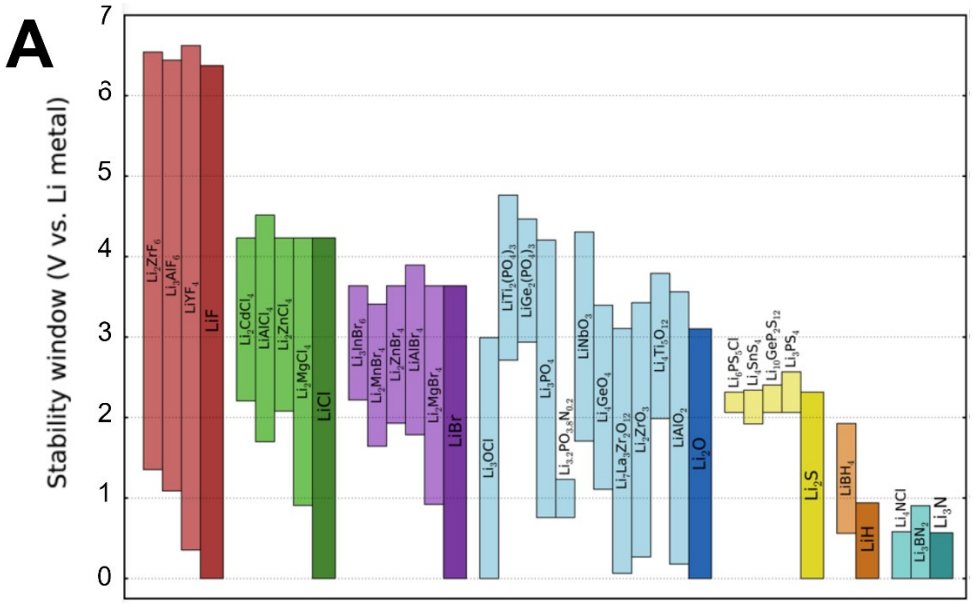

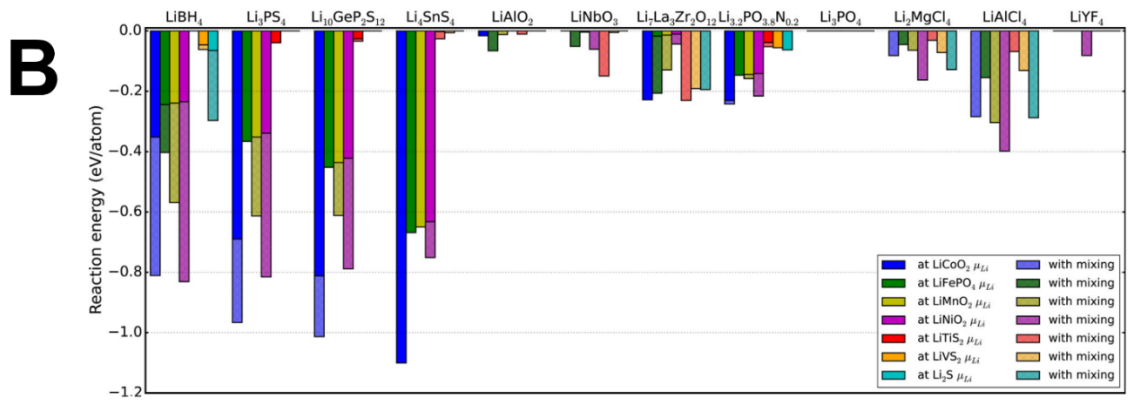

Figure 1.23 - A) Electrochemical stability windows of several solid electrolyte materials grouped by anion, with corresponding binary phase for comparison. The high-voltage stability of these materials is determined primarily by the anion. B) Reaction energies for the interfaces of a selection of cathode/electrolyte combination at μ_{Li} corresponding to the average cathode voltage. Energies are given both for the energy of the lithium extraction only (no mixing) and for energy of cathode/electrolyte mixing open to lithium. Combinations with decomposition energies close to zero are expected to form stable interfaces [259].

1.5.4 – Defects in solid electrolytes

We previously established in section 1.4.1.4 the direct link between the formation of defects and the ionic/electronic conductivities of solid electrolytes. However, controlling and characterizing defects are considered extremely difficult given their imperceptible presence in the materials. In this context, the recent emergence of first-principles methods to compute the formation energy of defects and the charge carrier concentrations in solid materials played a crucial role in understanding and quantifying defects in solid electrolytes [407-410]. These recent computational studies, including our work presented in chapter 5, managed to link the formation of defects in solid electrolytes to external conditions. For example, Gorai *et al.* predicted that argyrodite-type SEs are less likely to develop unwanted electronic conductivity in oxidizing conditions [407]. Squire *et al.* anticipated that the ionic conductivity of LLZO solid electrolyte would significantly decrease under Li-rich synthesis conditions, through the formation of immobile lithium antisites [409]. Gorai *et al.* also predicted an enhanced ionic conductivity for LGPS if synthesized under P-rich/Ge-poor conditions, through the formation of beneficial P_{Ge} antisites [410]. Despite the recency of these computational models, emerging experimental studies are confirming the theoretical predictions regarding the dependency of defects' formation on environmental conditions and their effect on ionic/electronic conductivities. For example, a recent experimental study led by Gorai *et al.* proved

that Na_3SbS_4 synthesized under different sets of conditions demonstrated noticeable difference in the bulk ionic conductivity, confirming their theoretical predictions [408]. This proves yet again that first-principles modeling is a precious asset for the exploration and development of solid electrolytes.

Through these different research axes, computational studies have proved to play a critical role in understanding the intrinsic and extrinsic properties of solid electrolytes. Furthermore, the predictive power of these theoretical tools can accelerate the discovery of novel solid electrolytes by enabling the design of original and optimized structural frameworks. Computational methods like the bond valence method, structural prediction and substitution algorithms are suited for a scaled up, high-throughput screening of inorganic materials, and their predictive power can be perfectioned with the help of machine-learning [411-418].

1.6 – Objectives of the thesis

The present manuscript addresses different aspects of stability in solid electrolytes, using both experiments and first-principles. A description of all the characterization techniques and theoretical methods used throughout this manuscript is found in chapter 2. The core of this manuscript focuses on two intrinsic properties of solid electrolytes: the electrochemical stability window and electronic conductivity, outlined in chapters 3, 4 and 5. Our interest on the matter is rooted in the lack of documentation and consistency observed in reporting on these two aspects in current literature.

On one hand, the performance of ASSLBs relies partly on the electrochemical stability window of the solid electrolyte. Assessing a solid electrolyte's ESW is conventionally done using cyclic voltammetry. However, different values of the ESW reported for the same material in the literature appeared very divergent from one another, with ESWs computed using DFT being much narrower than their experimental counterparts. Recent studies have come to decry the overestimation of ESWs when traditional CV is used, for the following reasons: 1) ceramic solid electrolytes are pressed or sintered into pellets, coated with a conductive metal and tested between an inert blocking electrode, allowing only a very limited contact area between the SE and the inert blocking electrode. The redox currents generated from this planar cell configuration are therefore relatively small and hardly noticeable on CV curves. 2) Using high sweeping rates and omitting the ohmic drop correction can alter considerably the CV curve, giving the impression of very wide ESWs. For these reasons, assessing the ESWs of solid electrolytes using CV with high

sweeping rates and planar cell configurations became a subject of heated debate when the first inconsistencies were observed in 2016.

Within this frame of reference, the first objective of this research project was to develop a methodology that could address all the current limitations (high sweeping rate CV, planar cell configuration) to efficiently assess the electrochemical stability window of solid electrolytes. Our methodology was optimized and validated on flagship ceramic solid electrolytes such as NASICON-type materials $Li_{1.5}Al_{0.5}Ge_{1.5}(PO_4)_3$ (LAGP) and $Li_{1.3}Al_{0.3}Ti_{1.7}(PO_4)_3$ (LATP) and garnet-type material $Li_7La_3Zr_2O_{12}$. These three materials are the subject of extensive research because they were first reported with high ionic conductivities (> 10^{-3} $S.cm^{-1}$ at RT) and a very wide electrochemical stability window using the conventional method described above. Our methodology, outlined in the chapters 3 and 4 of this manuscript, challenges the ESWs previously reported for these three materials by bringing together theoretical computations and an original experimental setup.

On the other hand, despite the electronic conductivity being detrimental to solid electrolytes, research on the electronic conductivity in solid electrolytes had been neglected at the expense of research on their ionic conductivity. Indeed, the focus was put on achieving the highest ionic conductivity possible while the electronic conductivity was assumed to be negligible given the usually wide band gap of such materials. It was not until recently that the stability of solid electrolytes with respect to their own electronic conductivity was questioned and then linked to intrinsic and extrinsic factors. Pioneering work on the subject was focused on $Li_7La_3Zr_2O_{12}$, Li_3PS_4 and $Li_{10}Ge(PS_6)_2$ solid electrolytes in 2019 and established a link between electronic conductivity in solid electrolytes and the formation of lithium dendrites in ASSLBs, proving that the plating of Li in SEs was proportional to the increase of their electronic conductivity. As mentioned in section 1.4.1.4, the electronic conductivity is proportional to the concentration of charge carriers and their mobility within the structure. Charge carriers are generated by thermal excitation of electrons to current-carrying states. These charge carriers are intrinsically present in the structure and brought by defects in the structure. Therefore, there is a direct link between the spontaneous formation of defects in solid electrolytes and the generation of electronic conductivity. Moreover, the formation of defects is strongly driven by the environment surrounding the material, which implies that the external environment has a direct influence on the electronic conductivity in solid electrolytes. Due to their negligible concentration and spontaneous formation, controlling the formation of defects in materials is extremely difficult and characterizing them is hardly possible using standard characterization techniques. For this reason, computational tools are being developed to bring

more insight on the defect chemistry of materials. First-principles defects computations have recently been more and more applied to solid electrolytes but remain scarce as the number of publications on the subject doesn't exceed a dozen.

In this context, the second objective of this thesis project was to use first-principles computations to explore the formation of intrinsic defects in solid electrolytes and to investigate how changes of the external environment can affect the electronic conductivity of solid electrolytes. More specifically, we introduce in the chapter 5 of this manuscript a computational study of the defect chemistry in several solid electrolytes, including $LiTi_2(PO_4)_3$, $LiGe_2(PO_4)_3$ and $Li_7La_3Zr_2O_{12}$, to assess their robustness against building unwanted electronic conductivity, despite a change of the external environment.

We hope that our contribution to these two topical issues (ESW and electronic conductivity) will help to further understand the complex behavior of solid electrolytes and to provide relevant tools to better probe new materials as promising solid electrolytes for ASSLBs.

2. EXPERIMENTAL AND THEORETICAL METHODS

This chapter is dedicated to the description and illustration of all the experimental techniques and theoretical methods used for this thesis. For the sake of conciseness, I provided a non-exhaustive description of the theory behind each technique presented. The technical details, such as the brand, model, parameters of the equipment and specifications on the experiments, will be specified in each chapter.

2.1 – Experimental techniques

2.1.1 – Solid-state chemistry

2.1.1.1 – Synthesis

Solid-state synthesis includes the preparation of inorganic materials in the form of single crystals, polycrystalline powders or thin-films. It requires steps like mixing, grinding/milling, compacting and heat treatment:

2.1.1.1.1 – Mixing and grinding

Powders can be mixed and ground/milled together manually, in agate or porcelain mortars, or using high-energy ball milling like SPEX (also planetary milling, attritors…etc.). For the latter, the powders are placed in a zirconia crucible with zirconia beads. The bead to powder weight ratio should be around 10:1, with a size of beads ranging from 1 mm to 1 cm diameter. The number of beads necessary to the milling depends on their size and on the amount of powder. After introducing the beads, the crucible is sealed and placed in a high-energy shaker as illustrated in **Figure 2.1A**. The powders are crushed and pulverized between the beads and the crucible at a speed of 1500-2000 rpm to effectively reduce their particle size and/or intimately mix them together in a homogeneous manner [419].

2.1.1.1.2 – Compacting

Powders can be compacted in the form of pellets to maximize the contact area between the grains, reducing the diffusion path and therefore increasing the reactivity between them. Powders can be compacted in a die (stainless steel) then cold - or hot - pressed using a hydraulic press. The size of the die, the temperature, the pressure, the amount of powder, the use of vacuum and the pressing time are all parameters one can vary to yield the most appropriate result.

2.1.1.1.3 – Heat treatment

The heat treatment is used on ceramics to trigger a reaction between precursors, to melt a sample, to grow crystallites...etc. Powders, or compact pellets, are introduced in an inert crucible, such as silica, alumina or platinum, and placed inside a high-temperature furnace for the heat treatment (usually between 400 °C and 1200 °C). The heat treatment can be done in ambient or controlled atmospheres (N_2, Ar, O_2-rich, H_2 or C). At high temperatures (>900 °C), a powder-bed might be used to prevent lithium loss by evaporation and prevent side reactions with the reaction crucible. A powder-bed consists of placing the pellet on a bed of its own powder, and covering it with the same powder, before the heat treatment [420].

2.1.1.2 – Sintering

Sintering is the process of making the grains of a powder coalesce into a compact mass by applying heat and/or pressure, without reaching liquefaction, as shown in **Figure 2.1B**. Sintering aims at densifying the material up to its theoretical density, the ratio between the achieved ($d_{achieved}$) and theoretical (d_{theory}) densities is called the compacity (%):

$$compacity = \frac{d_{achieved}}{d_{theory}} \times 100 \qquad \text{Eq. 2.1}$$

There are several ways to sinter ceramics, including microwave sintering and liquid phase sintering but we will focus on the two sintering methods used in this manuscript:

2.1.1.2.1 – Pressureless sintering

Also referred to as ‘’natural sintering’’, pressureless sintering involves heating, with no direct pressure, to densify the material. The powder is pre-compacted, referred to as a ‘’green’’, and molded using a uniaxial cold press prior to the heating step. The ‘’green’’ compact is then placed in a crucible (with or without powder-bed) and heated at the required temperature and period of time to sinter.

2.1.1.2.2 – Spark plasma sintering

Spark plasma sintering (SPS) is a technique that combines uniaxial pressure and high-intensity, low-voltage, pulsed current to sinter a powder [421]. The latter is loaded in an electrically conducting die (graphite, tungsten carbide, Ti-Mo-Zr mix) and heated by Joule effect when a current is flown directly through the conductive die [422], as shown in **Figure 2.1C**. Several techniques use electric current for sintering, but SPS is differentiated by the use of pulsed direct current (DC). SPS has been receiving growing attention in the last decades due to its remarkable effectiveness, allowing to achieve fully densified samples by using low processing temperatures and short sintering times [423]. For instance, LAGP solid electrolyte is sintered at 900 °C for 5 h using the conventional pressureless method to reach a compacity >95% [424]. A similar compacity is achieved at 650 °C for 3-10 mins using SPS [425]. The maximum temperature and applicable pressure depend on the type and size of die used to sinter the powder. In the context of this manuscript, 8 mm-diameter graphite dies were used to sinter SEs using SPS, one can be seen in **Figure 2.1D**. This type of die can withstand temperatures up to 1600 °C under vacuum and a constant applied pressure of 120 MPa [426]. It is interesting to mention that the name field assisted sintering technique (FAST) should be preferred to spark plasma sintering because the presence of spark plasma during the process has not been unequivocally proved [421].

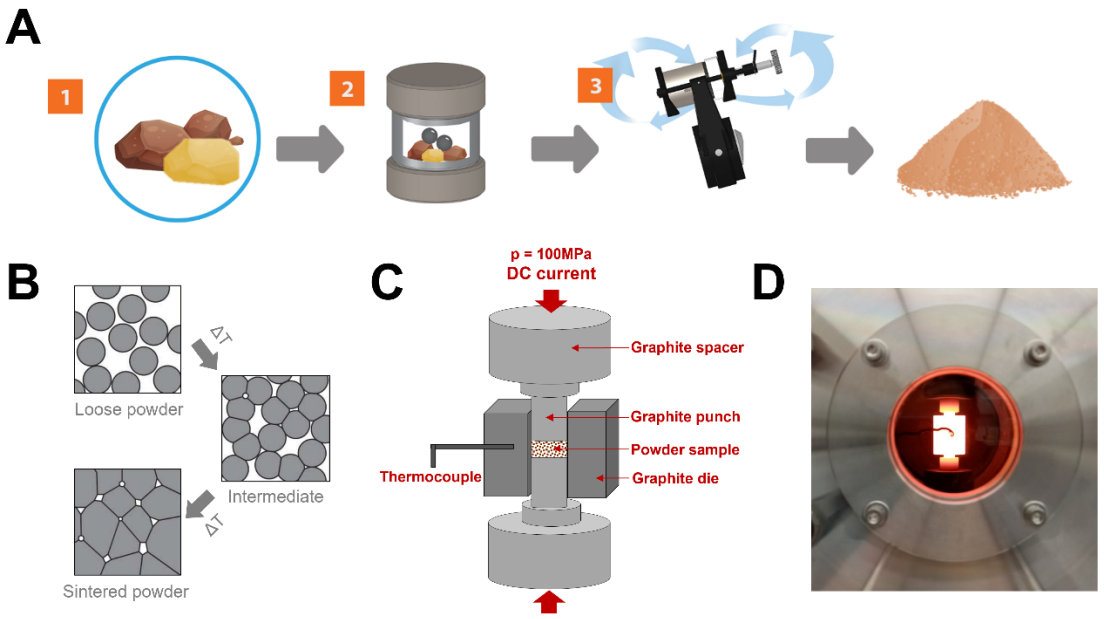

Figure 2.1 - Schematic representations of A) a high-energy ball milling device (SPEX) [419], B) particles sintering using heat and C) spark plasma sintering. Photography of a radiating graphite die during sintering at 800 °C under vacuum using SPS (D).

2.1.2 – Brunauer-Emmett-Teller theory

The Brunauer-Emmett-Teller (BET) theory is a technique used to measure the surface area of a solid material at an atomic level by adsorption of an inert gas. To determine the surface area, a sample is placed in a quartz test tube under vacuum and cooled to cryogenic temperatures using liquid nitrogen [427]. The test tube is then filled with an adsorbing gas, like N_2. The pressure and concentration of the adsorbing gas are increased gradually. At each N_2 increment, the relative pressure (p/p_0) goes back to equilibrium and the mass (m) of N_2 adsorbed is determined. Eventually, the N_2 gas pressure is increased until a monolayer of N_2 molecules covers the entire surface of the sample. The number of gas molecules in the monolayer is derived from the volume adsorbed. The surface area of the sample (S) is calculated from its cross-sectional area. A mathematical model was developed by Brunauer, Emmett and Teller to describe a linear relationship between gas adsorption and relative pressure [428]. The BET equation describes the evolution of the number of N_2 molecules adsorbed onto the sample (X) as a function of its relative pressure (p/p_0) as follows:

$$\frac{1}{X\left[{}^{p_0}/_{p}-1\right]} = \frac{1}{X_m C} + \frac{C-1}{X_m C}\left(\frac{p}{p_0}\right) \quad \text{and} \quad S_{BET} = \frac{X_m N_A s}{Vm} \quad \text{Eq. 2.2}$$

where X_m is the number of N_2 molecules forming the monolayer, p/p_0 is the relative pressure, C is a parameter related to the heat of adsorption. From X_m, Avogadro's constant (N_A), the cross-sectional area of adsorbed gas molecule (s), the molar volume of adsorbed gas (V) and the sample's mass (m), it is possible to extract the specific surface area (S_{BET}), measured in $m^2.g^{-1}$.

2.1.3 – X-ray diffraction

2.1.3.1 – Crystallography

X-ray diffraction (XRD) is a method used to characterize crystalline materials and relies on crystallography. The crystalline state is defined by the repetition of a regular arrangement of patterns (atoms, molecules, groups of molecules) in space. Each crystal has a translational symmetry, it is composed of an elementary pattern which is repeated *ad infinitum* [429]. The unit cell takes the form of a parallelepiped defined by a point of the cell as origin and three non-coplanar unit vectors *a*, *b* and *c* as axes which form three angles *α, β* and *γ*. The shape of the parallelepiped depends on the arrangement of the points in space. There are 14 possible arrangements, referred to as the Bravais lattices (named after the physicist who discovered them), categorized in 7 systems: triclinic, monoclinic ($\alpha = \gamma = 90°$), orthorhombic ($\alpha = \beta = \gamma = 90°$), tetragonal ($a = b$, $\alpha = \beta$

= γ = 90°), rhombohedral (a = b = c, α = β = γ), hexagonal (a = b, α = β = 90°, γ = 120°) and cubic (a = b = c, α = β = γ = 90°) [430].

Specific arrangements of atoms in a crystal can produce symmetry. A symmetry operation is an operation that transforms an initial spatial arrangement into another arrangement indistinguishable from the initial one. There are several symmetry operations, including axes of rotation, center of symmetry, mirror planes, translation planes… etc. Some symmetry elements are characteristic of a particular crystal system. For example, a C_6 axis of rotation is characteristic of a hexagonal crystal system. Also, the presence of a precise combination of symmetry elements in a crystal indicates the space group to which it belongs. There are 32 different point groups distributed in the 7 systems, according to their level of symmetry [429].

2.1.3.2 – X-ray diffraction

X-ray diffraction is used to describe the arrangement of atoms (i.e., the space group) in a crystal structure. It consists in exposing a crystalline sample to a beam of X-rays. Diffraction is based on the elastic diffusion of X-rays in determined directions after their interaction with the crystal. Depending on the arrangement of atoms in the crystal structure, this elastic scattering of X-rays will give rise to interferences. These interferences are governed by Bragg's law [431]:

$$2dsin\theta = n\lambda \qquad \text{Eq. 2.3}$$

where we define d (Å) as the interreticular distance between two planes, θ (rad) is the half-angle of deviation between the incident beam and the direction of the detector, λ (Å) is the wavelength of the X-ray, n is an integer. For each angle θ, if Bragg's law is respected, the interference is said to be constructive, as shown in **Figure 2.2A**. On the other hand, if Bragg's law is not satisfied, the interference is destructive (**Figure 2.2B**). Each interference has a phase and an amplitude. These interferences all interact with each other according to their phases and produce a single diffracted beam in each direction of space. This global beam gives rise to a diffraction pattern. Only the constructive interferences will appear on the diffraction pattern in the form of diffraction peaks. **Figure 2.2C** shows an example of a diffraction pattern, collected for NaCl crystal structure. Each diffraction pattern is specific to a precise crystal structure, like a signature, which allows an efficient characterization of crystalline materials.

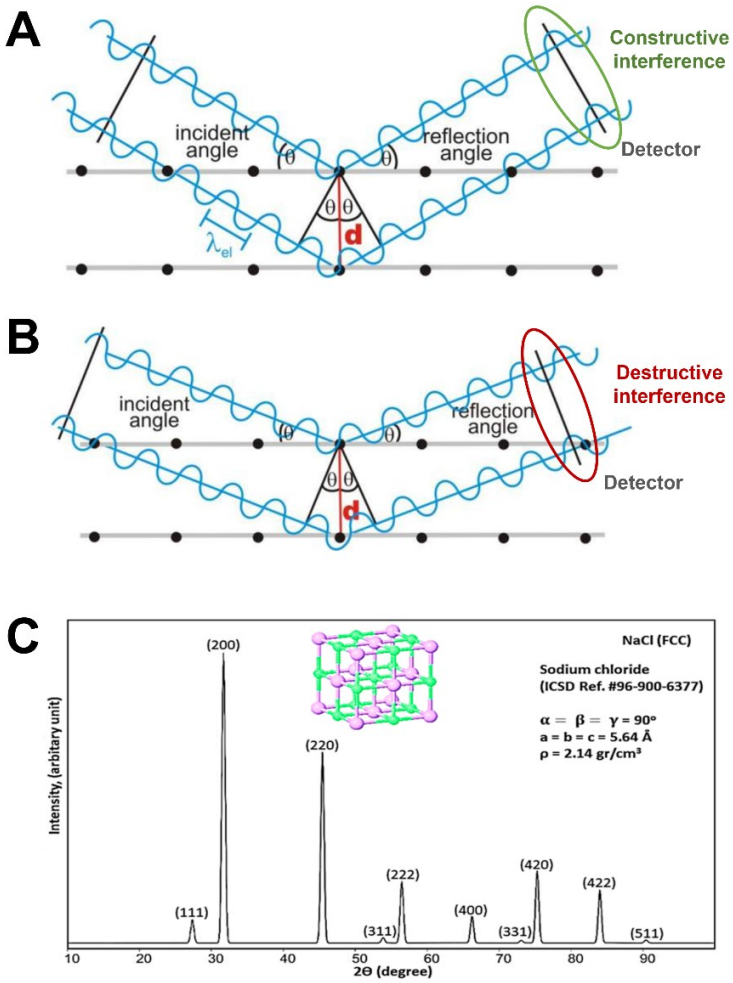

Figure 2.2 - Representative diagram of Bragg's law at a constructive (A) and destructive (B) interference [432]. C) An XRD pattern collected for NaCl using a Cu beam. Information on the space group and families of planes (hkl) observed are indicated on the pattern [433].

2.1.3.3 – Structural refinement

The structural refinement, known as the Le Bail method or the full pattern matching, is a refinement without lattice constraint [434]. It consists in refining the line profile (position and width) and the lattice parameters without considering the peak intensities (an arbitrary value of 1000 a.u. is assigned to all intensities). The shape of the peaks is described by the pseudo-Voigt function (pV) which is defined by a sum of gaussian (G) and lorentzian (L) functions:

$$pV = (1 - \eta)L + \eta G \qquad \text{Eq. 2.4}$$

where η is a normalization factor between 0 and 1. The Gaussian function can be modulated from the parameters U, V, W, Z and the Lorentzian function from X and Y following:

$$HG = \frac{(Utan2\theta + Vtan\theta + W + \frac{Z}{cos2\theta})}{2} \quad \textit{and} \quad HL = Xtan\theta + \frac{Y}{cos\theta} \qquad \text{Eq. 2.5}$$

where HG is the width at mid-height of the Gaussian component of the peak, HL that of the Lorentzian component as a function of the diffraction angle 2θ [435]. The U and X parameters are associated with the defects, Y and Z with the size and the V and W parameters with the instrument. These parameters are modulated until the theoretical diffractogram closest to the experimental diffractogram is obtained. To measure the process of convergence between the two, several crystallographic agreement factors can be used, in particular the χ^2 which is calculated according to the equation:

$$\chi^2 = \left(\frac{R_{wp}}{R_{exp}}\right)^2 \qquad \text{Eq. 2.6}$$

χ^2 is a ratio of squares between the two R factors. R_{wp} is the weight profile factor and R_{exp} is expected factor associated with the quality of the measurement:

$$R_{wp} = \sqrt{\frac{\sum_i w_i \left(y_{i(obs)} - y_{i(calc)}\right)^2}{\sum_i w_i y_{i(obs)}{}^2}} \times 100 \quad \textit{and} \quad R_{exp} = \sqrt{\frac{N-P+C}{\sum_i w_i y_{i(obs)}{}^2}} \times 100 \qquad \text{Eq. 2.7}$$

$y_{i(obs)}$ and $y_{i(calc)}$ are the intensities observed and calculated at any point *i* of the diffractogram, ω_i represents the statistical weight at point *i*. *N* is the total number of observations *i*, *P* is the number of parameters to be adjusted and *C* is the number of constraints applied during the adjustment. Generally, the term *N-P+C* is dominated by *N*.

Given the low quality of the diffractometers, it was not possible to further refine the scans using Rietveld refinement and access refined atomic positions. However, using the structural refinement, it is possible to determine the cell parameters *a, b, c, α, β* and *γ*. The structural refinement without lattice constraint was carried out with the HighScore© program.

2.1.4 – Electron-based techniques

2.1.4.1 – Scanning electron microscopy

Scanning electron microscopy (SEM) is an observation technique that produces images by scanning the surface of a sample with a low-energy, focused beam of electrons. Electrons interact with the sample to produce a signal that can be used to obtain information about the surface's topography and microstructure. The scanning electron microscope is composed of a setup under high vacuum (10^{-4} Pa) illustrated in **Figure 2.3**: 1) an electron gun (typically a

tungsten cathode), to produce the electron beam, 2) a condenser system, which focuses the beam onto the object via electromagnetic lenses (solenoids + magnetic poles), 3) an analysis chamber in which the sample is placed. 4) the image-producing system, consisting of objective and projector lenses, to focus the electrons passing through the specimen to form a real, highly magnified image, and 5) the image-recording system, which converts the electron signals to an actual image, it consists of a fluorescent screen and a digital camera [436]. Electrons are produced in the electron gun, they are accelerated down the microscope column, by applying a potential (typically from 1 to 30 keV),and passed through different electromagnetic lenses to produce a focused beam. The beam is finally aimed at the sample, mounted on a stage in the analysis chamber. As the electrons interact with the sample, it stimulates the emission of secondary electrons, backscattered electrons and characteristic X-rays [437]. These signals are collected by the detectors to produce images as shown in **Figure 2.3A**. When the electrons hit the surface of the sample, they penetrate to a depth of a few microns. The penetration depth depends on the molecular weight, the density of the sample and the voltage used to accelerate the electrons. State-of-the-art scanning electron microscopes provide a resolution ranging between 1 and 20 nm [438]. Because the electrons are expected to scan the surface only, no elaborate sample preparation is required. Large and thick samples can be accommodated, owing that their surface is electrically conducting. Otherwise, surficial conductivity is usually achieved by evaporating a nanometric film of metal, such as gold chromium or carbon, on the sample's surface.

2.1.4.2 – Transmission electron microscopy

Transmission electron microscopy (TEM) relies on the same type of microscope as SEM (section 2.1.4.1), see **Figure 2.3**. However, electrons used in TEM are of much higher energy (30–2000 kV) to be able to penetrate through the sample and to be collected at the other side. The electrons are focused again through electromagnetic lenses after they penetrated the sample and are collected on a fluorescent screen (**Figure 2.3B**). The high-energy electrons also result in a much higher spatial resolution than SEM (≈ 1 Å) [439]. Moreover, to be analyzed via TEM, a sample must be thin enough to allow the electrons to penetrate through it with minimum energy loss (usually 100 nm). Sample preparation is an important aspect of the TEM analysis, it requires ultrasonic disk cutting, dimpling, but mostly ion-milling using a focused ion beam (FIB).

2.1.4.3 – Energy-dispersive X-ray spectroscopy

Energy-dispersive X-ray spectroscopy (EDS) is an analytical characterization technique generally coupled to SEM and TEM. It allows the elemental composition of a material to be identified and quantified to 0.1 wt%, offering both semi-qualitative and semi-quantitative information. To run an EDS analysis, a beam of high-energy electrons (the same ones used for SEM/TEM) is focused on a sample. Atoms within the sample contain ground state electrons located on different energy levels, referred to as shells (M, L and K). When the incident electron beam interacts with the sample, it excites an electron in an inner shell of the atom (e.g., K shell), ejecting it from the shell to create an electron hole. An electron from an outer shell (e.g., L shell) then fills the hole left in shell K, and the difference of energy between the outer and inner shell is released in the form of an X-ray. This X-ray is characteristic of the atomic structure of the element interrogated. An energy dispersive detector analyzes these characteristic X-rays and a signature spectrum is obtained for each element analyzed, as shown in **Figure 2.3C**. The spectrum is then compared to reference spectra tables to assign each of its peaks and identify the elemental composition of the sample. The elemental 2D mapping of a selected surface of the sample is also possible with most EDS spectrometers.

2.1.4.4 – Selected area electron diffraction

Selected area electron diffraction (SAED) is a crystallographic characterization technique typically coupled to TEM. It relies on the diffraction of electrons by the sample to determine the orientation, lattice constants and defects in its crystal structure [440]. For SAED, a selected area aperture is used to virtually select the area from the sample that will produce a diffraction pattern (0.5 - 1 μm aperture). When a beam of parallel electrons is focused on the sample, a portion of the electrons is elastically scattered and diffracted by the sample following Bragg's law (13), as detailed in section 1.3. After interacting with the sample, the diffracted electrons intersect in a back focal plane forming a diffraction pattern. SAED diffraction patterns are either an arrangement of bright spots, when a single-crystal is analyzed as presented in **Figure 2.3D**, or a combination of concentric rings when a powder is analyzed. The latter is observed because a powder is comprised of multiple crystals with different orientations [441]. From the SAED pattern, it is possible to approximate the interreticular distance *d* characteristic of a crystal structure if the angle of the incident beam (θ in Bragg's law) is small, following equation 2.8:

$$d \approx \frac{D}{\lambda L} \qquad \text{Eq. 2.8}$$

where *D* is the distance between spots or rings on the SAED pattern, *L* is the distance from the sample to the camera and *λ* is the electron wavelength.

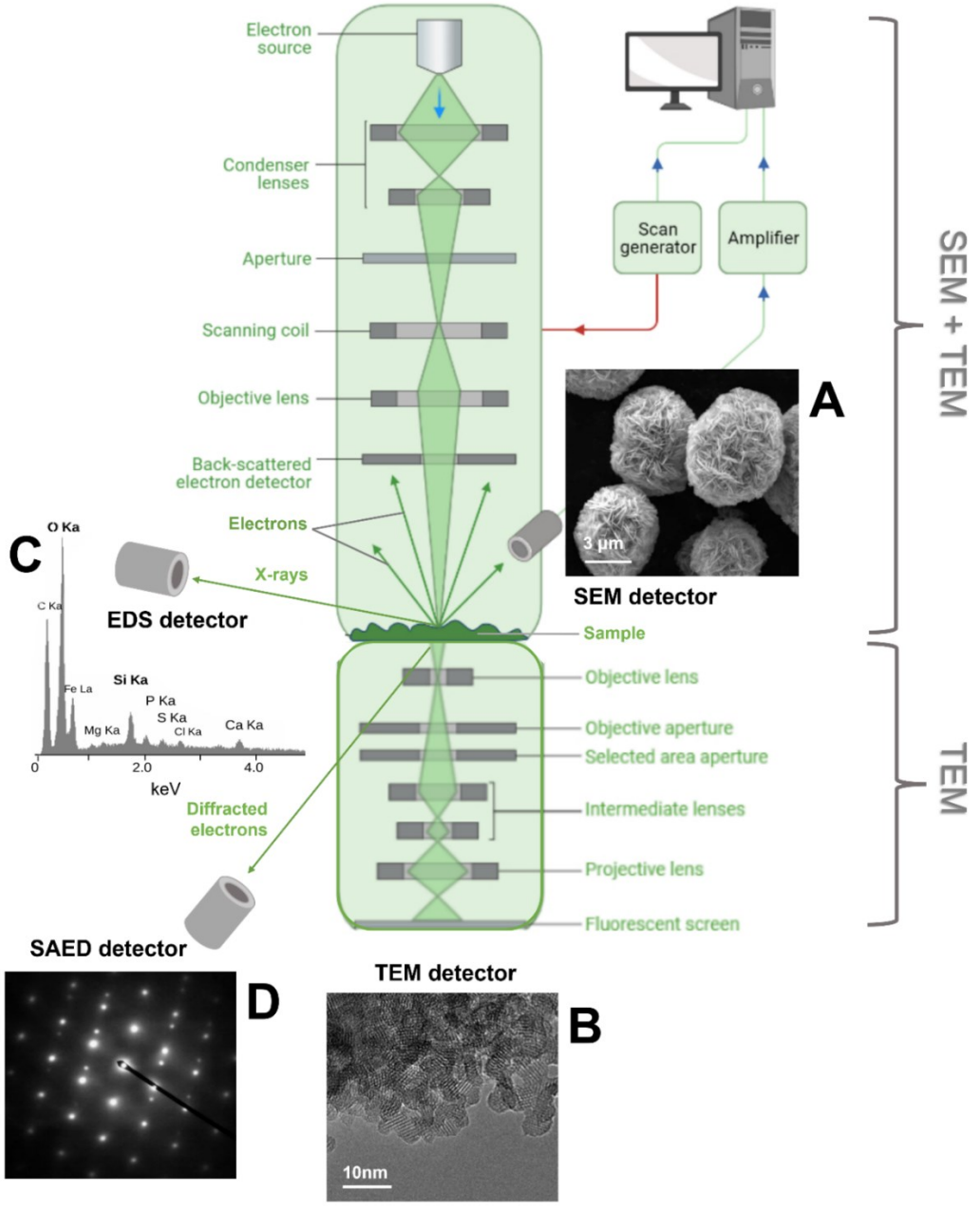

Figure 2.3 - Schematic representation of an electron microscope, the sample is targeted by the electron beam and A) produces secondary electrons used in SEM, B) is penetrated by the electrons that are detected on the other side (TEM), C) emits X-rays that are analyzed by EDS and D) diffracts electrons that form diffraction patterns in SAED.

2.1.5 – Electrochemistry

2.1.5.1 – Cell assembling

2.1.5.1.1 – All-solid-state configuration

In order to run electrochemical tests, the solid electrolyte powders need to be processed using an optimized procedure: they are mixed with gold powder into a composite, which will act as the positive electrode, and placed on top of a layer of pristine solid electrolyte. The two layers are sintered into a monolithic stack using natural sintering or SPS (both detailed in section 2.1.1.2). The stack is placed on top of a lithium foil, which acts as the negative electrode. A Mylar ring is placed between the stack and the lithium foil to prevent short circuiting. For some of the experiments, a polyethylene oxide (PEO) electrolyte is placed between the stack and the lithium foil to protect the solid electrolyte from a chemical reaction with metallic lithium. A Teflon ring is placed inside the Swagelok cell to prevent PEO from creeping and reaching the positive electrode. PEO electrolyte is prepared following a procedure detailed in chapter 3. The components are then mounted in a Swagelok-type electrochemical cell, as illustrated in **Figure 2.4A**. The Swagelok cell consists of a cylindrical stainless-steel body and pistons. The stack/PEO/lithium foil is secured inside the cylindrical body between the two pistons, used to ensure an electrical contact with the composite and lithium foil and to apply pressure. The Swagelok are assembled and sealed in an argon-filled glovebox. All the electrochemical tests are run between 60 °C and 80 °C. The ionic conductivity in solid electrolytes being temperature-dependent, such elevated temperatures are recommended to ensure a good conduction (ideally $>10^{-3}$ S.cm^{-1}) and allow slow-kinetic reactions to occur, which is required to accurately assess the ESWs of solid electrolytes.

2.1.5.1.2 – Liquid configuration

In a liquid cell configuration, the solid electrolyte is processed as an active material into a positive electrode and integrated in a coin cell. The active material is mixed with 11 wt% of carbon black and 8 wt% of a solution of polyvinylidenefluoride (PVDF) at 2.5% in N-methyl-2-pyrrolidone (NMP). Carbon black acts as an electronic conductor and PVDF as a binder. The latter allows the powder to adhere to the surface of the current collector and ensures permanent contact between the collector, the carbon black and the active material. The NMP is a solvent used to dissolve the PVDF and disperse the carbon black and active material, resulting in a homogeneous coating [442]. The components are thoroughly mixed and deposited on the current collector, either a carbon-coated aluminum or copper film, using the Doctor Blade technique to control the thickness

of the layer. The film (i.e., slurry) is then dried in a vacuum oven at 80 °C to remove the NMP. Once dried, the film is cut into 14 mm disc electrodes, each of which is assembled in a coin cell under an inert atmosphere with Li metal as the negative electrode and a liquid electrolyte ($LiPF_6$ lithium salt in EC/DEC organic solvents) as shown in **Figure 2.4B**. Celgard 2400 disks are used as a separator, to prevent the two electrodes from coming into contact. Once assembled, the coin cell is sealed under pressure and cycled at RT.

2.1.5.2 – Potentiostatic intermittent titration technique

The potentiostatic intermittent titration technique (PITT) is the method used to assess the electrochemical stability window of solid electrolytes in this project. PITT was first introduced to perform a thermodynamic and kinetic characterization of metal alloys such as LiAl [443]. It was later used to study the insertion of lithium into positive and negative electrode materials [444]. It is based on the principle of imposing small steps of potential ΔE on the system, holding the potential for a given amount of time Δt, and monitoring its current response i. The next potential step is imposed when the current response decreases to a selected threshold i_{min} or after Δt amount of time. Δt and i_{min} values determine the rate of a PITT cycle [445]. When a potential step is applied, a peak in the current signal is observed, as shown in **Figure 2.4C**. While the potential is held and if the system is only governed by diffusion, the system goes back to equilibrium and the current signal decreases exponentially overtime following equation 2.9:

$$i = \frac{2FS(C_S - C_0)D}{L} e^{\frac{-\pi^2 Dt}{4L^2}} \quad \text{Eq. 2.9}$$

where F is the Faraday constant, S is the surface area of the electrode, the term $Cs - C_0$ is the concentration gradient of Li ions at the surface at time t and the at the beginning of the potential pulse (t = 0), D is the diffusion coefficient and L is the characteristic length of the electrode active material [443].

When a redox reaction occurs, the system is not only governed by diffusion anymore because a charge transfer is now involved, and the current response changes accordingly (**Figure 2.4C**). This method is optimal to determine ESWs because it allows the system sufficient time (Δt) to go back to equilibrium after each potential step. Done this way, the system always remains close to thermodynamic equilibrium.

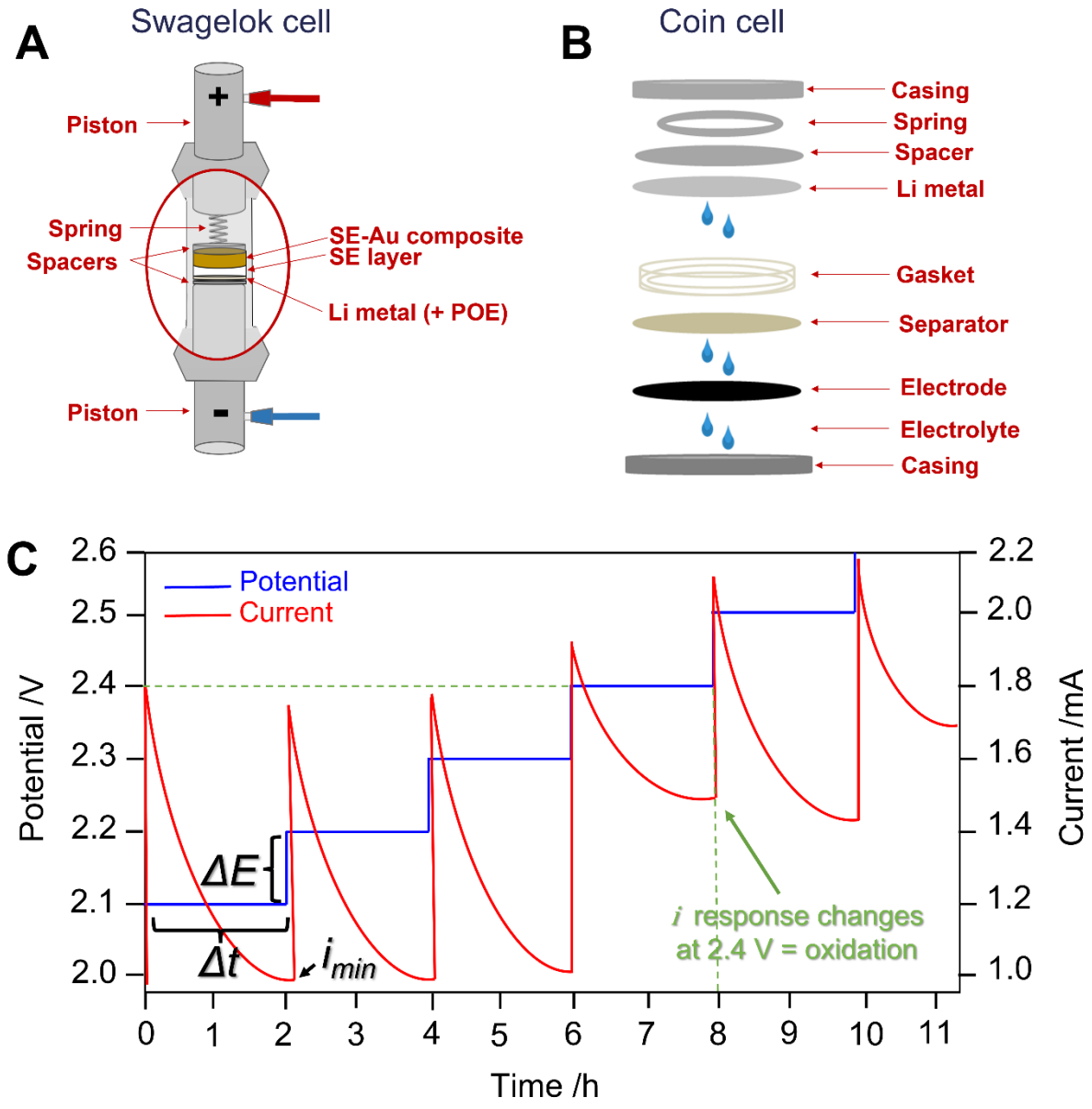

Figure 2.4 - A) Representation of a SE-Au/SE/Li system in a Swagelok cell. B) Illustration of a coin cell configuration [446]. C) Graph illustrating the potential steps and corresponding current response in PITT. At 2.4 V, the current doesn't decrease exponentially over time and does not decrease back to i_{min} threshold value, suggesting that an oxidation reaction is taking place.

2.1.5.3 – Electrochemical impedance spectroscopy

The most commonly used technique to measure the ionic conductivity in solids is the electrochemical impedance spectroscopy (EIS). However, EIS can also be used to characterize

the nature and evolution of different phenomena occurring in the system. Impedance is derived from Ohm's law :

$$E_{DC} = I \times R \qquad \text{Eq. 2.10}$$

where *E* is the potential in a direct current circuit, *I* is the current and *R* is the resistance. Impedance (*Z*) is the equivalence of resistance but when the current circuit is alternative (AC):

$$E_{AC} = I \times Z \qquad \text{Eq. 2.11}$$

Therefore, impedance is measured by applying an oscillating voltage at different frequencies (usually ranging from the MHz down to the mHz) and measuring the correspondingly oscillating current response (**Figure 2.5A**) [447]. Because the voltage and current are sinusoidal, they have an amplitude (|*E*|, |*I*|) and a frequency (*ω*), they can be expressed using the following:

$$E(t) = |E|\, sin(\omega t) \quad \text{and} \quad I(t) = |I|\, sin(\omega t + \theta) \qquad \text{Eq. 2.12}$$

The current is shifted in phase by *θ* and in amplitude because of phenomena like reactance (capacitance, inductance) and resistance [448]. The impedance can be expressed as follows:

$$Z = \frac{E(t)}{I(t)} = \frac{|E|\, sin(\omega t)}{|I|\, sin(\omega t+\theta)} = |Z| \frac{sin(\omega t)}{sin(\omega t+\theta)} \qquad \text{Eq. 2.13}$$

Using Euler's formula ($e^{i\theta} = cos\theta + isin\theta$), we express impedance as a complex number, with real (*Z*') and imaginary (*iZ''*) parts:

$$Z = \frac{|E|\, e^{i\theta}}{|I|\, e^{i\omega t+\theta}} = |Z| e^{i\theta} \quad \text{and} \quad Z = \overbrace{Z'}^{Re(Z)} + \overbrace{iZ''}^{Im(Z)} \qquad \text{Eq. 2.14}$$

The real part of impedance (Re(Z)) represents the resistance while the imaginary part of the impedance (Im(Z)) represents the reactance (capacitance and inductance) [447]. -Im(Z) is plotted as a function of Re(Z) and referred to as a Nyquist plot, where each point of the plot is a measure of impedance at a given frequency. Impedance measurements can also be presented as Bode plots (not used in this manuscript).

The impedance in a Nyquist plot is the smallest at high frequencies and increases at lower frequencies, from left to right. In theory, the shape of the curve on a Nyquist plot allows to distinguish between the contribution for each elementary electrochemical mechanism occurring in the system [449]. These contributions are represented by basic electrical circuit components: resistors (R) and capacitors (C), as illustrated in **Figure 2.5B**. As mentioned earlier, resistance corresponds to the real part of impedance, therefore pure resistors are only measured on the Re(Z) x-axis of the Nyquist plot. On the other side, pure capacitors correspond to the imaginary part of impedance, they don't depend on Re(Z). A pure capacitive contribution is then represented

by a vertical line on a Nyquist plot [447]. Resistors and capacitors can represent many mechanisms like the electronic/ionic resistance (R), the double-layer capacitance (C), the dielectric capacitance (C), the grain boundary (C) …etc. In more complex mechanisms like charge transfers, resistors and capacitors are combined to give semi-circles on the Nyquist plot. In addition to R and C, other electric circuit elements are found to represent real mechanisms: the constant phase element (CPE), used to model imperfect capacitors, the Warburg impedance (W), used to model a diffusion mechanism… etc (**Figure 2.5B**). Combining these electric elements, a fit of the impedance curve can be modeled and the resulting electrical model is referred to as the equivalent circuit, shown as an insert in **Figure 2.5C**. Some equivalent circuits are known to best represent the electrochemical mechanisms occurring in LIBs, including Debye and Randles circuits. The latter is often used in the literature, it's illustrated in **Figure 2.5C** [450].

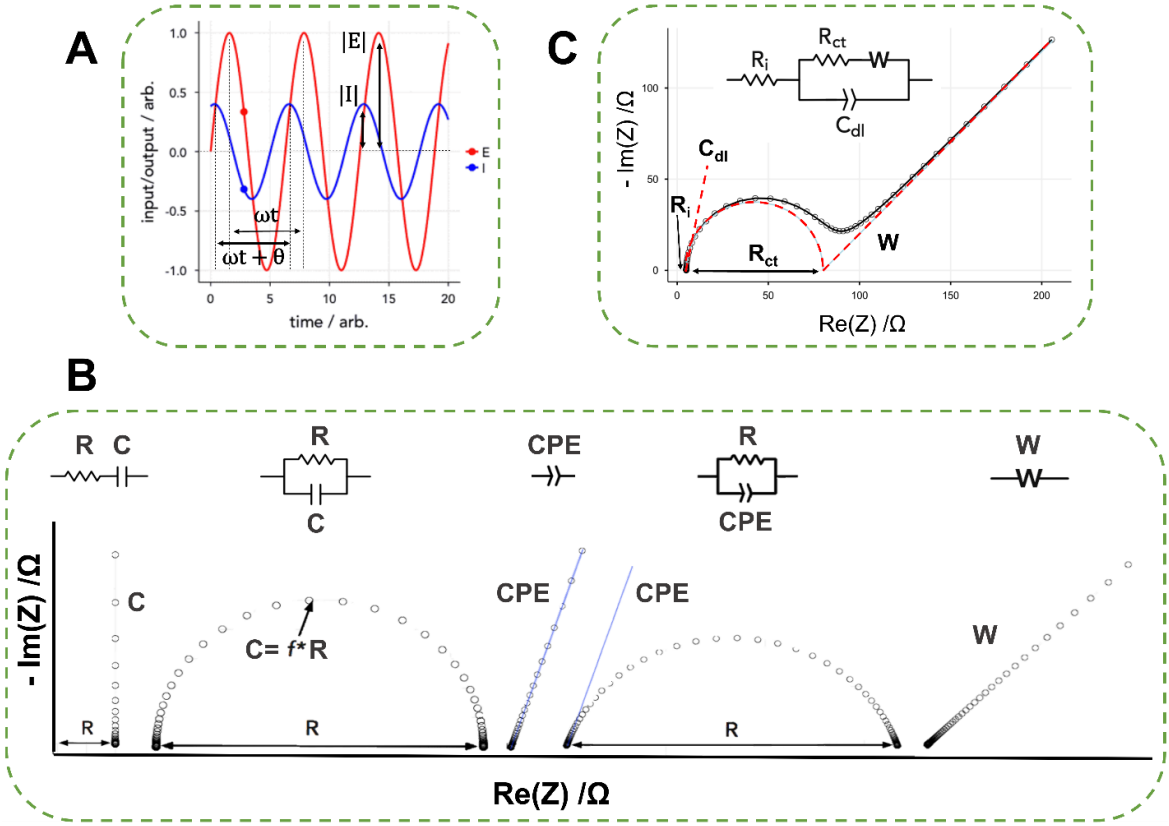

Figure 2.5 - A) Representation of the sinusoidal behavior of the potential and current response in an alternative current circuit. |E|, |I| are their amplitudes and ω their frequencies, the phase shift of the current response (θ) is observed. B) A Nyquist plot (-Im(Z) as a function of Re(Z)), where each point is the measure of impedance at the frequency ***f***, showing different electrical circuit components: resistors (R), capacitors (C), constant phase element (CPE) and Warburg impedance (W). C) Randles equivalent circuit and a corresponding Nyquist plot [447].

2.1.6 – O_2 sensing

The oxidation of solid electrolytes might lead to their decomposition into O_2 gas. In order to detect the presence of trace amounts of O_2 (1ppm) during the oxidation of our materials, an electro-galvanic fuel cell is used as a trace oxygen sensor. The electro-galvanic fuel cell device uses oxygen as a precursor to fuel a chemical reaction that generates an electrical signal [451]. The electro-galvanic fuel cell used in this manuscript is a Pb-O_2 cell and is illustrated in **Figure 2.6**. It involves the following redox reaction:

Reduction (cathode): $O_2 + 2H_2O + 4e^- \rightarrow 4HO^-$ Eq. 2.15

Oxidation (anode): $2Pb + 4HO^- \rightarrow 2PbO + 2H_2O + 4e^-$ Eq. 2.16

Oxygen from the sample is dissolved into the fuel cell electrolyte (typically KOH) through a Teflon membrane and migrates to the cathode. Pb is oxidized at the anode with the electrolyte to produce PbO and electrons. The electrons are then used to reduce O_2 at the cathode. The electrical signal generated from the redox reaction is proportional to the O_2 partial pressure in the sample [451].

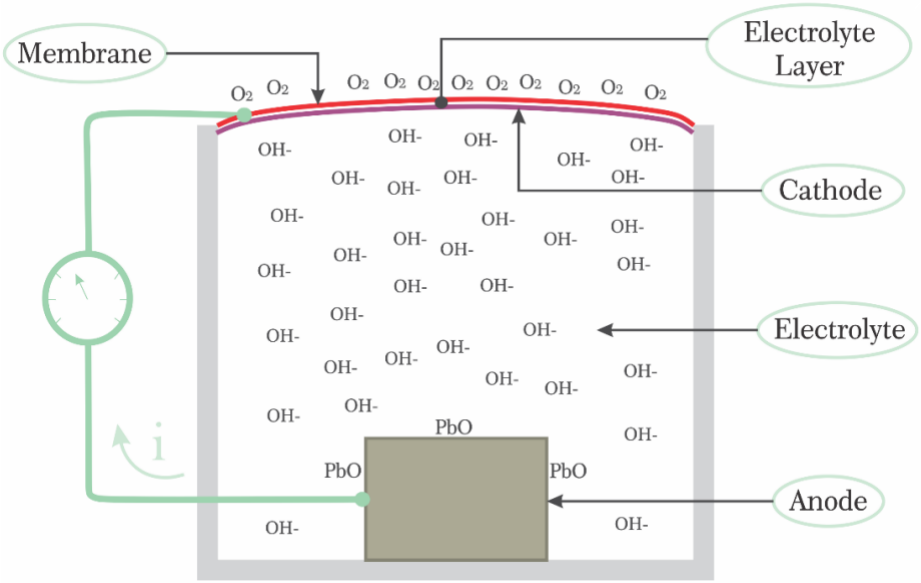

Figure 2.6 - Representation of an electro-galvanic fuel cell based on Pb-O_2 redox couple [451].

2.1.7 – Nuclear magnetic resonance spectroscopy

Nuclear magnetic resonance (NMR) spectroscopy uses a magnetic field to probe the intrinsic spin properties of the atomic nuclei of a sample. The spin of a nucleus is found in its protons and neutrons. Inside the nucleus, protons and neutrons cancel each other's spins unless the number of protons or neutrons is odd, in which case the cancellation is not complete, and the nucleus acquires a net spin. Spin also depends on the mass of the nucleus; only odd mass numbers lead to a net spin. Nuclei with even numbers of protons/neutrons and even mass numbers have zero spin and are therefore inactive in NMR [452]. This particularity reduces the number of atoms detected by NMR, the most observed atoms in NMR include: ^{1}H (spin 1/2), ^{7}Li (3/2), ^{13}C (1/2), ^{15}N (1/2), ^{17}O (5/2), ^{23}Na (3/2), ^{27}Al (5/2), ^{29}Si (1/2) and ^{31}P (1/2). ^{7}Li-based NMR is used for this project. As mentioned above, ^{7}Li has a spin of 3/2; referred to as a quadrupolar nuclei (involves any spin greater than 1/2). However, the following explanation will be focused on simpler dipolar spins (½). Under the magnetic field influence, the 1/2 spin nuclei behave like magnets that change orientations, thus change spins, to align with (parallel) or against (antiparallel) the magnetic field, defined as resonance [453]. For each value of spin ''I'', there are ''2I + 1'' different orientations possible under a magnetic field, this splitting is referred to as the Zeeman effect (**Figure 2.7A**). ½ spins will split into two energy levels, as seen in **Figure 2.7A**, while 3/2 spins will split into four. These changes of orientation require specific and quantified amounts of energy, which depend on the magnetic field applied, following equation 2.17:

$$E = -l\hbar\gamma B_0 \qquad \text{Eq. 2.17}$$

where *E* is the energy required to change spin, *I* is the value of the spin, $\hbar$ is the Planck constant ($h/2\pi$), γ is gyromagnetic ratio (specific to the nucleus) and B_0 is the applied magnetic field. For instance, a spin that aligns with the magnetic field has low energy. On the other hand, a spin that aligns against the magnetic field requires higher energy. The difference in energy (ΔE) between two spins generated by the Zeeman splitting is illustrated in **Figure 2.7A**. It is derived from the following equation 2.18:

$$\Delta E = \hbar\gamma B_0 \qquad \text{Eq. 2.18}$$

These energies have a frequency (v) associated to them, referred to as the Larmor or precession frequency. The Larmor frequency represents the frequency at which charged nuclei will precess when placed in a magnetic field. It is specific to each nucleus and is in the order of magnitude of the radio-frequency (MHz-GHz). It is derived from equation 2.19:

$$\nu = \frac{\gamma B_0}{2\pi} \qquad \text{Eq. 2.19}$$

Zeeman splitting describes interactions between dipolar nuclei and the external magnetic field. However, for quadrupolar nuclei, such as ^{7}Li, these interactions are perturbed by an additional interaction, called quadrupolar coupling, because they possess a quadripolar moment. This quadrupolar moment arises from the asymmetric distribution of charge in the quadrupolar nucleus, which creates an electric field gradient around the nuclei that interacts with the nuclear spin. These quadrupolar interactions are much weaker than the Zeeman interaction. They cause the splitting of the Zeeman energy levels, resulting in 1st and 2nd order quadrupolar interactions.

In NMR, nuclei in a sample are surrounded by gravitating electrons, these charged particles create a distinct and very localized magnetic field [454]. This local magnetic field will inhibit the effect of the external magnetic field B_0 on the neighboring nuclei, consequently affecting the energies *E* expressed in equation 2.17. This phenomenon is referred to as shielding [453]. To compensate for the loss of the effective signal and achieve resonance, the external magnetic field must be increased. The difference in frequency (*v*) required to close the gap is called a chemical shift and is expressed in parts per million (ppm). The chemical shift induced by shielding allows to distinguish between atoms in different local environments, making NMR a powerful and precise characterization technique for non-zero spin nuclei. The NMR signal is modulated using Fourier transform. In a typical NMR spectrum, the intensity of the signal is plotted as a function of the chemical shift. Each peak corresponds to a distinct environment of the probed nucleus. The NMR signals of quadrupolar nuclei are generally wider than those of dipolar nuclei due to rapid quadrupolar relaxation. Also, because of the Zeeman energy levels splitting, the NMR spectra of quadrupolar nuclei have broader and distorted line shapes. The NMR signal for quadrupolar nuclei is processed differently than dipolar nuclei but also provides more information on the chemical environment of the NMR-active nucleus.

Traditionally, NMR is used to characterize liquid samples in which orientation-dependent interactions are averaged out by molecular motion in solution. However, the same is not true for solid-state samples which, given their limited mobility, tend to contain significant anisotropy due to orientation-dependent interactions occurring at slightly different frequencies in the same material [452]. Therefore, each signal in NMR becomes a sum of the different anisotropic contributions, resulting in a significant broadening of the peaks. Nevertheless, this phenomenon is minimized and high resolution is possible when solid-state NMR spectra are measured under magic-angle spinning (MAS), as shown in the two spectra of **Figure 2.7B**. MAS NMR consists of spinning the sample at a frequency, ranging from 1 to 130 kHz, at the precise angle of 54.74° with

respect to the direction of the applied magnetic field. This angle is used as it serves to eliminate line broadening caused by dipolar coupling interactions and chemical shift anisotropy. Typical MAS does not eliminate line broadening or line shape distortion caused by quadrupolar interactions. However, as quadrupolar interactions in ^{7}Li are generally weak, MAS NMR yields well-resolved spectra.

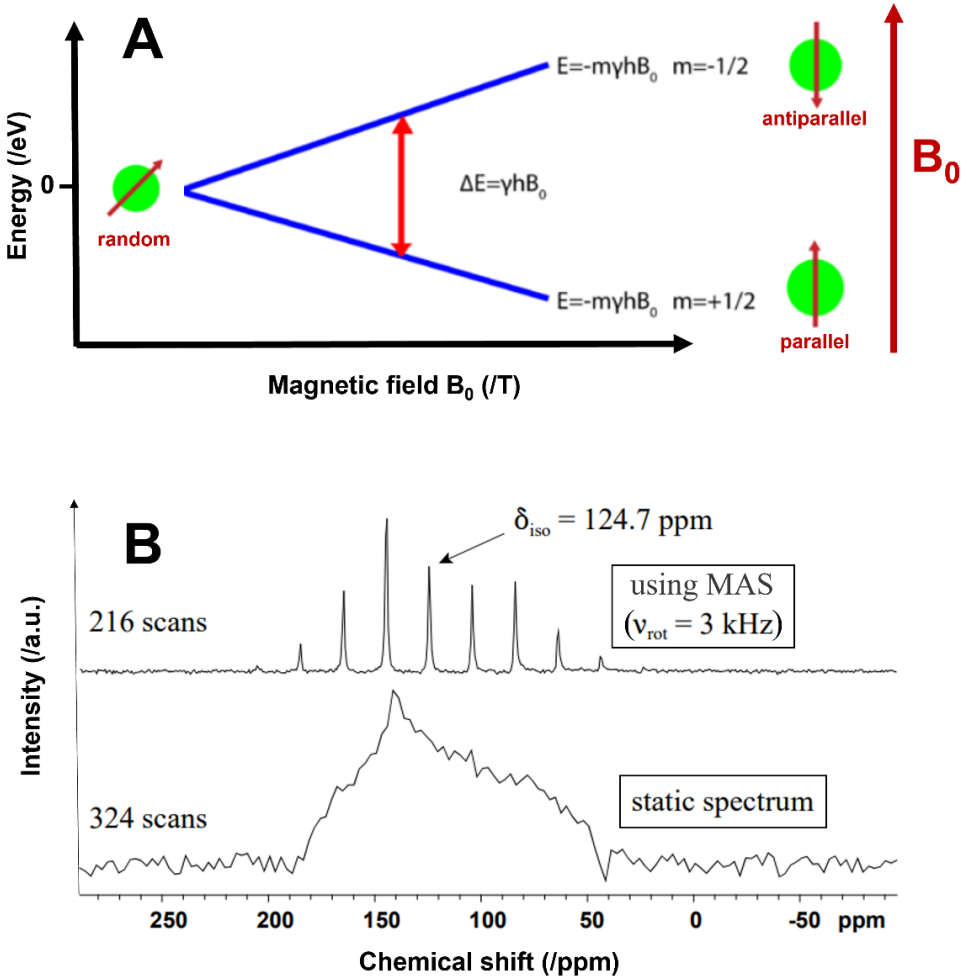

Figure 2.7 - A) Schematic representation of the Zeeman splitting: the nuclear spin (m = 1/2), initially randomly oriented, align with (parallel) or against (antiparralel) the applied magnetic field B_0. The two orientations have different energies, and the difference of energy between the two is illustrated on the figure (ΔE) [454]. B) Comparison of two solid-state ^{119}Sn NMR spectra taken with and without MAS for a $Cp^*_2SnMe_2$ crystal (rotation frequency = 3kHz, B_0 = 9.4 T). For a similar number of scans, the resolution is significantly higher under MAS [455].

2.2 – Theoretical methods

2.2.1 – First-principles calculations

First-principles calculations are a computational method that uses quantum mechanics to study the electronic structure of a system. Also referred to as *ab initio*, these computations are expensive but essential to describe electronic structures, covalent bonds formation and redox reactions [456]. In quantum mechanics, the complete description of atoms and electrons in a quantum system is obtained by solving the time-independent Schrödinger equation [457]:

$$\hat{H}\Psi(\boldsymbol{r},\boldsymbol{R}) = E\Psi(\boldsymbol{r},\boldsymbol{R}) \qquad \text{Eq. 2.20}$$

where $\Psi(\boldsymbol{r},\boldsymbol{R})$ represents the system's wavefunction, dependent on the position vector of the electrons $\boldsymbol{r}$ and the atoms $\boldsymbol{R}$ of the system, E the ground state energy and $\hat{H}$ the Hamiltonian operator:

$$\hat{H} = \underbrace{-\sum_I^{N_{at}} \frac{\hbar^2}{2M_I}\nabla_I^2}_{\hat{T}_n} \underbrace{-\sum_i^{N_e} \frac{\hbar^2}{2m_i}\nabla_i^2}_{\hat{T}_e} + \underbrace{\sum_{I\neq J}^{N_{at}} \frac{Z_I Z_J e^2}{4\pi\varepsilon_0|\boldsymbol{R}_I-\boldsymbol{R}_J|}}_{\hat{V}_{nn}} + \underbrace{\sum_{i\neq j}^{N_e} \frac{e^2}{4\pi\varepsilon_0|\boldsymbol{r}_i-\boldsymbol{r}_j|}}_{\hat{V}_{ee}} - \underbrace{\sum_I^{N_{at}}\sum_j^{N_e} \frac{Z_I e^2}{4\pi\varepsilon_0|\boldsymbol{R}_I-\boldsymbol{r}_j|}}_{\hat{V}_{en}} \qquad \text{Eq. 2.21}$$

The Hamiltonian operator is the sum of five operators: $\hat{T}_n$ is the operator for the kinetic energy of atoms, with N_{at} the number of atoms and M_I the mass of an atom I. The operator $\hat{T}_e$ is the kinetic energy of electrons, with N_e the number of electrons and m the mass of an electron e. $\hat{V}_{nn}$ is the operator of the coulombic potential between atoms, with Z_I the charge and $\boldsymbol{R}_I$ the position vector of nucleus I, e the absolute value of the charge of an electron and ε_0 the vacuum permittivity. $\hat{V}_{ee}$ is the operator of the coulombic potential between electrons, with $\boldsymbol{r}$ the position vector of an electron. $\hat{V}_{en}$ is the operator for the coulombic potential between atoms and electrons. The contribution of the nuclear coordinates $\boldsymbol{R}$ can be neglected following the Born-Oppenheimer approximation [458], only the position vector of electrons $\boldsymbol{r}$ is considered passed this point.

The analytical resolution of Schrödinger's equation is only possible for one-electron systems. For a multielectron system, the wave function $\Psi(\boldsymbol{r})$, being correlated between the particles of the system, is not allowed to be separated into several independent equations and, therefore, does not allow to find an analytical solution. This limitation gave way to numerical approaches to solve the Schrödinger equation for multielectron systems, like the density functional theory (DFT).

2.2.1.1 – Density functional theory

DFT is based on the Hohenberg-Kohn theorem [459], stating that the overall energy *E* of a ground state electron system is a unique functional of the electron density. By extension, all measurable physical quantities of a ground-state system are unique functionals of the electron density of that ground-state system. Thus, the electron density probability function $\rho_0(\boldsymbol{r})$ is expressed as:

$$\rho_0(\boldsymbol{r}) = \sum_{s=-1/2}^{1/2} \int |\Psi_0(\boldsymbol{r}, \boldsymbol{r}_2, \dots \boldsymbol{r}_n, s_1, s_2, \dots s_n)|^2 d\boldsymbol{r}_2 \dots d\boldsymbol{r}_n \qquad \text{Eq. 2.22}$$

$\boldsymbol{r}$ is the electron position vector and *s* the spin, Ψ_0 is the ground state wave function, $\boldsymbol{r}_2 \dots \boldsymbol{r}_n$ represent the position vectors of the *2…n* electrons, $s_1 \dots s_n$ represent the spin values of the *1…n* electrons. Equation 2.22 highlights how the multi-electronic system problem can be simplified when density probability function is used: the wave function of an n-body system $\Psi_0(\boldsymbol{r}, \boldsymbol{r}_2, \dots \boldsymbol{r}_n, s_1, s_2, \dots s_n)$ depends on *3n* spatial position coordinates and *n* spin coordinates. In contrast, the electron density probability $\rho_0(\boldsymbol{r})$ only depends on 3 spatial position coordinates.

2.2.1.2 – Kohn-Sham theory

The universal functional of the density ($F[\rho]$) is approximated as a sum of three functionals:

$$F[\rho] = T_s[\rho] + J[\rho] + E_{xc}[\rho] \qquad \text{Eq. 2.23}$$

In this equation, the first functional $T_s[\rho]$ represents the contribution of the kinetic energy, it depends on one-electron orbitals. The second functional $J[\rho]$ corresponds to the coulombic repulsion generated by the charge density ρ, including the electron's self-interaction (also called the Hartree term). The last functional is the exchange-correlation energy $E_{xc}[\rho]$, it considers the energy contributions that are not included in the two previous functionals, in particular the energy of repulsion of the electrons with themselves. This equation attempts to compute the energy of interacting electrons in a system as a functional of the total density. However, this method is not accurate because the functional of the kinetic energy $T_s[\rho]$ is not well approximated. Kohn and Sham proposed an alternative approach in order to circumvent this issue [460]. They suggested the use of non-interacting electrons. Non-interacting electrons have different wavefunctions and density than that of the interacting ones. For this reason, the Kohn-Sham approach uses a fictitious non-interacting system which density is the same as that of the interacting electrons. Therefore, the Hamiltonian expressed in equation 2.21, which describes the interacting electrons, is converted to a sum of one-electron Hamiltonians:

$$\widehat{H}_{KS} = \sum_{i=1}^{N_e} \hat{h}\,(\boldsymbol{r_i})$$ Eq. 2.24

where $\widehat{H}_{KS}$ is the Hamiltonian suggested by Kohn and sham, $\hat{h}(r_i)$ is the one-electron Hamiltonian for electron *i* of position vector $\boldsymbol{r}_i$. The Schrödinger equation 2.20 can now be expressed with Kohn-Sham one-electron wavefunctions (φ_i) following equation 2.25:

$$\left(-\frac{\hbar^2}{2m}\nabla^2 + \vartheta_{eff}(r)\right)\varphi_i(r) = \varepsilon_i\varphi_i(r)$$ Eq. 2.25

where the one-electron Hamiltonian proposed by Kohn and Sham is expressed in terms of a local effective and fictitious potential v_{eff} (Kohn-Sham potential) in which the non-interacting particles move. The density probability functional, previously expressed in equation 2.23, is now expressed using Kohn-Sham theory as follows:

$$F[\rho]_{KS} = T_s[\rho]_{KS} + \int d\boldsymbol{r}\vartheta_{ext}(\boldsymbol{r})\rho(\boldsymbol{r}) + J[\rho] + E_{xc}[\rho]$$ Eq. 2.26

where $T_s[\rho]_{KS}$ is the Kohn-Sham kinetic energy functional for non-interacting electrons and is computed from Kohn-Sham one-electron wavefunctions:

$$T_s[\rho]_{KS} = \sum_{i=1}^{N}\int d\boldsymbol{r}\varphi_i{}^*(\boldsymbol{r})\left(-\frac{\hbar^2}{2m}\nabla^2\right)\varphi_i(\boldsymbol{r})$$ Eq. 2.27

ϑ_{ext} is an external potential accounting for the contribution of the nuclei. The difference between the initial kinetic energy ($T_s[\rho]$) and the Kohn-Sham kinetic energy ($T_s[\rho]_{KS}$) is smaller than the error of pure DFT and is usually included in the exchange-correlation functional. Allowing more accurate approximations of the electronic density.

2.2.1.3 – Exchange-correlation functionals

The accuracy of DFT lies in the accuracy of the exchange-correlation functional. Several approximations have been developed to determine this functional, like the generalized gradient approximation (GGA), expressed in equation 2.28:

$$E_{xc}^{GGA}\left[\rho^{\uparrow},\rho^{\downarrow}\right] = \int f\left(\rho^{\uparrow}(\boldsymbol{r}),\rho^{\downarrow}(\boldsymbol{r}),\nabla\rho^{\uparrow}(\boldsymbol{r}),\nabla\rho^{\downarrow}(\boldsymbol{r})\right)dr$$ Eq. 2.28

where the exchange-correlation functional $E_{xc}^{GGA}\left[\rho^{\uparrow},\rho^{\downarrow}\right]$ is calculated according to the local electron density at spins up $\rho^{\uparrow}(\mathbf{r})$ and down $\rho^{\downarrow}(\mathbf{r})$ but also according to density gradients of spins up $\nabla\rho^{\uparrow}(\boldsymbol{r})$ and down $\nabla\rho^{\downarrow}(\boldsymbol{r})$. These local density gradients are used in GGA to create an asymptote of the density and help to better describe the behavior and the heterogeneity of a real

electronic density [461]. The most used GGA-type functional for the computation of inorganic materials is the one proposed by Perdew, Burke and Ernzerhof (PBE), known to yield a good accuracy-over-computation-cost ratio for the calculation of dissociation energies (when it comes to molecules) and band gaps in transition metals (although it has shown some shortcomings for the latter) [461]. Following the GGA functionals, hybrid exchange-correlation functionals were also developed to combine Kohn-Sham DFT-based functionals, like GGA, with exact Hartree-Fock (HF) exchange [462], illustrated in equation 2.29:

$$E_{xc}^{hybrid} = \alpha E_x^{HF} + (1-\alpha)E_x^{GGA} + E_c^{GGA} \qquad \text{Eq. 2.29}$$

where *α* is the relative proportion of the HF exchange. Hybrid functionals are more accurate than semi-local methods like GGA, especially when computing band gaps for non-metallic systems. A commonly used hybrid functional is the one introduced by Heyd, Scuseria and Ernzerhof (HSE) [463, 464].

2.2.1.3 – Pseudo-potentials

At this stage, research has only focused on calculating electronic energies for a well-defined system. However, when it comes to studying periodic systems, the use of a basis is necessary. The most widely used basis is the sinusoidal plane wave, which describes the valence electrons of a periodic system well. However, the sinusoidal plane wave does not correctly describe the orbitals of the core electrons, which are subject to too large oscillations with high frequencies, requiring very small-wavelength plane waves to describe them properly. In this case, we apply an indirect treatment of the core electrons, called pseudo-potentials. It consists of replacing the effect of the nucleus and the core electrons by an effective operator which is similar to the effect of a nucleus on the valence electrons [465].

2.2.1.4 – Hubbard parameter

The GGA method presents significant limitations when applied to correlated systems like transition metal oxides [466]. GGA-type exchange-correlation functionals are known to over-delocalize valence electrons and to over-stabilize metallic ground states. In consequence, several semiconductor materials, with a non-negligible band gap, are predicted to be conductors by GGA [467]. A way to deal with these highly correlated d and f valence electrons is to think of them as subject to an additional quasi-atomic interaction. This type of interaction is well described by the Hubbard model [468]. An additional energy term is then used for the transition elements, referred

to as the Hubbard parameter (U), to make the delocalization of d and f electrons more difficult. The U parameter is a semi-empirically tuned numerical parameter, determined by imposing consistency between calculations and experimental results.

2.2.1.5 – K-points

The description of molecular orbitals in a finite system (an elementary box) is done using three discrete quantum numbers: m_s (spin quantum number), m_ℓ (magnetic quantum number) and ℓ (orbital quantum number). On the other hand, in an infinite periodic system the orbitals require an additional parameter which can describe how the molecular orbital of the system was obtained according to the electronic orbitals of the elementary boxes. It is a continuous number *k* called k-point [469]. In other words, the periodicity implies an infinite number of elementary boxes and the parameter k makes it possible to distinguish how the orbitals of each box are combined between them. In solids, **k** is a wavevector, it is defined in the reciprocal space and depends on the shape of the elementary box in direct space. If the box is a rectangular parallelepiped of dimensions l_x, l_y and l_z, then the wavevector ***k*** is also defined in a rectangular parallelepiped in reciprocal space (Brillouin zone) of dimensions $2\pi/l_x$, $2\pi/l_y$ and $2\pi/l_z$.

To perform calculations, the orbitals in a solid will be indexed by two types of indices: a discrete index (quantum numbers ℓ, m_ℓ, m_s), which will label the molecular orbitals inside a box, and a continuous index, represented by the wavevector ***k*** which takes continuous values everywhere inside the first Brillouin zone. As it is impossible to solve the Kohn-Sham equation for all wavevectors, one samples this Brillouin zone through a grid of so-called k-points of reasonable density. The denser the grid, the more precise the description of the system will be. A grid with a reasonable accuracy-over-computational-cost ratio to use in calculations depends on the size of the unit cell and the number of atoms involved.

2.2.1.6 – DFT implementation

DFT methods are implemented in computer software such as ABINIT [470], SIESTA [471] and VASP [472]. The Vienna *ab initio* simulation package (VASP) is the program used in this manuscript, it solves the Schrödinger equation for a multi-electronic system using DFT and plane wave-based, or hybrid, exchange-correlation functionals like GGA and HSE. Using VASP, it is possible to model materials at the atomic scale, several types of molecular dynamics, the response to an electric field, the optical properties, the magnetism of a system… etc.

2.2.2 – Grand potential phase diagram

The grand potential phase diagram (GPPD) code can be found in the Pymatgen© library [473]. This open-source python library provides a significant number of codes for the study of materials. Pymatgen is used to compute the properties of inorganic materials and feed the Materials Project© database previously mentioned in section 1.5 [370].

The grand potential phase diagram is constructed to study the electrochemical stability window of the solid electrolyte materials. GPPDs are phase diagrams constructed with an element kept open. If we assume that Li is the main mobile ion in Li-based batteries, we can model the system as a GPPD open with respect to Li. Also, GPPDs represent the phase equilibria of a SE's system that is open to lithium, which is relevant when the SE is in contact with a reservoir or sink of lithium, as experienced in a Li-based battery [379]. The relevant thermodynamic potential is then the grand potential (ϕ), a state function of the grand canonical ensemble [259, 474], expressed as:

$$\phi = E - \mu_{Li} N_{Li} \qquad \text{Eq. 2.30}$$

where E is the internal energy, μ_{Li} is Li chemical potential and N_{Li} is the number of Li atoms in the open system [475]. ESW of SEs are predicted by following the stability of a SE as a function of a changing chemical potential of lithium (μ_{Li}) [379]. The stability of a SE ($\phi < 0$ eV) is determined from the convex hull constructed for each value of μ_{Li}. The convex hull is a plot of the formation energy as a function of the composition for all the phases of a phase diagram, it connects phases that have the lowest energy for each given composition, as illustrated in **Figure 2.8**. The phases that lie on the convex hull are thermodynamically stable. The ones above it are metastable or unstable and will eventually decompose into the thermodynamically stable ones. The stability of a solid electrolyte is determined by its location on the convex hull at each value of μ_{Li}. If a SE lies on the convex hull, it is considered stable (e.g., Li_xB in **Figure 2.8**) [406]. To predict the ESW, we calculate the range of μ_{Li} over which the SE is present on the convex hull, and therefore stable, and convert this range of chemical potentials into a range of potentials vs. Li^+/Li using equation 2.31, allowing the GPPD to describe the electrochemical lithiation and delithiation of materials under an applied potential [365].

$$\boldsymbol{V} = -\frac{\boldsymbol{\mu_{Li} - \mu^{\circ}_{Li}}}{e} \qquad \text{Eq. 2.31}$$

where V is the potential vs. Li^+/Li, μ°_{Li} is the standard computed energy for lithium metal, e is the elementary electron charge.

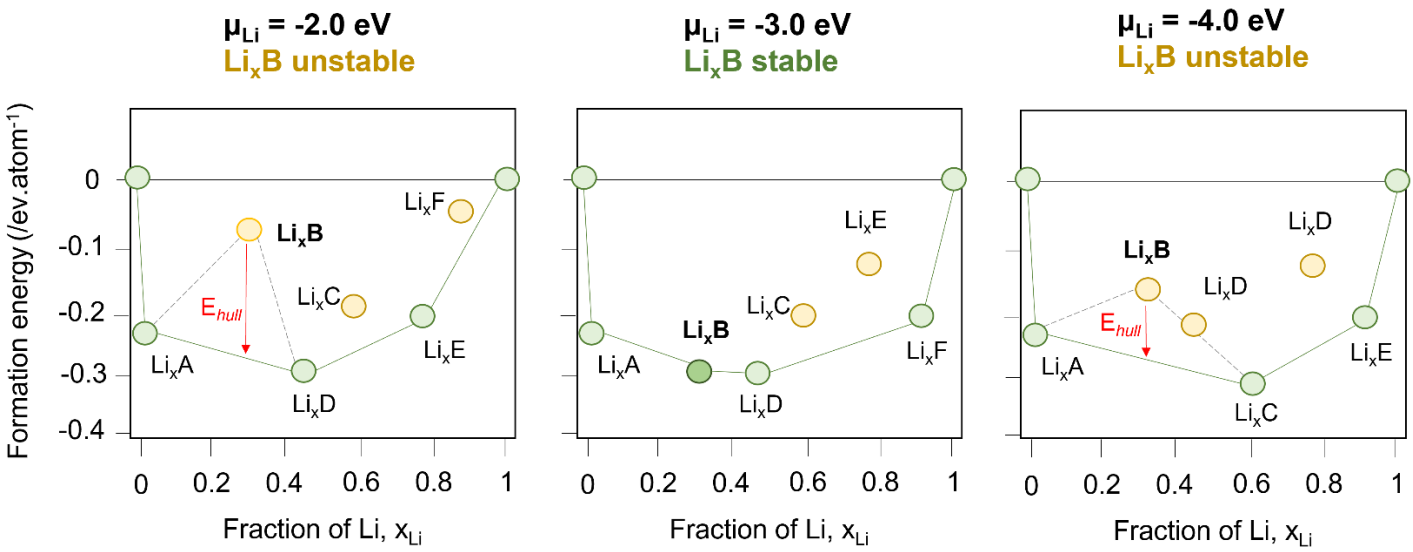

Figure 2.8 - A schematic convex hull at different chemical potentials (μ_{Li}): thermodynamically stable phases in green lie on the convex hull, unstable phases are illustrated in yellow. Li_xB is unstable at μ_{Li} = -2.0 eV. At μ_{Li} = -3.0 eV, the formation energies of all the phases change and Li_xB becomes stable. This same phase becomes unstable at μ_{Li} = -4.0 eV. E_{hull} in red represents the energy above hull of Li_xB.

2.2.3 – Charged point defects

A defect is an irregularity or imperfection in the regular geometrical arrangement of the atoms in a crystal structure. There are several types of defects, including point defects (vacancies, interstitials and antisites), linear defects (dislocations) and surfacial defects (grain boundaries). The presence of defects in a crystal structure has a profound effect on the behavior of the material, many properties and phenomena in materials are controlled by defects such as the electronic, ionic and thermal conductivities as mentioned in sections 1.4.1.1 and 1.4.1.4 (controlled by point defects), the plastic deformation (controlled by dislocation), the color and the mechanical strength. Computing the formation of defects is therefore essential to the understanding of the materials' intrinsic properties. Charged point defects are computed in the manuscript using the python charged defect toolkit (PyCDT) [476].

2.2.3.1 – Formation energy

In the context of this manuscript, only charged point defects are considered, illustrated in **Figure 2.9A.** They are commonly computed using the supercell approach, where a point defect is

manually introduced inside a supercell of the initial material before it's relaxed using DFT. The formation energy of the defect is computed using the following equation 2.32:

$$E_{form}[X^q] = E_{tot}[X^q] - E_{tot}^{bulk} - \sum n_i \mu_i + qE_F + E_{corr} \quad \text{Eq. 2.32}$$

where E_{tot} is the total energy of the defective supercell (for a given defect *X* in the charge state *q*) and E_{tot}^{bulk} is the energy of the host supercell. The third term represents the energy needed to exchange atoms with thermodynamic reservoirs where n_i indicates the number of atoms of the species *i* removed or added to create the defect, and μ_i are their corresponding chemical potentials. The fourth term is the Fermi level E_F (electron chemical potential) relative to the valence band maximum, it accounts for electrons added to (q < 0) or removed from (q > 0) the supercell. The last term E_{corr} of the equation is a correction term accounting for the finite size of the supercell, arising from the electrostatic interaction between defects and their periodic images. The size of the supercell is chosen according to the convergence of E_{corr}. These five contributions are illustrated in **Figure 2.9B**.

The formation energy depends on the Fermi level (E_F) and the chemical potential (μ_i) as shown in equation 2.32. The formation energy of a defect is plotted as a function of the Fermi level, for each value of μ_i as illustrated in **Figure 2.9C**. The Fermi energy (x-axis) is normalized by the valence band maximum (VBM). The energy difference between the VBM and the conduction band minimum (CBM) is the band gap. Charged defects form in different charge states, the defect transition level, in purple on **Figure 2.9C**, is used to represent the energetic level at which a defect captures (or emits) a free carrier [477]. The upper and lower dopability limits, given in orange circles on **Figure 2.9C,** represent the Fermi level that first produces defects with negative formation energy, making the structure unstable. Pushing the Fermi level beyond the dopability limits violates the thermodynamic condition of structural stability [477]. More details on the dopability limits will be given in chapter 5.

2.2.3.2 – Determination of the Fermi level at equilibrium

The concentration of charge carriers (electrons and holes) is determined by the position of the Fermi level following these equations :

$$n_0 = N_C e^{-\left(\frac{E_C - E_F}{k_B T}\right)} \quad \text{and} \quad p_0 = N_V e^{-\left(\frac{E_F - E_V}{k_B T}\right)} \quad \text{Eq. 2.33}$$

where n_0 and p_0 are the concentrations of electrons and holes, N_C and N_V are the effective density of states for the conduction and valence bands, respectively, E_C and E_V are the energies of the

CBM and VBM respectively, E_F is the Fermi level, k_B is the Boltzmann constant and T is the temperature [478]. On the other hand, the concentration of donor or acceptor charged defects depends on their formation enthalpy (ΔH_f) following equation 2.34:

$$n_d = N_{site} g_q e^{(\frac{-\Delta H_f}{k_B T})} \quad \text{Eq. 2.34}$$

where n_d is the defect concentration of a charged donor or acceptor, N_{site} is the number of lattice sites, g_q is the degeneracy factor of a charged state (e.g., different spin configurations for the same charged state) and ΔH_f is the formation enthalpy of the point defect [478].

In defect theory, the concentrations of electrons (n_0) and charged acceptors A^- (n_A) must balance the concentration of holes (p_0) and charged donors D^+ (n_D) to yield neutrality:

$$p_0 + n_D = n_0 + n_A \quad \text{Eq. 2.35}$$

The equilibrium concentrations of charge carriers (electrons and holes) and charged defects (acceptors and donors) can be calculated self-consistently by determining the Fermi level at equilibrium (E_{F_eq}) that meet the charge neutrality requirement expressed in equation 2.35. **Figure 2.9D** summarizes the self-consistent scheme used to compute the Fermi level at equilibrium and the corresponding defect concentrations.

2.2.3.3 – Correction schemes

The introduction of defects brings a non-zero charge to the supercell. Extended to the bulk, which is formed of an infinite number of supercells, the total charge (electrostatic energy) tends to infinity. To circumvent this issue, a homogenous background charge is added to artificially bring the supercell back to neutrality. Another issue related to the periodic boundary condition is the presence of significant unwanted interactions between neighboring defects in the unit cells comprising the supercell. In an infinite crystal, the defects are scattered in distant unit cells, they have no effect on one another, but it is not the case in a single supercell used for DFT calculations. Cancelling the effect of neighboring defects will require a sufficiently large supercell to allow enough distance between two neighboring defects for their interaction on one another to be negligible. Both these corrective measures are included in the correction schemes proposed by Freysoldt *et al.* [479, 480] and Kumagai *et al.* [481], implemented to compute defects in PyCDT [477].

Defects are computed using GGA-based exchange-correlation functionals (PBE). GGA-based approximations are known to severely underestimate the band gap of semiconductors. To correct this miscomputation, VBM and CBM are computed using a hybrid functional (HSE) instead of GGA. HSE functional, mentioned in section 2.2.1.2, is an expensive but high-level computation functional used to determine more accurate band gaps than GGA. The corrected values of VBM and CBM give an extended band gap and are plotted in the formation energy plots instead of the GGA-based values.

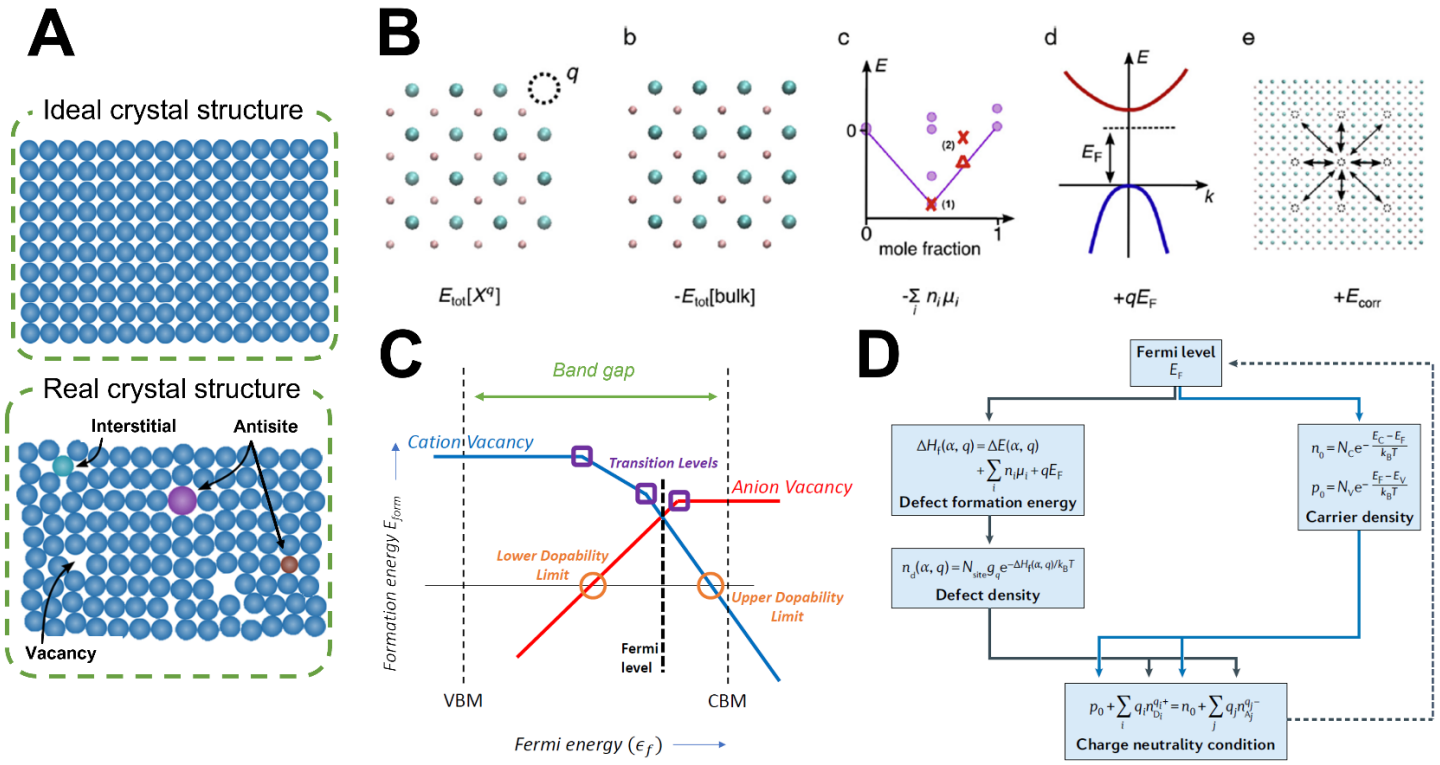

Figure 2.9 - A) Schematic representation of an ideal crystal structure and a real crystal structure with defects (only point defects are shown). B) Illustration of the different contributions to the defect formation energy [476]. C) Formation energy diagram computed for a material at a set of chemical potentials (μ_i). A cation vacancy (blue) and anion vacancy (red) are given as examples of defects. Band edges are shown in light dashed lines, the E_F at equilibrium is displayed in a thick dashed line. Transition levels are shown in purple boxes. The upper and lower dopability limits are shown as orange circles, where the defect formation energies become negative [477]. D) Framework detailing how to self-consistently compute the defect concentration, the E_F at equilibrium is determined to meet the charge neutrality requirement [478].

The techniques described above were used to produce the experimental and theoretical results presented in the following chapters. First, solid state synthesis was used to synthesize LAGP and LATP solid electrolytes in chapter 3. These two materials were sintered into dense pellets using spark plasma sintering (SPS), while pressureless sintering was used in chapter 4 on M:LLZO (M = Al, Ta, Nb) materials. The purity of the materials was confirmed using X-ray diffraction (XRD). LAGP, LATP and M:LLZO processed pellets were then closely observed under a scanning electron microscope (SEM) and investigated using energy-dispersive X-ray spectroscopy (EDS). Then, the processed pellets were assembled into electrochemical cells in order to assess their electrochemical stability window using the potentiostatic intermittent titration technique (PITT) in both chapters 3 and 4, and the electrochemical impedance spectroscopy (EIS) in chapter 3. Density functional theory (DFT) computations, focused on the construction of the grand potential phase diagram (GPPD), were performed on LAGP and LATP to assess their thermodynamic electrochemical stability window and the consequent decomposition products in chapter 3. The decomposition of these two materials following the oxidation reaction was investigated using *operando* O_2 sensing, *ex situ* transmission electron microscopy (TEM) and selected-area electron diffraction (SAED). In chapter 4, the reduction of Al:LLZO was investigated instead, using *operando* XRD and *ex situ* nuclear magnetic resonance spectroscopy (NMR). Finally, a computational study was performed on many common solid electrolytes to investigate their point defect chemistry in chapter 5. The computations were carried out using DFT, focusing on the formation energy of selected defects, followed by the computation of the Fermi level at equilibrium and the dopability limits of all the solid electrolytes of interest.

3. ASSESSING THE ELECTROCHEMICAL STABILITY WINDOW OF NASICON-TYPE SOLID ELECTROLYTES

Yasmine Benabed[1,2], Maxime Rioux[1], Steeve Rousselot[1], Geoffroy Hautier[2,3] and Mickaël Dollé[1]*

[1] Department of Chemistry, Université de Montréal, Montréal, QC, Canada.

[2] Institute of Condensed Matter and Nanosciences, Université Catholique de Louvain, Louvain-la-Neuve, Belgium.

[3] Thayer School of Engineering, Dartmouth College, Hanover, NH, United States.

Keywords - electrochemical stability window, potentiostatic intermittent titration technique, spark plasma sintering, solid electrolyte, all-solid-state lithium batteries, grand potential phase diagram, NASICON.

The results presented in the following chapter are extracted from an article published in Frontiers in Energy Research journal in May 2021 (Front. Energy Res. 9:682008 DOI: 10.3389/fenrg.2021.682008). This article focused on the development of a robust procedure to assess the electrochemical stability window of inorganic solid electrolytes. Two SEs were studied in this chapter, the NASICON-type $Li_{1.3}Al_{0.3}Ti_{1.7}(PO_4)_3$ and $Li_{1.5}Al_{0.5}Ge_{1.5}(PO_4)_3$ materials. The ESW is first predicted for these two solid electrolytes using first-principles, particularly the grand potential phase diagram previously mentioned in sections 1.5.2 and 2.2.2. Along with the stability window, it was possible to predict the decomposition products at LAGP and LATP oxidation and reduction. First-principles calculations were followed by thorough experimental work on processing the solid electrolytes into a cell configuration deemed the most suited to assess the ESW and on optimizing the PITT procedures and parameters, introduced in section 2.1.5.2, chosen as the electrochemical technique of choice to characterize the stability windows. The decomposition products were investigated using an *operando* O_2 sensing setup developed at *université de Montréal*, transmission electron microscopy and electrochemical impedance spectroscopy. In the context of this study, my contribution lies in conceiving the project, carrying out all the experiments (except for the TEM observations), performing the computations, interpreting the results and writing the article. Maxime Rioux synthesized LAGP and LATP materials. Steeve Rousselot participated greatly in conceiving the project, interpreting the results and reviewing the manuscript. Geoffroy Hautier supervised and reviewed the computational part. Mickaël Dollé conceived, supervised the project and reviewed the manuscript as principal investigator.

3.1 – Abstract

All-solid-state lithium batteries (ASSLBs) are promising since they may enable the use of high potential materials as the positive electrode and lithium metal as the negative electrode. This is only possible through solid electrolytes (SEs) stated large electrochemical stability window (ESW). Nevertheless, reported values for these ESWs are very divergent in the literature. Establishing a robust procedure to accurately determine SEs' ESWs has therefore become crucial. Our work focuses on bringing together theoretical results and an original experimental set up to assess the electrochemical stability window of the two NASICON-type SEs $Li_{1.3}Al_{0.3}Ti_{1.7}(PO_4)_3$ (LATP) and $Li_{1.5}Al_{0.5}Ge_{1.5}(PO_4)_3$ (LAGP). Using first principles, we computed thermodynamic ESWs for LATP and LAGP and their decomposition products upon redox potentials. The experimental set-up consists of a sintered stack of a thin SE layer and a SE-Au composite electrode to allow a large contact surface between SE and conductive gold particles, which maximizes the redox currents. Using potentiostatic intermittent titration technique (PITT) measurements, we were able to accurately determine the ESW of LATP and LAGP solid electrolytes. They are found to be [2.65 V - 4.6 V] and [1.85 V - 4.9 V] for LATP and LAGP respectively. Finally, we attempted to characterize the decomposition products of both materials upon oxidation. The use of an O_2 sensor coupled to the electrochemical setup enabled us to observe *operando* the production of O_2 upon LAGP and LATP oxidations, in agreement with first-principles calculations. Transmission electron microscopy (TEM) allowed to observe the presence of an amorphous phase at the interface between the gold particles and LAGP after oxidation. Electrochemical impedance spectroscopy (EIS) measurements confirmed that the resulting phase increased the total resistance of LAGP. This work aims at providing a method for an accurate determination of ESWs, considered a key parameter to a successful material selection for ASSLBs.

3.2 – Introduction

Since their commercialization in 1990, rechargeable lithium-ion batteries (LIBs) have revolutionized global communication and enabled the democratization of portable electronics. LIBs have grown to become a well-established, efficient energy-storage technology in terms of power density and life span. However, commercialized LIBs contain highly flammable and toxic organic liquids as the electrolyte ($LiPF_6$ in carbonate-based solvents), entailing significant safety hazard. Moreover, currently used liquid electrolytes hinder the use of lithium metal as a negative

electrode material and the commercialization of high-energy-density Li-metal battery systems [482, 483]. Lithium metal displays a remarkably high theoretical capacity and is considered the best negative electrode material for lithium batteries (3860 mA.h.g^{-1}, -3.05 V vs. SHE) [484]. Nevertheless, lithium metal batteries fail to achieve commercialization with conventional carbonate-based liquid electrolytes because of lithium metal's low cycling efficiency and its detrimental formation of lithium dendrites [485]. Upon cycling, the growth of dendrites at the surface of Li-metal electrodes can lead to short-circuits and thermal runaways. Moreover, the limited electrochemical stability window (ESW) of organic liquid electrolytes (up to 4.2 V vs. Li^+/Li) limits the choice of positive electrode materials in LIBs. High potential positive electrode materials, such as $LiNi_{0.5}Mn_{1.5}O_4$ [80], $LiNi_{0.8}Co_{0.15}Al_{0.05}O_2$ [81] and $LiNi_xMn_yCo_zO_2$ [82, 83], require the use of an electrolyte stable in the range of their operation potentials. To tackle these problems, researchers have been working toward developing a new generation of high-power lithium batteries, namely all-solid-state lithium batteries (ASSLBs).

ASSLBs are sparking rising interest thanks to their enhanced safety, achieved by replacing the flammable and reactive conventional liquid electrolyte with a safer and more thermally stable ceramic or polymer solid-state electrolyte (SE) [49, 84-86]. Several families of ceramic SEs have been investigated based on their ionic conductivity as well as thermal and chemical stability. Sulfur-based SE such as $Li_{10}GeP_2S_{12}$ from the thio-LiSICON family (derived from β-Li_3PO_4 crystal structure) and argyrodites (products of the Li_2S-P_2S_5-LiX phase diagram with X = Cl, Br, I), display very promising conductivities (up to 10^{-2} S.cm^{-1} at room temperature [206]) but suffer from severe chemical instability/sensitivity to air or moisture, causing the generation of toxic H_2S gas [486, 487]. Studies have also demonstrated the thermal and electrochemical instability of sulfide-based SE, leading to harmful battery degradation and safety issues [294, 405, 486, 488-490]. Oxide-based SE families, such as NASICONs ($Na_{1+x}Zr_2P_{3-x}Si_xO_{12}$), garnets ($A_3B_2X_3O_{12}$) and perovskites ($ABO_3$) display good conductivities ($10^{-3/-4}$ S.cm^{-1} at room temperature) and have the advantage over sulfides to be less air and moisture-sensitive, leading to much easier handling despite requiring higher sintering temperatures [4, 86, 205]. Therefore, oxide-based ceramics appear to be the most practical and reliable type of SE developed to date. NASICON-type SEs such as $Li_{1.5}Al_{0.5}Ge_{1.5}(PO_4)_3$ (LAGP) and $Li_{1.3}Al_{0.3}Ti_{1.7}(PO_4)_3$ (LATP) were particularly investigated for their ionic conductivities up to 1.09×10^{-3} S.cm^{-1} and 5.08 x 10^{-3} S.cm^{-1} at room temperature respectively [140, 141] and their stability against water and air [142, 143]. ASSLBs are developed with the prospect of using lithium metal as the negative electrode and high potential materials as the positive electrode to significantly increase LIBs power and energy densities.

ASSLBs can only meet these expectations because of the SEs presumed large electrochemical stability windows. However, assessing ESWs relies strongly on the type of characterization technique and experimental settings. Therefore, values for these electrochemical windows are very divergent in the literature published through the last decade. For example, as shown in **Table 3.1**, reported values for the ESWs of LAGP and LATP depend on the electrochemical technique used. Recently, several studies have come to specifically decry the frequent overestimation of solid electrolytes ESWs [49, 175, 491, 492], which are proven to be much more limited in practice [175, 287, 493, 494]. To characterize the ESW using cyclic voltammetry (CV), ceramic solid electrolytes are pressed into pellets and coated with a conductive metal (Au) before placing them between an inert blocking electrode (stainless steel, Pt or Au) and a polymer protected lithium metal electrode for cycling. In this configuration, a very limited contact area is available between the SE and the inert blocking electrode. Being in a solid-state medium, only the portion of SE in contact with the coated metal is expected to react. If the reaction forms a solid insulating phase, only the first few nanometers of the SE will react at the SE-Au coating interface as electrons cannot reach the reaction front. Resulting redox currents are therefore relatively small and hardly noticeable on CV curves. Moreover, using high sweeping rates and omitting the ohmic drop correction can also alter the CV curve [495]. Tested through this method, very wide ESWs can be reported. However, solid electrolytes including LAGP, LATP, $Li_{0.35}La_{0.55}TiO_3$ (LLTO) and $Li_{3.5}Zn_{0.25}GeO_4$ (LiSICON) were investigated through alternative techniques, such as *in situ* X-ray photoelectron spectroscopy (XPS) and energy-dispersive X-ray spectroscopy (EDS), the results revealed much higher reduction potentials than previously established by CV [282, 496-498]. Based on first-principles studies, most ESWs appear much narrower than expected experimentally [259, 392, 393, 499]. Zhu *et al.* suggest that the practical stability of SE materials is not thermodynamically intrinsic but is rather due to kinetic phase stabilizations [392]. The sluggish kinetics of the decomposition reactions happening at the extremes of the ESWs cause a high overpotential, leading to wider experimental electrochemical windows. To justify this difference, Schwietert *et al.* suggested that the favorable decomposition pathway for some SE was indirect rather than direct, via (de)lithiated states of the solid electrolyte, into the thermodynamically stable decomposition products [492].

Table 3.1 - Electrochemical stability windows for LAGP and LATP SEs reported in the literature. **These values are reported for PVDF/LATP composites but are attributed to the contribution of LATP.*

SE	E_{red} /V	E_{ox} /V	Technique used	Cell config.	Scan rate	Year	Reference
LAGP	**0**	**> 6**	CV	Au@LAGP@Au	0.5 mV.s^{-1}	2007	[129]
	0.85	**7**	CV	Ag@LAGP|Li	0.1 mV.s^{-1}	2010	[147]
	0.6	**> 6**	CV	$LiMn_2O_4$|LAGP|Li	0.1 mV.s^{-1}	2013	[500]
	1	**> 6**	CV	Au@LAGP|Li	0.5 mV.s^{-1}	2017	[148]
	1.5		CV	Au@TiO_2|LAGP|Li	1 mV.s^{-1}	2011	[149]
LATP	**2.3**	**6**	Galvanostatic	Li_2S|LATP|Li	Nd	2019	[144]
	2.45		Galvanostatic	Li|LATP|Li	Nd	2020	[501]
	2.4		CV	Liquid config.	0.5 mV.s^{-1}	2006	[502]
	2.4		Coulombic titration	Mo@LATP|Li	Nd	1999	[503]
	<2	**5.67***	LSV	Liquid config.	10 mV.s^{-1}	2018	[504]
		5.5*	LSV	$LiMn_2O_4$|LATP|Li	0.1 mV.s^{-1}	2018	[505]

In this study, we intend to establish a robust way to efficiently assess ESWs for the two NASICON-type materials $Li_{1+x}Al_xM_{2-x}(PO_4)_3$ (M = Ge, Ti). Using first principles, we computed thermodynamic ESWs for LATP and LAGP and predicted their decomposition products upon redox potentials to gain more insight on the decomposition mechanisms. Experimentally, spark plasma sintering (SPS) technology was used to sinter together active material (SE) and conductive metal (Au) into a composite electrode to maximize the contact area between them and therefore increase the decomposition currents. Using Au as the conductive metal instead of commonly used carbon black prevent any side/decomposition reaction during sintering. Additionally, carbon black has the disadvantage to absorb a significant amount of moisture despite extensive drying [506-508], resulting in electrochemical artefacts above 4 V vs. Li^+/Li. Gold is inert and stable through a large electrochemical window [509, 510] and allows an excellent electronic conductivity. Potential intermittent titration technique (PITT) was used instead of CV to ensure a constant return to equilibrium and allow locating the redox potentials with great precision. The technique is coupled with an O_2 sensing probe in order to observe the production of O_2 from the materials' decomposition. Transmission electron microscopy (TEM) and electrochemical impedance spectroscopy (EIS) measurements were carried out to gain more insight on the oxidation process of LAGP. The collected results challenge the claimed electrochemical stability windows of LAGP and LATP materials measured until now. This paper provides a more accurate determination of the ESW for solid electrolytes and should allow a more thought-through material selection of SEs for ASSLBs.

3.3 – Materials and methods

3.3.1 – Grand potential phase diagram

The GPPD is used to compute the ESWs of LAGP and LATP. The GPPD is constructed from a phase diagram by keeping the system open to Li. To construct such phase diagrams, the relevant free energy is the grand potential Φ, it is determined for each composition c at a given chemical potential μ_{Li}. The grand potential is derived from the Legendre transform of the energy [511], following equation 2.30. The GPPD is constructed from the grand potentials of all relevant compositions at 0 K and incorporates all the stable phases of the initial phase diagram. The electrochemical stability window of a SE is the range of potentials over which the SE phase is considered stable. When using the GPPD, the ESW is the range of chemical potentials μ_{Li} over which the SE composition is considered stable (energy above Hull = 0) relatively to competing compositions of the phase diagram. The conversion from chemical potential to potential vs. Li^+/Li is achieved following the equation 2.31. Decomposition products for the SEs are identified to be the most stable compositions (energy above Hull = 0) in which the SE decomposes, at the ESW limits.

All relevant compositions and their computed enthalpies are collected from The Materials Project database [512]. The GPPD is generated for LAGP and LATP phase diagrams over a [0 V- 8 V] vs. Li^+/Li potential range, using Pymatgen software package [473]. Composition energies were computed with DFT within the projector augmented wave (PAW) formalism [513], using the Pedrew-Burke-Ernzerhof (PBE) generalized gradient approximation (GGA) to the exchange-correlation energy [461], implemented in the Vienna ab initio simulation package (VASP) [514]. Calculation parameters include a cutoff energy of 520 eV and a k-point grid of $500/n_{atoms}$.

3.3.2 – Reactants syntheses

LAGP ceramic was synthesized using $LiOH{\cdot}H_2O$ (Nemaska Lithium), $Al(OH)_3$ (Alfa Aesar), GeO_2 (Strem) and $(NH_4)_2HPO_4$ (Sigma Aldrich) in stoichiometric ratios. The starting materials were ground manually for 10 minutes in a porcelain mortar and heated in a Pyrex beaker at 400 °C (2 $°C.min^{-1}$ heating rate) for 18 hours to allow complete phosphating and gradually remove all decomposition gases (e.g., NH_3, H_2O). The powder was melted at 1200 °C inside a fused silica crucible for one hour and the resulting liquid was casted into a stainless-steel mold at room temperature. The resulting colorless glass was ground into a fine powder during 20 minutes in a

zirconia high energy ball mill (SPEX 8000M Mixer Mill). To obtain the LAGP ceramic, the glass powder was annealed at 580 °C in a fused silica crucible for 48 hours, between the glass transition (T_g = 520 °C) and crystallization (T_c = 610 °C) temperatures [515], allowing complete crystallization of the glass. All the heating steps were performed in an electric furnace. LATP was synthesized by dissolving stoichiometric amounts of $NH_4H_2PO_4$ and TiO_2 (Sigma Aldrich) in deionized water [516]. The resulting solution was stirred continuously and heated under reflux at 160 °C for 16 hours. After cooling down to 80 °C, $Al(OH)_3$ was added to the solution and stirred for 30 minutes. Dissolved $LiOH \cdot H_2O$ in deionized water was added at last before drying the final mixture at 300 °C overnight. The resulting powder was milled using a zirconia high energy ball mill (SPEX 8000M Mixer Mill) for 30 minutes. Finally, the powder was loaded in a crucible and annealed at 900 °C for 6 hours (2 °C.min^{-1} heating rate).

3.3.3 – Spark plasma sintering

SPS experiments were carried out to sinter SE-Au/SE stacks using a Dr. Sinter Lab Jr. series 632Lx SPS. Au powder (Sigma Aldrich, CAS number 265772, <45 µm, 99.99% trace metals basis) and SE ceramic powder (LAGP or LATP) were mixed in an agate mortar following a 25:75 wt% ratio of SE:Au (2:1 v%). Au is introduced in large quantities to make up for its high density and allow a large surface area of contact with LAGP or LATP. 150 mg of the resulting powder were loaded into a Grafoil® coated graphite die (Ø = 8 mm) and pressed between two graphite punches. The Grafoil® is used to favor the demolding. The graphite die was placed inside the SPS chamber between two graphite spacers and uniaxially pressed at 100 MPa for 15 min to maximize particle cohesion. 75 mg of the SE powder were homogenously spread on top of the pre-compressed SE-Au pellet. The graphite die was placed inside the SPS chamber a second time and pressed at 100 MPa under vacuum. The sintering was performed up to 650 °C for LAGP-Au/LAGP and 850 °C for LATP-Au/LATP at a 50 °C.min^{-1} heating rate, where it was kept for 3 to 5 min before cooling down to room temperature at a 100 °C.min^{-1} rate. Voltage and current used in the process were applied under automatic operation mode. The resulting SE-Au/SE stacks were then placed in an electric furnace and heated to 750 °C at a 5 °C.min^{-1} rate, under air for 18 h, to gradually calcinate and remove the remaining Grafoil® off the pellets. The pellets were then manually polished using Buehler® silicon carbide papers of different grain sizes (280, 400 and 1000 grits) followed by diamond polishing paper to reach a final surface finish of 1 µm.

3.3.4 – Specific surface area

The specific surface area of the gold particles was determined by the Brunauer-Emmett-Teller (BET) theory using a Micromeritics Gemini V. Prior to measurements, 500 mg of gold were degassed for 1 h at 200 °C under N_2 gas to remove water.

3.3.5 – Powder X-ray diffraction

PXRD measurements were carried out on pellets using a Panalytical Empyrean diffractometer with copper X-ray sealed tube (CuKα, operated at 45 kV / 40 mA, automatic optics iCore and dCore, reflection transmission spinner and a hybrid pixel detector PIXcel 3D). PXRD measurements were collected at a $0.4°.min^{-1}$ rate from 10° to 80° in 2θ.

3.3.6 – Scanning electron microscopy

Analyses of the stacks were carried out on an Oxford Instrument JEOL JSM-7600TFE microscope equipped with a field emission gun (FEG). Samples were mounted in epoxy resin, polished with Buehler® silicon carbide papers of different grain sizes (280, 400 and 1000 grits) followed by diamond polishing paper to reach a final surface finish of 1 µm. The samples were then sputtered with chromium (10 nm). Views were taken with zooms ranging from x30 to x10k. SEM analyses were coupled to energy-dispersive X-ray spectroscopy (EDS) measurements using an Oxford Instruments X-Max N 80 with an 80 mm^2 silicon drift detector (SDD).

3.3.7 – Electrochemical measurements

The SE-Au/SE stacks were tested in electrochemistry using two-electrode stainless steel Swagelok cells. All the stacks and Swagelok parts were thoroughly dried at 140 °C before mounting them inside an argon-filled glovebox (4 ppm O_2 and 0.1 ppm H_2O). SE-Au/SE stacks acted as working electrode and electrolyte. A lithium metal electrode protected with a thin layer of polyethylene oxide (PEO) polymer-based electrolyte was placed against the SE part of the stack. A protective teflon ring was introduced to impede the PEO or Li metal from coming in contact with the positive electrode in case of PEO creeping. PEO electrolyte was prepared by mixing PEO (5M, Sigma Aldrich) with Lithium Bis(trifluoromethylsulfonyl)amine (Solvionics) using a [EO]:[Li] ratio of 20:1 in a closed internal mixer Brabender® (30 mL volume of the working chamber) at 170 °C ± 5 °C. The blend is then laminated between steel plates. The polymer synthesis was carried out in an argon-filled glovebox to minimize exposure to air and water [517, 518]. The electrochemical

tests were performed at 60 °C on a VMP2 series multichannel potentiostat (Bio-Logic Science Instruments). The ESWs were measured using potential intermittent titration technique (PITT), small voltage increments of 50 mV were applied to cycle the stacks from E_{oc} down to 0 V vs. Li^+/Li for reduction and up to 6 V vs. Li^+/Li for oxidation. The next 50 mV increment was applied each time the current dropped below 10 nA or after a relaxation time of 3 hours. When coupled to the O_2 sensing probe, an accelerated version of the PITT was used instead; voltage increments of 100 mV were applied after the current dropped below 10 nA or after a relaxation time of 1 hour. Electrochemical impedance spectroscopy (EIS) measurements were carried out on Au-coated LAGP pellets, at frequencies ranging from 200 kHz to 2 mHz with an amplitude of 10 mV, from E_{oc} to 5.6 V. Prior to EIS measurements, each potential step was stabilized for 3h, similarly to PITT settings. EC-Lab® software was used to analyze the data.

3.3.8 – O_2 sensing

Oxygen sensing measurements were performed using a southland sensing OMD-501D oxygen sensor. The setup combines O_2 sensing and accelerated PITT cycling on SE-Au/SE stacks for an *operando* measure of O_2. The O_2 sensor was assembled using a T-Swagelok cell under argon. The electrochemical cells were left at open-circuit potential for at least 6 hours prior to cycling in order to establish an O_2 baseline.

3.3.9 – Transmission electron microscopy

Milling of samples by FIB was performed using a Hitachi FB2000A focused ion beam (FIB) system operating at 30 keV with a 50–100 nm resolution. An intense beam of Ga ions is produced using a high-brightness liquid–metal ion source and a double lens focusing system. A gun to deposit tungsten was used to cover and protect areas selected for characterization. An *in situ* lift-out FIB technique was used to prepare TEM samples, it was used to extract a thin lamella, which was then fixed to a Cu half-disk TEM support using tungsten deposition and welding. TEM observations were carried out using an Oxford Instruments JEOL JEM 2100 F FEG-TEM microscope, operated at 200 kV. Image acquisition was done on bright field mode.

3.4 – Results and Discussion

3.4.1 – Grand potential phase diagram

Table 3.2 shows the ESWs for LAGP and LATP computed in this study and compare them to other values found in the literature. LAGP was found stable between 2.72 V and 4.29 V vs. Li^+/Li, LATP between 2.19 V and 4.67 V vs. Li^+/Li. Zhu *et al.* also computed LATP and LAGP electrochemical stability windows, they are presented in **Table 3.2**, and are in good agreement with our results. Other similar values were found in the literature for non-doped NASICON $LiGe_2(PO_4)_3$ and $LiTi_2(PO_4)_3$ which compare fairly with our results of [2.72 V - 4.30 V] for $LiGe_2(PO_4)_3$ and [2.17 V - 4.65 V] for $LiTi_2(PO_4)_3$. Computed results are coherent with one another, it proves that GPPD is a robust and appropriate method to use to compute ESWs. It was possible to derive from the GPPD the decomposition products for LATP and LAGP upon oxidation and reduction. Regarding LAGP, the decomposition products are found to be GeO_2, Ge, $Li_4P_2O_7$ and $AlPO_4$ for reduction and are in perfect agreement with the computed results of Zhu *et al* and the experimental results from Sun *et al.* [519, 520]. Similarly, O_2, $Ge_5O(PO_4)_6$ and $AlPO_4$ as the decomposition products of LAGP upon oxidation are recurrent in our study and for Zhu *et al*.

Regarding LATP, the decomposition product upon reduction are $AlPO_4$ and $Li_2Ti_2(PO_4)_3$. $AlPO_4$ is found in our work and for Zhu *et al*. Our computations also predict the production of $Li_2Ti_2(PO_4)_3$, indicating a possible insertion of lithium in LATP at low potential. Upon oxidation, the decomposition products are found to be O_2, $AlPO_4$, TiP_2O_7 and $Ti_5(PO_5)_4$. The production of O_2 and $AlPO_4$ was also predicted by Zhu *et al*. The computed values for thermodynamic ESW are expected to differ from the experimental values due to the kinetic contribution but guide us in the coming experimental part. In the same manner, the computed decomposition products for oxidation, especially $AlPO_4$ and O_2, give a valuable insight of the degradation mechanism of LAGP and LATP and guide us in characterizing the decomposition products experimentally.

Table 3.2 - Computed electrochemical stability windows for LAGP and LATP using the GPPD and their computed decomposition products.

SE	E_{red} /V	Decomposition products	E_{ox} /V	Decomposition products	Reference
LAGP	**2.72**	GeO_2, Ge, $Li_4P_2O_7$, $AlPO_4$	**4.29**	O_2, $Ge_5O(PO_4)_6$, $AlPO_4$, $LiPO_3$	This work
	2.70	GeO_2, Ge, $Li_4P_2O_7$, $AlPO_4$	**4.27**	O_2, $Ge_5O(PO_4)_6$, $AlPO_4$, $Li_4P_2O_7$	[392]
LGP	**2.72**		**4.30**		This work
	2.95	GeO_2, Ge, $LiPO_3$	**4.40**	O_2, GeO_2, GeP_2O_7	[259]
LATP	**2.19**	$AlPO_4$, $Li_2Ti_2(PO_4)_3$	**4.67**	O_2, $AlPO_4$, TiP_2O_7, $Ti_5(PO_5)_4$	This work
	2.16	$AlPO_4$, P, $LiTiPO_5$, Li_3PO_4	**4.31**	O_2, $AlPO_4$, $LiTi_2(PO_4)_3$, $Li_4P_2O_7$	[392]
LTP	**2.17**		**4.65**		This work
	2.70	$Li_2Ti_2(PO_4)_3$	**4.75**	$Ti_5P_6O_{25}$, TiP_2O_7, Ti_2O_7	[259]
	2.37		**4.59**		[521]

3.4.2 – Synthesis and sintering of SE-Au/SE stacks

Prior to any electrochemical measurement, it is essential to validate the quality of the stack preparation both from a chemical and a mechanical point of view. Unexpected reactions between SE and gold particles are likely to occur during the sintering at high temperature [318]. **Figure 3.1** displays the PXRD patterns of the pristine materials used in the present study, after sintering the solid electrolyte pellets and after sintering the composite electrodes. In **Figure 3.1A**, the PXRD pattern of the sintered LAGP pellet overlaps perfectly with the pattern of the pristine material (non-sintered) and corresponds to the NASICON-type structure crystallizing in the R-3c space group. No other peak is visible on the pattern confirming that, based on PXRD analyses, no impurity is present, and no side reaction occurred after the sintering of LAGP. The sintered stack was also analyzed, the pattern of the SE-Au side is presented in the figure. It matches exactly that of the sintered LAGP except for four peaks ascribed to Au (at 38.26°, 44.46°, 64.64° and 77.62° for Au crystallized in a cubic Fm-3m space group). This indicates that no reaction between LAGP and gold particles has occurred during sintering. No peak shift is neither detected, meaning that no elemental interdiffusion occurred at the interface between LAGP and Au. In **Figure 3.1B**, the patterns of pristine LATP powder, sintered LATP pellet and sintered LATP-Au composite are presented. As observed for LAGP, the PXRD pattern of the sintered LATP pellet coincides perfectly with the pattern of the pristine LATP powder. It presents only peaks expected from the R-3c space group. The peaks observed on the pattern of the LATP-Au composite electrode fit with that of the sintered LATP and Au structures. The presence of a smooth baseline and sharp peaks on the sintered LATP and LAGP pellets discards the possibility of forming an amorphous phase

during sintering. Based on these PXRD analyses, we confirm that SPS does not affect the structural integrity of LATP nor LAGP and that gold particles do not interact with the SEs at any point of the sintering process.

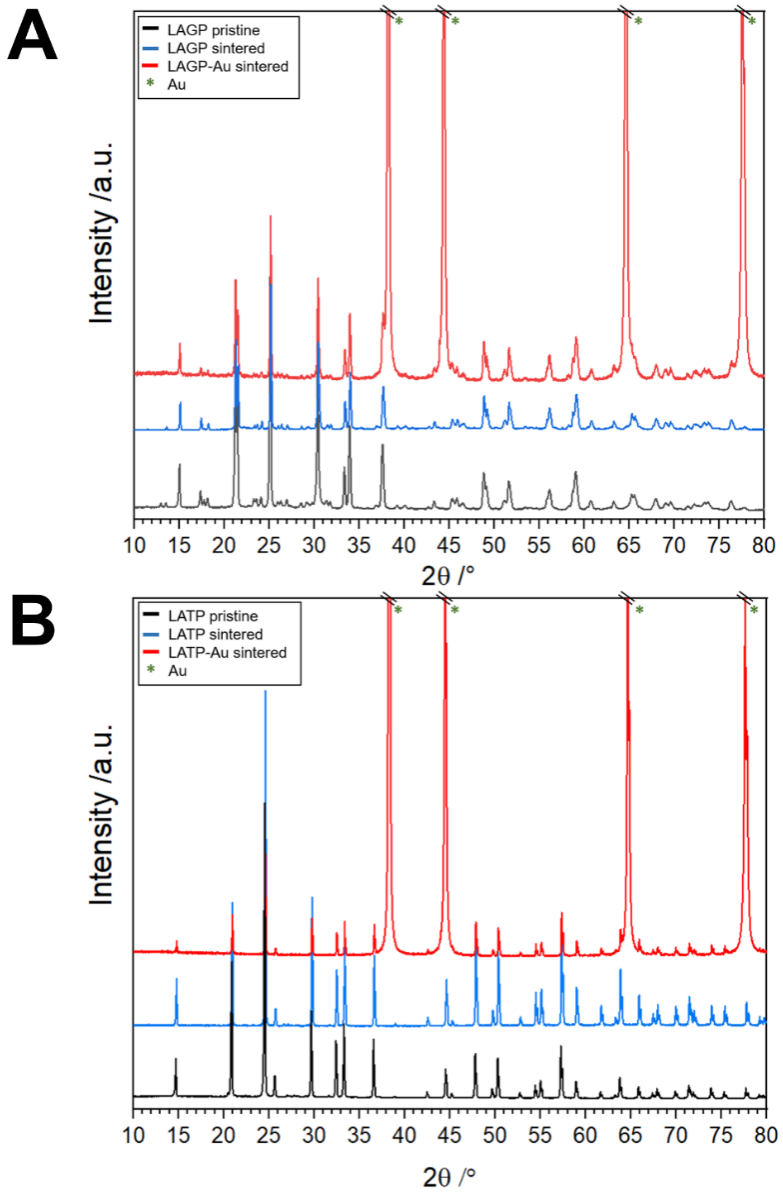

Figure 3.1 - PXRD pattern of A) LAGP and B) LATP pristine powders compared to the sintered pellets, with and without gold particles, using SPS.

The SPS technique allows the densification of ceramic pellets from 80% up to 95% compacity (computed using equation 2.1). Such high densities are required to ensure grain cohesion and minimize the cell polarization during electrochemical cycling [522]. Grain cohesion is important to provide proper electronic conductivity in the composite and proper ionic conductivity

throughout the whole system. In this regard, the electronic conductivity of our system was measured using a Keithley 2401 multimeter in 'in plane 4-points' measuring mode. It was found to be around 5 $S.cm^{-1}$ for the SE-Au composite, proving that the sintering of gold particles successfully formed an electronic network in the composite. The complete SE-Au/SE stack was insulating (infinite resistance), proving that the sintering did not affect the insulating properties of the solid electrolyte. After sintering, the resulting pellet is shown in **Figure 3.2A**. It consists of a bilayered pellet with a clear separation line, visible all around the pellet's circumference, between the electrolyte (white) and the composite (golden) parts. To observe the SE-Au/SE interface in more details, the stack was polished in its cross-section and ran through SEM. A large-scale view of the cross section is displayed in **Figure 3.2B** where both layers of the stacks are still visible and appear clean and homogeneous across several millimeters. The electrolyte side appears less bright due to its electronic insulating character. In contrast, the composite is bright all over the area owing to the electronic conduction of the gold particles. In **Figure 3.2C**, higher magnifications are used and allow us to determine the thickness of each part of the bilayer. Thicknesses of 200 µm and 400 µm were measured for SE-Au and SE sections respectively for this sample. All the sintered pellets displayed roughly the same dimensions, although the SE layer of some samples was further polished to a thickness of 150 µm before undergoing electrochemical tests. Moreover, very low internal porosity is observed on the micrographs indicating that the stack is sufficiently dense. EDS analyses were run with a highlight on Ge and Au elemental distributions over the surface of the SE-Au/SE interface. It shows a homogeneous distribution of Au in the SE-Au composite. For the sake of conciseness, only micrographs of LAGP-Au/LAGP stacks were shown, but the exact same construction is observed for LATP-Au/LATP stacks.

SPS allows the sintering of SE-Au and SE pellets into one compact stack while avoiding any side reaction between the SE and Au components. This confirms the suitability of SPS for producing optimal ceramic stacks for the determination of solid electrolytes ESWs. The specific surface area of the gold powder was measured using BET, it was estimated to be 0.4165 $m^2.g^{-1}$. The sintered SE-Au pellets contain 100 mg of gold resulting in a contact area between SE and Au largely superior to 0.5 cm^2, which is the contact surface calculated for an 8 mm diameter SE pellet covered by an Au layer. Sintered SE and Au composite electrodes offer more electrochemical surface than conventional Au-coating on SE pellets, ensuring greater decomposition currents.

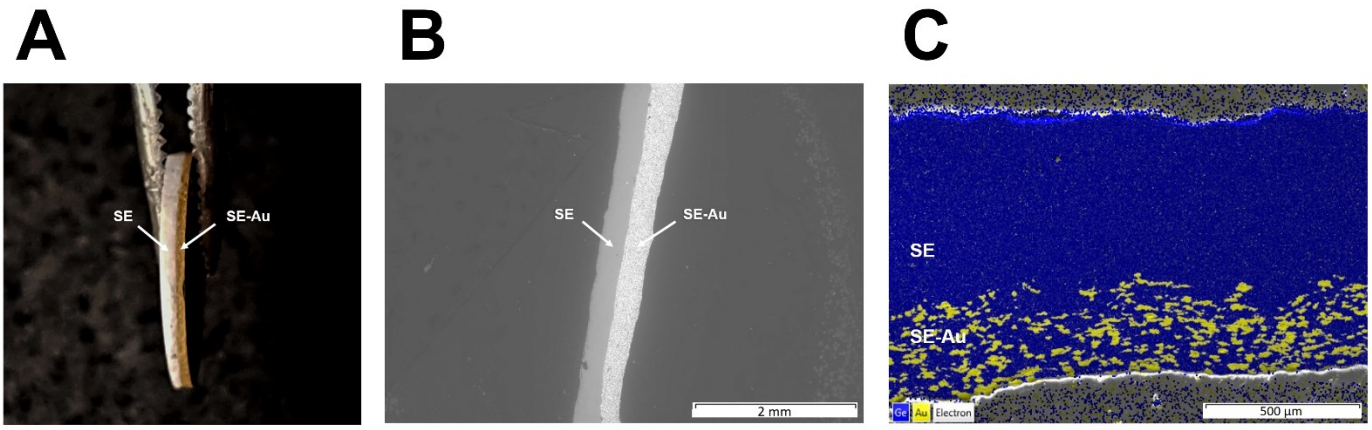

Figure 3.2 - A) Picture of a SE-Au/SE stack after completing sintering , calcination and polishing processes, B) SEM micrograph of an LAGP-Au/ LAGP stack cross section (x30), gold particles appear in light grey, C) SEM micrograph and corresponding EDS analysis map of an LAGP-Au/LAGP stack cross section (x120), Au is represented in yellow, Ge in blue.

3.4.3 – Electrochemical measurements

To determine the electrochemical stability windows, LAGP-Au/LAGP and LATP-Au/LATP Swagelok cells were assembled. Two cells of each were used for the study of the oxidation and reduction separately. The cells were cycled using PITT, a widely used method in electrochemistry that allows the system to remain close to the thermodynamic equilibrium and to neglect interfacial resistances. This method is also used, along with galvanostatic intermittent titration technique (GITT), for determining the diffusion coefficient in electrochemical materials, such as lithium diffusion in lithium-ion battery electrodes [523, 524]. In the context of this study, PITT is used to observe the current response at each potential step after the system returns to equilibrium. Using PITT allows the observation of the first redox currents generated by LAGP and LATP, which provides us with a precise ESW. The same approach was recently used by W. Zhang *et al.* to determine the electrochemical stability of single-ion conducting polymer electrolytes [525]. The experiment starts by recording the E_{oc} of the battery. A potential increment of 50 mV is applied for oxidation and reduction respectively. During oxidation and reduction, the SE-Au layer acts as a positive electrode and PEO protected lithium metal as the negative electrode. PITT curves for LAGP are given in **Figure 3.3**. The graph is presented as a current response vs. potential for the ease of reading, however the typical PITT response, i.e., I vs. t, is displayed in **Annex 1**. Observing the reduction curve, each potential step from the E_{oc} at *ca.* 3.0 to 1.85 V vs. Li^+/Li is followed by a small current jump that rapidly decreases to 0. Below 1.85 V, the current response increases drastically after every potential step. This current response is the signature of a possible

conversion reaction of LAGP into Ge + $Li_4P_2O_7$ + $AlPO_4$ + GeO_2 initiated at this potential, as suggested by our first-principles calculations. When further decreasing the potential, another reaction starts at 1.05 V vs. Li^+/Li associated with the formation of Li_xGe alloy. This is in agreement with the experimental value reported by Zhang *et al.* [148]. Upon oxidation, the current response remains small and steady from 3.0 to 4.9 V vs. Li^+/Li. Above this point, a drastic increase of the current response is observed from 4.9 to 5.3 V and another increase occurs starting at 5.7 V up to above 6 V vs. Li^+/Li.

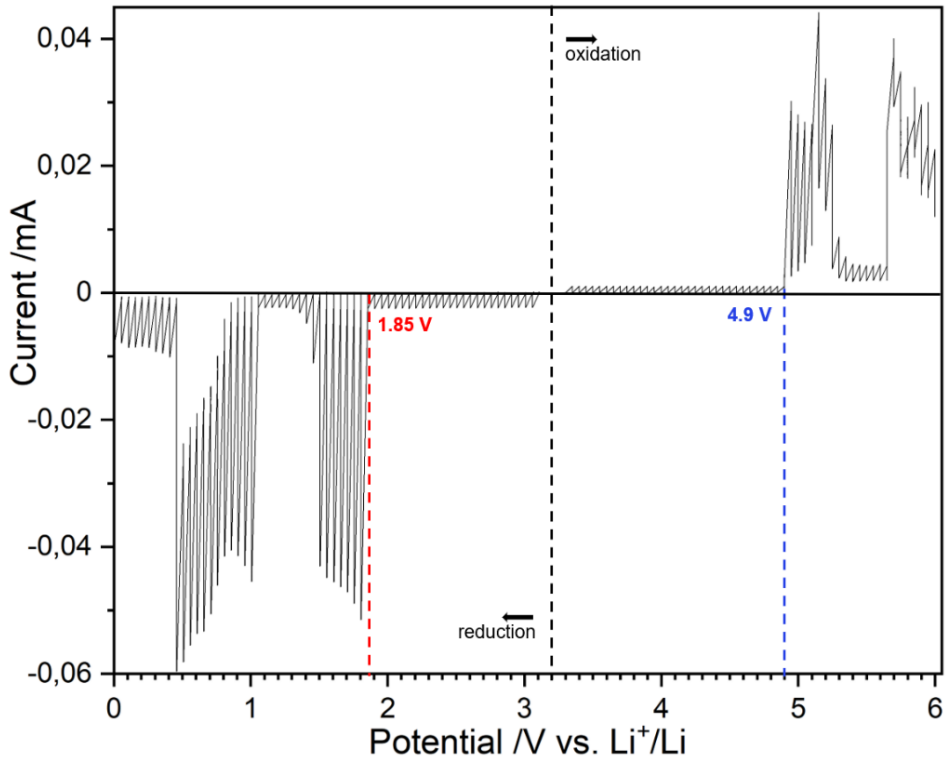

Figure 3.3 - PITT measurements on a stack LAGP-Au/LAGP represented using the current response as a function of potential. The two measures were taken on two distinct stacks at 60 °C, from E_{oc} to 6 V for oxidation and from E_{oc} to 0 V vs. Li^+/Li for reduction. A potential step of 50 mV, a current limit of 10 nA and a time limit of 3 h were used.

Similarly, the electrochemical stability window for LATP is presented in **Figure 3.4** (i.e., I vs. t, is displayed in **Annex 2**). A noticeable reduction current is observed as early as 2.65 V and becomes more significant at 2.5 V vs. Li^+/Li. The latter value corresponds to the operating potential of $LiTi_2(PO_4)_3$ active material [526]. Upon oxidation, a noticeable oxidation current appears at 4.6 V vs. Li^+/Li. It is crucial to set the oxidation and reduction potentials for solid electrolytes at the appearance of any noticeable current response, albeit small, because they mark the presence of

irreversible reactions within SEs that can lead to significant capacity loss over time. In this regard, we estimate the electrochemical stability windows to be [2.65 V – 4.6 V] vs. Li^+/Li for LATP and [1.85 V – 4.9 V] vs. Li^+/Li for LAGP. These ESWs, assessed using PITT, are much narrower than any value presented in **Table 3.1**. Regarding the oxidation potential, all the values reported resulting from CV measurements are above 5.5 V vs. Li^+/Li. Reduction potentials found in the literature are very divergent from a study to another. For LAGP, the values for the reduction potential presented are all below 1.5 V vs. Li^+/Li. It is significantly lower than the value of 1.85 V vs. Li^+/Li presented in this study. Regarding LATP, the studies found in the literature using galvanostatic cycling define the reduction potential of LATP to be the reduction potential of the Ti^{4+}/Ti^{3+} couple, around 2.5 V vs. Li^+/Li. However, the PITT curve reveals that a small LATP current response is present before that value. It is worth mentioning that PITT measurements were run at 60 °C in the present study, as opposed to RT which, by compliance to Nernst law, has a direct influence on the potential. However, temperature differences of this order are expected to only alter the ESW in a negligible way.

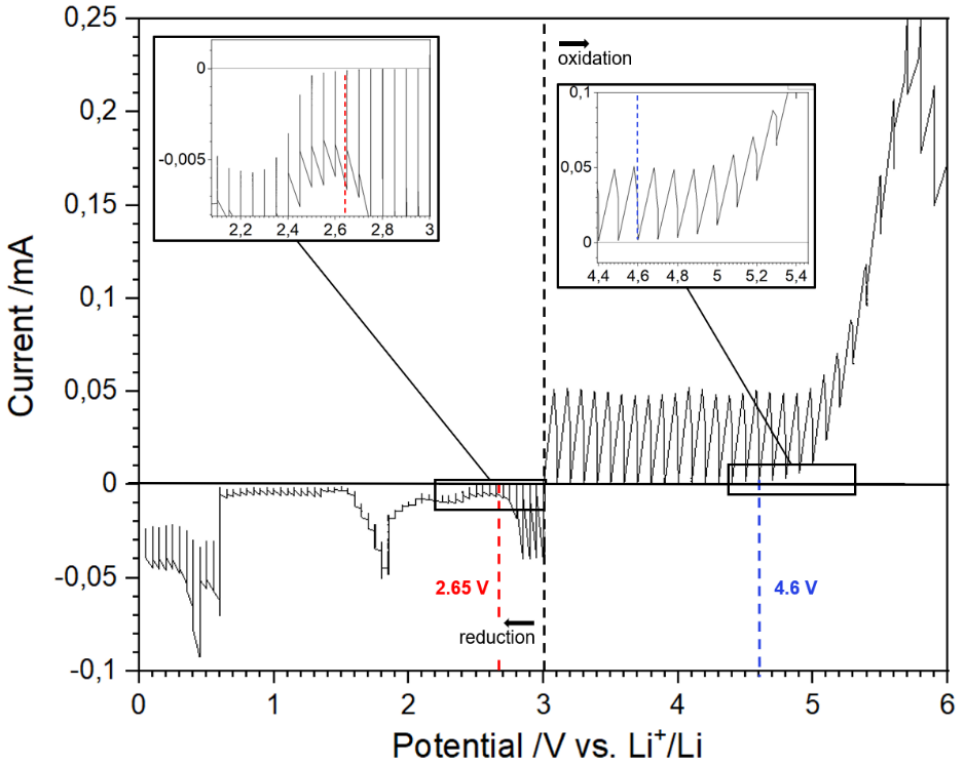

Figure 3.4 - PITT measurements on a stack LATP-Au/LATP. The two measures were taken on two distinct stacks at 60 °C, from E_{oc} to 6 V for oxidation and from E_{oc} to 0 V vs. Li^+/Li for reduction. A potential step of 50 mV, a current limit of 10 nA and a time limit of 3 h were used.

3.4.4 – O_2 sensing measurements

Decomposition products upon reduction, especially against lithium metal, were widely investigated for LAGP [519, 520] and LATP [493, 501, 527, 528]. However, experimental studies on their decomposition upon oxidation are nonexistent. First-principles calculations have been used to foresee these products but to the best of our knowledge, no experimental study has been successful yet in the determination of such decomposition products at high potential. O_2 being among the decomposition products predicted by first-principles calculations (**Table 3.2**), we used an oxygen sensing probe to investigate the possibility of O_2 production at LATP and LAGP oxidation potentials. The setup is presented in **Figure 3.5**, the electrochemical cell is coupled to the sensing probe so that the amount of O_2 produced is detected *operando*. Results of this experiment are shared in **Figure 3.6**. The objective of this experiment was to correlate the amount of charge going through the system with the amount of O_2 released, as expected from our calculations. Accelerated PITT was used to avoid diluting the O_2 signal in extended relaxation times. Done this way, it is possible to observe a sharper signal for O_2 generated as a function of time. The ESW might be slightly altered by this change of parameters, but the experiment is focused primarily on detecting a clear evolution of O_2 upon oxidation.

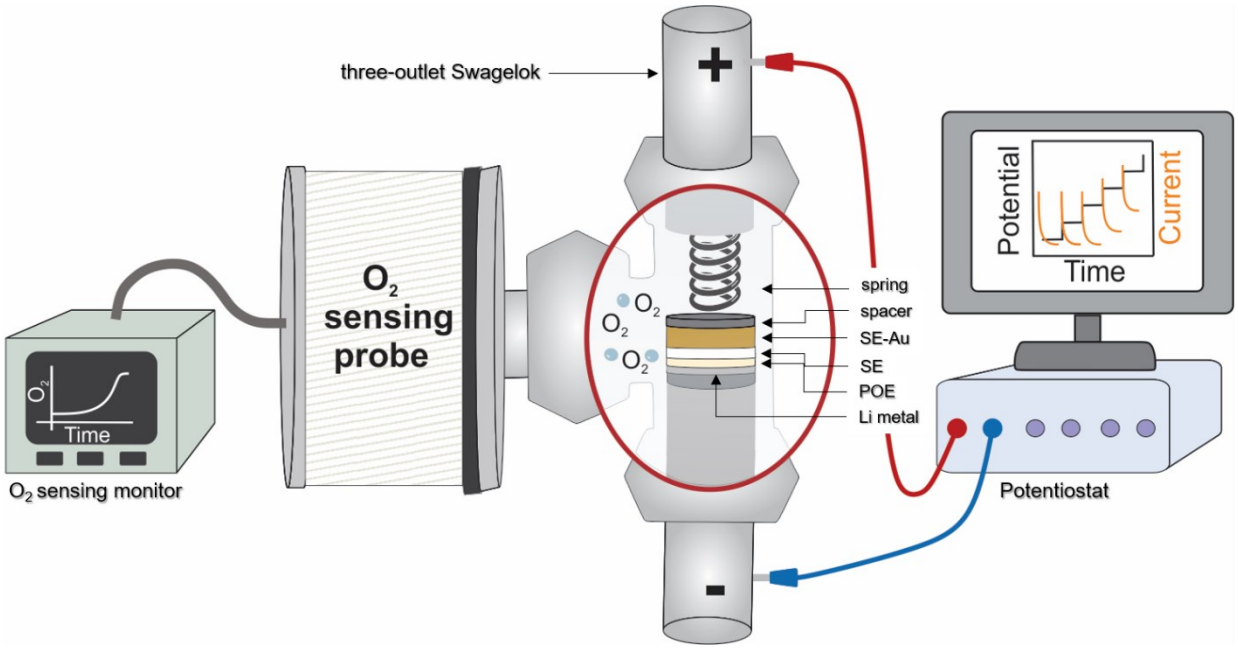

Figure 3.5 - Schematic representation of the setup combining O_2 sensing and PITT measurements.

For both LAGP and LATP, the amount of O_2 detected follows a smooth baseline during the relaxation period (left at E_{oc} for 6 hours) and during the beginning of the accelerated PITT, confirming that no O_2-producing reaction is occurring in this potential range. When the oxidation potentials are reached at 4.9 V and 4.6 V vs. Li^+/Li for LAGP (**Figure 3.6A**) and LATP (**Figure 3.6B**) respectively, we observe a slow increase of the amount of O_2 at start, followed by a rapid increase when the potential and charge increase. The curve representing the charge as a function of time is in perfect overlap with the evolution of O_2, showing the direct relation between the generated electric charges and the production of O_2. This first observation validates that O_2 is a decomposition product of LATP and LAGP, as predicted by first-principles calculations. It is worth mentioning that, although LAGP and LATP were introduced in the same quantities (≈ 40 mg), the electric charge from the degradation of LATP is 10x that of LAGP. Due to the lack of control over the initial amount of O_2 present in the cell, it was only possible to present qualitative results of O_2 production. An optimization of the setup is currently considered to traceback the quantitative amount of O_2 released from LATP and LAGP oxidations.

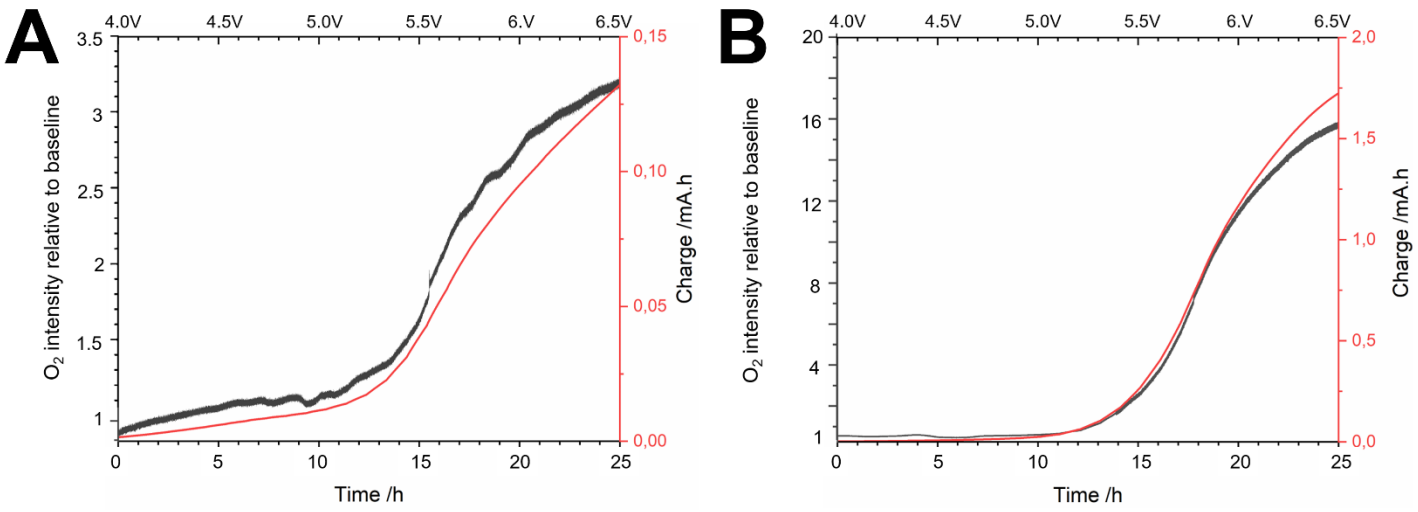

Figure 3.6 - Operando O_2 sensing measurements for A) LAGP and B) LATP coupled to accelerated PITT in oxidation. SE-Au/SE stacks of LAGP and LATP were used within three-outlet Swagelok cells. The accelerated PITT is presented as the charge Q as a function of time. A potential step of 100 mV, a current limit of 10 nA and a time limit of 1 h were used.

Using PXRD, a first attempt to characterize the decomposition products predicted by our computations failed to show the presence of crystalline phases such as $AlPO_4$, $Ge_5O(PO_4)_6$, TiP_2O_7 and $LiPO_3$ after LAGP or LATP oxidations. Our hypotheses are that the decomposition products are 1) amorphous and/or 2) present in very small amount due the solid character of our

compounds. Indeed, only the grains of SE that are directly in contact with gold particles get to react. The effective potential vehicled by the gold particles reaches this first layer of SE. However, assuming that the SE particles and their decomposition products are electronic insulators, the second layer of SE grains will not be affected by the potential applied on the gold particles. This system impedes the effective potential to reach the rest of the SE layers which are, therefore, not oxidized.

3.4.5 – Transmission electron microscopy

TEM observations were carried out to investigate the oxidation reaction of LAGP within the LAGP-Au composite before and after cycling. The micrograph presented in **Figure 3.7A** displays a sintered LAGP-Au thin lamella. The conductive gold particles (in black) are surrounded by LAGP ceramic grains (in grey). It was possible to measure the size of LAGP particles, they lie between 500 and 800 nm (**Annex 3A**). Selected area electron diffraction (SAED) measurements confirmed the crystalline nature of Au and LAGP particles. The selected patterns show interplanar spacings of 2.36 Å for Au-(111) [529] and 3.66 Å for LAGP-(113) [530] (**Annex 4A** and **B**). Very few cavities are observed between the grains (except the ones created by the ion beam), confirming the good sintering of the particles. Micrographs collected for the LAGP-Au composite after oxidation are displayed in **Figure 3.7B**. The same distribution is observed for LAGP grains with sizes ranging from 500 to 800 nm. A layer is observed at the LAGP-Au interface with a thickness ranging from 10 to 30 nm (**Annex 3B, C** and **D**), the bright white color seen on the TEM micrograph and the continuous circle observed from SAED measurements point out to an amorphous phase (**Annex 4C**). Information collected through TEM and SAED measurements indicate that the LAGP layer in contact with Au underwent a phase transformation leading to the formation of amorphous decomposition products, possibly $Ge_5O(PO_4)_6$, $AlPO_4$ and $LiPO_3$ predicted by first-principles calculations, but which is difficult to confirm experimentally at this stage.

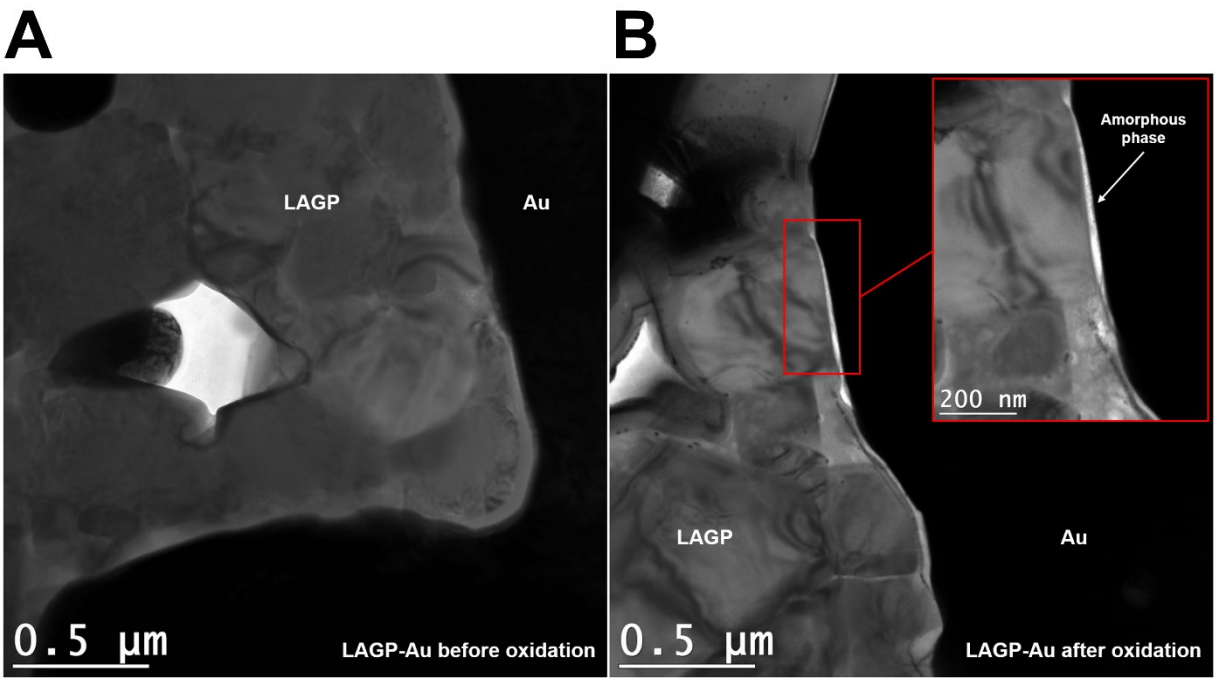

Figure 3.7 - Bright-field TEM micrographs (x10k) of two LAGP-Au composite samples A) before and B) after oxidation. The inset was observed at x25k.

EIS measurements were carried out from E_{oc} to 5.6 V and are presented in **Annex 5**. The first semi-circle observed at high frequencies (7 kHz) is attributed to the bulk SE and remains constant, independently of the applied potential. At lower frequencies, we observe a tail, which is attributed to the charge accumulation at the Au blocking electrode from E_{oc} to 4.9 V. Passed this potential, another large semi-circle (i.e., associated resistance above 4 MΩ) appears, which confirms that a sluggish charge transfer process now occurs at the SE-Au interface above 4.9 V vs. Li^+/Li. This is in agreement with the PITT measurement showing that a faradaic reaction starts above this potential.

3.5 – Conclusion

The experimental setup used in this study enabled the determination of accurate ESWs for LAGP and LATP solid electrolytes with carefully selected parameters: using inert gold particles instead of carbon black singled out the redox mechanisms of the solid electrolytes, sintering SEs with gold particles into composites enhanced the redox current responses and using PITT allowed to work close to the thermodynamic equilibrium of the system. The electrochemical stability windows were found to be [1.85 V - 4.9 V] vs. Li^+/Li for LAGP and [2.65 V - 4.6 V] vs. Li^+/Li for LATP. An oxygen sensing probe coupled to the PITT was used to observe *operando* the

decomposition of LAGP and LATP upon oxidation to produce O_2, as predicted by first-principles calculations. The presence of an amorphous phase at the SE-Au interface after cycling was observed through TEM measurements. EIS results indicate that the amorphous phase might be insulating. The values reported in the present manuscript are much narrower than commonly admitted in the community. An accurate determination of the SEs' ESWs and their decomposition processes is crucial to the successful development of ASSLBs with prolonged cycle life and high coulombic efficiency. The experimental setup coupling PITT and *operando* O_2 sensing put in place herein is accessible to all, it will be the object of further optimization to enable a precise quantification of O_2. It is believed to allow many other studies involving the release of O_2. Assessing the ESW of other solid electrolytes; ceramic, polymer and/or composites, is currently investigated and will be the subject of future publications.

3.6 – Acknowledgements

Yasmine Benabed is grateful for the financial support of the *fond national de la recherche scientifique* – FNRS of Belgium through a FRIA grant (FC31481) and the natural sciences and engineering research council of Canada - NSERC through a BESC D grant (BESCD3-534841-2019). Maxime Rioux, Steeve Rousselot and Mickaël Dollé acknowledge the financial support received from the natural sciences and engineering research council of Canada (NSERC RDCPJ 528052-18).

We thank Dr. David Lepage for his valuable insight into the experimental part, Dr. George Bokas and Dr. Sergy Posada-Pérez for their help on the computational section. We acknowledge the contribution of Dr. Jean-Philippe Masse to the analysis and interpretation of the TEM results. The present research benefited from computational resources provided by the *Université catholique de Louvain* (CISM/UCLouvain) and by the *consortium des équipements de calcul intensif en fédération Wallonie-Bruxelles* (CÉCI).

4. SOLVING THE $Li_7La_3Zr_2O_{12}$ ELECTROCHEMICAL STABILITY WINDOW PUZZLE

Yasmine Benabed[1,2], Alexis Vanacker[1], Gabrielle Foran[1], Steeve Rousselot[1], Geoffroy Hautier[2,3] and Mickaël Dollé[1]

[1] Department of Chemistry, Université de Montréal, Montréal, QC, Canada

[2] Institute of Condensed Matter and Nanosciences, Université Catholique de Louvain, Louvain-la-Neuve, Belgium

[3] Thayer School of Engineering, Dartmouth College, Hanover, NH, United States

Keywords - electrochemical stability window, potentiostatic intermittent titration technique, solid electrolyte, all-solid-state lithium batteries, $Li_7La_3Zr_2O_{12}$.

The study outlined in the following chapter is extracted from an article published in the journal *Materials Today Energy* in April 2023 (https://doi.org/10.1016/j.mtener.2023.101320). In this article, we use the methodology developed in the previous chapter to assess the electrochemical stability window of a well-documented and controversial solid electrolyte; $Li_7La_3Zr_2O_{12}$ (LLZO). The ESW was determined for three doped-LLZO materials: $Li_{6.25}Al_{0.25}La_3Zr_2O_{12}$ (Al:LLZO), $Li_{6.4}La_3Zr_{1.4}Ta_{0.6}O_{12}$ (Ta:LLZO) and $Li_{6.5}La_3Zr_{1.5}Nb_{0.5}O_{12}$ (Nb :LLZO) after processing M:LLZO (M = Al, Ta, Nb), despite its problematic chemical instability, into the cell configuration developed in the previous chapter. PITT, introduced in the previous chapter and more thoroughly in section 2.1.5.2, was also chosen as the electrochemical technique to characterize the stability window. After assessing the ESW, the study focused on the reduction reaction of Al:LLZO using electrochemical impedance spectroscopy, solid-state NMR and *operando* XRD measurements. In the context of this study, my contribution lies in conceiving the project, carrying out most of the experiments with the help of my intern Alexis Vanacker. I interpreted the results and wrote the article. The NMR measurements were carried out by Gabrielle Foran, who also reviewed the article. Steeve Rousselot participated greatly in conceiving the project, interpreting the results and reviewing the manuscript. Mickaël Dollé conceived, supervised the project and reviewed the manuscript as principal investigator.

4.1 – Abstract

The use of ceramic solid electrolytes (SEs) to produce all-solid-state lithium batteries (ASSLBs) can overcome the safety issues related to conventional liquid electrolytes and enable Li batteries to operate at high voltage, therefore producing high power density. To make this happen, one of the most crucial requirements for the SE is to possess a large electrochemical stability window (ESW). $Li_7La_3Zr_2O_{12}$ (LLZO) solid electrolyte has attracted a lot of attention given its high ionic conductivity and because it was first reported with a very wide ESW (0-9 V vs. Li^+/Li). It was not until recently that this value of the ESW was challenged, mainly proving that the oxidation of LLZO happened at a much earlier potential than 9 V. The present manuscript describes a methodology to accurately determine the ESW of doped M:LLZO (M = Al, Ta and Nb). To do so, M:LLZO is processed into a composite with gold powder to allow a large contact surface between SE and conductive gold particles, which maximizes the redox currents. To characterize the ESW, potentiostatic intermittent titration technique (PITT) was used. PITT allowed to remain close to the thermodynamic equilibrium to observe the redox currents. The ESW of M:LLZO was found to be [1.65 – 3.7] V vs. Li^+/Li for all three dopants. The reduction reaction occurring at 1.65 V was evidenced for Al:LLZO through *ex situ* ^7Li nuclear magnetic resonance (NMR) and *operando* powder X-ray diffraction (PXRD) analyses.

4.2 – Introduction

The field of solid superionic conductors is developing exponentially with the goal of improving Li battery technology and moving past the limitations of liquid electrolytes. To this end, different families of solid-state superionic conductors have been investigated and can be divided into two major groups: inorganic (ceramic, glass or glass-ceramic) solids and organic polymers. Polymers have the advantage of flexibility and adaptability to volume expansion during cycling, providing good interfacial contact with the electrodes, and stability against lithium metal [101]. Nevertheless, promising polymer-Li salt combinations such as PEO-LiTFSI have limited stability toward high potentials (up to 3.8 V vs. Li^+/Li for PEO-LiTFSI) [531] and often can only operate at rather high temperatures (> 60 °C for PEO). Additionally, their transference number ($t_+ \approx 0.2$) and rate capability are low, preventing fast charging and the utilization of high energy-density active materials [106-110]. On the other side, several ceramic solid electrolytes (SE) have been reported with promising properties such as: 1) a high thermal stability; at least > 400 °C [532-534], way above the 80-120 °C safety threshold of liquid electrolytes [535]. 2) good ionic conductivity at RT, although the ionic conductivity varies significantly depending on the type of solid electrolyte and

its microstructure. The most promising have been reported for sulfur-based materials such as LISICON-type $Li_{10}Ge(PS_6)_2$ and argyrodite-type (Li6PS5Cl among others) SEs which have bulk ionic conductivities that come close to that of liquid electrolytes, on the order of 10^{-2} S.cm^{-1} at RT [206, 536]. 3) a theoretical lithium transference number of $t_+ = 1$ [537, 538] versus $t_+ = 0.2$-0.5 for liquid electrolytes [539]. 4) an alleged wide electrochemical stability window [110, 540] allowing the use of high potential active materials as the positive electrode and lithium metal as the negative electrode, assuming that the mechanical strength of solid electrolytes might inhibit dendrite formation, which was proven not to be so straightforward [541].

A leading candidate for all-solid-state batteries is the garnet-type solid electrolyte $Li_7La_3Zr_2O_{12}$ (LLZO). LLZO reportedly possesses many of the sought after properties in SEs; a high ionic conductivity, chemical stability against metallic lithium and an alleged wide electrochemical stability window ranging from 0 to 9 V vs. Li^+/Li [128]. Two phases of LLZO were successfully synthesized; the tetragonal-type phase (t-LLZO) [160] and the higher temperature forming cubic-type phase (c-LLZO) [542]. The latter was the subject of increased interest as it has a high bulk ionic conductivity of 10^{-3} S.cm^{-1} at RT (vs. a bulk ionic conductivity of 10^{-6} S.cm^{-1} at RT for t-LLZO). The partial substitution of LLZO by dopants such as Al^{3+} has proven to stabilize the higher ion conducting c-LLZO phase. This practice resulted not only in increasing Li transport but also in increasing c-LLZO stability with respect to moisture and metallic lithium and in decreasing its sintering temperature [543, 544]. Substitutions of each of the elements of LLZO were performed to produce $Li_{7-x}\mathbf{A}_xLa_{3-y}\mathbf{B}_yZr_{2-z}\mathbf{M}_zO_{12}$ compositions with **A** = Al, Fe, Ge, Ga, **B** = Sr, Y, Ce and **M**= Nb, Ti, Ta, Sb, Mg, Sc, Zn, Ru, W, Te [130, 167, 168, 545-566]. An extensive analysis of the relationship between composition and ionic conductivity, led by Samson *et al.*, concluded that ionic conductivity in LLZO was mainly lattice-parameter dependent instead of dopant dependent. The highest Li-ion conductivities were obtained when the lattice parameters ranged from 12.91 to 12.98 Å [567]. Nevertheless, Al, Ta, Fe, Y, Te, Ga, Nb and Y doped LLZO were reported to yield promising bulk ionic conductivities, ranging from 10^{-4} to 10^{-3} S.cm^{-1}. Specifically, Ta, Al, Nb and Ga doped LLZO attracted a lot of attention because they simultaneously obtained the best results in terms of bulk ionic conductivity, cubic phase stabilization, sintering temperature and stability against metallic lithium [170, 543, 567].

However, the stability of doped and undoped LLZO against metallic lithium, which was at first undisputed [166, 332, 542, 568-570], is being increasingly questioned as no definitive answer has been formulated yet on whether LLZO forms a passivating layer when it is in contact with metallic lithium. The formation of a thin t-LLZO layer at the Li/c-LLZO interface was observed

through *in situ* transmission scanning electronic microscopy (STEM) measurements but was considered benign [571] while X-ray photoelectron spectroscopy (XPS) analyses showed the reduction of Zr^{4+} for all doped LLZO samples following the formation of an oxygen-deficient interphase (ODI) layer [173, 175, 501]. Other studies have shed light on the dependance of Li/LLZO stability on the resulting reaction kinetics [501]. Recent work published by Kim *et al.* exhibited evident reactivity between metallic lithium and doped M:LLZO (M = Al, Ta, Nb, Ga/W) through visual observations, powder X-ray diffraction (PXRD) and electrochemical impedance spectroscopy (EIS) [170]. Likewise, the electrochemical stability window (ESW) of LLZO was first reported to range from 0 to 9 V vs. Li^+/Li [128]. Despite this very large ESW and high ionic conductivity, the electrochemical performances of ASSLBs assembled with LLZO are not close to competing with those of liquid-electrolyte-based batteries, suggesting that some limitations of LLZO were overlooked. Traditionally, the ESW is determined using cyclic voltammetry (CV) at high sweeping rates (>10 $mV.s^{-1}$), where the solid electrolyte is pressed into a pellet, coated with a thin layer of conductive gold and placed between an inert stainless steel (SS) blocking electrode and a polymer protected lithium metal electrode for electrochemical testing, forming a planar Li/LLZO/Au cell configuration. However, an increasing number of studies have come to challenge the use of CV to assess ESWs [175, 572-574], attributing the overestimated values to 1) the limited contact surface between the SE and the blocking electrode, leading to an undetectable redox current [575], 2) the high sweeping rate used for CV, not allowing enough time for the sluggish redox reactions to take place and/or 3) the presence of a high overpotential attributed to the reactions' slow kinetics, artificially widening the ESW [49, 175, 219, 287, 394, 491, 493, 494, 576, 577]. First-principles calculations also predict narrower ESWs than experimentally determined for most solid electrolytes, although part of the observed difference is justified by the fact that first-principles computations only account for the thermodynamic stability and cannot include the contribution of reaction kinetics [259, 392, 393, 499]. Other studies used XPS and energy-dispersive X-ray spectroscopy (EDS) techniques on various solid electrolytes to reveal narrower ESWs than previously established by CV [282, 496-498].

Table 4.1 gathers the electrochemical stability windows of doped LLZO reported in the literature ($ESW = V_{ox} - V_{red}$). An evident relationship is observed between high oxidation potentials (> 5 V vs. Li^+/Li) and the use of CV with planar Li/LLZO/Au cell configurations. Meanwhile, DFT computations (references [259], [392] and [586] in **Table 4.1**) and techniques using composite electrodes and/or electrochemical techniques alternative to CV all led to lower oxidation potentials. Specifically, the experiment ran by Jalem *et al.* in 2016 sheds light on the impact of using a composite (Li/LLZO/LLZO+C) versus coated solid electrolyte (Li/LLZO/Al) in the determination of

the ESW [574]. The stability window of Ta:LLZO was investigated using CV in both configurations: in the Li/LLZO/Al planar configuration, no oxidation potential was observed up to 5 V vs. Li^+/Li. Concurrently, the same experiment was run with a Li/LLZO/LLZO+C composite cell configuration and an oxidation potential of LLZO was observed at 3.7 V vs. Li^+/Li. These results are in agreement with a study that was performed by Han *et al*. in the same year, who used a similar cell configuration to determine that the oxidation potential of Ta:LLZO was around 4 V vs. Li^+/Li [175].

The many contrasting conclusions surrounding the electrochemical stability window of LLZO and its stability against metallic lithium provide resounding proof that LLZO redox chemistry has yet to be fully understood. In this context, our work focuses on the use of a robust methodology to efficiently assess the ESW of LLZO. This methodology, first developed for NASICON solid electrolytes in a previous study [394], was adapted to overcome the limitations related to LLZO's unstable nature and allow a precise assessment of its ESW. In order to bring an extra dimension to the study, our investigation was extended to three promising doped c-LLZO; aluminum (Al:LLZO), tantalum (Ta:LLZO) and niobium (Nb:LLZO), allowing to investigate the effect of the dopant's nature on LLZO's electrochemistry. The methodology includes the annealing of the SE as active material and micrometric gold powder as conductive metal into a composite electrode to maximize the contact area between them and therefore increase the redox currents. Gold is used as an alternative to carbon black to prevent side reactions and the reduction of LLZO during annealing. Moreover, gold is an excellent electronic conductor, inert to most elements, stable through a large electrochemical window and can be efficiently dried [509, 510] - unlike carbon black, known to retain moisture despite extensive drying, resulting in electrochemical artifacts above 4 V vs. Li^+/Li and possible side reactions with LLZO [506-508]. The potentiostatic intermittent titration technique (PITT), used as an alternative to CV for electrochemical characterization, ensures that the system returns to equilibrium after each potential perturbation and provides enough time for sluggish reactions to take place [524, 578]. *Operando* PXRD analyses were carried out to better understand the nature and the effect of Al:LLZO reduction reaction, complemented by *ex situ* ^{7}Li nuclear magnetic resonance (NMR). Our findings challenge the misconception that LLZO has an incontestably wide electrochemical stability window and reopen the dialogue on the relevance of present standard methodologies used to assess ESWs, especially given how important they are as a performance metric for solid electrolytes.

Table 4.1 – Electrochemical stability windows for M:LLZO (M = Al, Nb, Ta, Ga, Mg) reported in the literature. Redox potentials V_{red} and V_{ox} are given in V vs. Li^+/Li. ** cyclic voltametry (CV), stepwise voltage increase (SVI), linear sweep voltametry (LSV), grand potential phase diagram (GPPD), density functional theory (DFT), stoichiometry stability window (SSW), phase stability window (PSW), **Li/LE/LLZO+C is a liquid cell configuration with liquid electrolyte (LE) $LiPF_6$ 1M in EC/EMC solvents, LLZO is processed in a slurry with carbon black (C) and PVDF binder.*

Formula	Dopant	V_{red}	V_{ox}	Technique used*	Cell configuration	Year	Ref.
Al_2O_3-$Li_7La_3Zr_2O_{12}$	Al_2O_3	<-0.5V	>5V	CV (0.16 $mV.s^{-1}$, 25°C)	Li/Al_2O_3+LLZO/Au	2011	[166]
$Li_{6.75}La_3Zr_{1.75}Nb_{0.25}O_{12}$	Nb	<0V	>9V	CV (1$mV.s^{-1}$, 25°C)	Li/LLZO/Au	2011	[130]
$Li_{6.5}La_3Zr_{1.5}Ta_{0.5}O_{12}$	Ta	<0V	>5V	CV (1$mV.s^{-1}$, 25°C)	Li/LLZO/Au	2012	[167]
$Li_{7.1}La_3Zr_{1.9}Cr_{0.1}O_{12}$	Cr	<-0.5V	>6V	CV (0.5$mV.s^{-1}$, 25°C)	Li/LLZO/Pt	2014	[555]
$Li_{6.4}Al_{0.2}La_3Zr_2O_{12}$	Al	<0V	>8V	CV (1 $mV.s^{-1}$, 25°C)	Li/LLZO/Au	2015	[579]
$Li_{6.75}La_3Zr_{1.75}Ta_{0.25}O_{12}$	Ta	<0V	4V	CV (0.01$mV.s^{-1}$, 25°C)	Li/LLZO/LLZO+C	2016	[175]
$Li_{6.625}La_3Zr_{1.625}Ta_{0.375}O_{12}$	Ta	-	>5V	CV (0.05 $mV.s^{-1}$, 100°C)	Li/LLZO/Al	2016	[574]
		-	3.7V		Li/LLZO/LLZO+C		
$Li_7La_3Zr_2O_{12}$	-	0-1V	>5V	CV (0.1$mV.s^{-1}$, 25°C)	Li/LLZO/Pt	2017	[263]
$Li_7La_3Zr_{1.7}Ti_{0.3}O_{12}$	Ti	<-0.5V	>4.5V	CV (0.1$mV.s^{-1}$, 25°C)	Li/LLZO/Au	2017	[553]
$Li_{7-x}La_3Zr_{2-x}Ta_xO_{12}$	Ta	<0V	>8V	CV (50$mV.s^{-1}$)	Li/LLZO/Au	2017	[580]
$Li_{6.5}Al_{0.5}La_3Zr_2O_{12}$	Al	<0V	>8V				
$Li_{6.6}Ge_{0.1}La_3Zr_2O_{12}$	Ge	<-0.5V	>5V	CV (1$mV.s^{-1}$, 25°C)	Li/LLZO/Au	2019	[581]
$Li_6La_3ZrTaO_{12}$	Ta	-	4.1V	SVI (0.2V, 1.4 h, 350°C)	LLZO/Au	2021	[582]
$Li_{5.8}Ga_{0.4}La_3Zr_2O_{12}$	Ga	-	4.3V				
$Li_{6.25}Al_{0.2}La_3Zr_{1.85}Nb_{0.15}O_{12}$	Al/Nb	-	6.1V	LSV (1$mV.s^{-1}$, 60 °C)	Li/LLZO/SS	2021	[583]
$Li_{6.6}La_3Zr_{1.6}Nb_{0.4}O_{12}$	Nb	<-1V	>6V	CV (1$mV.s^{-1}$, 25°C)	Li/LLZO/Au	2022	[584]
$Li_{6.6}La_{2.8}Mg_{0.2}Zr_{1.4}Nb_{0.6}O_{12}$	Mg/Nb	<-1V	>6V				
$Li_{6.6}La_{2.6}Mg_{0.4}Zr_{1.2}Nb_{0.8}O_{12}$	Mg/Nb	<-1V	>6V				
$Li_7La_3Zr_2O_{12}$	-	<0V	4V	CV (0.027$mV.s^{-1}$, 25°C)	Li/LE/LLZO+C**	2022	[585]
$Li_7La_3Zr_2O_{12}$	-	0.05V	2.91V	GPPD (DFT)	-	2015	[392]
$Li_7La_3Zr_2O_{12}$	-	0.07V	3.2V	GPPD (DFT)	-	2016	[259]
$Li_7La_3Zr_2O_{12}$	-	-0.83V	3.52V	SSW (DFT)	-	2020	[586]
$Li_7La_3Zr_2O_{12}$	-	0.02V	2.16V	PSW (DFT)	-	2020	[586]

4.3 – Experimental section

4.3.1 – Stack preparation

$Li_{6.25}Al_{0.25}La_3Zr_2O_{12}$ (Al:LLZO, d = 5.2 g.cm^{-3}), $Li_{6.4}La_3Zr_{1.4}Ta_{0.6}O_{12}$ (Ta:LLZO, d = 5.5 g.cm^{-3}) and $Li_{6.5}La_3Zr_{1.5}Nb_{0.5}O_{12}$ (Nb :LLZO, d = 5.2 g.cm^{-3}) nanopowders (D50 = ~500 nm) were purchased from MSE Supplies®. Gold micropowder (> 10 µm) was purchased from Fisher Scientific® (99.96% metal basis). All powders were stored and handled in an argon-filled glovebox. To prepare M:LLZO-Au composites, 40 mg of M:LLZO were mixed with 140 mg of gold powder in an agate mortar, placed into a 10 mm diameter stainless steel die and pre-compacted inside an argon-filled glovebox. 70 mg of M:LLZO were then added on top of the composite layer to form a stack within the die. The die was placed in a hydraulic press and compacted at a constant pressure of 625 MPa for 30 min. The resulting M:LLZO-Au/M:LLZO stack was placed in a platinum crucible on a powder bed and annealed under a dry air flow at 650 °C for 10 h (5 °C.min^{-1} heating and cooling rates). After annealing, the pellets were kept at a temperature above 200 °C to avoid reacting with moisture and CO_2 during their transfer back to an argon-filled glovebox.

M:LLZO single layers were also prepared by pressing 100 mg of M:LLZO powder in a 10 mm diameter stainless steel die and pre-compacted inside an argon-filled glovebox. The die was placed in a hydraulic press and compacted at a constant pressure of 625 MPa for 30 min. The resulting M:LLZO pellets were placed in a platinum crucible in a powder bed and sintered under dry air at 1210 °C for 75 min (5 °C.min^{-1} heating and cooling rates). After sintering, the pellets were kept at a temperature above 200 °C to avoid reacting with moisture and CO_2 during their transfer back to an argon-filled glovebox.

4.3.2 – Electrochemical measurements

Electrochemical measurements were performed on the M:LLZO-Au/M:LLZO stacks using stainless steel Swagelok cells, inside an argon-filled glovebox. The M:LLZO-Au composite part of the stacks acted as the positive electrode and the M:LLZO layer as the electrolyte. Three types of electrochemical cells were mounted: 1) two-electrode cells with unprotected metallic lithium as the negative electrode, 2) two-electrode cells where the metallic lithium is protected with a thin layer of polyethylene oxide (PEO) polymer-based electrolyte and 3) three-electrode cells that include metallic lithium as the reference, protected between two pieces of PEO. A protective Teflon ring was introduced to impede the PEO or Li metal from coming in contact with the positive electrode in case of PEO creeping. PEO electrolyte was prepared by mixing PEO (5M, Sigma Aldrich) with

lithium bis(trifluoromethylsulfonyl) amine (Solvionics) using a [EO]:[Li] ratio of 20:1 in a closed internal mixer Brabender® (30 mL volume of the working chamber) at 170 ± 5 °C. The blend is then laminated between two steel plates. The electrochemical tests were performed at 80 °C on a VMP2 series multichannel potentiostat (Bio-Logic Science Instruments). M:LLZO single layer pellets were also cycled in a planar configuration by coating them with a thin layer of Au and placing them between a metallic lithium foil and a stainless steel blocking electrode inside a Swagelok cell.

For comparison, M:LLZO (M = Al, Ta, Nb) materials were also cycled in a liquid configuration: M:LLZO electrodes were prepared by mixing M:LLZO powder, carbon black C65, and polyvinylidene fluoride (PVDF), at an 81:11:8 w/ ratio, in N-methyl-2-pyrrolidone (NMP) solvent to obtain a slurry. The resulting slurry was deposited on a sheet of current collector using the doctor blade technique. Carbon-coated aluminum foil was used as the current collector for oxidation and copper foil was used for reduction. The electrodes were dried overnight at 80 °C in a vacuum oven. Electrodes were cut, pressed with a 2.5 ± 0.5 $mg.cm^{-2}$ loading and assembled in coin cells (2032) inside an argon-filled glovebox. A lithium metal foil was used as the negative electrode, 1 M LiPF6 in a mix of ethylene carbonate (EC) and diethyl carbonate (DEC) (1:2 v/ ratio) solvents was used as the electrolyte, and a Celgard 2400 was used as the separator.

The ESWs were measured using PITT; small voltage increments of 50 mV were applied to cycle the stacks from open-circuit potential (OCP) down to 0 V vs. Li^+/Li for reduction and up to 6 V vs. Li^+/Li for oxidation. The next 50 mV increment was applied after a relaxation time of 3 h. When coupled to the operando XRD analysis, an accelerated version of the PITT was used instead; voltage increments of 100 mV were applied after relaxation times of 3 h. EC-Lab® software was used to analyze the data. For *operando* X-ray diffraction, the pellets were mounted, M:LLZO-Au composite layer face up, in perforated stainless steel 2032 coin cells (4 mm diameter centered holes). The electrochemical tests were performed at 80 °C on a VMP2 series multichannel potentiostat (Bio-Logic Science Instruments).

4.3.3 – Powder X-Ray diffraction

PXRD measurements were performed using a Panalytical Empyrean diffractometer with a monochromatic copper X-ray sealed tube (CuKα λ = 1.5418 Å source, operated at 45 kV/40 mA, automatic optics iCore and dCore, reflection transmission spinner and a hybrid pixel detector PIXcel 3D). The samples, powders and ground stack pellets, were prepared inside an argon-filled glovebox and placed in an Anton Paar® airtight polycarbonate (PC) domed sample holder for

analysis. The data were collected in a Theta-2Theta configuration and continuous reflection scan mode, using HighScore® - Data Analyzer software, at a 0.6 °.min^{-1} rate from 10 to 80 ° in 2θ.

Operando PXRD coupled to PITT - measurements were carried out using a Panalytical Empyrean diffractometer with a monochromatic cobalt X-ray sealed tube (CoKα λ = 1.7903 Å source, operated at 45 kV/40 mA, with a fixed anti-scatter slit on GaliPIX^{3D} detector). The perforated coin cells were mounted inside an argon-filled glovebox and placed in an Anton Paar® airtight low-temperature chamber TTK600 covered with Kapton© tape. They were analyzed at a constant temperature of 80 °C under a constant argon flow. The data were collected in a Theta-2Theta configuration and continuous reflection scan mode, using HighScore® - Data Analyzer software, at a 1°.min^{-1} rate from 10 to 70 ° in 2θ.

4.3.4 – Scanning electronic microscopy

SEM analyses of the M:LLZO-Au/M:LLZO stacks were carried out on an Oxford Instrument JEOL JSM-7600TFE microscope equipped with a field emission gun (FEG). Samples were mounted in epoxy resin, polished with Buehler® silicon carbide papers of different grain sizes (180, 280, 600, and 1000 grits) followed by diamond polishing paper with 3 µm and 0.5 µm grain sizes to reach a final surface finish. The samples were then sputtered with carbon (15 nm). Images were taken at magnifications ranging from ×150 to ×1000 using a voltage of 15 kV. SEM analyses were coupled to energy-dispersive X-ray spectroscopy (EDS) measurements using an Oxford Instruments X-Max N 80 with an 80 mm^2 silicon drift detector (SDD).

4.3.5 – Nuclear magnetic resonance

Ex situ solid-state magic angle spinning (MAS) ^{7}Li NMR analyses were performed on reduced M:LLZO. Finely crushed M:LLZO pellets were packed into 4 mm rotors inside of a glovebox. The quantity of LLZO available was less than the total volume of the rotor. Excess rotor volume was occupied by a combination of polyether ether-ketone spacers and compressed parafilm. NMR experiments were performed on a Bruker Avance 14.1 T wide-bore spectrometer. Samples were spun at 10 kHz using a two-channel 4 mm wide-bore MAS probe. Sample temperature was calibrated to 30 °C with spinning. Single pulse ^{7}Li spectra were acquired using a 5.50 µs π/2 pulse at a power level of 4.10 dB (98.7 W). 64 scans were acquired for all samples and a recycle delay of 5 s was used.

4.4 – Results and discussion

4.4.1 – Stack preparation

In order to prepare M:LLZO-Au composite electrodes, it was necessary to first evaluate the thermal stability between M:LLZO (M = Al, Ta, Nb) solid electrolytes and Au. Ideally, M:LLZO and Au should be stable up to the M:LLZO sintering temperature (1050-1250 °C [543, 587]) to achieve high-density, low-interfacial-resistance composites. To assess M:LLZO-Au stability, PXRD measurements were performed on pellets of M:LLZO and Au powders (compacted at a pressure of 625 MPa for 30 min), summarized in **Table 4.2**. For all three dopants, M:LLZO reacted with Au at temperatures as low as 700 °C if annealed for 10 h (**Annex 6)**. On the other hand, M:LLZO-Au samples were stable at temperatures above 700 °C for shorter periods of time (3 to 5 h), but these time periods were insufficient to produce a percolated electronic network of gold in the composites, resulting in an electronically insulating material (R>20 MΩ). The only chemically stable and electronically conductive sample was obtained after annealing the M:LLZO-Au composite at 650 °C for 10 h under dry air (**Figure 4.1**). The PXRD patterns showed pure phases of cubic M:LLZO and cubic Au. The pellets also displayed negligible electronic resistance with R<0.5 Ω. These conditions were selected to anneal M:LLZO and Au together to prepare M:LLZO-Au/M:LLZO stacks for the rest of this study. It is worth mentioning that a temperature of 650 °C does not allow for the full sintering of M:LLZO. For this reason, the use of ‘’annealing’’ instead of ‘’sintering’’ is deemed more appropriate to describe the heat treatment undergone by LLZO. Nevertheless, the annealing of LLZO at 650 °C yields an acceptable compacity of ≈ 60%, with sufficiently percolated grains to run the electrochemical tests, although it is expected to cause high grain boundary resistances within the stacks.

Table 4.2 – Characteristics of M:LLZO + Au pellets as a function of annealing temperatures and times. Chemical stability is assessed using PXRD analyses and electronic conductivity using direct current measurements. *The same results were observed for Al, Ta and Nb doped LLZO.

M:LLZO* + Au	**800°C/10h**	**800°C/5h**	**700°C/10h**	**700°C/5h**	**650°C/10h**
Chemical stability	unstable	stable	unstable	stable	stable
Electronic conductivity	conductive (R=0.07Ω)	insulating (R=20MΩ)	conductive (R=0.1Ω)	insulating (R=∞)	conductive (R=0.5Ω)

After annealing, Al:LLZO, Ta:LLZO and Nb:LLZO stacks were observed through SEM and analyzed by EDS. **Figure 4.2** shows the optical and SEM micrographs taken for M:LLZO stacks. **Figure 4.2A** is an optical microscope photograph showing the cross section of an annealed M:LLZO-Au/M:LLZO pellet. Both composite (M:LLZO-Au) and solid electrolyte (M:LLZO) layers have uniform and homogeneous thicknesses of 175 µm and 250 µm respectively, throughout the entire cross-section (a longer cross section is provided in **Annex 7A**). From these preliminary optical inspections, no microscopic-scale diffusion of Au particles is observed in the solid electrolyte layer after annealing. **Figure 4.2B**, **C** and **D** show the SEM micrographs and EDS mapping of M:LLZO-Au/M:LLZO (M = Al, Ta and Nb) cross-sectioned stacks. For all three dopants, the EDS mappings show a homogeneous distribution of Au in the composite layer and a clean separation between the composite and solid electrolyte layers. No diffusion of Au is observed in the solid electrolyte layer.

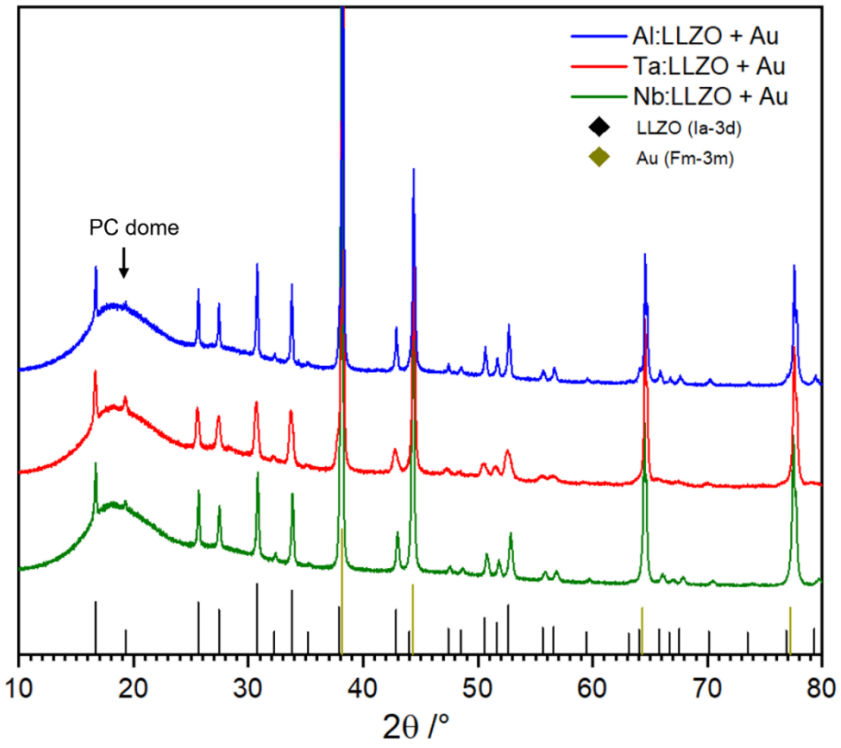

Figure 4.1 – PXRD diffractograms for M:LLZO (M = Al, Ta, Nb) + Au pellets after annealing at 650°C for 10h under dry air. The samples were prepared inside an argon-filled glovebox and analyzed under an airtight domed sample-holder (PC-based).

The EDS spectrum of an Al:LLZO-Au/Al:LLZO stack and its corresponding elemental distribution are presented in **Annex 7B**. The EDS spectrum reveals the presence of Al, La and Zr as well as impurities of Si and Na. They are attributed to the polishing and cleaning reagents used

to condition the samples for SEM analyses. The elemental distribution of Al, La and Zr corresponds to stoichiometries of 0.2, 3 and 1.9 respectively, and confirm the initial stoichiometry of Al:LLZO (Al:0.25, La:3 and Zr:2). For the sake of conciseness, the EDS spectra of Ta and Nb doped LLZO samples are not displayed but identical results were obtained for both dopants, with corresponding stoichiometries.

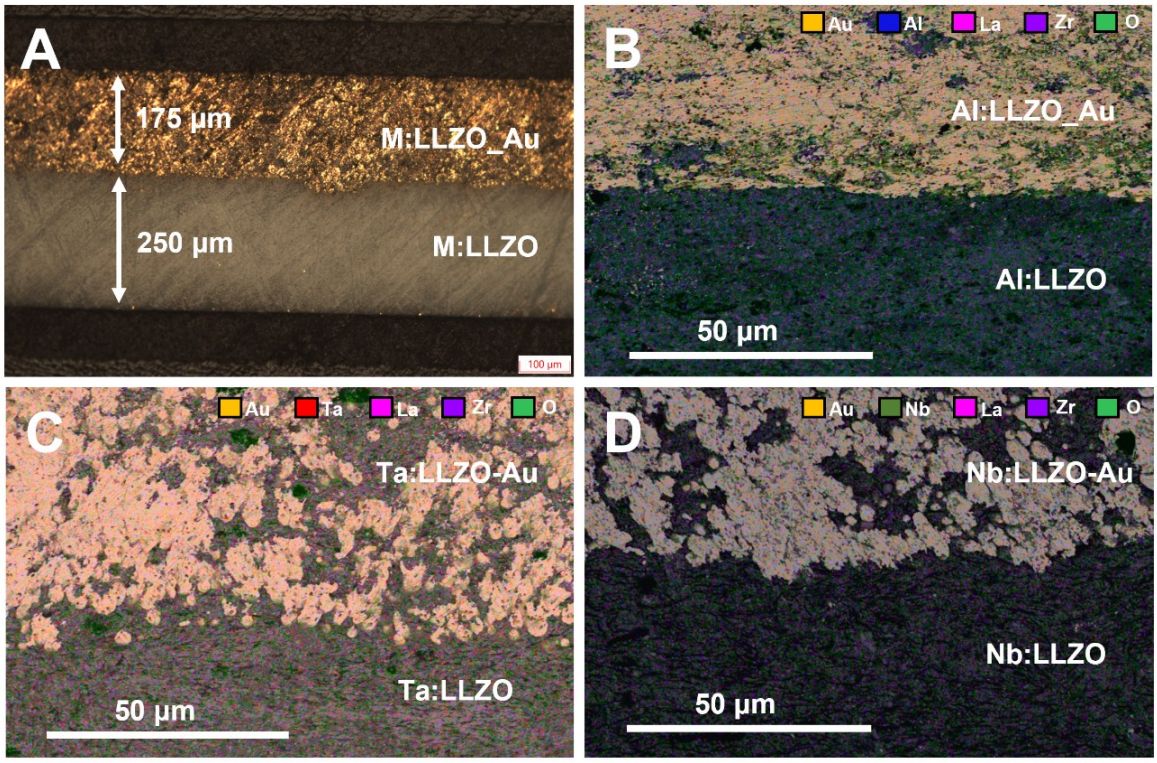

Figure 4.2 – A) Optical microscope photographs of an M:LLZO-Au/M:LLZO cross sectioned pellet at a x10 magnification. SEM micrographs (x1000) and corresponding EDS elemental mapping of M:LLZO-Au/M:LLZO cross sectioned pellets for M = Al (B), Ta (C) and Nb (D).

4.4.2 – M:LLZO electrochemical stability window

The M:LLZO-Au/M:LLZO stacks were prepared to allow optimal surface contact between M:LLZO and Au conductive metal in the composite and to increase the current signals arising from M:LLZO redox. To assess the ESW of M:LLZO, all three doped LLZO stacks were placed inside Swagelok cells, in the following configuration: the M:LLZO+Au composite acts as the positive electrode. The following layer of M:LLZO is the solid electrolyte and metallic lithium is the negative and reference electrode. Given the recent findings on doped LLZO's chemical instability against

metallic lithium [170], we decided to test M:LLZO stacks against pristine and PEO-protected metallic lithium in two-electrode setups.

The cells were cycled using PITT, which allows the system to remain close to the thermodynamic equilibrium and to neglect the interfacial resistances expected from non-sintered LLZO [525, 394]. The electrochemical tests were also carried out at 80 °C to minimize the grain boundary resistance of the non-sintered stacks. Oxidation and reduction of the M:LLZO-Au/M:LLZO stacks were tested separately by applying a potential increment of 50 mV for a duration of 3 h from OCP up to 6 V vs Li^+/Li for oxidation or down to 0 V vs Li^+/Li for reduction. After each potential step, a current response is produced and decreases exponentially as the system returns to equilibrium. The deviation from this exponential decay, coupled to the increase of the current signal's intensity, is representative of a redox reaction.

Figure 4.3 displays the PITT curves for Al, Ta and Nb-doped LLZO oxidation and reduction. Two cells of each were cycled separately to study on one hand the oxidation (up to 6 V) and on the other hand the reduction (down to 0 V) reactions, starting at 2.5. Observing the reduction curves in **Figure 4.3A**, each potential step from 2.5 V to 1.65 V vs. Li^+/Li is followed by a small current jump that exponentially decreases to 0 for all three dopants, indicating no reaction of M:LLZO. Below 1.65 V, the current response increases drastically after every potential step and does not decrease back to 0 A. The current intensity peaks at 1.45 - 1.35 V vs. Li^+/Li. This current response might be the signature of a possible insertion of lithium in the M:LLZO lattice or the decomposition of M:LLZO, possibly into Li_2O, Zr_3O, La_2O_3 and Zr_3O, as suggested by first-principles calculations [175]. The reduction potential of 1.65 V vs. Li^+/Li observed using PITT is significantly higher than any reported in the literature (**Table 4.1**). In a study done by Yan *et al.,* the ESW of LLZO was determined by CV [263]. A significant current response was observed starting at 1.5 V vs. Li^+/Li but was attributed to impurities from the remaining dispersant/surfactant used during the synthesis, or to the side reaction at the Li/LLZO interface, with no further explanation. Another study done by Brugge *et al*. [581] assessed the ESW of Ge-doped LLZO using CV and observed significant reduction peaks at 1.5 V vs. vs. Li^+/Li that they attributed to the Au-Li alloying reaction. Kotobuki *et al.* [166, 169] investigated the ESW of Ta:LLZO and Al_2O_3+LLZO using CV and observed reduction peaks at 1.6 V and 2.5 V that they also attributed to the formation of Au-Li alloys. However, previous studies from Kulova *et al.* and Bach *et al.*, focusing on the electrochemical characterization of Li-Au alloying reactions, demonstrated in both cases the formation of Au-Li alloys only around 0.47 V vs. Li^+/Li [588, 589], suggesting that the current response observed at 1.5 V might in fact be coming from LLZO. Renner *et al.* observed

the kickstart of Li-Au alloying at 0.8 V [590] and used the scan collected at 1.6 V as reference. Consequently, we can attribute the reduction peaks observed at 0.45 V vs. Li^+/Li in **Figure 4.3A** to the formation of Li-Au alloys. In addition, Thompson *et al.* [580] investigated the ESW of Ta and Al-doped LLZO using CV. Small reduction peaks can be observed at 1.6 V on three of the five CV curves presented in their supporting information, none of which was discussed in the main manuscript. The same observation is made on the CV curves presented by Ma *et al.* [584] for Mg and Nb-doped LLZO, where reduction peaks starting around 1.5 V were overlooked. Often in literature, reduction peaks around 1 V were observed on the CV curves of various doped LLZO phases and were all attributed the plating and stripping of Lithium [130],[580],[579, 584]. However, lithium stripping and plating were proved to occur at much lower potentials, between -0.1 and 0.1 V vs. Li^+/Li [591], depending on the ohmic drop and overpotential occurring in the system. These signals might in fact find their origin in Li-Au alloying reactions. On the other side, the reduction of M:LLZO (M = Al, Ta and Nb) in contact with metallic lithium was confirmed in previous studies [170]. The formation of metallic Zr was observed experimentally at the LLZO/Au interface by Han *et al.* using XPS [175].

Upon oxidation, the current response remains small and steady from 2.5 V to 3.7 V vs. Li^+/Li for all three dopants, decreasing to 0 A at each step, as observed in **Figure 4.3B**. A drastic increase of the current response is observed starting from 3.7 V vs. Li^+/Li. The current response peaks between 4.0 and 4.2 V vs. Li^+/Li for Al, Ta and Nb doped stacks. Smetaczek *et al.* also observed the oxidation of Ta and Ga-doped LLZO starting at 3.7 and 3.9 V vs. Li^+/Li respectively using a PITT-like technique, the stepwise voltage increase (SVI) at 350 °C [582]. These oxidations culminate at 4.1 and 4.3 V vs. Li^+/Li and agree with the results of the present manuscript.

For comparison, we investigated M:LLZO using different cell configurations including composite, planar and liquid cell configurations. The results are presented in **Annex 8**. A significant difference is observed in the current response between the composite and planar cell configurations. In fact, no current response is observed in the planar configuration for neither reduction nor oxidation at 1.65 V and 3.7 V, confirming the importance of using composite electrodes to enable a relevant characterization of the ESW. This observation is in agreement with the findings of Jalem *et al.* who investigated the oxidation of Ta:LLZO using CV on two different cell configurations, a planar Li/LLZO/Al and a composite Li/LLZO/LLZO+C [574]. In the first configuration, no oxidation peak could be observed in the range [2.0 V – 5.0 V]. However, the oxidation of LLZO at 3.7 V vs. Li^+/Li was observed when the second cell configuration was used,

confirming our results, and demonstrating the importance of using a composite cell configuration. The same comparison was drawn in the literature using $Li_{10}Ge(PS_6)_2$ [175, 206, 572].

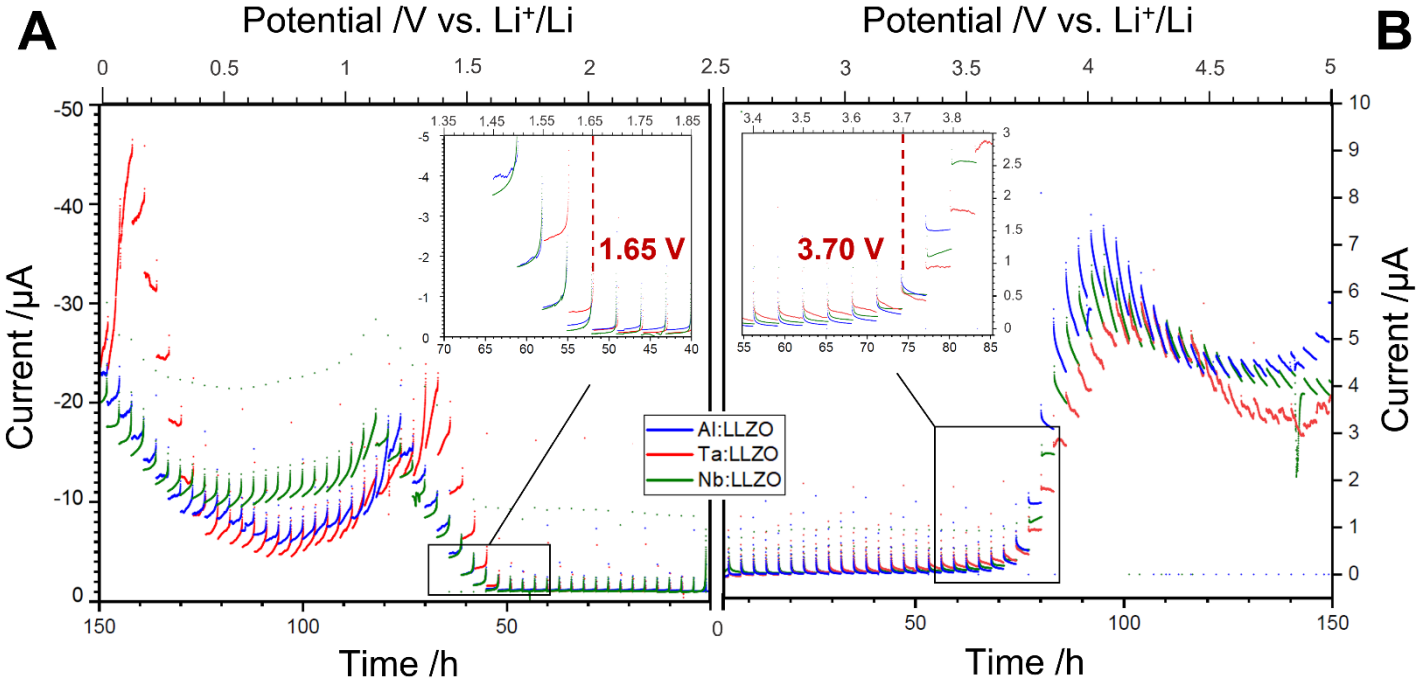

Figure 4.3 - PITT measurements on M:LLZO+Au (M = Al, Ta, Nb) stack pellets where the current response is plotted as a function of time and potential. The stacks were cycled separately A) from 2.5 V to 0 V vs. Li^+/Li for reduction and B) from 2.5 V up to 6 V vs. Li^+/Li for oxidation. A potential step of 50 mV, a time limit of 3 h and a temperature of 80 °C were used to run the experiment. No current limit was applied.

The comparison of the PITT curves of Al, Ta and Nb doped LLZO for oxidation or reduction revealed that all three doped LLZO displayed quasi-identical current responses globally, suggesting that the nature of the dopant played no role in the electrochemical behavior of M:LLZO. This hypothesis agrees with observations from Zhu *et al.* [173] and computations ran by Han *et al.* [175], which suggested that, considering the low amount of dopants in LLZO, the effects of dopants on the stability window are small. Another study on Al, Ta and Nb-doped LLZO concluded that the reduction of Zr^{4+} was the most significant consequence of the contact of LLZO with metallic Li [173], suggesting that LLZO reduction potential comes from the reduction of Zr^{4+}, justifying why the reduction potential is the same for all three dopants in **Figure 4.3A**.

4.4.3 – Al:LLZO reduction reaction

The oxidation potential found for M:LLZO and its agreement with other studies confirms the relevance of our methodology to assess the ESW of solid electrolytes. As detailed above, the oxidation of LLZO below 4 V vs Li^+/Li was investigated through several means. On the other side, the reduction of LLZO at 1.65 V has not been seen in the literature. For this reason, we will focus on the reduction reaction of Al:LLZO going on forward. The reduction of Al:LLZO was further investigated in electrochemistry by cycling the electrochemical cells down to 0 V vs. Li^+/Li for two cycles. The initial current response observed for reduction at 1.65 V does not appear when cycled back to 2.5 V and is not observed in the second cycle, as seen in **Figure 4.4**. The reduction of Al:LLZO is characterized by an irreversible and non-continuous reaction. An attempt to understand this phenomenon using EIS measurements were inconclusive. The measurement, first conducted using a 2-electrode cell configuration, was not deemed relevant given the inevitable reactivity of LLZO with the Li metal negative electrode, which also acted as a reference. For this reason, a 3-electrode cell configuration was used to run the experiment instead. However, this configuration required the use of two layers of PEO and their overlapping contributions to the total impedance made the interpretation of the Nyquist plots too strenuous.

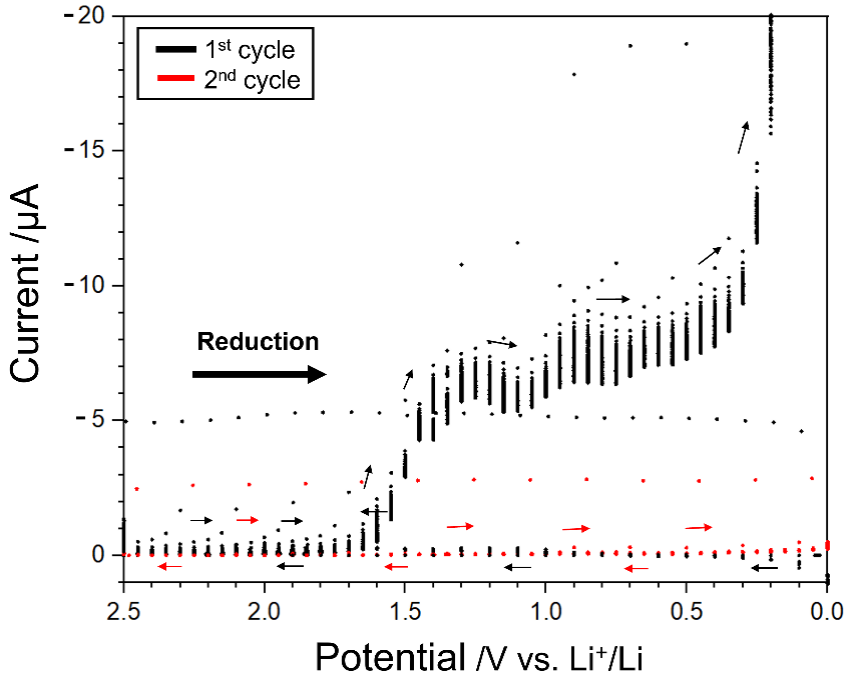

Figure 4.4 - PITT measurements on Al:LLZO+Au stack pellets where the current response is plotted as a function of the potential. The stack was reduced from 2.5 V to 0 V vs. Li^+/Li for two cycles. A potential step of 50 mV, a time limit of 3 h and a temperature of 80 °C were used to run the experiment. No current limit was applied.

The reduction reaction of Al:LLZO occurring at 1.6 V was investigated via *ex situ* solid-state ^{7}Li MAS NMR. A first Al:LLZO stack was reduced down to 1.3 V and a second stack was reduced down to 0 V then oxidized back to OCP. After the reduction reactions, the pellets were grinded, inserted in an airtight rotor and analyzed using NMR. The spectra are presented in **Figure 4.5**. The peak (1) of the initial Al:LLZO sample at 2.36 ppm corresponds to the environment of Li in the pristine Al:LLZO structure and is in agreement with the literature [592, 593]. When Al:LLZO is reduced to 1.3 V, the corresponding spectrum displays a main peak (2) that can be deconvoluted in two coalesced peaks (2a) and (2b). The peak (2a) corresponds to the initial environment of Li in Al:LLZO at 2.30 ppm while (2b) appears at a chemical shift of -0.17 ppm, suggesting the presence of two different Li environments in the sample. When Al:LLZO is further reduced to 0 V and oxidized back to OCP, the corresponding spectrum also displays a main peak (3) that can be deconvoluted in two more distinct peaks (3a) and (3b). The peak (3a) is attributed to the initial signal of Li in Al:LLZO at 2.30 ppm while the peak (3b) appears at a chemical shift of -0.17 ppm, like (2b), confirming the creation of a new Li environment after the reduction of Al:LLZO. The presence of this peak after a return to OCP proves the irreversibility of the Al:LLZO reduction reaction. The much lower chemical shift of peak (3b) represents a significant decrease in electronic density around the lithium nuclei, possibly due to a structural change in Al:LLZO. The peak (3b) is also observed in reduced Ta:LLZO and Nb:LLZO (**Annex 9A** and **B** respectively), confirming the little role played by the dopants in LLZO's redox behavior. The presence of this extra site could be attributed to the irreversible insertion of Li^{+} ions in Al:LLZO during reduction, like previously observed in positive electrode materials using NMR [573]. The insertion of Li^{+} in Al:LLZO should cause observable changes in the Al:LLZO crystal structure that can be evidenced using XRD.

To confirm that the peak (3b) does not come from the presence of an impurity (mainly LiOH and Li2CO3), NMR spectra were also acquired for LiOH and Li2CO3 powders. Li2CO3 had a chemical shift of 0.22 ppm and a T1 relaxation time of 28 s. LiOH had a chemcial shift of 0.26 ppm and a T1 relaxation time of 27 s. Neither of these materials had chemical shifts matching the one of peak (3b) found at -0.17 ppm, confirming that this peak is not a result of the contamination of Al:LLZO with either Li2CO3 or LiOH.

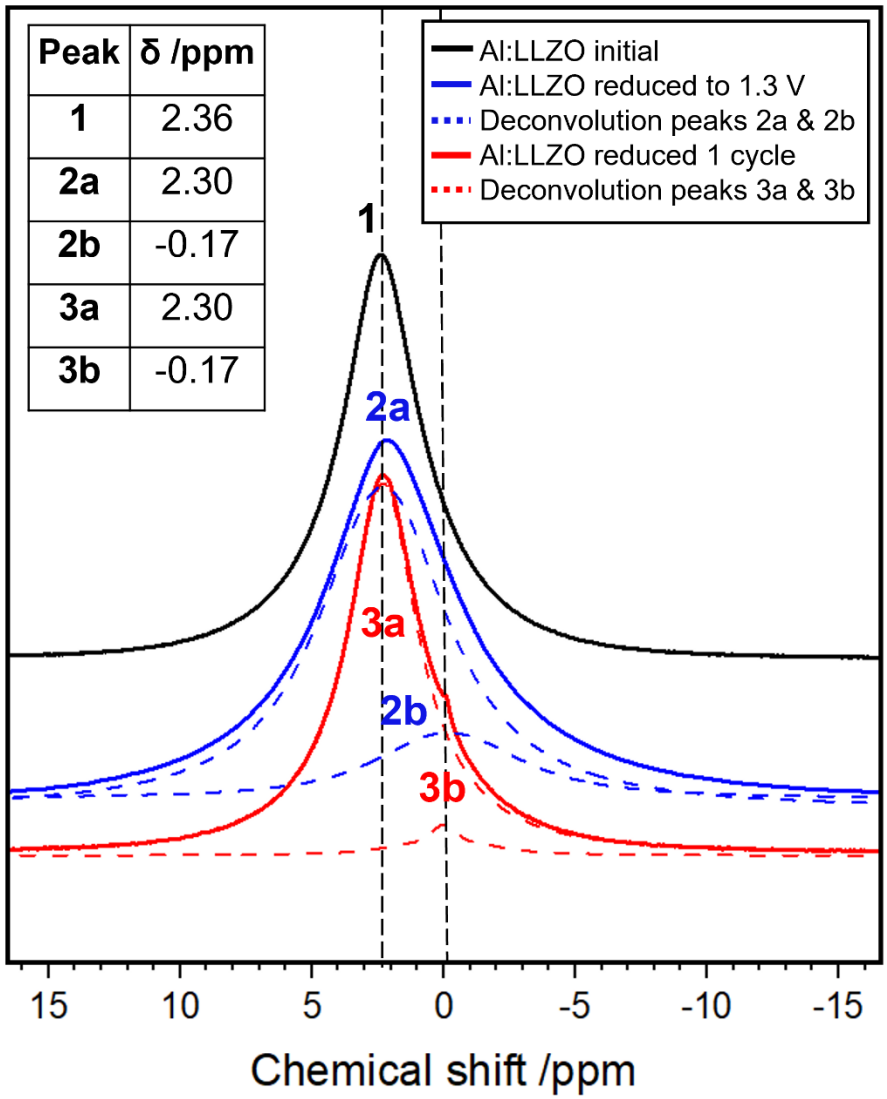

Figure 4.5 - ^{7}Li MAS NMR spectra of Al:LLZO stacks recorded at ν_{rot} = 10 kHz and a resonance frequency of 600 MHz (14.1 T) for the initial sample (at OCP), the sample reduced up to 1.3 V and the sample reduced 1 cycle (reduced down to 0 V and back to OCP). The chemical shifts are given in a table on the top left corner.

The Al:LLZO reduction reaction was therefore investigated using *operando* PXRD coupled with PITT measurements. An Al:LLZO stack and lithium foil were assembled in a punctured coin cell for an optimal signal (shown in **Annex 10**). The coin cell was sealed inside an argon-filled glovebox and introduced in an airtight heating chamber to prevent any contamination of the sensitive Al:LLZO during the experiment. Using PITT with a 100 mV potential step and a 3 h time step, Al:LLZO was reduced from its open-circuit potential (OCP) of 2.5 V down to 0 V vs. Li^{+}/Li and oxidized back to 2.5 V. 1 h scans were collected after 2 h of relaxation, at each potential step.

The resulting diffraction scans from each potential step are gathered in **Figure 4.6A**. We can distinguish the three signals coming from the Al:LLZO material, the gold powder and the stainless-steel (SS) coin cell casing. Through the reduction, the SS peaks S1 and S2 remain at a fix position. SS will therefore be used as reference to the two other contributions. The peaks attributed to gold, A1 and A2, shift to slightly bigger angles with a displacement of 0.1 ° 2θ occurring gradually from OCP to 1.5 V, before stabilizing for the rest of the reduction. On the other hand, the peaks attributed to Al:LLZO (L1-5) move toward smaller angles starting at 1.6 V, the shift becomes more significant at every potential step down to 0.8 V, corresponding to a lattice expansion. After 0.8 V, their peak positions stabilize, accumulating a maximum shift of 0.5 °. Throughout the reduction, the number of peaks in all the Al:LLZO diffractograms remains the same, suggesting that the space group symmetry is conserved and that no decomposition of Al:LLZO is occurring. Instead, the expansion of Al:LLZO might be caused by the insertion of Li ions into the lattice. Correspondingly, the observed peak shift suggests the formation of a solid solution after Li insertion.

The structural refinement of the curves allowed to follow the evolution of the lattice parameter *a* of Al:LLZO and Au cubic phases, the results are presented as a function of the cell potential in **Figure 4.6B**. First, we observe the parameter *a* of gold decreases slightly, which indicates that the gold lattice is contracting in the beginning of the analysis. However, the change of the gold lattice parameter is negligible compared to the one observed for Al:LLZO. No change of this parameter a is observed at low potential. A study led by Renner *et al.* observed a change of the parameter *a* in the gold lattice from 4.08 Å to 3.97 Å [590]. However, the above experiment was ran using the liquid electrolyte $LiPF_6$ in EC/DEC, allowing for a significantly bigger surface of reaction between Au and Li, and cycled repetitively between -0.1 and +0.1 V vs Li^+/Li in order to encourage the alloying reaction.

From **Figure 4.6B**, we observe a stable lattice parameter of Al:LLZO from 2.5 to 2 V then fluctuates slightly up to 1.7 V but remains within the standard deviation. However, passed this potential, the lattice parameter increases significantly from 13 to 13.06 Å, in agreement with the reduction potential of 1.65 V observed in electrochemistry. This volume expansion can be attributed to the insertion of lithium in the Al:LLZO lattice. When the material is oxidized back to 2.5 V, the initial structure is not recovered, as seen in **Figure 4.6A**. The Al:LLZO lattice does not recover its initial parameter either, as highlighted in **Figure 4.6B,** proving that the reaction is irreversible, in agreement with the PITT and ^7Li NMR observations.

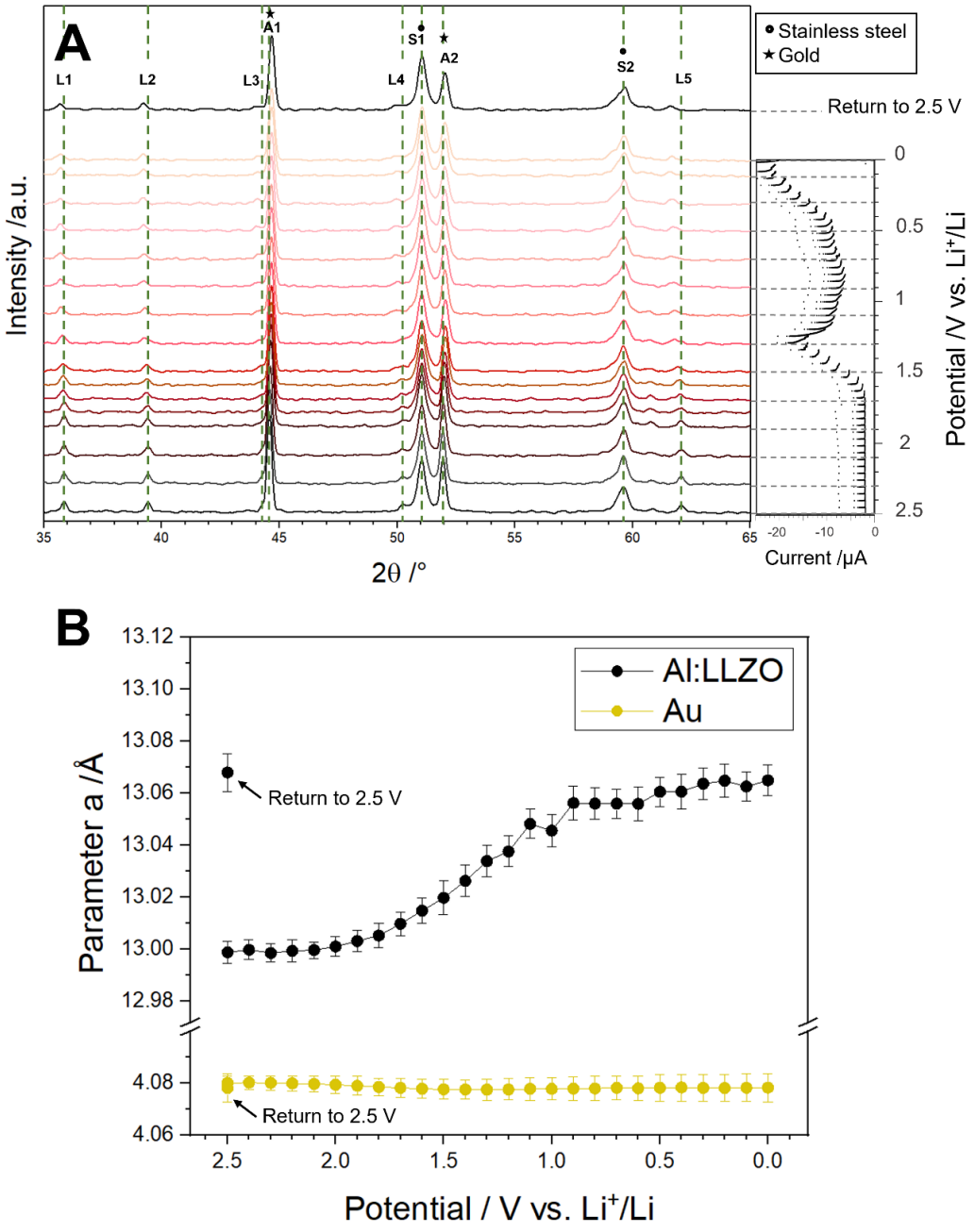

Figure 4.6 - *Operando* PXRD (CoKα, λ = 1.7903 Å) of the reduction of an Al:LLZO stack using PITT, from 2.5 to 0 V and oxidized back to the OCP of 2.5 V. A) PXRD patterns shown every 200 mV. B) Evolution of the lattice parameter *a* for Al:LLZO and Au as a function of the cell potential.

4.5 – Conclusion

The electrochemical stability window was assessed for LLZO solid electrolyte using a tailored experimental setup. Al, Ta and Nb-doped LLZO were investigated to determine the role of the dopant in LLZO redox chemistry. The optimized experimental setup included processing M:LLZO with gold particles into composites to enhance the redox current responses and using potentiostatic intermittent titration to remain close to the thermodynamic equilibrium of the system. The electrochemical stability window was found to be the same for all three dopants: 1.65 V - 3.7 V vs. Li^+/Li. Several cell configurations were used to determine the ESW of LLZO. The significant difference of signal between composite and planar cell configurations highlighted the importance of using the herein experimental setup. The study of Al:LLZO reduction reaction through two cycles showed that the phenomena occurring at the reduction were neither reversible nor continuous. The reduction of Al:LLZO and its irreversibility were evidenced using *ex situ* ^{7}Li NMR and *operando* PXRD techniques. The value of the ESW reported in the present manuscript is much narrower than commonly admitted in the literature. The oxidation potential determined is in agreement with previous studies on LLZO while the reduction potential is the highest ever observed for LLZO. These observations highlight the complex and subtle electrochemical behavior of LLZO, proving that there is still a lot to understand on LLZO before it can be successfully implemented as a reliable solid electrolyte in ASSLBs.

4.6 – Acknowledgements

Yasmine Benabed is grateful for the financial support of the Natural Sciences and Engineering Research Council of Canada - NSERC through a BESC D grant and a Michael-Smith Foreign Study Supplement (BESCD3-534841-2019) and the *Ministère de l'enseignement supérieur du Québec* through a PMCSI mobility grant. Co-authors Alexis Vanacker, Gabrielle Foran, Steeve Rousselot, and Mickaël Dollé acknowledge the financial support received from the Natural Sciences and Engineering Research Council of Canada (NSERC RDCPJ 528052-18).

Yasmine Benabed would like to thank Dr. David Lepage for his valuable insights throughout the realization of this study, Dr. Daniel Chartrand for his technical support with PXRD and Rietveld refinements, Dr. Cedric Barcha for his help running adjacent experiments, Jean-François Myre, Jean-Sebastien Mayer and François Vaillancourt for their help in building the *operando* PXRD setup.

5. EXPLORING DEFECTS AND DOPABILITY LIMITS OF SOLID ELECTROLYTES, A COMPUTATIONAL STUDY

Yasmine Benabed[1,2], Diana Dahliah[1,4], Mickaël Dollé[2] and Geoffroy Hautier[1,3]*

[1] Institute of Condensed Matter and Nanosciences, Université Catholique de Louvain, Louvain-la-Neuve, Belgium.

[2] Department of Chemistry, Université de Montréal, Montréal, QC, Canada.

[3] Thayer School of Engineering, Dartmouth College, Hanover, NH, United States.

[4] Department of Physics, An-Najah National University, Nablus, Palestine.

Keywords - solid electrolytes, all-solid-state lithium batteries, charged defects, dopability limits.

The study presented in the following chapter is the subject of an article submitted to the *Journal of Materials Chemistry A* (TA-ART-01-2023-000534) and is currently under revision. The article focuses on a computational study of the defect chemistry in several ceramic solid electrolytes. Intrinsic charged point defects are produced, and their formation energy is computed using DFT, as detailed in section 2.2. From the defects formation energy diagrams, we extract valuable metrics such as the Fermi level at equilibrium and the dopability limits. These two quantities allow us to evaluate the robustness of solid electrolytes to developing electronic conductivity. These computations also allowed to link the formation of defects in solid electrolytes with the nature of their environment, suggesting that the electronic conductivity in solid electrolytes is not an immutable property but rather depends on many intrinsic and extrinsic factors. In the context of this computational study, my contribution lies in conceiving the project, carrying all the computations, interpreting the results and writing the article. Diana Dahliah helped setting up the computational methodology and contributed greatly to the results interpretation. Mickaël Dollé provided valuable insight on the study and reviewed the manuscript. Geoffroy Hautier conceived the project, supervised the computations and reviewed the manuscript as principal investigator.

5.1 – Abstract

Negligible electronic conductivity is a crucial requirement that solid electrolytes must meet before they can be considered in all-solid-state lithium batteries. Electronic conductivity is strongly driven by charged defects. Understanding the defect chemistry of solid electrolytes is therefore essential to assess their performance and suitability. In this work, we use first-principles computations to investigate the intrinsic defect chemistry of six solid electrolytes in order to determine their robustness to developing electronic conductivity. We conclude that some electrolytes can be prone to problematic levels of electronic conductivity (e.g., $LiTi_2(PO_4)_3$) while others such as Li_3PS_4 have intrinsically low electronic conductivities. We also show that most solid electrolytes are more likely to develop electronic conductivity in S/O-rich|Li-poor environments, translating to more sulfur-rich or oxidative atmospheres and higher electrochemical potentials (> 4 V vs. Li^+/Li).

5.2 – Introduction

All-solid-state lithium batteries (ASSLBs) have received considerable attention as the next generation of lithium batteries [7, 98]. This shift is operated from conventional Li-ion batteries because ASSLBs can offer better safety, higher energy and power density [96, 128-131]. The key component of all-solid-state lithium batteries is the solid electrolyte (SE) [262]. Solid electrolytes must meet a number of requirements before they can be considered in ASSLBs. Ideally, they should have a wide electrochemical stability window, a high ionic conductivity at room temperature and a negligible electronic conductivity [95]. For a while, the focus was put on achieving the highest ionic conductivity possible on these materials, comparable to the one in liquid electrolytes (10^{-2} S.cm^{-1}). There is however a recent increased interest in the electronic conductivity of solid electrolytes. Electronic conductivity is detrimental to SEs because it leads to short-circuit, self-discharge and overheating. A necessary but not sufficient condition for SEs is for their electronic conductivity not to exceed 10^{-6} S.cm^{-1} at any temperature [264]. Ideally, it should be around 10^{-12} S.cm^{-1} and remain at least four orders of magnitude smaller than the ionic conductivity [95] Han *et al.* suggested for instance that electronic conductivity was probably the root cause for dendrite formation in both $Li_7La_3Zr_2O_{12}$ and Li_3PS_4 solid electrolytes [267].

In insulators and semiconductors, electronic conductivity is strongly driven by charged defects which act as dopants. The understanding of these point defects in solid electrolytes is

therefore essential to the assessment of the performance of an electrolyte, next to other quantities such as ionic conductivity. Due to their negligible concentration, characterizing point defects is strenuous and is hardly possible using standard characterization techniques such as X-ray diffraction or scanning electron microscopy. Even for extensively studied materials, such as semi-conducting (Si, GaAs) and optoelectronic (ZnO, GaN) materials, the defect chemistry remains a long-standing subject of debate [594-596]. Identifying defect-induced signals often requires a combined approach of experimental and computational analyses. To that end, point defect calculations have greatly evolved in the last decades, from the first classical simulations to first-principles studies using density functional theory [409, 597, 598]. First-principles defects computations have recently been more and more used in the solid electrolyte field. Canepa *et al.* introduced the idea of exploring defects to understand electronic conductivity in chalcogenide solid electrolytes [599]. Squires *et al.* used such computational methods to explore the defect chemistry of $Li_7La_3Zr_2O_{12}$ solid electrolyte [409]. Gorai *et al.* linked the formation of defects to the increase of the electronic conductivity in Li_6PS_5Cl, Li_6PS_5I, and Na_3PS_4 [600]. More recently, Swift *et al.* used the same method to predict the intrinsic interfacial resistance between solid electrolytes, such as Li_2PO_2N, Li_3PO_4, $Li_7La_3Zr_2O_{12}$ or Li_3PS_4, and positive electrode materials [601].

The formation of point defects in crystalline materials can be observed in nature as well as manmade. Although atoms in a crystal are initially organized in a regular lattice, some of them will shift from their regular sites after thermal equilibrium is reached, creating disorder. There are mainly three different types of point defects found in a crystal structure : vacancies, interstitials and antisites [602, 603]. They are conventionally represented using the Kroger–Vink notation which specifies the nature, location and effective charge of a defect relative to the unperturbed lattice: 1) the vacancy ($V_{M}^{\cdot\bullet}$ or $Vac_{M}^{\cdot\bullet}$) is when ion $M^{\mp}$ is missing from its initial crystallographic site, 2) the interstitial (M_i) is when atom $M^{\mp}$ is found in an interstitial site of the lattice and 3) the antisite (M_X) is when atom M occupies the crystallographic site of atom X. The concentration of these defects in a material at equilibrium is determined by their formation energies, which depends on the chemical potentials of the system and its Fermi level [478]. The chemical potential relates to the change of the system's energy when a specie is removed from it. Intuitively, it can be related to synthesis conditions. For instance, a high oxygen chemical potential is applied under an oxidative atmosphere, which can be achieved by maintaining a high oxygen partial pressure during synthesis.

In this work, we use first-principles computations to investigate the intrinsic defect chemistry of various SEs in order to assess their robustness to developing electronic conductivity.

For each SE, we computed the formation energies for intrinsic defects, their Fermi levels at equilibrium and their dopability limits in different environments. Using the dopability limits, it was possible to determine each SE's intrinsic robustness to developing electronic conductivity and to single out which environments promoted the formation of charge carriers. The results indicate that SEs resist differently to the formation of defects and charge carriers. Because there is no adequate way of controlling the formation of defects in solid electrolytes during battery processing and cycling, we insist on the importance of selecting optimal environments for their synthesis and handling. The outcoming properties of these materials, such as the ionic and electronic conductivities, depend on it.

5.3 – Theoretical methods

Structural relaxations and defect formation energies were computed using the Perdew-Burke-Ernzerhof (PBE) [461] functional from the generalized gradient approximation (GGA) to the density functional theory (DFT) [604]. Projector Augmented Wave (PAW) pseudo-potentials [513] were used as implemented in the Vienna Ab initio Simulation Package (VASP) [514]. The wavefunctions were expanded on a plane-wave basis set employing a cutoff energy of 520 eV. The point defects were studied using the supercell approach for point defects in solids [605]. The different defective structures were generated using the Python Charge Defects Toolkit (PyCDT) [476] starting from supercells of 128 atoms. When needed, the supercells were extended up to 512 atoms to meet the convergence criteria. The Brillouin zone was sampled using a range of k-point grids from 1x1x1 to 6x6x6, depending on the supercell size of each material. All the models were relaxed at fixed volume until the maximum force on the ions became smaller than 0.01 $eV.A^{-1}$. Spin-polarized calculations were performed. The occupation of the electronic states was determined through the Gaussian smearing method with a smearing width of 0.05 eV. The formation energy E_{form} of each charged defect state X^q was computed as a function of the Fermi level E_F following equation 2.32 [606, 607]. The size of the supercell is chosen according to the convergence of E_{corr}. Here, we used the extended Freysoldt's (Kumagai) correction scheme [480, 481]. The equilibrium Fermi level is calculated by finding a self-consistent solution, to all the defects, that meets an overall charge neutrality requirement [608]. The equilibrium Fermi level was computed at a temperature of 300 K for all the solid electrolytes. VBM and BG were computed from relaxed structures using the Heyd–Scuseria–Ernzerhof (HSE) hybrid functional with an exact-exchange fraction of 0.25 and a screening length of 0.2 Å [463].

5.4 – Results and discussion

We investigated a selection of six solid electrolytes considered for ASSLBs. NASICON-type materials $LiTi_2(PO_4)_3$ and $LiGe_2(PO_4)_3$, garnet $Li_7La_3Zr_2O_{12}$, phosphates Li_3PO_4 and $LiPO_3$ and thio-LISICON material Li_3PS_4. The crystal structures were retrieved from the Materials Project website [512], details on the structures are given in **Table 5.1.** Before introducing defects into the selected solid electrolytes, we computed their band gaps using the HSE hybrid functional (**Table 5.1**). It was possible to compare some of the computed band gaps with experimentally measured band gaps. Garnet-type $Li_7La_3Zr_2O_{12}$ displays a band gap of 5.9 eV, in agreement with former computational work [409] and experimental value of 5.6 eV [580]. NASICON-type material $LiTi_2(PO_4)_3$ has a band gap of 4.28 eV, comparable to the experimental value of 3.68 eV (15% discrepancy) [609]. Li_3PO_4 has a computed band gap of 7.81 eV, in agreement with the experimental value of 8.16 eV (4% discrepancy) [610]. According to their band gaps, it is possible to split the SEs into two categories: large and medium band gaps. Phosphates, most of the NASICON structures and $Li_7La_3Zr_2O_{12}$ possess a large band gap (> 5eV). These materials are expected to be little influenced by the introduction of defects. Li_3PS_4 and $LiTi_2(PO_4)_3$ display medium band gaps, between 4 and 5 eV. Medium band gaps facilitate the formation of charge carriers which can result in a significant increase of the electronic conductivity.

Table 5.1 - references for all the solid electrolytes crystal structures retrieved from Materials Project (MP) and their computed valence bands and band gaps*. Large band gaps are highlighted in green, medium ones in yellow. **VBMs and band gaps were computed from HSE relaxed structures, zero energy reference level is set so the average potential from all atoms in the unit cell is zero (G=0).*

SE	Space group	MP-ID	Space group in MP	E above hull /eV	VBM /eV	Band gap /eV
$LiTi_2(PO_4)_3$	R3-c	mp-18640	[Trig] R3c	0.001	0.04	4.28
$LiGe_2(PO_4)_3$	R3-c	mp-541272	[Trig] R3c	0.002	0.47	6.04
$Li_7La_3Zr_2O_{12}$	$Ia\bar{3}d$	mp-942733	[Q] I41/acd	0	2.42	5.93
Li_3PO_4	Pmn21	mp-13725	[O] Pmn21	0	-0.71	7.81
$LiPO_3$	$P2_1/c$	mp-29195	[M] P21/c	0	-1.31	7.59
Li_3PS_4	Pmn21	mp-985583	[O] Pnma	0	0.46	4.06

Unlike the semiconducting industry where the precise control of defects is possible in ultra-clean settings, battery manufacturing is not clean enough to precisely control defects and thus electronic conductivity. However, there are intrinsic limits to a material's conductivity due to the compensation between charged defects [611-616]. Some materials will intrinsically offer low

electronic conductivity in all synthesis conditions (i.e., in all chemical potentials), making them robust insulating solid electrolytes. The concept of dopability limit (DL) is key here to understand the intrinsic limits of a material towards doping.

The dopability limits indicate the minimum and maximum values that the Fermi level can thermodynamically reach [617-621]. The Fermi level is directly linked to charge carriers. Highly doped, electrically conductive materials require a Fermi level close to either the valence band or the conduction band. Thus, DLs represent an intrinsic boundary that prevents a SE from forming charge carriers, regardless of the type of defects computed. **Figure 5.1** introduces the concept of dopability limits. In general, the DLs (upper and lower) are reached when the two most dominant defects (acceptor and donor) have a negative formation energy. In **Figure 5.1**, the system produces two defects, a donor defect α (in blue) and an acceptor defect β (in pink). For simplicity, we took two defects with only one charge state +1 or -1 but this can be generalized. At equilibrium, and only if these two defects are present, both defects will compensate each other and lead to a Fermi level located approximately at the crossing of the charged defect states. Defect β has a negative formation energy when the Fermi level reaches 3 eV, labelled region **1**. This point is considered a dopability limit because passed this point, *any* defect with a positive charge (including defects beyond alpha and beta) will be spontaneously compensated by the negative charge (q=-1) of the defect β, impeding the formation of any new charge carrier. Defect β is defined as an electron 'killer' defect because it compensates any attempt to dope the material p-type, i.e. to move the Fermi level close to the valence band [615, 619]. Therefore, the Fermi level at equilibrium E_F (red dashed line) cannot be driven beyond this point in any way [622, 623]. On the other side of the band gap, the electron 'killer' defect β is mirrored by a hole 'killer' defect α. This positively charged (q=+1) defect has a negative formation energy up to 2 eV, labelled region **2**, and will compensate for any defect with a negative charge produced within this region. The dopability window (upper DL – lower DL) is therefore confined in region **3,** where existing donor and acceptor defects have a positive formation energy, and where no compensation is possible. The dopability window gives therefore an allowed and intrinsic energy window for the Fermi level and sets if a material will be potentially p/n-type dopable or not. A material that is robust to doping would need a narrow dopability window, located as far from the band edges as possible.

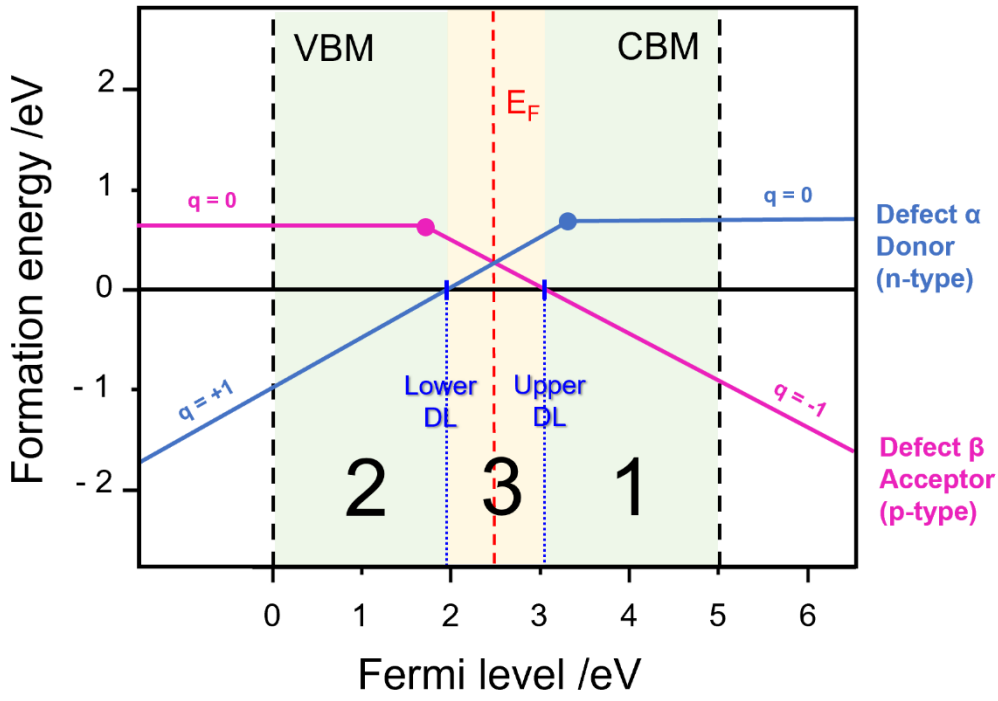

Figure 5.1 - A schematic representation of how to determine the upper and lower dopability limits (DLs). The dopability window is shown between the blue dashed lines. E_F at equilibrium is represented in a red dashed line.

After the introduction of intrinsic defects, the formation energy diagrams were computed for all the solid electrolytes. We have considered all possible vacancies and anti-sites for each SE but refrained from introducing interstitials to reduce the computing cost. We do not expect this to strongly affect our qualitative conclusions on the intrinsic dopability limits of these materials. Comparison with previous work, which includes interstitials in $Li_7La_3Zr_2O_{12}$, indicates that the interstitials do not change the dopability limits and fermi level in these materials [409],[410]. We did not include complex defects (e.g., vacancy-interstitial complexes) or extrinsic defects such as hydrogen or carbon impurities neither. Despite these simplifications, important conclusions can still be made as additional defects (e.g., complexes, extrinsic, interstitials) will need to compete with the defects we have already considered.

The formation energy diagrams for all solid electrolytes are presented in **Figure 5.2**. In the interest of clarity, only the most relevant defects are displayed in the figure, they correspond to the defects with the lowest formation energy for each SE (the full diagrams are presented in **Annex 11**). The diagrams are presented according to a distinct set of chemical potentials, called a chemical limit. The values of their elemental chemical potentials are provided in **Annex 12**. It was possible to separate the chemical limits into two types of environments: **S/O-poor|Li-rich** and

S/O-rich|Li-poor. Although many types of environments are possible (O-rich|P-poor, Ti-poor|Li-poor…etc), we decided to select the environments with respect to Li and the anion, because they are considered the most relevant in the context of solid electrolytes. An ion-poor environment is described by a low chemical potential of the said ion (more negative), while an ion-rich environment correlates to a high chemical potential (less negative). Even in their simplified versions, these formation energy diagrams are complex, with many defects competing, as SEs are ternary or quaternary materials.

In **Figure 5.2A-F**, the formation energy diagrams for all studied solid electrolytes show how the different charged defects behave and compete with each other. Donor defects (giving electrons, positively charged) are often compensated by acceptor defects (generating holes, negatively charged). The competition between all defects set the Fermi level. Fermi levels at equilibrium are represented with a red dashed line. The dopability windows, introduced in **Figure 5.1**, are highlighted in yellow in each diagram. All the defect computations have been performed at the GGA level and the GGA band gap is plotted as green dashed lines. We also indicate the HSE band edges as computed in the bulk and referred to the GGA band edges. These HSE band edges are closer to experimental values. Computational cost is again motivating this approach as full HSE defect computations are significantly more demanding in computational resources. While this approach will affect the exact position of the fermi level, we expect the dopability limits to be less affected. Indeed, work from Peng *et al.* has shown that *for fully ionized defects* (which set the dopability limit), DFT computations with a band edge shift from bulk hybrid or GW computations reproduce the full hybrid defect computation [624]. Our own larger benchmark agrees with this finding [625].

In both S/O-poor|Li-rich and S/O-rich|Li-poor environments, p-type Li vacancies have the lowest formation energies and are considered the most dominant type of defect. This observation is in agreement with the findings of Gorai *et al*. [600] and is coherent since solid electrolytes are lithium conductors, where vacancies might be needed for lithium diffusion. For all oxide-based solid electrolytes (**Figure 5.2A-E**), the compensating defect to Li vacancies is the O vacancy. In Li_3PS_4 (**Figure 5.2F**), Vac_S and P_{Li} are both compensating for Vac_{Li}.

The Fermi level directly controls conductivity as it sets the charge carrier concentration in the conduction or valence band. We remind that the Fermi level might be affected by missing defects from our analysis (e.g., interstitial, complex defects, or extrinsic impurities) as well as our HSE band edge shift. It is nevertheless an interesting quantity to observe at this stage. To ensure an electronic insulation of SEs, it is important that the Fermi level is located deep into the band

gap. Traditionally, the Fermi level is considered deep at 0.1 eV from the band edges for semiconductors [626, 627]. Values below the threshold of 0.1 eV are considered **critical** because they can lead to significant electronic conductivity, high enough to form semiconductors [627]. However, this threshold is necessary but not sufficient for solid electrolytes, which require a greater distance from the band edges in order to be considered safe from developing electronic conductivity.

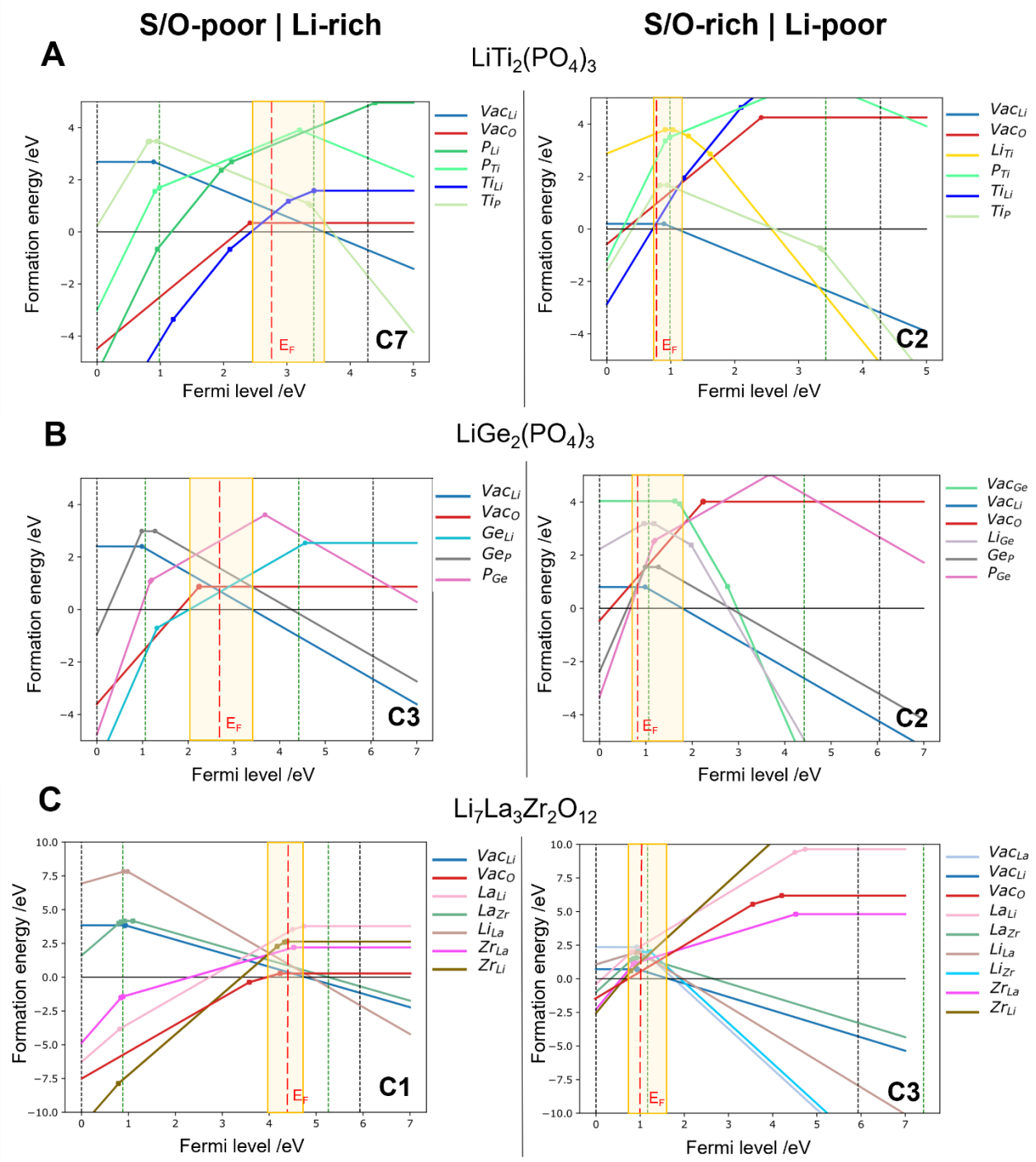

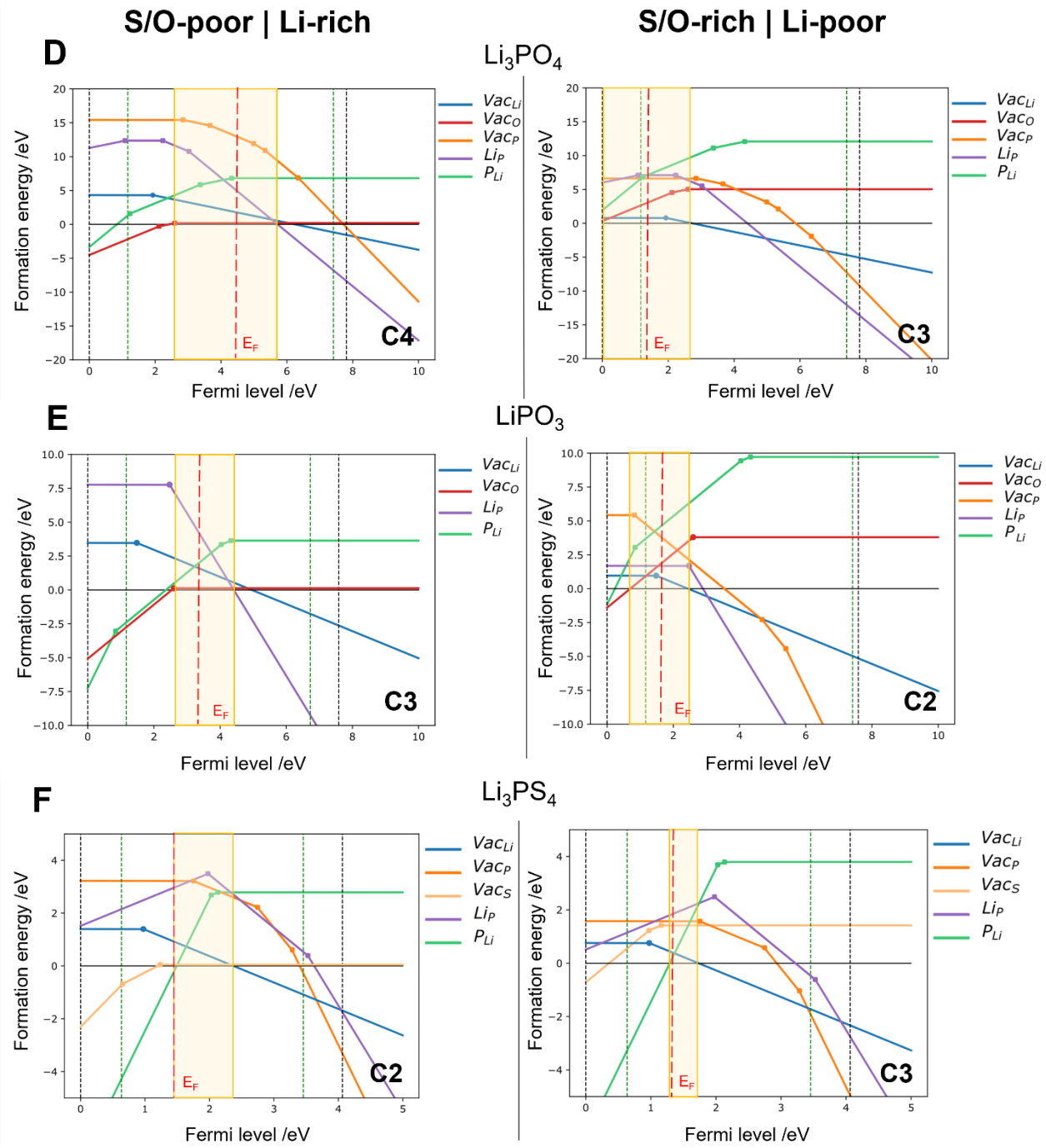

Figure 5.2 - Selected formation energy diagrams in S/O-poor|Li-rich and S/O-rich|Li-poor environments for all solid electrolytes (A-F). The black dashed lines represent valence and conduction bands computed using HSE. The green dashed lines represent initial valence and conduction bands computed using GGA. The red dashed line is the Fermi level at equilibrium. The yellow highlighted regions are the dopability windows. **C1-8** symbols refer to the chemical limit involved; all chemical limits can be found in **Annex 11** and **Annex 12**.

As mentioned earlier, the expected value of an electronic conductivity should be smaller than 10^{-12} S.cm^{-1} in solid electrolytes [95]. Using this value of electronic conductivity, with an approximate value for electron mobility in solid electrolytes of ≈1cm^2/(V·s) (which is likely to be an upper bound) and an approximate value for the effective density of states of $N_{c/v}$ of ≈ 10^{20} cm^{-3}, it is possible to estimate the expected distance of E_F from the band edges ($E_F - E_{C/V}$) at 0.8 eV using equations 2.33, 2.34 and 2.35 (more details can be found in annex). Values below the threshold of 0.8 eV are considered **problematic** for the electronic insulation of a SE because they are considered not ideal and can contribute to a non-negligible electronic conductivity. The closer the Fermi level is from the conduction and valence bands, the more likely it is for the material to form charge carriers and therefore to develop electronic conductivity. The two thresholds of 0.1 eV and 0.8 eV will be used as references to describe a ‘’**critical**’’ and a ‘’**problematic**’’ behavior of SEs, respectively.

We investigate the position of E_F in the S/O-rich|Li-poor and S/O-poor|Li-rich environments. We observe that $LiGe_2(PO_4)_3$, $Li_7La_3Zr_2O_{12}$, Li_3PO_4, $LiPO_3$, and Li_3PS_4 (**Figure 5.2B-D**) maintain a deep Fermi level (E_F located at 0.8 eV or more from the band edges) in both chemical environments, suggesting they might be robust to the formation of defects no matter the environment. On the other hand, $LiTi_2(PO_4)_3$ has its E_F shift problematically close to the valence band in the O-rich|Li-poor environment (**Figure 5.2A**), suggesting that oxidative atmospheres might promote the formation of charge carriers in this material. We also pay attention to the shift operated by the Fermi level from an environment to another. This criterium allows to understand how the environment affects the ability of SEs to form charge carriers. Li_3PS_4 displays a negligible shift of the Fermi level from an environment to another, its ability to form charge carriers is not affected by the nature of the environment (**Figure 5.2F**). On the other hand, all the other SEs see the position of their Fermi level change from an environment to another. Their Fermi levels remain deep into the band gap in S/O-poor|Li-rich environment, occasionally shifting toward the conduction band as observed in $Li_7La_3Zr_2O_{12}$ (**Figure 5.2C**), but shifts toward the valence band in S/O-rich|Li-poor environments. From these observations, we can hypothesize that most SEs are more likely to form charge carriers in S/O-rich|Li-poor environments. This trend is justified by the fact that a Li-poor environment will favor the formation of Li vacancies within the structure. Li vacancies being the dominant defect in all six solid electrolytes, the position of the Fermi level will most likely be greatly affected by the increase of Li vacancies.

A more important indicator of electronic conductivity is given by the dopability limits. The dopability limits are intrinsic and show the range in which the Fermi level could be even if other

defects (e.g., extrinsic defects such as impurities) are present in the material. A SE that is robust to unwanted electronic conductivity should have a dopability window located as far from the band edges as possible. If the dopability window remains deep in the band gap, the Fermi level cannot be driven at the vicinity of the band edges, preventing any n-type or p-type doping. The example given in **Figure 5.1** showcases the ideal behavior for a solid electrolyte, with a deep and narrow dopability window. The dopability limits were computed for each solid electrolyte and at all chemical limits, giving several values for each material. To better represent the evolution of the DLs, we computed the difference of energy between the dopability limits and the band edges, DL_{lower}-E_V and E_C-DL_{upper} where E_V represent the energy of the VBM and E_C the energy of the CBM. For each solid electrolyte, only the smallest of these two values, labelled |DL-$E_{C/V}$|, is represented in **Figure 5.3**. From the figure, we can see that $LiTi_2(PO_4)_3$, $LiGe_2(PO_4)_3$, $Li_7La_3Zr_2O_{12}$ and $LiPO_3$ show problematic electronic conductivity for their S/O-rich|Li-poor chemical limits, it is even critical for Li_3PO_4. This means that careful synthesis conditions are needed when synthesizing them to ensure that electronic conductivity is not encouraged. In contrast, Li_3PS_4 shows exceptional robustness with respect to doping and should stay highly electrically insulating in a wide range of conditions. Interestingly, the robustness of SEs to developing electronic conductivity does not seem to directly correlate with the nature of their anion or their band gap. Indeed, previous studies established a link between the band gaps of solid electrolytes and their ESWs [378, 628-631]. In the same manner, Wei *et al.* investigated the ability of large band gap halide perovskites to compensate for their defects through a self-regulation mechanism and remain electronic insulators despite the formation of defects [632]. However, the correlation between band gap and formation of charge carriers might not be as obvious as previously stated. For example, Li_3PO_4 displays one of the largest band gaps (7.81 eV) but displays critical dopability limits at some of its chemical limits. In contrast, Li_3PS_4 maintains deep dopability limits throughout its ESW despite having a medium band gap (4.06 eV). Moreover, despite its medium band gap, the electronic conductivity of Li_3PS_4 was determined to be 2.2×10^{-9} $S.cm^{-1}$ at 30 °C, one order of magnitude lower than the electronic conductivity of a large band gap material such as $Li_7La_3Zr_2O_{12}$ (experimentally confirmed to be 5.5×10^{-8} $S.cm^{-1}$ at 30 °C) [267, 633, 634]. Therefore, it might be relevant to challenge the direct correlation between the value of the band gap and the stability of a material against forming charge carriers.

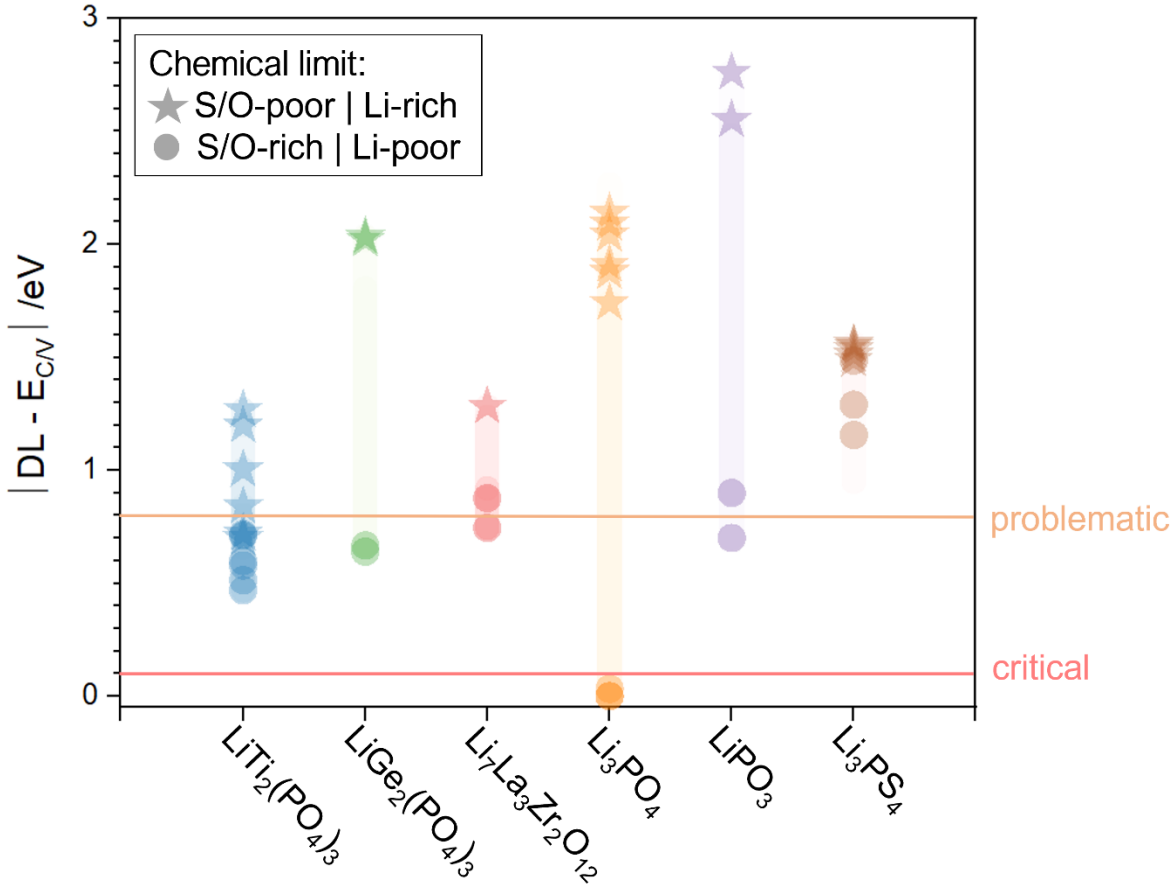

Figure 5.3 - Smallest difference of energy between the lower dopability limit and VBM or between the upper dopability limit and CBM calculated for all chemical limits of all solid electrolytes. Each floating column gathers the values of $|DL - E_{C/V}|$ at all chemical limits, given for each solid electrolyte. S/O-poor|Li-rich (stars) and S/O-rich|Li-poor (circles) chemical limits are illustrated.

For oxides, the oxygen chemical potential is commonly controlled by the atmosphere used during synthesis. Reducing atmospheres such as Ar or H_2 lead to low oxygen chemical potential, while syntheses under air will lead to higher oxygen chemical potentials [511]. The distances of the upper and lower dopability limits from the band edges $|DL - E_{C/V}|$ were represented as a function of O chemical potential for each solid electrolyte, only the smallest of these two values is represented in **Figure 5.4**. The reference oxygen chemical potential (μ_O) is set to be zero in air at room temperature (298 K, 0.21 atm) [635]. The O_2 energy used was computed by Wang *et al.* [636]. Referenced this way, the chemical potentials > 0 eV correspond to atmospheres that are more oxidative than air while chemical potentials < 0 eV correspond to more reducing atmospheres. We observe from the figure that all the SEs have their dopability limits at a problematic distance (< 0.8 eV) to the band edges when μ_O > 0 eV (even critical for Li_3PO_4), indicating a risk of developing electronic conductivity if they are synthesized or handled under an

oxidative atmosphere. In a reducing atmosphere, all solid electrolytes are safe from forming charge carriers, with the exception of $LiTi_2(PO_4)_3$. Generally, all selected solid electrolytes have deeper dopability limits when the chemical potential of oxygen is decreased, translating to more reducing atmospheres. This tendency can be rationalized as moving toward oxygen-poor environments encourages the formation of oxygen vacancies. Vac_O being the most dominant compensating defect for most solid electrolytes, it compensates for the lithium vacancies and consequently decreases the amount of charge carriers for instance produced by lithium vacancies.

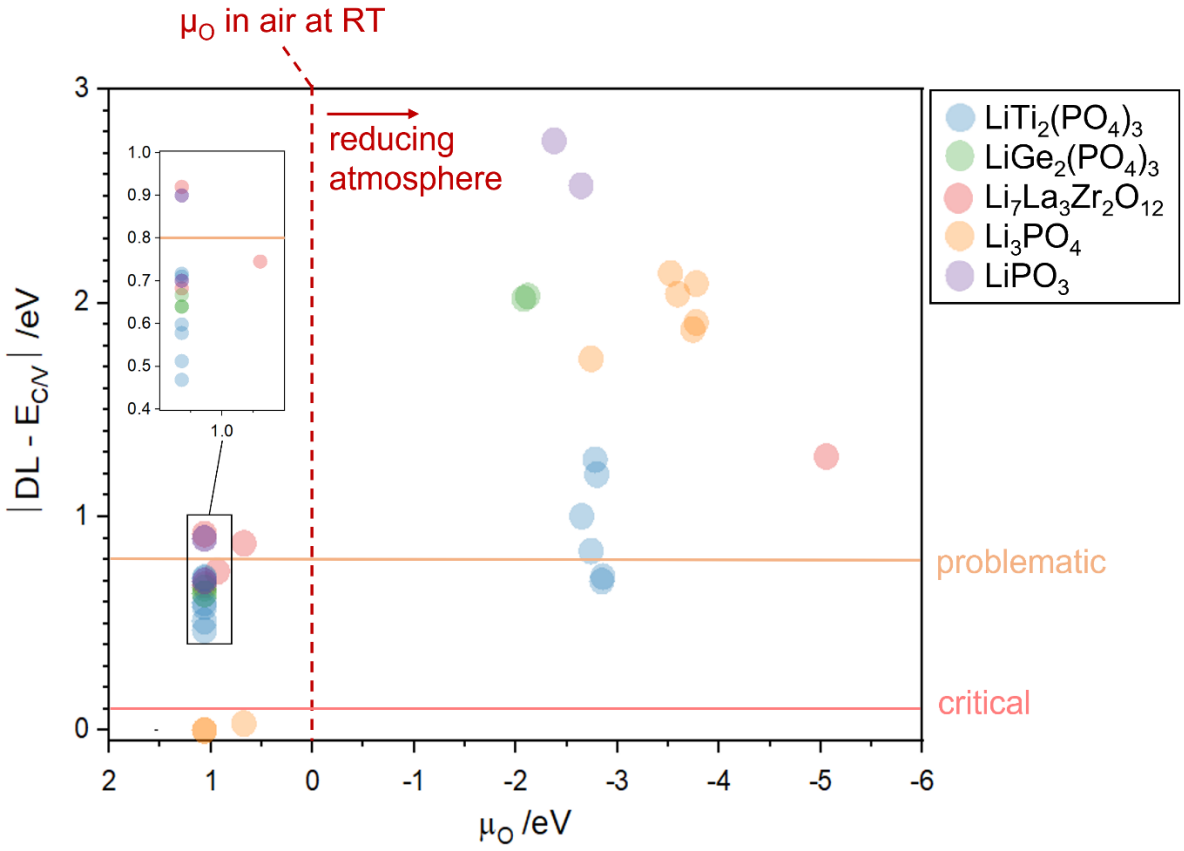

Figure 5.4 - Smallest difference of energy between the lower dopability limit and VBM, or between the upper dopability limit and CBM, computed for oxide-based solid electrolytes as a function of the chemical potential of oxygen (μ_O). The red arrow points toward a reducing atmosphere. The reference μ_O = 0 eV is set in air at room temperature (298 K, 0.21 atm).

We have just discussed how synthesis conditions and chemical potential influence the electronic conductivity of SEs. Additionally, the lithium chemical potential experienced by the SE when assembled in a battery also varies depending on the applied electrochemical potential. The chemical potential of lithium is directly related to the electrochemical potential following the

equation 2.31. When the electrochemical cell is cycling, the chemical potential of lithium changes according to the electrochemical potential of the cell. Therefore, it is relevant to study the formation of charge carriers in SEs as the chemical potential of lithium evolves. In **Figure 5.5**, μ_{Li} is converted to electrochemical potential. In the figure are also presented the computed electrochemical stability windows (ESWs) for all SEs. ESWs were computed using the grand potential phase diagram, following a computational method detailed in previous work [637]. ESWs are a range of μ_{Li} within which each SE is considered thermodynamically stable. Beyond these ESWs, the SE does not have an energy above hull equal to 0 and theoretically decomposes to more stable products of the phase diagram. However, it is still possible to compute points outside the SEs thermodynamic ESWs because we can consider their phases to be metastable outside the stability range. The decomposition reaction of SEs is a sluggish process involving the nucleation and growth of new phases and is limited by its kinetic. This explains why thermodynamic ESWs are significantly narrower than kinetic ESWs determined experimentally. Concretely, a SE outside its ESW will probably not decompose rapidly. In contrast, we do not expect the formation of intrinsic defects to be slow, it is far more likely to happen than a phase decomposition. Therefore, SEs are believed to be more likely to form defects outside their ESWs. For this reason, we computed the dopability limits for all solid electrolytes at Li chemical potentials corresponding to 0, 4.2 and 5 V vs. Li^+/Li (half-filled circles in **Figure 5.5**). These results are presented to gain an insight on the behavior of SEs within an operating battery; a potential of 0 V is an indication on how the SEs could behave against metallic lithium, 4.2 V corresponds to the operating potential of state-of-the-art positive electrodes such as $LiNi_xMn_yCo_zO_2$ (x+y+z = 1) and $LiCoO_2$ [638, 639]. The solid electrolytes were also investigated at a potential of 5 V to assess their behavior against new-generation positive electrodes such as spinel-type material $LiNi_{0.5}Mn_{1.5}O_4$ or olivine-type material $LiCoPO_4$ [640, 641].

Figure 5.5 gathers the results for all the selected solid electrolytes given as a function of the electrochemical potential vs. Li^+/Li. $LiTi_2(PO_4)_3$ and $LiGe_2(PO_4)_3$ see their DLs shift below the 0.8 eV threshold at high potentials (> 4 V vs. Li^+/Li). Worse, $LiTi_2(PO_4)_3$ is only able to prevent from forming charge carriers between 2.7 V and 4 V vs. Li^+/Li. $Li_7La_3Zr_2O_{12}$ has dopability limits at a safe distance from the band edges throughout the entire range of potential, the only exception being around 3.2 V vs. Li^+/Li. The dopability limits of $LiPO_3$ reach a problematic distance from the band edges around 5 V vs. Li^+/Li while Li_3PO_4 dopability limits can only prevent from forming charge carriers up to 3 V vs. Li^+/Li, then they shift below the 0.1 eV threshold at higher potentials. In contrast, Li_3PS_4 is safe from forming charge carriers throughout the whole potential range, even

outside its ESW. As a general trend, we notice that all solid electrolytes are more likely to form charge carriers at higher electrochemical potentials vs. Li^+/Li (S/O-rich|Li-poor environment). This indicates that the part of the SE in contact with the cathode might show more electronic conductivity issues than the part in contact with the anode.

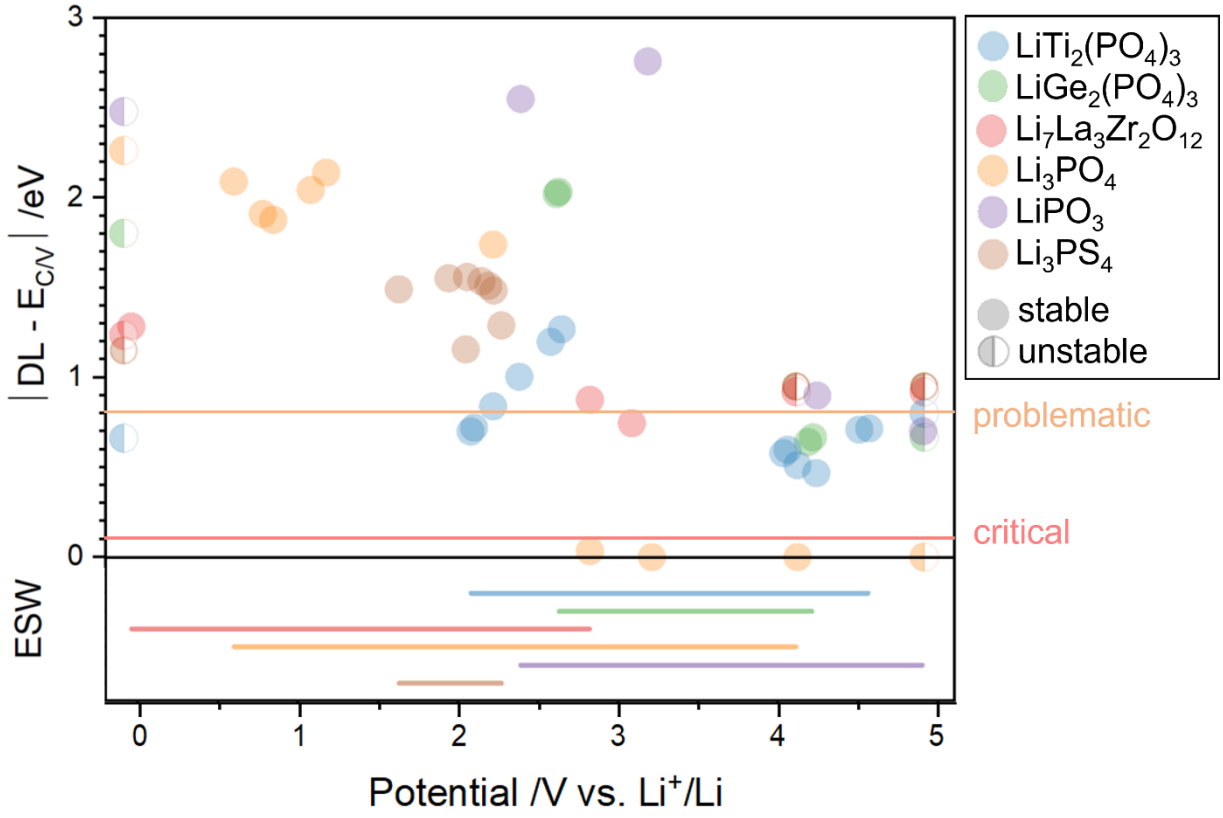

Figure 5.5 - Smallest difference of energy between the lower dopability limit and VBM, or between the upper dopability limit and CBM, calculated for all the solid electrolytes as a function of the electrochemical potential.

5.5 – Conclusion

Although a definitive ideal value of the electronic conductivity has not yet been determined for solid electrolytes, electronic insulation must be considered as a primordial criterium to comply with when looking for promising SE materials. Knowing that electronic conductivity in insulators and semiconductors is driven by charged defects and considering that the formation of defects, specifically intrinsic defects, is a spontaneous process that cannot be precisely controlled or monitored, it is important to figure out ways to foresee the creation of such defects. Our work uses first-principles calculations to investigate the robustness of several solid electrolytes to developing electronic conductivity under different conditions. We evaluate the robustness of SEs against the

change of environment by monitoring the evolution of their dopability limits. The most reliable materials are the ones able to always maintain a deep and narrow dopability window. The dopability limits were monitored for each solid electrolyte as a function of lithium and oxygen chemical potentials in order to translate our results to concrete experimental conditions. From our observations, it was possible to come to the following conclusions:

1. In both environments, Li vacancies are considered the most dominant type of defect for all selected solid electrolytes. For most solid electrolytes, the compensating defect to Li vacancies is the anion vacancy.

2. $LiTi_2(PO_4)_3$ displays a problematic distance of its dopability limits from the band edges throughout the whole potential range. It ought to be closely monitored during the synthesis, handling and while operating the battery.

3. On the other hand, Li_3PS_4 displays great robustness against developing electronic conductivity, regardless of Li and S chemical potentials.

4. The direct correlation between large band gaps and the absence of electronic conductivity might be questioned when defects are accounted for.

5. All selected solid electrolytes have deeper dopability limits when the chemical potential of oxygen is decreased, translating to a lower partial pressure of oxygen (i.e., a more reducing atmosphere).

6. Most SEs are more likely to develop electronic conductivity in S/O-rich|Li-poor environments. The latter corresponds to lower Li chemical potentials, therefore to higher electrochemical potentials (> 4 V vs. Li^+/Li). The cathode-side of the SE might therefore be more problematic for electronic conductivity than the anode-side.

We believe that dopability limits should be favored over the band gap or the Fermi level as it is a more relevant criteria to use if we want to properly evaluate the robustness of solid electrolytes against the generation of electronic conductivity. Computing these dopability limits, relying mostly on GGA with HSE corrected band edges, require reasonable computing power and can be introduced in high-throughput studies on solid electrolytes for ASSLBs [247, 259, 521, 642-645].

5.6 – Acknowledgements

The authors would like to thank Dr. George Bokas for his technical support and Dr. Francesco Ricci for providing the effective masses. Financial support by the *Fonds de la Recherche Scientifique de Belgique* (F.R.S.-FNRS) through a FRIA grant (FC31481), the Natural Sciences and Engineering Research Council of Canada - NSERC through a BESC D grant (BESCD3-534841-2019) and MITACS through a Globalink grant (IT12707 - FR30741) are gratefully acknowledged as well as the *Communauté Française de Belgique* for their support under Grant ARC 18/23-093. The present research benefited from computational resources made available on the Tier-1 supercomputer of the *Fédération Wallonie-Bruxelles*, infrastructure funded by the Walloon Region under the grant agreement no. 1117545. Computational resources have been provided by the supercomputing facilities of the Université catholique de Louvain (CISM/UCL) and the *Consortium des Equipements de Calcul Intensif en Fédération Wallonie Bruxelles* (CECI) funded by the Walloon Region and the F.R.S.-FNRS under convention 2.5020.11.

6. GENERAL CONCLUSION

This last chapter brings together the conclusions drawn from the previous chapters and outlines the challenges encountered in the process of producing the results. In addition, it formulates specific and more general perspective on the work accomplished and forecasts potential directions for further research on the stability in solid electrolytes and energy storage in general.

6.1 – Summary

We outline in this manuscript our investigation on two intrinsic properties of solid electrolytes: the electrochemical stability window and the electronic conductivity. The electrochemical stability windows of most solid electrolytes were initially reported to be large enough to enable the use of lithium metal as the negative electrode and high potential materials as the positive electrode. However, values for these ESWs were very inconsistent in the literature published through the last decade. Several studies specifically decried the frequent overestimation of ESWs and questioned the legitimacy of using cyclic voltammetry and planar cell configurations to establish them. In this context, we worked toward developing a robust methodology to assess the electrochemical stability window of $Li_{1.5}Al_{0.5}Ge_{1.5}(PO_4)_3$, $Li_{1.3}Al_{0.3}Ti_{1.7}(PO_4)_3$ and M-$Li_7La_3Zr_2O_{12}$ (M = Al, Ta and Nb), three very well documented solid electrolytes for their promising ionic conductivity (>10^{-3} S.cm^{-1} at RT). Our methodology, based on the use of inert gold particles to process the three SEs into composites and the use of PITT as the electrochemical characterization technique to stabilize the system, allowed to observe the SEs redox currents that might have been overlooked in previous studies. After processing the composites and running the electrochemical tests, we focused our investigation on the oxidation and reduction reactions. Using an *operando* O_2 sensing probe, we observed the production of dioxygen gas upon LAGP and LATP oxidation, as predicted by our first-principles calculations. The presence of an amorphous phase at the SE-Au interface after cycling was observed through TEM measurements, this amorphous phase was

proven to be insulating via EIS measurements. Using *operando* PXRD and *ex situ* NMR techniques, we were able to evidence the irreversible and non-continuous reduction reaction of Al:LLZO, as initially suggested by the PITT measurements.

The electrochemical stability windows of LAGP, LATP and LLZO assessed in this manuscript are much narrower than the ones reported in the literature, as seen in **Figure 6.1**, illustrating the inconsistency surrounding the ESW of solid electrolytes. Using the experimental setup herein, we attempted to determine the thermodynamic electrochemical stability window of the three materials. It is worth mentioning that the kinetic limitations in the redox reactions of solid electrolytes might extend the electrochemical stability window and make it artificially larger at higher cycling regimes, referred to as the kinetic ESW. Nevertheless, we advocate that fundamental studies like this one constitute a crucial step in the understanding of solid electrolytes and in the development of strategies to implement them in ASSLBs.

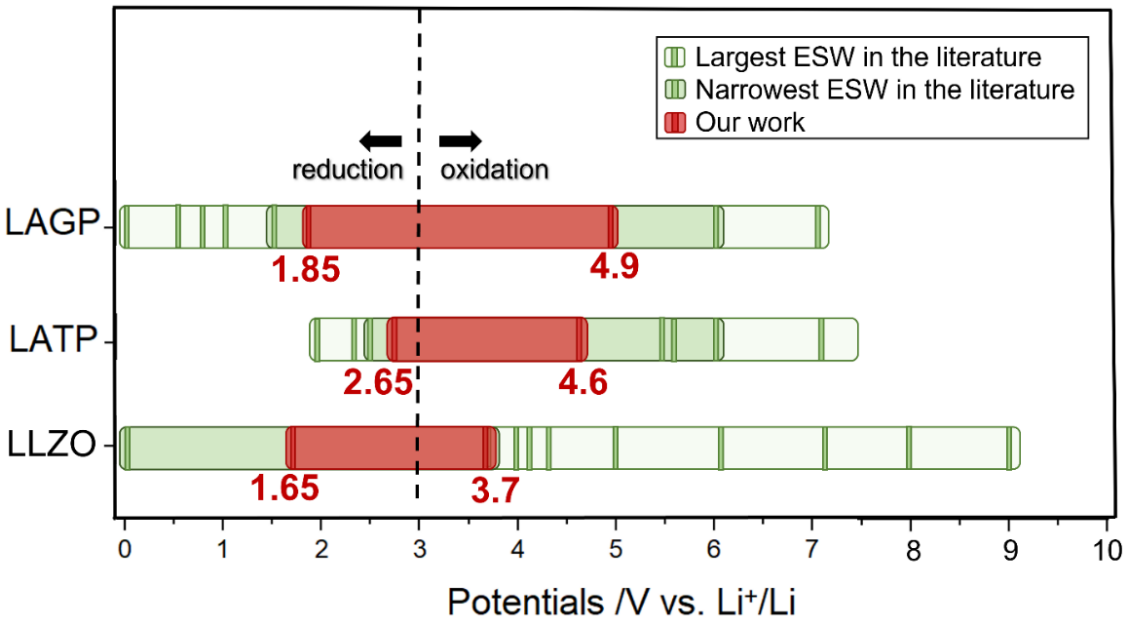

Figure 6.1 - Electrochemical stability windows for LAGP, LATP and LLZO solid electrolytes reported in the literature, including the ones reported in this manuscript.

In the fifth chapter, we used first-principles to investigate the formation of defects in solid electrolytes as a proxy to their electronic conductivity. The electronic conductivity in SEs was assumed to be negligible and stable regardless of the synthesis, handling or cycling conditions. It was not until recently that the stability of solid electrolytes with respect to their own electronic conductivity was questioned. The electronic conductivity in solid electrolytes should be around 10^{-12} S.cm^{-1}. However, this threshold is not achieved for most known solid electrolytes as

illustrated in **Figure 6.2** (with the exception of LIPON). The link between electronic conductivity and the formation of point defects was well established in the field of semi-conductors but was overlooked in solid electrolytes, which were always thought of as immutable insulators. The understanding of these point defects is essential to foreseeing the evolution of electronic conductivity in solid electrolytes. However, the negligible concentration of defects in these materials make their characterization strenuous. In this context, we consider first-principles calculations to be a key element for the fundamental understanding of defect chemistry in solid electrolytes. We used DFT computations to investigate the intrinsic defect chemistry of various SEs, including $LiTi_2(PO)_3$, $LiGe_2(PO)_3$ and LLZO. For each solid electrolyte, we computed the formation energies for the intrinsic defects, their Fermi levels at equilibrium and their dopability limits. Using the concept of dopability limits, we assessed the robustness of these materials to developing electronic conductivity in different environments. Among the solid electrolytes investigated, we reported that undoped $LiTi_2(PO_4)_3$ displays a problematic behavior through the whole range of potentials and will require close monitoring during the synthesis, handling and cycling processes. In contract, Li_3PS_4 displayed great robustness against developing electronic conductivity, regardless of the environment, despite its medium band gap. From our investigation, we conclude that most solid electrolytes are better insulators at lower partial pressures of oxygen (applicable to oxide-based materials) and lower electrochemical potentials.

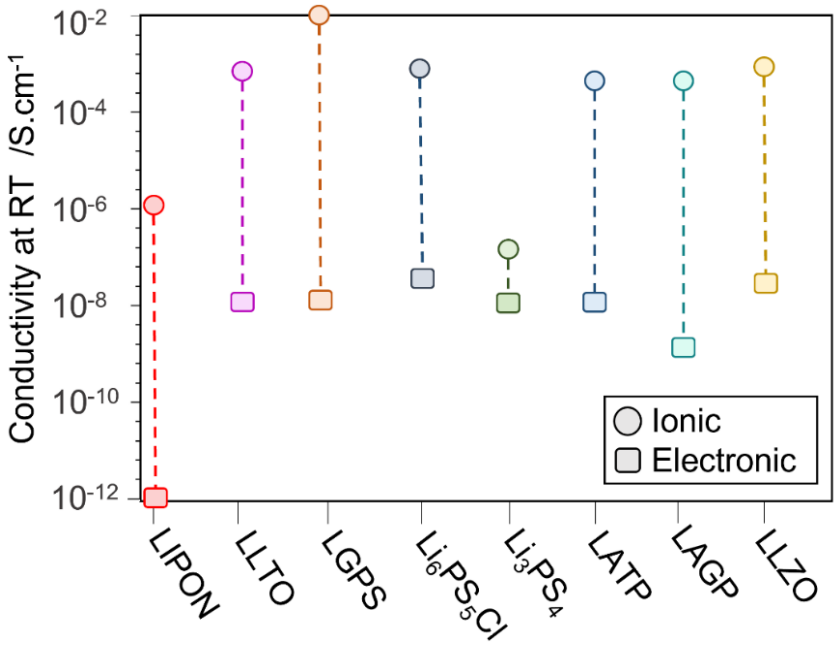

Figure 6.2 - Experimental ionic and highest electronic conductivities reported for LIPON [646], LLTO [647], LGPS [206], Li_6PS_5Cl [648], Li_3PS_4 [649], LATP [650], LAGP [651] and LLZO [633] solid electrolytes in the literature.

6.2 – Challenges

The three studies presented throughout this manuscript shared a load of challenges we thought relevant to address. When assessing the ESW, using gold powder as conductive metal to process LAGP and LATP into composite pellets was crucial to prevent any side reaction or parasitic signals coming from moisture. However, the high price of gold precursors limited the number of samples available. The setup coupling *operando* O_2 sensing and PITT was complex and required a lot of optimization (including the airtightness, the presence of a gas flow, the real-time data acquisition… etc). LLZO's instability with gold compelled us to work with extremely brittle non-sintered pellets. LLZO's instability with respect to moisture and CO_2 required to constantly handle the material under a controlled atmosphere. The operando XRD setup demanded significant optimizing, principally to compensate for the lack of pressure in perforated coin cells. Regarding the computation study of defects in solid electrolytes, several materials of interest were reported with a positive energy above Hull in the Materials Project database (i.e., unstable) despite them existing in a stable or metastable state in real life. Preliminary computations of defects in these materials were deemed not reliable enough, limiting us to the stable materials in the database, justifying why we decided to focus on the six solid electrolytes mentioned above. Furthermore, computing the electron/hole mobility of the selected materials was extremely time-and-CPU expensive, therefore not possible in a reasonable timescale. On the other hand, the lack of documentation made it difficult to come up with an empirical average value of the electron/hole mobility in solid electrolytes. These two limitations prevented us from pushing our investigation further and estimate the electronic conductivities of the selected materials.

6.3 – Perspectives

Regarding our work on the ESW presented in chapters 3 and 4, it would be interesting to further investigate the decomposition or the Li insertion/disinsertion in LAGP, LATP and LLZO upon redox, especially using XPS and DFT. Another perspective, regarding LLZO particularly, would be to investigate the role played by the impurities (such as Li_2CO_3) in the electrochemical behavior of the material. Finally, a significant perspective is to apply the methodology we developed to assess an accurate ESW to all the relevant solid electrolytes reported in the literature. As for the computational study on defects outlined in chapter 5, the possibility of creating phase diagrams from scratch should be considered to study all the solid electrolytes of interest independently. The use of meta-GGA or HSE functionals to compute the band gaps and the formation energies of defects would be of great interest in order to yield more accurate energies.

Including interstitials, combined defect pairs and extrinsic defects in our study would help achieve results that are closer to reality. Finally, computing the electron/hole mobility would allow to estimate the electronic conductivity, considered the missing element of this kind of computational studies.

In larger perspective, this manuscript emphasizes the importance of fundamental studies in science and the relevance of combining theoretical and experimental expertise to better understand fundamental phenomena. In this work, both computational and experimental approaches were used to challenge the idea that solid electrolytes were unequivocally stable, suggesting the need to look for more suitable candidates. Furthermore, the quest for widely stable solid electrolytes might be vain if no high potential positive electrode materials are presently commercialized, thus emphasizing the importance of constantly prospecting for new materials. The rise of machine-, deep- and active-learning models in the field of energy storage can significantly accelerate the discovery and design of novel solid electrolytes and electrode materials. However, the full potential of such tools can only unfold when trained on large and properly annotated databases, which have yet to be built for experimental materials. In this context, the use of computational-based databases becomes ever more apropos in bridging the gap between the predictive power of artificial intelligence and concrete experimental data. Nevertheless, if computational-based databases can be used as a proxy to experimental data, the ultimate step in the search for new materials remains the limiting experimental validation (synthesis, electrochemical testing… etc). Therefore, serious efforts will have to be made, and sufficient resources allocated, into in the construction and proper annotation of experimental databases.

ANNEXES

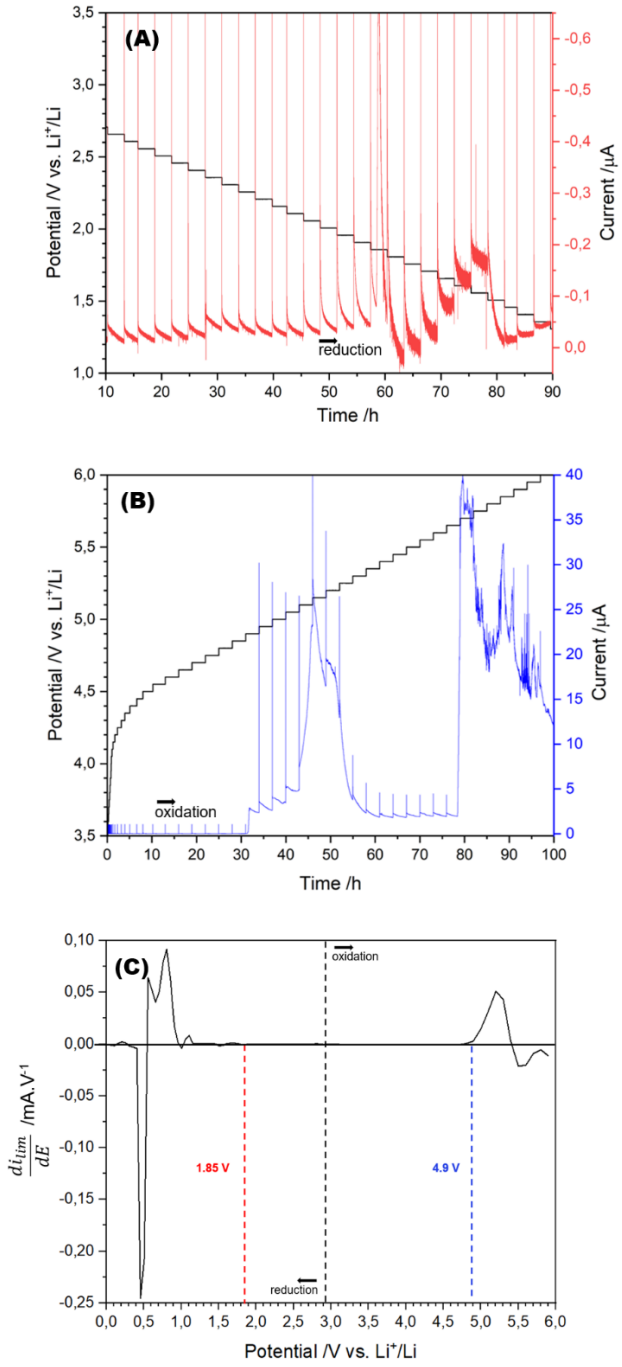

Annex 1 - PITT measurements at 60 °C on a stack LAGP/LAGP-Au for A) reduction and B) oxidation. A potential step of 50 mV, a current limit of 10 nA and a time limit of 3 h were used. C) PITT curves represented as the derivative of the limit current i_{lim} as a function of the potential.

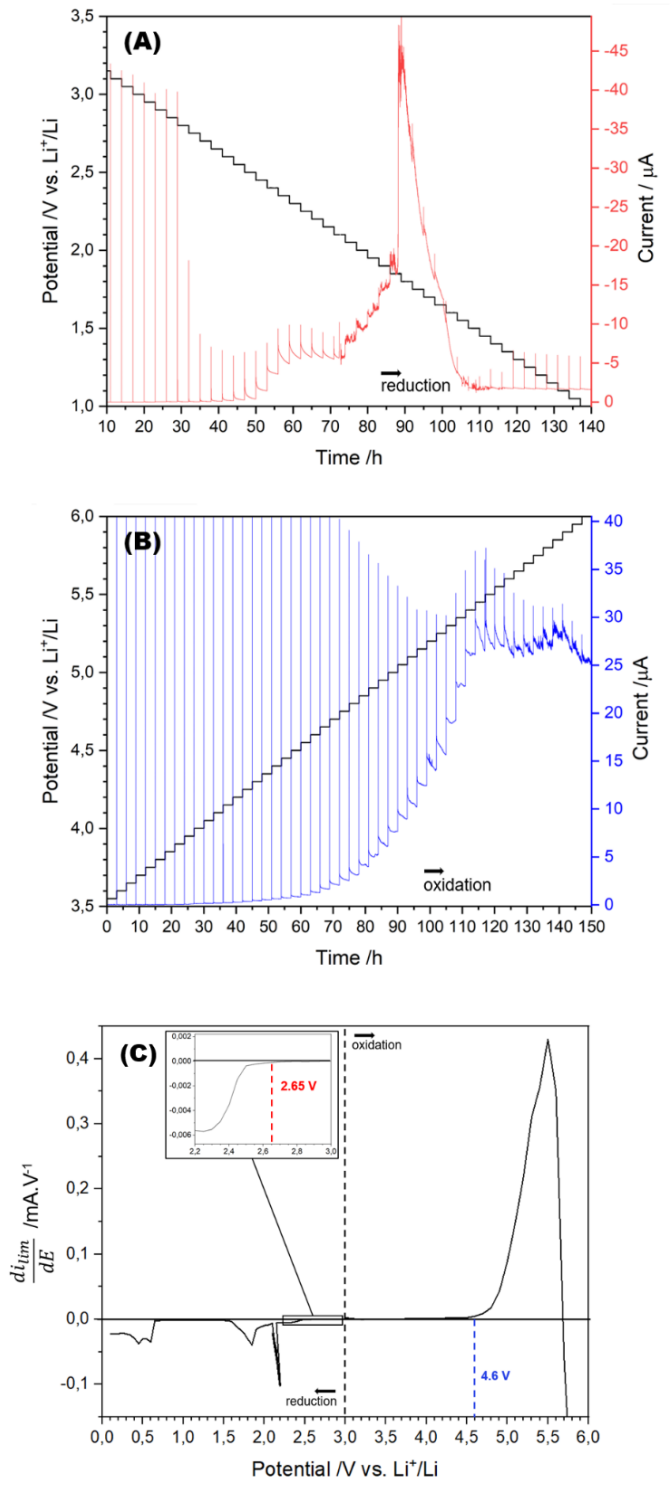

Annex 2 - PITT measurements at 60 °C on a stack LATP/LATP-Au for A) reduction and B) oxidation. A potential step of 50 mV, a current limit of 10 nA and a time limit of 3 h were used. C) PITT curves represented as the derivative of the limit current i_{lim} as a function of the potential.

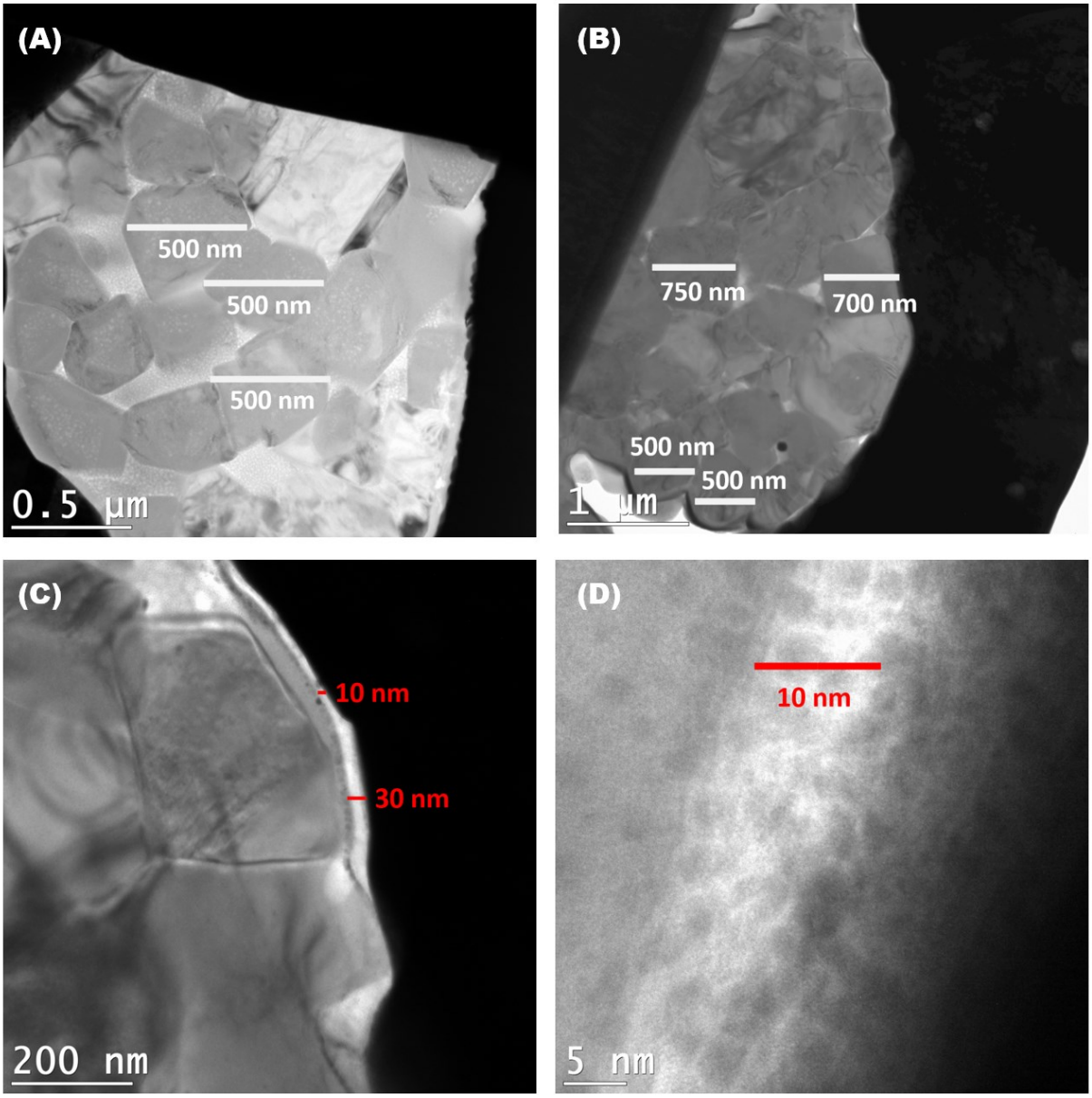

Annex 3 - Bright-field TEM micrographs of LAGP-Au composite samples A) before oxidation observed at x10k and after oxidation observed at B) x5k C) x25k and D) x500k.

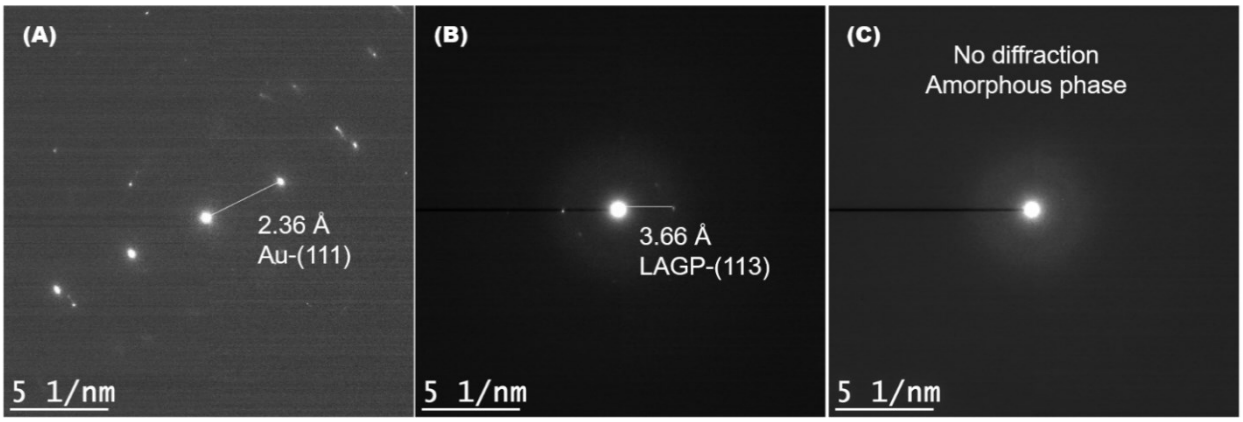

Annex 4 - Selected Area Electron Diffraction (SAED) patterns for A) gold particles, B) LAGP grains and C) the amorphous phase at the LAGP-Au interface.

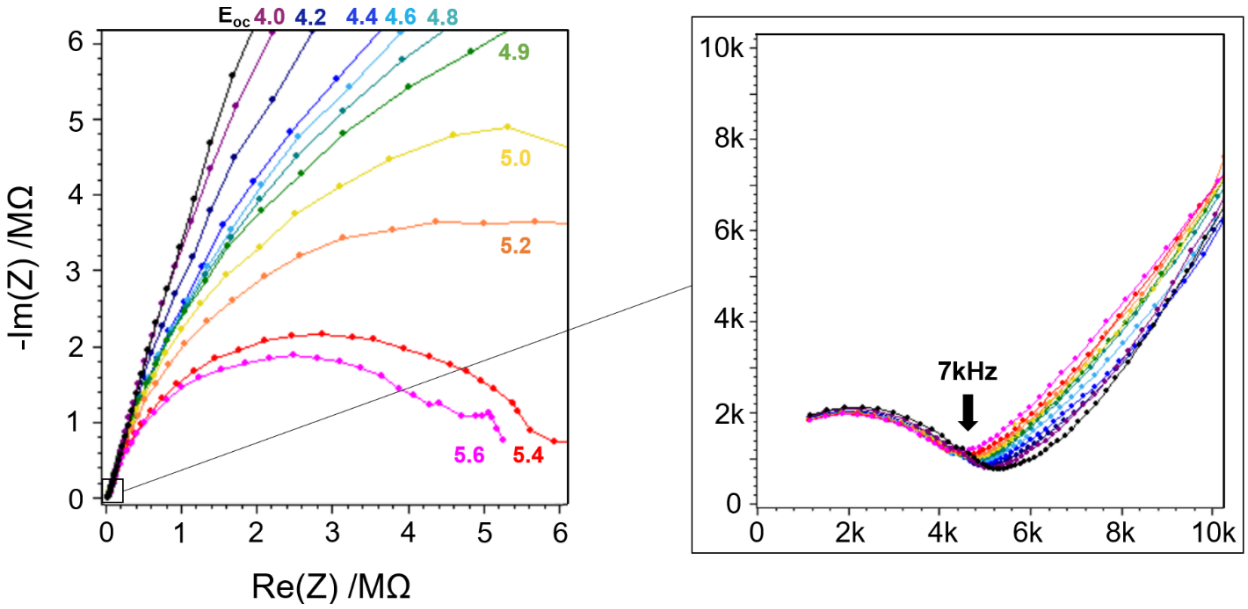

Annex 5 - Electrochemical Impedance Spectroscopy measurements on LAGP observed in the frequency range [200 kHz – 2 mHz] from E_{oc} (3.04 V vs. Li^+/Li) to 5.6 V vs. Li^+/Li.

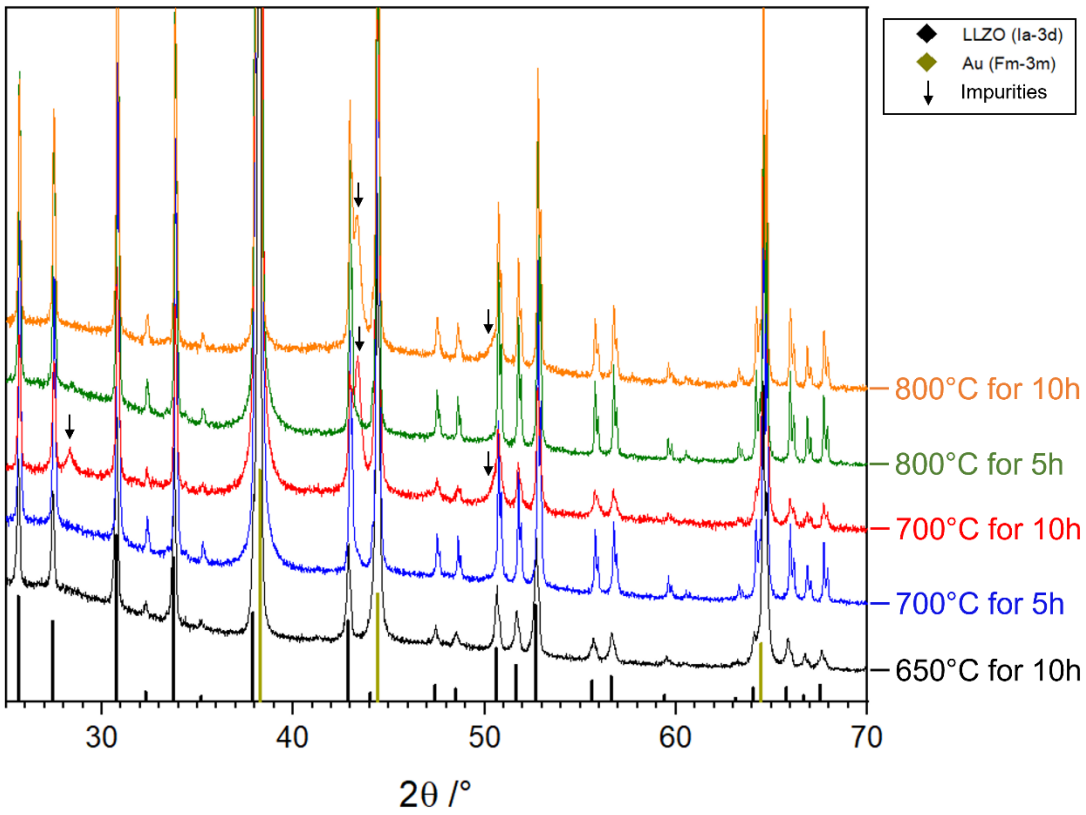

Annex 6 - PXRD diffractograms for Al:LLZO + Au pellets after annealing at different temperatures and periods of time under dry air. The samples were prepared inside an argon-filled glovebox and analyzed under an airtight domed sample holder.

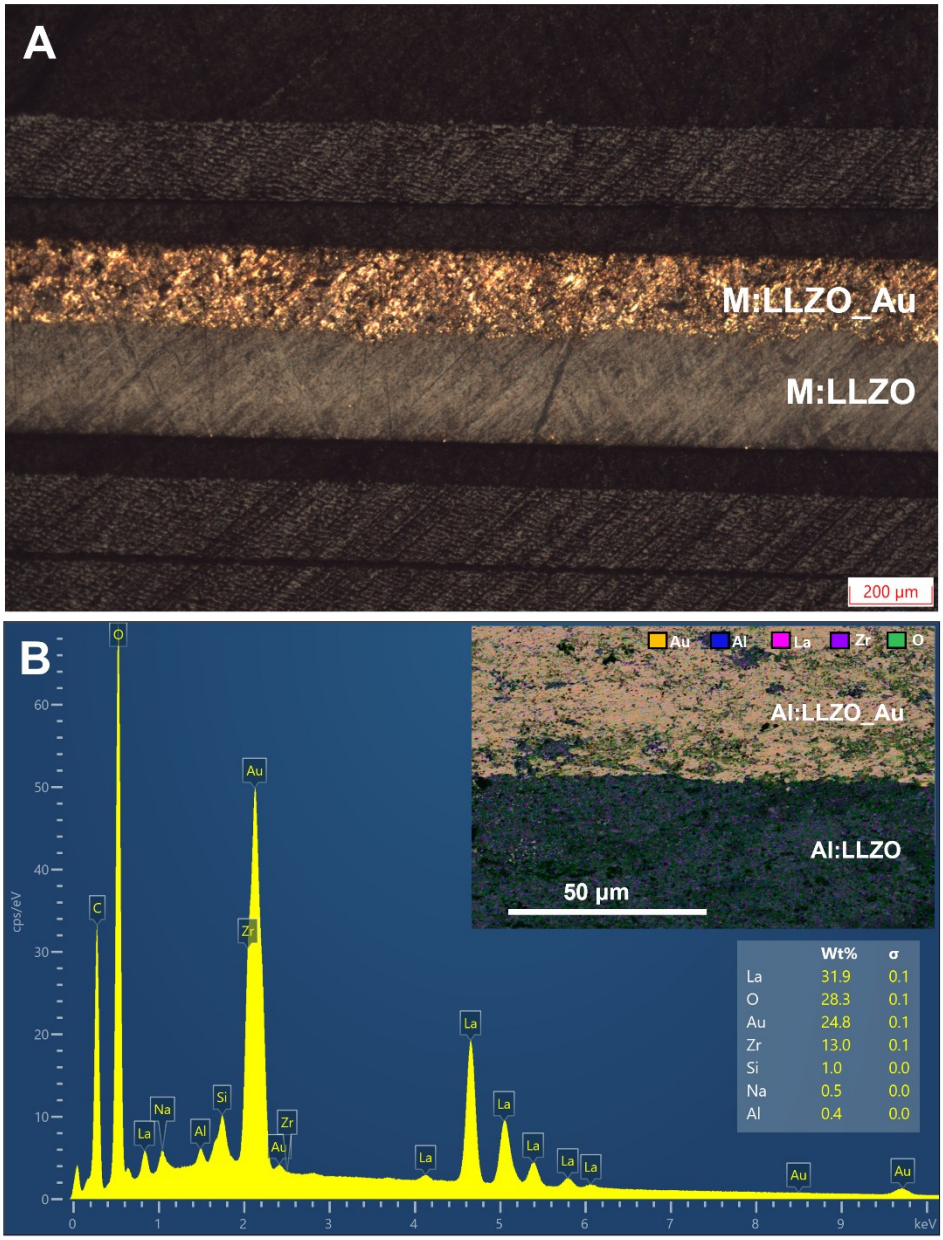

Annex 7 - A) Optical microscope photographs of an M:LLZO-Au/M:LLZO cross sectioned pellet at x5. B) EDS spectrum with the corresponding elemental weight distribution of an Al:LLZO-Au/Al:LLZO stack, SEM micrograph (x1000) and corresponding EDS elemental mapping.

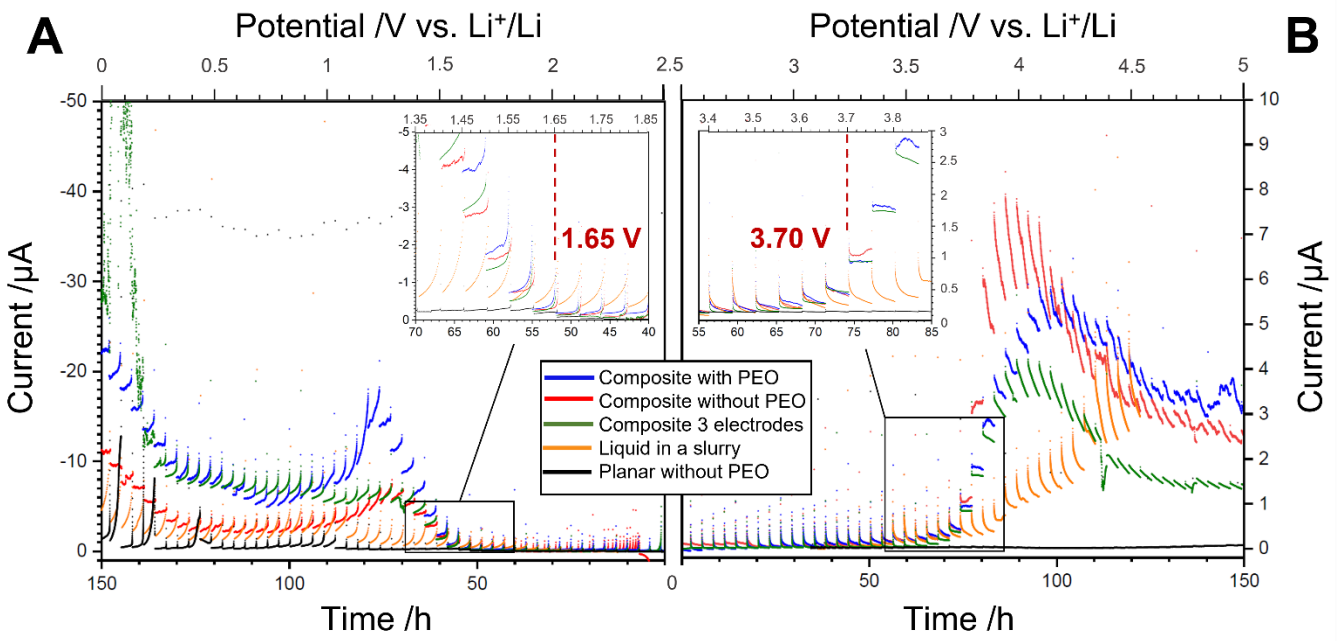

Annex 8 - PITT measurements on M:LLZO+Au (M = Al, Ta, Nb) stack pellets where the current response is plotted as a function of time and potential. The composite cell configurations are plotted in blue with PEO (Li/PEO/LLZO/LLZO+Au), in red without PEO (Li/LLZO/LLZO+Au) and in green with 3 electrodes (Li/PEO/Li_{ref}/PEO/LLZO/LLZO+Au). The liquid electrolyte configuration is plotted in orange (Li/$LiPF_6$+EC+DEC/LLZO+C+ PVDF). The planar configuration is plotted in black (Li/LLZO/Au). The stacks were cycled separately A) from 2.5 V to 0 V vs. Li^+/Li for reduction and B) from 2.5 V up to 4.5 V (liquid) or 6 V vs. Li^+/Li for oxidation. A potential step of 50 mV, a time limit of 3 h and a temperature of 25 °C (liquid) or 80 °C were used to run the experiment. No current limit was applied.

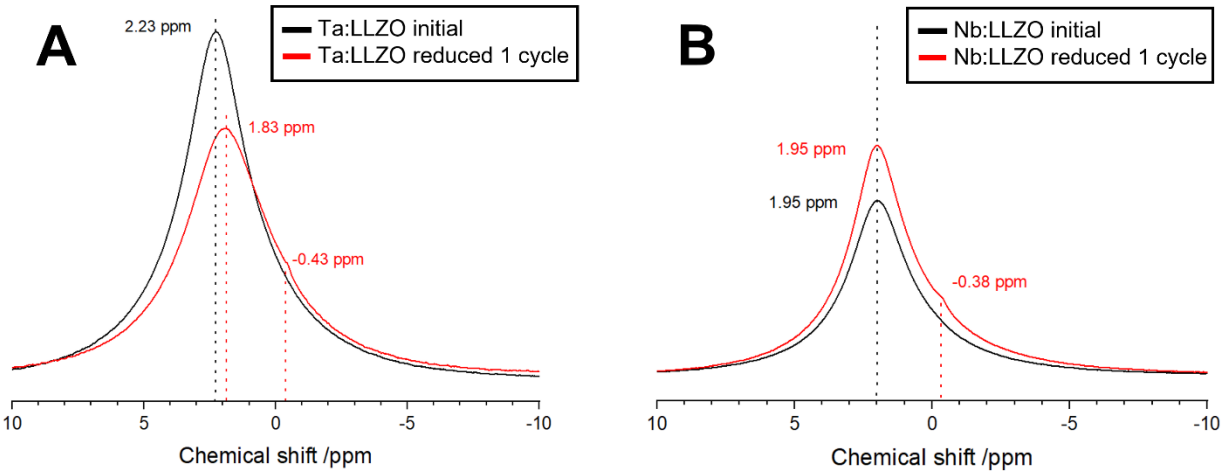

Annex 9 - ^{7}Li MAS NMR spectra recorded at v_{rot} = 10 kHz and a resonance frequency of 600 MHz (14.1 T) for the initial sample (at OCP) and the sample reduced 1 cycle (reduced down to 0 V and back to OCP) for A) Ta:LLZO and B) Nb:LLZO stacks.

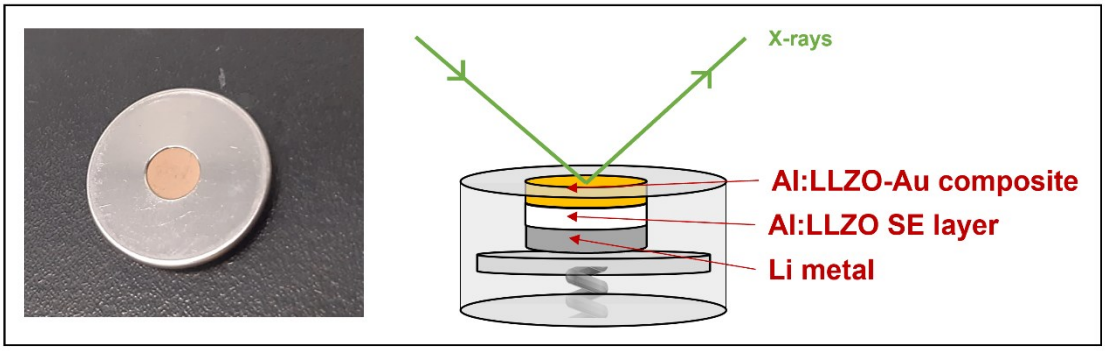

Annex 10 - Photography and schematic representation of the coin cell used in the *operando* PXRD setup.

Approximation of the distance of E_F from the band edges $|E_F - E_{c/v}|$

Electronic conductivity is related to the charge carrier concentration and the mobility [265]:

$$\sigma = e(n\mu_e + p\mu_h)$$

The charge carrier concentrations of electrons and holes *n* and *p* are deduced from this equation using an electronic conductivity of 10^{-12} S.cm^{-1} [95] and an approximate value for the Hall mobility ($\mu_e + \mu_h$). Measured or computed values for the mobility of solid electrolytes are very scarce in the literature but we approximated it to 1 cm^2/(V.s) [652, 653]. Once *n* and *p* are computed, we can deduce (E_C -E_F) and (E_F -E_V) from the following equation 2.33:

$$n = N_C e^{-\frac{(E_C - E_F)}{k_B T}} \quad \text{and} \quad p = N_V e^{-\frac{(E_F - E_V)}{k_B T}}$$

where N_C and N_V are the effective density of states for the conduction and valence bands respectively. E_C and E_V are the energies of the conduction and valence bands respectively. k_B the Boltzmann constant and T the temperature. N_C and N_V are derived from the effective mass *m** following the relations:

$$N_C = 2\left(\frac{2\pi m_e^* k_B T}{h^2}\right)^{3/2} \quad \text{and} \quad N_V = 2\left(\frac{2\pi m_h^* k_B T}{h^2}\right)^{3/2}$$

Where m_e* and m_h* are the effective masses of electron and hole respectively, h is the Planck constant. N_c and N_v were computed for all the selected solid electrolytes and their values oscillated between 10^{18} and 10^{22} cm^{-3}, which brings us to the average value of 10^{20} cm^{-3}, in agreement with the literature [652, 653].

Example: if σ = 10^{-12} S.cm^{-1} and the total mobility is μ = 1 cm^2/(V.s), the charge carrier concentration of electrons is estimated to be the following:

$$n = \frac{\sigma_e}{\mu_e . e} = \frac{10^{-12}\ S/cm}{1\frac{cm^2}{V.s} \times 1.6 \times 10^{-19}\ C} \approx 7 \times 10^7 cm^{-3}$$

From the computed value of N_c (10^{20} cm^{-3}), we can extract the distance between the band edge and Fermi level (E_c-E_F):

$$E_C - E_F = \ln\left(\frac{n}{N_C}\right) \times k_B T = -\ln\left(\frac{7 \times 10^7}{10^{20}}\right) \times 8.62 \times 10^{-5} eV/K \times 300\ K \approx 0.8\ eV$$

$LiTi_2(PO_4)_3$

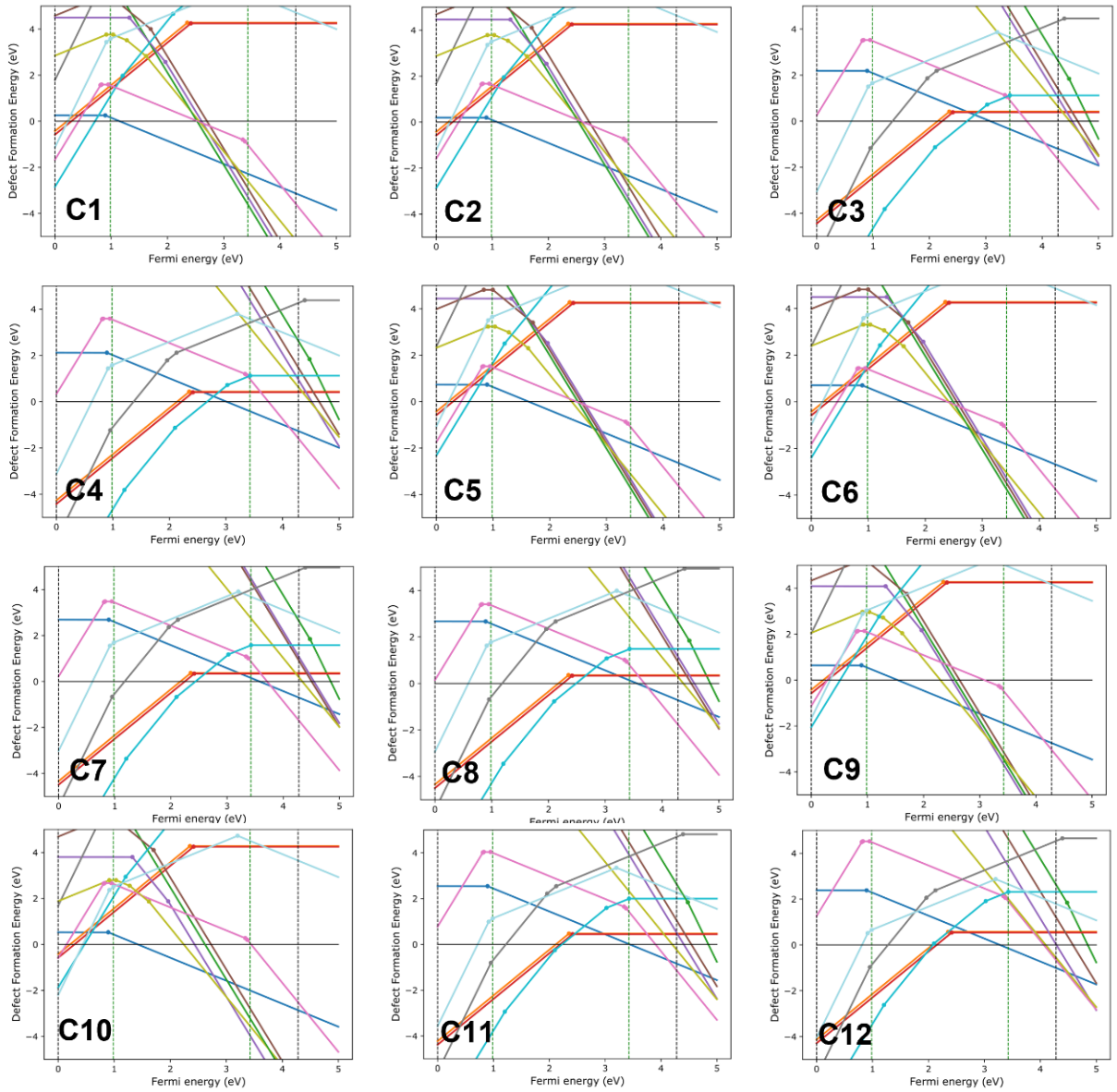
C1
C2
C3
C4
C5
C6
C7
C8
C9
C10
C11
C12
Defect Formation Energy (eV)
Fermi energy (eV)
Vac_{Li}
Vac_O
Vac_P
Vac_O
Vac_{Ti}
Li_P
Ti_P
P_{Li}
Li_{Ti}
Ti_{Li}
P_{Ti}

$LiGe_2(PO_4)_3$

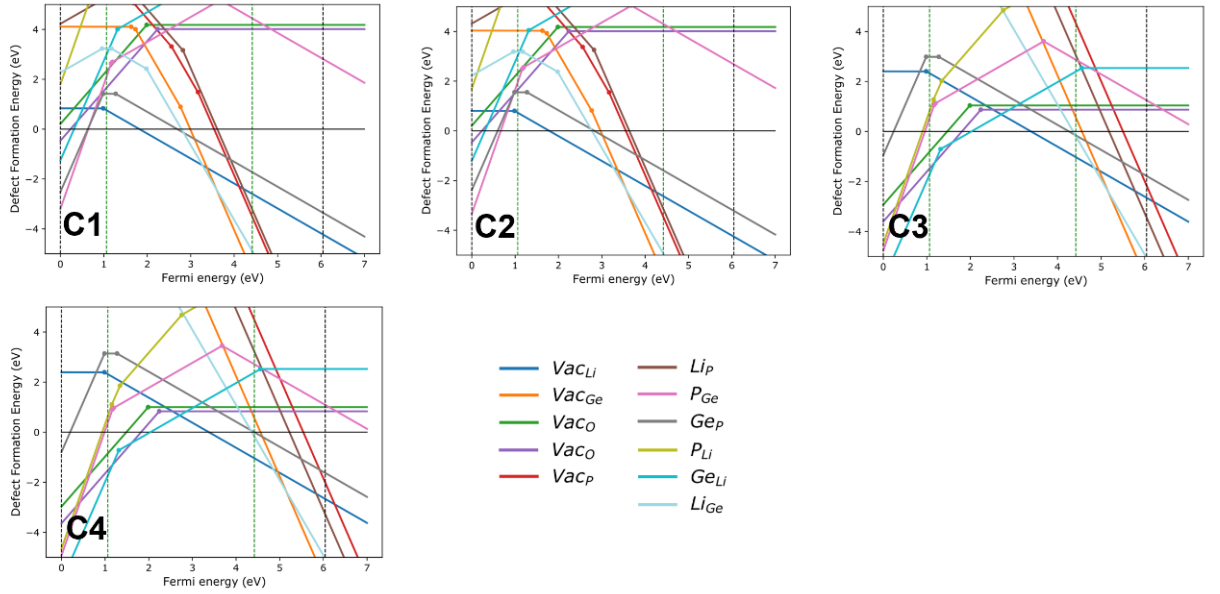

$Li_7La_3Zr_2O_{12}$

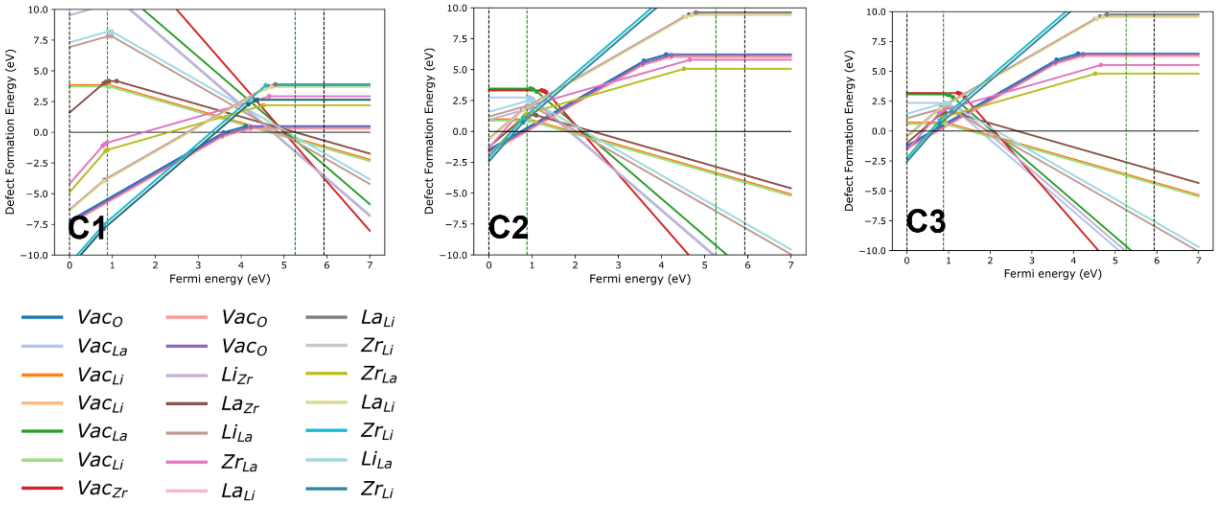

Li_3PO_4

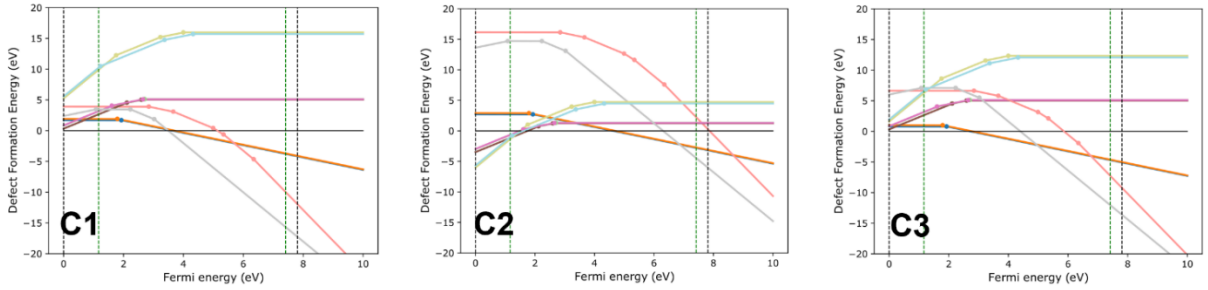

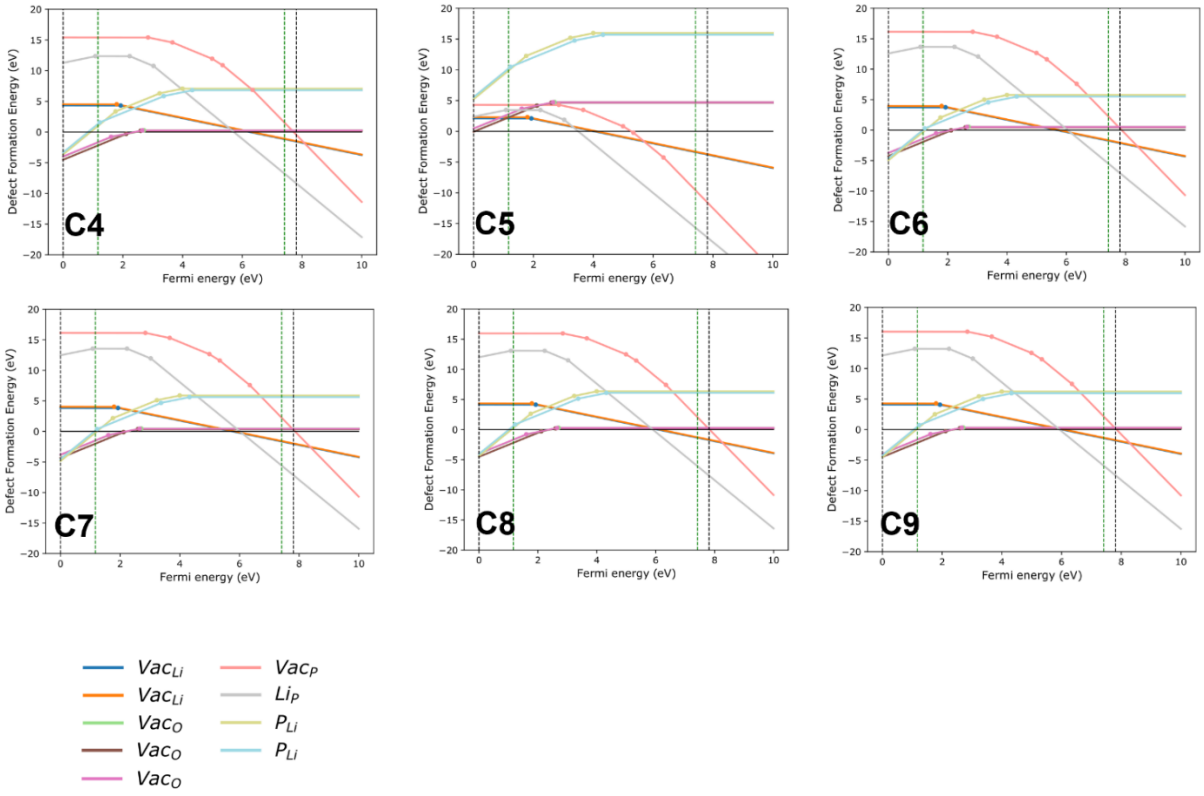
C4
C5
C6
C7
C8
C9
Defect Formation Energy (eV)
Fermi energy (eV)
Vac_{Li}
Vac_{Li}
Vac_O
Vac_O
Vac_O
Vac_P
Li_P
P_{Li}
P_{Li}

$LiPO_3$

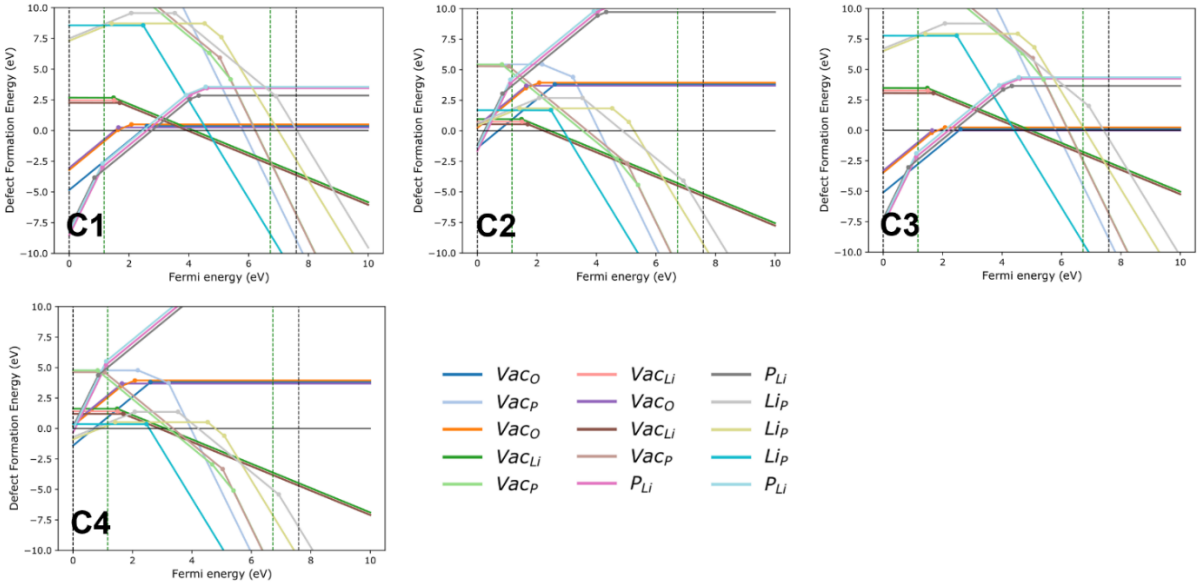
C1
C2
C3
C4
Defect Formation Energy (eV)
Fermi energy (eV)
Vac_O
Vac_P
Vac_O
Vac_{Li}
Vac_P
Vac_{Li}
Vac_O
Vac_{Li}
Vac_P
P_{Li}
P_{Li}
Li_P
Li_P
Li_P
P_{Li}

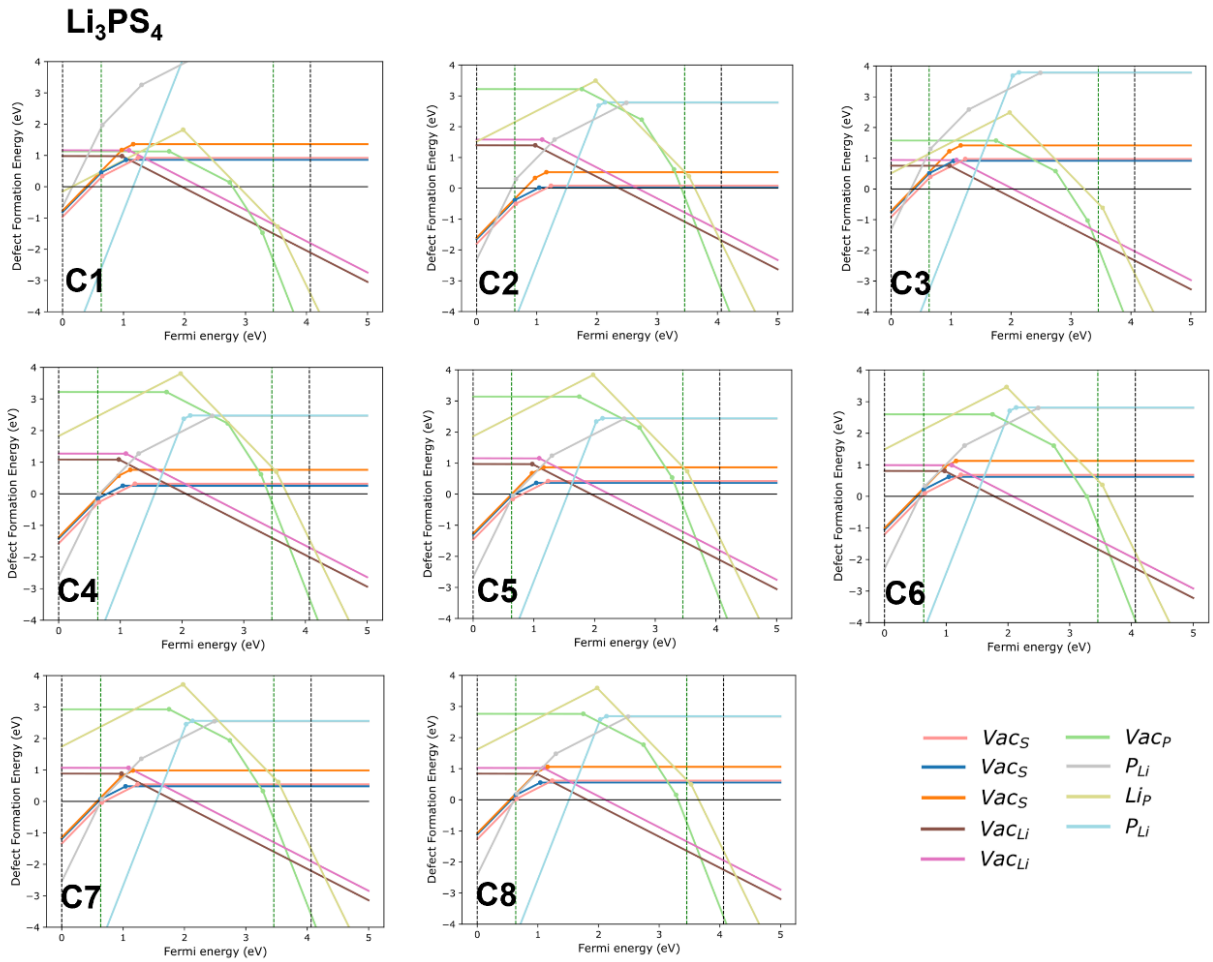

Annex 11 - Formation energy diagrams computed for all chemical limits. The diagrams show all computed defects. The black dashed lines represent valence and conduction bands computed using HSE. The green dashed lines represent initial valence and conduction bands computed using GGA. The red dashed line is the Fermi level at equilibrium. **C1-12** symbols refer to the chemical limits, they can be all found in **Annex 12**.

Annex 12 - Thermodynamically stable chemical limits and corresponding atomic chemical potentials computed for each solid electrolyte.

SE		Chemical Limit	Chemical potentials /eV								S/O	Li	E_F eq /eV	DL_{min} /eV	DL_{max} /eV
$LiTi_2(PO_4)_3$															
	C1	O_2-$Ti_5(PO_5)_4$-TiO_2	Li	-6.51	O	-4.94	P	-15.06	Ti	-18.45	rich	poor	0.81	0.71	1.15
	C2	O_2-$Ti_5(PO_5)_4$-TiP_2O_7	Li	-6.57	O	-4.94	P	-15.01	Ti	-18.49	rich	poor	0.80	0.72	1.09
	C3	P-$Ti_5(PO_5)_4$-TiO_2	Li	-4.58	O	-8.79	P	-5.41	Ti	-10.74	poor	rich	2.81	2.66	3.08
	C4	P-$Ti_5(PO_5)_4$-TiP_2O_7	Li	-4.65	O	-8.78	P	-5.41	Ti	-10.81	poor	rich	2.79	2.66	3.01
	C5	Li_3PO_4-$LiTiPO_5$-O_2	Li	-6.03	O	-4.94	P	-15.18	Ti	-18.51	rich	poor	0.80	0.58	1.63
	C6	$LiTiPO_5$-O_2-TiO_2	Li	-6.06	O	-4.94	P	-15.21	Ti	-18.45	rich	poor	0.81	0.60	1.60
	C7	Li_3PO_4-$LiTiPO_5$-P	Li	-4.08	O	-8.84	P	-5.41	Ti	-10.69	poor	rich	2.82	2.44	3.58
	C8	$LiTiPO_5$-P-TiO_2	Li	-4.10	O	-8.85	P	-5.41	Ti	-10.62	poor	rich	2.85	2.48	3.56
	C9	Li_3PO_4-$Li_4P_2O_7$-O_2	Li	-6.12	O	-4.94	P	-14.92	Ti	-18.86	rich	poor	0.75	0.51	1.54
	C10	$Li_4P_2O_7$-O_2-TiP_2O_7	Li	-6.23	O	-4.94	P	-14.68	Ti	-19.15	rich	poor	0.69	0.47	1.42
	C11	Li_3PO_4-$Li_4P_2O_7$-P	Li	-4.22	O	-8.74	P	-5.41	Ti	-11.25	poor	rich	2.64	2.23	3.44
	C12	$Li_4P_2O_7$-P-TiP_2O_7	Li	-4.38	O	-8.64	P	-5.41	Ti	-11.73	poor	rich	2.54	2.14	3.28
$LiGe_2(PO_4)_3$															
	C1	$Ge_5P_6O_{25}$-GeO_2-$Li_4P_2O_7$-O_2	Li	-6.18	O	-4.94	P	-14.79	Ge	-10.90	rich	poor	0.89	0.64	1.82
	C2	$Ge_5P_6O_{25}$-GeP_2O_7-$Li_4P_2O_7$-O_2	Li	-6.21	O	-4.94	P	-14.72	Ge	-10.98	rich	poor	0.87	0.67	1.79
	C3	Ge-$Ge_5P_6O_{25}$-GeO_2-$Li_4P_2O_7$	Li	-4.61	O	-8.08	P	-6.93	Ge	-4.62	poor	rich	2.71	2.02	3.39
	C4	Ge-$Ge_5P_6O_{25}$-GeP_2O_7-$Li_4P_2O_7$	Li	-4.63	O	-8.11	P	-6.78	Ge	-4.62	poor	rich	2.71	2.03	3.38
$Li_7La_3Zr_2O_{12}$															
	C1	La_2O_3-Li_2O-$Li_6Zr_2O_7$-Zr_3O	Li	-1.96	O	-11.05	La	-5.49	Zr	-8.58	poor	rich	4.29	3.92	4.65
	C2	La_2O_3-Li_2O-Li_2O_2-$Li_6Zr_2O_7$	Li	-4.8	O	-5.323	La	-14.08	Zr	-20.04	rich	poor	1.19	0.88	1.79
	C3	La_2O_3-$La_2Zr_2O_7$-Li_2O_2-$Li_6Zr_2O_7$	Li	-5.1	O	-5.061	La	-14.47	Zr	-20.17	rich	poor	1.01	0.75	1.52
Li_3PO_4															
	C1	Li_2O_2-O_2	Li	-5.20	O	-4.936	P	-17.64			rich	poor	1.78	0.00	3.49
	C2	$Li_4P_2O_7$-P	Li	-4.22	O	-8.74	P	-5.41			poor	rich	3.01	1.74	4.63
	C3	$Li_4P_2O_7$-O_2	Li	-6.12	O	-4.94	P	-14.92			rich	poor	1.32	0.00	2.73
	C4	Li_2O-Li_3P	Li	-2.60	O	-9.77	P	-6.13			poor	rich	4.34	2.41	5.72
	C5	Li_2O-Li_2O_2	Li	-4.8	O	-5.323	P	-17.26			rich	poor	1.97	0.03	3.49
	C6	LiP_7-P	Li	-3.17	O	-9.52	P	-5.41			poor	rich	3.92	2.16	5.67
	C7	Li_3P_7-LiP_7	Li	-3.08	O	-9.59	P	-5.42			poor	rich	4.01	2.23	5.77
	C8	Li_3P-LiP	Li	-2.78	O	-9.77	P	-5.59			poor	rich	4.25	2.41	5.90
	C9	Li_3P_7-LiP	Li	-2.84	O	-9.74	P	-5.52			poor	rich	4.20	2.38	5.93
$LiPO_3$															
	C1	P-P_2O_5	Li	-5.18	O	-8.37	P	-5.41			poor	rich	3.16	2.76	3.95
	C2	O_2-P_2O_5	Li	-6.90	O	-4.936	P	-14.01			rich	poor	1.47	0.70	2.23
	C3	$Li_4P_2O_7$-P	Li	-4.39	O	-8.64	P	-5.41			poor	rich	3.30	2.55	4.45
	C4	$Li_4P_2O_7$-O_2	Li	-6.2	O	-4.936	P	-14.67			rich	poor	1.73	0.90	2.56
Li_3PS_4															
	C1	Li_2S-LiS_4	Li	-4.05	S	-4.53	P	-7.50			rich	poor	1.29	1.16	1.95
	C2	Li_2S-P	Li	-3.63	S	-5.37	P	-5.41			poor	rich	1.76	1.49	2.37
	C3	LiS_4-P_2S_7	Li	-4.27	S	-4.48	P	-7.05			rich	poor	1.37	1.29	1.73
	C4	P-P_4S_3	Li	-3.94	S	-5.14	P	-5.41			poor	rich	1.64	1.55	2.06
	C5	P_4S_3-P_4S_7	Li	-4.05	S	-5.03	P	-5.49			poor	rich	1.63	1.56	1.95
	C6	P_2S_5-P_2S_7	Li	-4.22	S	-4.77	P	-6.03			rich	poor	1.54	1.48	1.78
	C7	P_4S_7-P_4S_9	Li	-4.14	S	-4.91	P	-5.70			poor	rich	1.59	1.54	1.86
	C8	P_2S_5-P_4S_9	Li	-4.19	S	-4.84	P	-5.87			poor	rich	1.57	1.51	1.81

REFERENCES

1. Solutions, C.f.c.a.e., *Global Manmade Greenhouse Gas Emissions by Sector 2013.* World Resources Institute, 2022.
2. *A Brief History of Nuclear Accidents Worldwide*, in *Union of concerned scientists*. 2013.
3. Goodenough, J.B. and Y. Kim, *Challenges for Rechargeable Li Batteries.* Chemistry of Materials, 2010. **22**(3): p. 587-603.
4. Meesala, Y., et al., *Recent Advancements in Li-Ion Conductors for All-Solid-State Li-Ion Batteries.* ACS Energy Letters, 2017. **2**(12): p. 2734-2751.
5. Park, J.-K., *Principles and applications of lithium secondary batteries*. 2012.
6. Schultz, C. *Anti-aging for batteries?* 2022 [cited 2022 20-10].
7. Janek, J. and W.G. Zeier, *A solid future for battery development.* Nature Energy, 2016. **1**(9): p. 16141.
8. Armand, M. and J.M. Tarascon, *Building better batteries.* Nature, 2008. **451**(7179): p. 652-657.
9. Noori, A., et al., *Towards establishing standard performance metrics for batteries, supercapacitors and beyond.* Chemical Society Reviews, 2019. **48**(5): p. 1272-1341.
10. Torabi, F. and P. Ahmadi, *Chapter 1 - Battery technologies*, in *Simulation of Battery Systems*, F. Torabi and P. Ahmadi, Editors. 2020, Academic Press. p. 1-54.
11. Kasemchainan, J., et al., *Critical stripping current leads to dendrite formation on plating in lithium anode solid electrolyte cells.* Nature Materials, 2019. **18**(10): p. 1105-1111.
12. *Lithium battery costs have fallen by 98% in three decades.* The economist, 2021.
13. Laidler, K.J., *The chemical history of a current.* Canadian Journal of Chemistry, 1997. **75**(11): p. 1552-1565.
14. Martins, G.F., *Why the Daniell cell works!* Journal of Chemical Education, 1990. **67**(6): p. 482.
15. Scrosati, B., *History of lithium batteries.* Journal of Solid State Electrochemistry, 2011. **15**(7): p. 1623-1630.
16. Kurzweil, P., *Gaston Planté and his invention of the lead–acid battery—The genesis of the first practical rechargeable battery.* Journal of Power Sources, 2010. **195**(14): p. 4424-4434.
17. Brodd, R.J., *Nickel-Based Battery SystemsNickel-Based Battery Systems*, in *Encyclopedia of Sustainability Science and Technology*, R.A. Meyers, Editor. 2012, Springer New York: New York, NY. p. 6938-6950.
18. Whittingham, M.S., *Chemistry of intercalation compounds: Metal guests in chalcogenide hosts.* Progress in Solid State Chemistry, 1978. **12**(1): p. 41-99.
19. Nishi, Y., *The Dawn of Lithium-Ion Batteries.* Interface magazine, 2016. **25**(3): p. 71-74.
20. Goodenough, J.B. and K.-S. Park, *The Li-Ion Rechargeable Battery: A Perspective.* Journal of the American Chemical Society, 2013. **135**(4): p. 1167-1176.
21. Budde-Meiwes, H., et al., *A review of current automotive battery technology and future prospects.* Proceedings of the Institution of Mechanical Engineers, Part D: Journal of Automobile Engineering, 2013. **227**(5): p. 761-776.
22. Armand, M., *Intercalation electrodes*, in *Materials for advanced batteries*. 1980, Springer. p. 145-161.
23. Solar, R. *Battery Bank*. 2022.

24. https://www.nobelprize.org/prizes/chemistry/2019/summary/, *The Nobel Prize in Chemistry 2019*, in *NobelPrize.org*. 2022, Nobel Prize Outreach AB 2022.
25. Whittingham, M.S., *Electrical Energy Storage and Intercalation Chemistry.* Science, 1976. **192**(4244): p. 1126-1127.
26. Dines, M.B., *Intercalation of Metallocenes in the Layered Transition-Metal Dichalcogenides.* Science, 1975. **188**(4194): p. 1210-1211.
27. Dines, M.B., *Lithium intercalation via n-butyllithium of the layered transition metal dichalcogenides.* Materials Research Bulletin, 1975. **10**(4): p. 287-291.
28. Whittingham, M.S., *The Role of Ternary Phases in Cathode Reactions.* Journal of The Electrochemical Society, 1976. **123**(3): p. 315-320.
29. Murphy, D.W. and P.A. Christian, *Solid State Electrodes for High Energy Batteries.* Science, 1979. **205**(4407): p. 651-656.
30. Whittingham, M.S., *Lithium Batteries and Cathode Materials.* Chemical Reviews, 2004. **104**(10): p. 4271-4302.
31. Delmas, C., et al., *The $Li_xV_2O_5$ system: An overview of the structure modifications induced by the lithium intercalation.* Solid State Ionics, 1994. **69**(3): p. 257-264.
32. Murphy, D.W., et al., *Vanadium Oxide Cathode Materials for Secondary Lithium Cells.* Journal of The Electrochemical Society, 1979. **126**(3): p. 497-499.
33. Mizushima, K., et al., *Li_xCoO_2 (0<x<-1): A new cathode material for batteries of high energy density.* Materials Research Bulletin, 1980. **15**(6): p. 783-789.
34. Madhavi, S., et al., *Effect of aluminium doping on cathodic behaviour of $LiNi_{0.7}Co_{0.3}O_2$.* Journal of Power Sources, 2001. **93**(1): p. 156-162.
35. Eddahech, A., O. Briat, and J.-M. Vinassa, *Performance comparison of four lithium–ion battery technologies under calendar aging.* Energy, 2015. **84**: p. 542-550.
36. Yamazaki, M., *Exclusive: Panasonic aims to boost energy density in Tesla batteries by 20% - executive.* Reuters, 2020.
37. Thackeray, M.M., et al., *Electrochemical extraction of lithium from $LiMn_2O_4$.* Materials Research Bulletin, 1984. **19**(2): p. 179-187.
38. Armstrong, A.R. and P.G. Bruce, *Synthesis of layered $LiMnO_2$ as an electrode for rechargeable lithium batteries.* Nature, 1996. **381**(6582): p. 499-500.
39. Pistoia, G., A. Antonini, and D. Zane, *Synthesis of $LiMnO_2$ and its characterization as a cathode for rechargeable Li cells.* Solid State Ionics, 1995. **78**: p. 115-122.
40. Capitaine, F., P. Gravereau, and C. Delmas, *A new variety of $LiMnO_2$ with a layered structure.* Solid State Ionics, 1996. **89**(3): p. 197-202.
41. Liu, Z., A. Yu, and J.Y. Lee, *Synthesis and characterization of $LiNi_{1-x-y}Co_xMn_yO_2$ as the cathode materials of secondary lithium batteries.* Journal of Power Sources, 1999. **81**: p. 416-419.
42. Ngala, J.K., et al., *The synthesis, characterization and electrochemical behavior of the layered $LiNi_{0.4}Mn_{0.4}Co_{0.2}O_2$ compound.* Journal of Materials Chemistry, 2004. **14**(2): p. 214-220.
43. Padhi, A.K., K.S. Nanjundaswamy, and J.B. Goodenough, *Phospho-olivines as Positive-Electrode Materials for Rechargeable Lithium Batteries.* Journal of The Electrochemical Society, 1997. **144**(4): p. 1188-1194.
44. Ravet, N., et al., *Electroactivity of natural and synthetic triphylite.* Journal of Power Sources, 2001. **97-98**: p. 503-507.

45. Janina, M. and M. Marcin, *Composite Cathode Material for Li-Ion Batteries Based on $LiFePO_4$ System*, in *Metal, Ceramic and Polymeric Composites for Various Uses*, C. John, Editor. 2011, IntechOpen: Rijeka. p. Ch. 30.
46. Julien, C.M. and A. Mauger, *NCA, NCM811, and the Route to Ni-Richer Lithium-Ion Batteries.* Energies, 2020. **13**(23): p. 6363.
47. Julien, C.M., et al., *Comparative Issues of Cathode Materials for Li-Ion Batteries.* Inorganics, 2014. **2**(1): p. 132-154.
48. Tarascon, J.M. and M. Armand, *Issues and challenges facing rechargeable lithium batteries.* Nature, 2001. **414**(6861): p. 359-367.
49. Zhang, Z., et al., *New horizons for inorganic solid state ion conductors.* Energy & Environmental Science, 2018. **11**(8): p. 1945-1976.
50. Gao, M., et al., *Lithium metal batteries for high energy density: Fundamental electrochemistry and challenges.* Journal of Energy Chemistry, 2021. **59**: p. 666-687.
51. Chandrashekar, S., et al., *7Li MRI of Li batteries reveals location of microstructural lithium.* Nat Mater, 2012. **11**(4): p. 311-5.
52. Dresselhaus, M.S. and G. Dresselhaus, *Intercalation compounds of graphite.* Advances in Physics, 2002. **51**(1): p. 1-186.
53. Megahed, S. and B. Scrosati, *Lithium-ion rechargeable batteries.* Journal of Power Sources, 1994. **51**(1): p. 79-104.
54. Huggins, R.A., *Lithium alloy negative electrodes formed from convertible oxides.* Solid State Ionics, 1998. **113-115**: p. 57-67.
55. Feng, K., et al., *Silicon-Based Anodes for Lithium-Ion Batteries: From Fundamentals to Practical Applications.* Small, 2018. **14**(8): p. 1702737.
56. Idota, Y., et al., *Tin-Based Amorphous Oxide: A High-Capacity Lithium-Ion-Storage Material.* Science, 1997. **276**(5317): p. 1395-1397.
57. Ohzuku, T., A. Ueda, and N. Yamamoto, *Zero-Strain Insertion Material of $Li[Li_{1/3}Ti_{5/3}]O_4$ for Rechargeable Lithium Cells.* Journal of The Electrochemical Society, 1995. **142**(5): p. 1431-1435.
58. Garcia, J.C., et al., *Graphite Lithiation under Fast Charging Conditions: Atomistic Modeling Insights.* The Journal of Physical Chemistry C, 2020. **124**(15): p. 8162-8169.
59. Baur, W., *Uber die Verfeinerung der Kristallstrukturbestimmung einiger Vertreter des Rutiltyps: TiO_2, SnO_2, GeO_2 und MgF_2.* Acta Crystallographica, 1956. **9**(6): p. 515-520.
60. Kataoka, K., et al., *Single crystal growth and structure refinement of $Li_4Ti_5O_{12}$.* Journal of Physics and Chemistry of Solids, 2008. **69**(5): p. 1454-1456.
61. Guyomard, D. and J.M. Tarascon, *High voltage stable liquid electrolytes for $Li_{1+x}Mn_2O_4$/carbon rocking-chair lithium batteries.* Journal of Power Sources, 1995. **54**(1): p. 92-98.
62. Hayashi, K., et al., *Mixed solvent electrolyte for high voltage lithium metal secondary cells.* Electrochimica Acta, 1999. **44**: p. 2337-2344.
63. Imhof, R. and P. Novák, *Oxidative Electrolyte Solvent Degradation in Lithium-Ion Batteries: An In Situ Differential Electrochemical Mass Spectrometry Investigation.* Journal of The Electrochemical Society, 1999. **146**(5): p. 1702-1706.
64. Egashira, M., et al., *Measurement of the electrochemical oxidation of organic electrolytes used in lithium batteries by microelectrode.* Journal of Power Sources, 2001. **92**(1): p. 267-271.

65. Zhang, X., et al., *Electrochemical and infrared studies of the reduction of organic carbonates.* Journal of The Electrochemical Society, 2001. **148**(12): p. A1341.
66. Arakawa, M. and J.-I. Yamaki, *The cathodic decomposition of propylene carbonate in lithium batteries.* Journal of Electroanalytical Chemistry and Interfacial Electrochemistry, 1987. **219**(1): p. 273-280.
67. Sloop, S.E., et al., *Chemical Reactivity of PF_5 and $LiPF_6$ in Ethylene Carbonate/Dimethyl Carbonate Solutions.* Electrochemical and Solid-State Letters, 2001. **4**(4): p. A42.
68. Tarascon, J.M., et al., *Performance of Bellcore's plastic rechargeable Li-ion batteries.* Solid State Ionics, 1996. **86-88**: p. 49-54.
69. Koch, V.R., et al., *The Intrinsic Anodic Stability of Several Anions Comprising Solvent-Free Ionic Liquids.* Journal of The Electrochemical Society, 1996. **143**(3): p. 798-803.
70. Sakaebe, H., H. Matsumoto, and K. Tatsumi, *Application of room temperature ionic liquids to Li batteries.* Electrochimica Acta, 2007. **53**(3): p. 1048-1054.
71. Kim, G.T., et al., *Development of ionic liquid-based lithium battery prototypes.* Journal of Power Sources, 2012. **199**: p. 239-246.
72. Fuller, J., R.T. Carlin, and R.A. Osteryoung, *The Room Temperature Ionic Liquid 1-Ethyl-3-methylimidazolium Tetrafluoroborate: Electrochemical Couples and Physical Properties.* Journal of The Electrochemical Society, 1997. **144**(11): p. 3881-3886.
73. Christie, A.M. and C.A. Vincent, *The Li/Li^+ couple in propylene carbonate electrolytes and poly(methyl methacrylate) gels.* Journal of Applied Electrochemistry, 1996. **26**(3): p. 255-267.
74. Imhof, R., *Oxidative Electrolyte Solvent Degradation in Lithium-Ion Batteries: An In Situ Differential Electrochemical Mass Spectrometry Investigation.* Journal of The Electrochemical Society, 1999. **146**(5): p. 1702.
75. Zhang, X., et al., *Electrochemical and Infrared Studies of the Reduction of Organic Carbonates.* Journal of The Electrochemical Society, 2001. **148**: p. A1341-A1345.
76. Gachot, G., et al., *Deciphering the multi-step degradation mechanisms of carbonate-based electrolyte in Li batteries.* Journal of Power Sources, 2008. **178**(1): p. 409-421.
77. Xu, W., et al., *Lithium metal anodes for rechargeable batteries.* Energy & Environmental Science, 2014. **7**(2): p. 513-537.
78. Cheng, X.-B., et al., *A Review of Solid Electrolyte Interphases on Lithium Metal Anode.* Advanced Science, 2016. **3**(3): p. 1500213.
79. Valøen, L.O. and J.N. Reimers, *Transport Properties of $LiPF_6$-Based Li-Ion Battery Electrolytes.* Journal of The Electrochemical Society, 2005. **152**(5): p. A882.
80. Thackeray, M.M., et al., *Lithium insertion into manganese spinels.* Materials Research Bulletin, 1983. **18**(4): p. 461-472.
81. Li, W., *Morphology Effects on the Electrochemical Performance of $LiNi_{1-x}Co_xO_2$.* Journal of The Electrochemical Society, 1997. **144**(8): p. 2773.
82. Yoshio, M., et al., *Preparation and properties of $LiCo_yMn_xNi_{1-x-y}O_2$ as a cathode for lithium ion batteries.* Journal of Power Sources, 2000. **90**(2): p. 176-181.
83. Liu, Z., A. Yu, and J.Y. Lee, *Synthesis and characterization of $LiNi_{1-x-y}Co_xMn_yO_2$ as the cathode materials of secondary lithium batteries.* Journal of Power Sources, 1999. **81-82**: p. 416-419.

84. Gao, Z., et al., *Promises, Challenges, and Recent Progress of Inorganic Solid-State Electrolytes for All-Solid-State Lithium Batteries.* Advanced Materials, 2018. **30**(17): p. 1705702.
85. Bag, S. and V. Thangadurai, *CHAPTER 3 - Electrolyte Development for Solid-state Lithium Batteries*, in *Energy Storage and Conversion Materials*. 2020, The Royal Society of Chemistry. p. 100-135.
86. Zheng, F., et al., *Review on solid electrolytes for all-solid-state lithium-ion batteries.* Journal of Power Sources, 2018. **389**: p. 198-213.
87. Siraj, K., *Past, present and future of superionic conductors.* Int. J. Nano Mater. Sci, 2012. **1**: p. 1-20.
88. Yung-Fang Yu, Y. and J.T. Kummer, *Ion exchange properties of and rates of ionic diffusion in beta-alumina.* Journal of Inorganic and Nuclear Chemistry, 1967. **29**(9): p. 2453-2475.
89. Minkoff, I., *The chemistry of extended defects in non-metallic solids edited by L. Eyring and M. O'Keeffe.* Acta Crystallographica Section B, 1971. **27**(9): p. 1839.
90. Kennedy, J.H., *Comments Regarding Electronic Conductivity in Solid Electrolytes.* Journal of The Electrochemical Society, 1977. **124**(6): p. 865-866.
91. Goodenough, J.B., H.Y.P. Hong, and J.A. Kafalas, *Fast Na^+ ion transport in skeleton structures.* Materials Research Bulletin, 1976. **11**(2): p. 203-220.
92. Lowe, A.T., K.H. Lau, and L. Eyring, *The effect of crystal size on chemical hysteresis in praseodymium and terbium oxides.* Journal of Solid State Chemistry, 1975. **15**(1): p. 9-17.
93. Lucat, C., et al., *Synthese et etude de la conductivite anionique de nouveaux electrolytes $MBiF_4$ (M = K, Rb, Tl).* Materials Research Bulletin, 1977. **12**(2): p. 145-149.
94. Shilton, M.G. and A.T. Howe, *Rapid H^+ conductivity in hydrogen uranyl phosphate-A solid H^+ electrolyte.* Materials Research Bulletin, 1977. **12**(7): p. 701-706.
95. Dudney, N.J., *Glass and Ceramic Electrolytes for Lithium and Lithium-Ion Batteries*, in *Lithium Batteries: Science and Technology*, G.-A. Nazri and G. Pistoia, Editors. 2003, Springer US: Boston, MA. p. 624-642.
96. Lalère, F., et al., *An all-solid state NASICON sodium battery operating at 200 °C.* Journal of Power Sources, 2014. **247**: p. 975.
97. Kitaura, H. and H. Zhou, *All-solid-state lithium-oxygen battery with high safety in wide ambient temperature range.* Scientific Reports, 2015. **5**(1): p. 13271.
98. Dunn, B., H. Kamath, and J.-M. Tarascon, *Electrical Energy Storage for the Grid: A Battery of Choices.* Science, 2011. **334**(6058): p. 928.
99. Albertus, P. et al., *Challenges for and Pathways toward Li-Metal-Based All-Solid-State Batteries.* Sustainability, 2021. **6**(4): p. 1399-1404.
100. Wang, H., et al., *Reviewing the current status and development of polymer electrolytes for solid-state lithium batteries.* Energy Storage Materials, 2020. **33**: p. 188-215.
101. Scrosati, B. and R.J. Neat, *Lithium polymer batteries*, in *Applications of Electroactive Polymers*, B. Scrosati, Editor. 1993, Springer Netherlands: Dordrecht. p. 182-222.
102. Fenton, D.E., J.M. Parker, and P.V. Wright, *Complexes of alkali metal ions with poly(ethylene oxide).* Polymer, 1973. **14**(11): p. 589.
103. Wright, P.V., *Electrical conductivity in ionic complexes of poly(ethylene oxide).* British Polymer Journal, 1975. **7**(5): p. 319-327.

104. Armand, M., *Polymer solid electrolytes - an overview.* Solid State Ionics, 1983. **9-10**: p. 745-754.
105. Patrick Leblanc, F.C., Alain Vallee, Cedric Reboul-Salze *Lithum metal battery*, B.S.C. INC., Editor. 2021.
106. Manuel Stephan, A. and K.S. Nahm, *Review on composite polymer electrolytes for lithium batteries.* Polymer, 2006. **47**(16): p. 5952-5964.
107. Doyle, M., T.F. Fuller, and J. Newman, *The importance of the lithium ion transference number in lithium/polymer cells.* Electrochimica Acta, 1994. **39**(13): p. 2073-2081.
108. Sørensen, P.R. and T. Jacobsen, *Limiting currents in the polymer electrolyte: $PEO_xLiCF_3SO_3$.* Solid State Ionics, 1983. **9-10**: p. 1147-1153.
109. Bouridah, A., et al., *Potentiometric measurements of ionic transport parameters in poly(ethylene oxide)-LiX electrolytes.* Journal of Applied Electrochemistry, 1987. **17**(3): p. 625-634.
110. Xu, K., *Nonaqueous Liquid Electrolytes for Lithium-Based Rechargeable Batteries.* Chemical Reviews, 2004. **104**(10): p. 4303-4418.
111. Watanabe, M., et al., *Polymer electrolytes derived from dendritic polyether macromonomers.* Solid State Ionics, 2002. **148**(3): p. 399-404.
112. Devaux, D., et al., *Optimization of Block Copolymer Electrolytes for Lithium Metal Batteries.* Chemistry of Materials, 2015. **27**(13): p. 4682-4692.
113. An, S.Y., et al., *Effect of additives in PEO/PAA/PMAA composite solid polymer electrolytes on the ionic conductivity and Li ion battery performance.* Journal of Applied Electrochemistry, 2009. **39**(9): p. 1573-1578.
114. Fan, L.-Z., et al., *Succinonitrile as a Versatile Additive for Polymer Electrolytes.* Advanced Functional Materials, 2007. **17**(15): p. 2800-2807.
115. Quartarone, E. and P. Mustarelli, *Electrolytes for solid-state lithium rechargeable batteries: recent advances and perspectives.* Chemical Society Reviews, 2011. **40**(5): p. 2525-2540.
116. Gao, L., et al., *Designing of root-soil-like polyethylene oxide-based composite electrolyte for dendrite-free and long-cycling all-solid-state lithium metal batteries.* Chemical Engineering Journal, 2020. **389**: p. 124478.
117. Zhang, M.Y., et al., *A Sandwich PVDF/HEC/PVDF Gel Polymer Electrolyte for Lithium Ion Battery.* Electrochimica Acta, 2017. **245**: p. 752-759.
118. Rahman, M.Y.A., et al., *Fabrication and characterization of a solid polymeric electrolyte of PAN-TiO_2-$LiClO_4$.* Journal of Applied Polymer Science, 2010. **115**(4): p. 2144-2148.
119. Zhou, D., et al., *In Situ Synthesis of a Hierarchical All-Solid-State Electrolyte Based on Nitrile Materials for High-Performance Lithium-Ion Batteries.* Advanced Energy Materials, 2015. **5**(15): p. 1500353.
120. Zhao, Q., et al., *Solid-state polymer electrolytes with in-built fast interfacial transport for secondary lithium batteries.* Nature Energy, 2019. **4**(5): p. 365-373.
121. Mackanic, D.G., et al., *Crosslinked Poly(tetrahydrofuran) as a Loosely Coordinating Polymer Electrolyte.* Advanced Energy Materials, 2018. **8**(25): p. 1800703.
122. Gray, F.M., *Polymer Electrolytes*. RSC Materials Monographs, ed. J.A. Connor. 1997, Cambridge, UK: Royal Society of Chemistry.

123. Shin, B.R. and Y.S. Jung, *All-Solid-State Rechargeable Lithium Batteries Using $LiTi_2(PS_4)_3$ Cathode with Li_2S-P_2S_5 Solid Electrolyte.* Journal of The Electrochemical Society, 2013. **161**(1): p. A154-A159.
124. Popovic, J., et al., *Polymer-based hybrid battery electrolytes: theoretical insights, recent advances and challenges.* Journal of Materials Chemistry A, 2021. **9**(10): p. 6050-6069.
125. Li, S., et al., *Progress and Perspective of Ceramic/Polymer Composite Solid Electrolytes for Lithium Batteries.* Advanced Science, 2020. **7**(5): p. 1903088.
126. Lim, H.-D., et al., *A review of challenges and issues concerning interfaces for all-solid-state batteries.* Energy Storage Materials, 2020. **25**: p. 224-250.
127. Famprikis, T., et al., *Fundamentals of inorganic solid-state electrolytes for batteries.* Nature Materials, 2019. **18**(12): p. 1278-1291.
128. Thangadurai, V., et al., *Fast Solid-State Li Ion Conducting Garnet-Type Structure Metal Oxides for Energy Storage.* The Journal of Physical Chemistry Letters, 2015. **6**(2): p. 292-299.
129. Xu, X., et al., *Lithium Ion-Conducting Glass–Ceramics of $Li_{1.5}Al_{0.5}Ge_{1.5}(PO_4)_3$–$xLi_2O$ (x=0.0–0.20) with Good Electrical and Electrochemical Properties.* Journal of the American Ceramic Society, 2007. **90**(9): p. 2802-2806.
130. Ohta, S., T. Kobayashi, and T. Asaoka, *High lithium ionic conductivity in the garnet-type oxide $Li_{7-X}La_3(Zr_{2-X}, Nb_X)O_{12}$ (X=0–2).* Journal of Power Sources, 2011. **196**(6): p. 3342-3345.
131. Bohnke, O., *The fast lithium-ion conducting oxides $Li_{3x}La_{2/3-x}TiO_3$ from fundamentals to application.* Solid State Ionics, 2008. **179**(1): p. 9-15.
132. Mariappan, C.R., et al., *Correlation between micro-structural properties and ionic conductivity of $Li_{1.5}Al_{0.5}Ge_{1.5}(PO_4)_3$ ceramics.* Journal of Power Sources, 2011. **196**(15): p. 6456-6464.
133. Mariappan, C.R., et al., *Correlation between micro-structural properties and ionic conductivity of $Li_{1.5}Al_{0.5}Ge_{1.5}(PO_4)_3$ ceramics.* Journal of Power Sources, 2011. **196**(15): p. 6456-6464.
134. Bachman, J.C., et al., *Inorganic Solid-State Electrolytes for Lithium Batteries: Mechanisms and Properties Governing Ion Conduction.* Chemical Reviews, 2016. **116**(1): p. 140-162.
135. Francisco, B.E., C.R. Stoldt, and J.-C. M'Peko, *Lithium-Ion Trapping from Local Structural Distortions in Sodium Super Ionic Conductor (NASICON) Electrolytes.* Chemistry of Materials, 2014. **26**(16): p. 4741-4749.
136. Subramanian, M.A., R. Subramanian, and A. Clearfield, *Lithium ion conductors in the system $AB(IV)_2(PO_4)_3$ (B = Ti, Zr and Hf).* Solid State Ionics, 1986: p. 562-569.
137. Aono, H., et al., *Ionic Conductivity of the Lithium Titanium Phosphate $(Li_{1+X}M_XTi_{2-X}(PO_4)_3$, M = Al, Sc, Y and La) Systems.* Journal of The Electrochemical Society, 1989. **136**(2): p. 590.
138. Li, S.-c., J.-y. Cai, and Z.-x. Lin, *Phase relationships and electrical conductivity of $Li_{1+x}Ge_{2-x}Al_xP_3O_{12}$ and $Li_{1+x}Ge_{2-x}Cr_xP_3O_{12}$ systems.* Solid State Ionics, 1988. **28-30**: p. 1265-1270.
139. Hou, M., et al., *Challenges and perspectives of NASICON-type solid electrolytes for all-solid-state lithium batteries.* Nanotechnology, 2020. **31**(13): p. 132003.
140. Hupfer, T., et al., *Evolution of microstructure and its relation to ionic conductivity in $Li_{1+x}Al_xTi_{2-x}(PO_4)_3$.* Solid State Ionics, 2016. **288**: p. 235-239.
141. Thokchom, J.S. and B. Kumar, *Composite effect in superionically conducting lithium aluminium germanium phosphate based glass-ceramic.* Journal of Power Sources, 2008. **185**(1): p. 480-485.

142. Imanishi, N., et al., *Lithium anode for lithium-air secondary batteries.* Journal of Power Sources, 2008. **185**(2): p. 1392-1397.
143. Hasegawa, S., et al., *Study on lithium/air secondary batteries - Stability of NASICON-type lithium ion conducting glass–ceramics with water.* Journal of Power Sources, 2009. **189**(1): p. 371-377.
144. Xiao, W., et al., *Recent advances in $Li_{1+x}Al_xTi_{2-x}(PO_4)_3$ solid-state electrolyte for safe lithium batteries.* Energy Storage Materials, 2019. **19**: p. 379-400.
145. Hiromichi, A., et al., *Ionic Conductivity of $LiTi_2(PO_4)_3$ Mixed with Lithium Salts.* Chemistry Letters, 1990. **19**(3): p. 331-334.
146. Chen, R., et al., *The pursuit of solid-state electrolytes for lithium batteries: from comprehensive insight to emerging horizons.* Materials Horizons, 2016. **3**(6): p. 487-516.
147. Feng, J.K., L. Lu, and M.O. Lai, *Lithium storage capability of lithium ion conductor $Li_{1.5}Al_{0.5}Ge_{1.5}(PO_4)_3$.* Journal of Alloys and Compounds, 2010. **501**(2) : 255-258.
148. Zhang, Z., et al., *An advanced construction strategy of all-solid-state lithium batteries with excellent interfacial compatibility and ultralong cycle life.* Journal of Materials Chemistry A, 2017. **5**(32): p. 16984-16993.
149. Kotobuki, M., K. Hoshina, and K. Kanamura, *Electrochemical properties of thin TiO_2 electrode on $Li_{1+x}Al_xGe_{2-x}(PO_4)_3$ solid electrolyte.* Solid State Ionics, 2011. **198**(1): p. 22-25.
150. Chen, R., et al., *The Thermal Stability of Lithium Solid Electrolytes with Metallic Lithium.* Joule, 2020. **4**(4): p. 812-821.
151. Illbeigi, M., et al., *Effect of simultaneous addition of aluminum and chromium on the lithium ionic conductivity of $LiGe_2(PO_4)_3$ NASICON-type glass–ceramics.* Solid State Ionics, 2016. **289**: p. 180-187.
152. Cussen, E.J., *Structure and ionic conductivity in lithium garnets.* Journal of Materials Chemistry, 2010. **20**(25): p. 5167-5173.
153. Thangadurai, V., H. Kaack, and W.J.F. Weppner, *Novel Fast Lithium Ion Conduction in Garnet-Type $Li_5La_3M_2O_{12}$ (M = Nb, Ta).* Journal of the American Ceramic Society, 2003. **86**(3): p. 437-440.
154. Murugan, R., V. Thangadurai, and W. Weppner, *Lattice Parameter and Sintering Temperature Dependence of Bulk and Grain-Boundary Conduction of Garnet-like Solid Li-Electrolytes.* Journal of The Electrochemical Society, 2008. **155**(1): p. A90.
155. Awaka, J., et al., *Synthesis and crystallographic studies of garnet-related lithium-ion conductors $Li_6CaLa_2Ta_2O_{12}$ and $Li_6BaLa_2Ta_2O_{12}$.* Solid State Ionics, 2009. **180**(6): p. 602-606.
156. Goodenough, J., et al., *$Li_6La_3SnMO_{12}$ (M = Sb, Nb, Ta), a Family of Lithium Garnets with High Li-Ion Conductivity.* Journal of the Electrochemical Society, 2012. **159**.
157. Percival, J., et al., *Cation ordering in Li containing garnets: synthesis and structural characterisation of the tetragonal system, $Li_7La_3Sn_2O_{12}$.* Dalton Transactions, 2009(26): p. 5177-5181.
158. Wang, W.G., et al., *Lithium-ionic diffusion and electrical conduction in the $Li_7La_3Ta_2O_{13}$ compounds.* Solid State Ionics, 2009. **180**(23): p. 1252-1256.
159. Murugan, R., V. Thangadurai, and W. Weppner, *Fast lithium ion conduction in garnet-type $Li_7La_3Zr_2O_{12}$.* Angewandte Chemie (International ed. in English), 2007. **46**(41): p. 7778-7781.
160. Awaka, J., et al., *Synthesis and structure analysis of tetragonal $Li_7La_3Zr_2O_{12}$ with the garnet-related type structure.* Journal of Solid State Chemistry, 2009. **182**(8): p. 2046-2052.

161. Thangadurai, V. and W. Weppner, *$Li_6ALa_2Nb_2O_{12}$ (A=Ca, Sr, Ba): A New Class of Fast Lithium Ion Conductors with Garnet-Like Structure.* Journal of the American Ceramic Society, 2005. **88**(2): p. 411-418.
162. Thangadurai, V., S. Narayanan, and D. Pinzaru, *Garnet-type solid-state fast Li ion conductors for Li batteries: critical review.* Chemical Society Reviews, 2014. **43**(13): p. 4714-4727.
163. O'Callaghan, M.P., et al., *Switching on Fast Lithium Ion Conductivity in Garnets: The Structure and Transport Properties of $Li_{3+x}Nd_3Te_{2-x}Sb_xO_{12}$.* Chemistry of Materials, 2008. **20**(6): p. 2360-2369.
164. Cussen, E.J., et al., *A comparison of the transport properties of lithium-stuffed garnets and the conventional phases $Li_3Ln_3Te_2O_{12}$.* Journal of Solid State Chemistry, 2011. **184**(2): p. 470-475.
165. Geiger, C.A., et al., *Crystal Chemistry and Stability of $Li_7La_3Zr_2O_{12}$ Garnet: A Fast Lithium-Ion Conductor.* Inorganic Chemistry, 2011. **50**(3): p. 1089-1097.
166. Kotobuki, M., et al., *Fabrication of all-solid-state lithium battery with lithium metal anode using Al_2O_3-added $Li_7La_3Zr_2O_{12}$ solid electrolyte.* Journal of Power Sources, 2011. **196**(18): p. 7750-7754.
167. Li, Y., et al., *Optimizing Li+ conductivity in a garnet framework.* Journal of Materials Chemistry, 2012. **22**(30): p. 15357-15361.
168. Deviannapoorani, C., et al., *Lithium ion transport properties of high conductive tellurium substituted $Li_7La_3Zr_2O_{12}$ cubic lithium garnets.* Journal of Power Sources, 2013. **240**: p. 18-25.
169. Kotobuki, M. and K. Kanamura, *Fabrication of all-solid-state battery using $Li_5La_3Ta_2O_{12}$ ceramic electrolyte.* Ceramics International, 2013. **39**(6): p. 6481-6487.
170. Kim, S., et al., *High-energy and durable lithium metal batteries using garnet-type solid electrolytes with tailored lithium-metal compatibility.* Nature Communications, 2022. **13**(1): p. 1883.
171. Krauskopf, T., et al., *Lithium-Metal Growth Kinetics on LLZO Garnet-Type Solid Electrolytes.* Joule, 2019. **3**(8): p. 2030-2049.
172. Gao, B., R. Jalem, and Y. Tateyama, *Surface-Dependent Stability of the Interface between Garnet $Li_7La_3Zr_2O_{12}$ and the Li Metal in the All-Solid-State Battery from First-Principles Calculations.* ACS Applied Materials & Interfaces, 2020. **12**(14): p. 16350-16358.
173. Zhu, Y., et al., *Dopant-Dependent Stability of Garnet Solid Electrolyte Interfaces with Lithium Metal.* Advanced Energy Materials, 2019. **9**(12): p. 1803440.
174. Liu, W., et al., *LLZO@EmimFSI@PEO derived hybrid solid electrolyte for high-energy lithium metal batteries.* Materials Technology, 2020: p. 1-7.
175. Han, F., et al., *Electrochemical Stability of $Li_{10}GeP_2S_{12}$ and $Li_7La_3Zr_2O_{12}$ Solid Electrolytes.* Advanced Energy Materials, 2016. **6**(8): p. 1501590.
176. Familoni, O., Y. Zhou, and H. Duan, *Air Stability of LLZO Electrolytes*, in *Solid Electrolytes for Advanced Applications: Garnets and Competitors*, R. Murugan and W. Weppner, Editors. 2019, Springer International Publishing: Cham. p. 69-89.
177. Takahashi, T. and H. Iwahara, *Ionic conduction in perovskite-type oxide solid solution and its application to the solid electrolyte fuel cell.* Energy Conversion, 1971. **11**(3): p. 105-111.
178. Bohnke, O., J. Emery, and J.-L. Fourquet, *Anomalies in Li^+ ion dynamics observed by impedance spectroscopy and ^7Li NMR in the perovskite fast ion conductor ($Li_{3x}La_{2/3-x}\square_{1/3-2x})TiO_3$.* Solid State Ionics, 2003. **158**(1-2): p. 119-132.

179. Emery, J., et al., *Lithium-7 NMR and ionic conductivity studies of lanthanum lithium titanate electrolytes.* Solid State Ionics, 1997. **99**(1-2): p. 41-51.
180. Itoh, M., et al., *High lithium ion conductivity in the perovskite-type compounds $Ln_{12}Li_{12}TiO_3$ (Ln=La,Pr,Nd,Sm).* Solid State Ionics, 1994. **70-71**: p. 203-207.
181. Stramare, S., V. Thangadurai, and W. Weppner, *Lithium Lanthanum Titanates: A Review.* Chemistry of Materials, 2003. **15**(21): p. 3974-3990.
182. Inaguma, Y., et al., *High ionic conductivity in lithium lanthanum titanate.* Solid State Communications, 1993. **86**(10): p. 689-693.
183. Chen, C. and K. Amine, *Ionic conductivity, lithium insertion and extraction of lanthanum lithium titanate.* Solid State Ionics, 2001. **144**(1-2): p. 51-57.
184. Lu, J. and Y. Li, *Perovskite-type Li-ion solid electrolytes: a review.* Journal of Materials Science: Materials in Electronics, 2021. **32**(8): p. 9736-9754.
185. Bohnke, O., C. Bohnke, and J.L. Fourquet, *Mechanism of ionic conduction and electrochemical intercalation of lithium into the perovskite lanthanum lithium titanate.* Solid State Ionics, 1996. **91**(1): p. 21-31.
186. Chen, C.H. and K. Amine, *Ionic conductivity, lithium insertion and extraction of lanthanum lithium titanate.* Solid State Ionics, 2001. **144**(1): p. 51-57.
187. Deng, Z., B. Radhakrishnan, and S.P. Ong, *Rational Composition Optimization of the Lithium-Rich $Li_3OCl_{1-x}Br_x$ Anti-Perovskite Superionic Conductors.* Chemistry of Materials, 2015. **27**(10): p. 3749-3755.
188. Chen, B., C. Xu, and J. Zhou, *Insights into Grain Boundary in Lithium-Rich Anti-Perovskite as Solid Electrolytes.* Journal of The Electrochemical Society, 2018. **165**(16): p. A3946-A3951.
189. Zhao, Y., *Crystal Chemistry and Phase Transitions of Perovskite inP–T–XSpace: Data for $(K_xNa_{1-x})MgF_3$ Perovskites.* Journal of Solid State Chemistry, 1998. **141**(1): p. 121-132.
190. Zhao, Y. and L.L. Daemen, *Superionic Conductivity in Lithium-Rich Anti-Perovskites.* Journal of the American Chemical Society, 2012. **134**(36): p. 15042-15047.
191. Lü, X., et al., *Li-rich anti-perovskite Li_3OCl films with enhanced ionic conductivity.* Chemical Communications, 2014. **50**(78): p. 11520-11522.
192. Manthiram, A., X. Yu, and S. Wang, *Lithium battery chemistries enabled by solid-state electrolytes.* Nature Reviews Materials, 2017. **2**(4): p. 16103.
193. Kartini, E., et al., *Recent studies on lithium solid electrolytes $(LiI)_x(LiPO3)_{1-x}$ for secondary battery.* Journal of the Physical Society of Japan, 2010. **79**(Suppl. A): p. 54-58.
194. Senevirathne, K., et al., *A new crystalline LiPON electrolyte: Synthesis, properties, and electronic structure.* Solid State Ionics, 2013. **233**: p. 95-101.
195. Bates, J.B., et al., *Fabrication and characterization of amorphous lithium electrolyte thin films and rechargeable thin-film batteries.* Journal of Power Sources, 1993. **43**(1): p. 103-110.
196. Wang, B., et al., *Ionic conductivities and structure of lithium phosphorus oxynitride glasses.* Journal of Non-Crystalline Solids, 1995. **183**(3): p. 297-306.
197. Fleutot, B., et al., *Investigation of the local structure of LiPON thin films to better understand the role of nitrogen on their performance.* Solid State Ionics, 2011. **186**(1): p. 29-36.
198. Yu, X., *A Stable Thin-Film Lithium Electrolyte: Lithium Phosphorus Oxynitride.* Journal of The Electrochemical Society, 1997. **144**(2): p. 524.
199. Bates, J.B., et al., *Electrical properties of amorphous lithium electrolyte thin films.* Solid State Ionics, 1992. **53-56**: p. 647-654.

200. Redhammer, G.J., et al., *A single crystal X-ray and powder neutron diffraction study on NASICON-type $Li_{1+x}Al_xTi_{2-x}(PO_4)_3$ (0 ≤ x ≤ 0.5) crystals: Implications on ionic conductivity.* Solid State Sciences, 2016. **60**: p. 99-107.
201. Redhammer, G.J., G. Tippelt, and D. Rettenwander, *Deep hydration of an $Li_{7-3x}La_3Zr_2M_xO_{12}$ solid-state electrolyte material: a case study on Al- and Ga-stabilized LLZO.* Acta Crystallographica Section C, 2022. **78**(1): p. 1-6.
202. Lacivita, V., et al., *Resolving the Amorphous Structure of Lithium Phosphorus Oxynitride (LIPON).* Journal of the American Chemical Society, 2018. **140**(35): p. 11029-11038.
203. Kanno, R., et al., *Synthesis of a new lithium ionic conductor, thio-LISICON–lithium germanium sulfide system.* Solid State Ionics, 2000. **130**(1): p. 97-104.
204. Kanno, R. and M. Murayama, *Lithium Ionic Conductor Thio-LISICON: The Li_2S-GeS_2-P_2S_5 System.* Journal of The Electrochemical Society, 2001. **148**(7): p. A742.
205. Lau, J., et al., *Sulfide Solid Electrolytes for Lithium Battery Applications.* Advanced Energy Materials, 2018. **8**(27): p. 1800933.
206. Kamaya, N., et al., *A lithium superionic conductor.* Nature Materials, 2011. **10**(9): p. 682-686.
207. Murayama, M., et al., *Synthesis of New Lithium Ionic Conductor Thio-LISICON—Lithium Silicon Sulfides System.* Journal of Solid State Chemistry, 2002. **168**(1): p. 140-148.
208. Bron, P., et al., *$Li_{10}SnP_2S_{12}$: An Affordable Lithium Superionic Conductor.* Journal of the American Chemical Society, 2013. **135**(42): p. 15694-15697.
209. Kato, Y., et al., *Short communication.* Journal of Power Sources, 2014. **271**(C): p. 60-64.
210. Krauskopf, T., S.P. Culver, and W.G. Zeier, *Bottleneck of Diffusion and Inductive Effects in $Li_{10}Ge_{1-x}Sn_xP_2S_{12}$.* Chemistry of Materials, 2018. **30**(5): p. 1791-1798.
211. Kuhn, A., et al., *A new ultrafast superionic Li-conductor: ion dynamics in $Li_{11}Si_2PS_{12}$ and comparison with other tetragonal LGPS-type electrolytes.* Physical Chemistry Chemical Physics, 2014. **16**(28): p. 14669-14674.
212. Kato, Y., et al., *High-power all-solid-state batteries using sulfide superionic conductors.* Nature Energy, 2016. **1**: p. 16030.
213. Hayashi, A., A. Sakuda, and M. Tatsumisago, *Development of Sulfide Solid Electrolytes and Interface Formation Processes for Bulk-Type All-Solid-State Li and Na Batteries.* Frontiers in Energy Research, 2016. **4**.
214. Chen, H.M., C. Maohua, and S. Adams, *Stability and ionic mobility in argyrodite-related lithium-ion solid electrolytes.* Physical Chemistry Chemical Physics, 2015. **17**(25): p. 16494-16506.
215. Deiseroth, H.-J., et al., *Li_6PS_5X: A Class of Crystalline Li-Rich Solids With an Unusually High Li^+ Mobility.* Angewandte Chemie International Edition, 2008. **47**(4): p. 755-758.
216. Hayashi, A., et al., *Characterization of Li_2S–P_2S_5 glass-ceramics as a solid electrolyte for lithium secondary batteries.* Solid State Ionics, 2004. **175**(1): p. 683-686.
217. Ye, T., L. Li, and Y. Zhang, *Recent Progress in Solid Electrolytes for Energy Storage Devices.* Advanced Functional Materials, 2020. **30**(29): p. 2000077.
218. De Klerk, N.J., I. Rosłoń, and M. Wagemaker, *Diffusion Mechanism of Li Argyrodite Solid Electrolytes for Li-Ion Batteries and Prediction of Optimized Halogen Doping: The Effect of Li Vacancies, Halogens, and Halogen Disorder.* Chemistry of Materials, 2016. **28**(21): p. 7955-7963.

219. Schwietert, T.K., et al., *Clarifying the relationship between redox activity and electrochemical stability in solid electrolytes.* Nature Materials, 2020. **19**(4): p. 428-435.
220. Yu, C., et al., *Recent development of lithium argyrodite solid-state electrolytes for solid-state batteries: Synthesis, structure, stability and dynamics.* Nano Energy, 2021. **83**: p. 105858.
221. Lee, Y., et al., *Lithium Argyrodite Sulfide Electrolytes with High Ionic Conductivity and Air Stability for All-Solid-State Li-Ion Batteries.* ACS Energy Letters, 2022. **7**(1): p. 171-179.
222. Tsukasaki, H., et al., *Deterioration process of argyrodite solid electrolytes during exposure to humidity-controlled air.* Journal of Power Sources, 2022. **524**: p. 231085.
223. Matsuo, M., et al., *Lithium superionic conduction in lithium borohydride accompanied by structural transition.* Applied Physics Letters, 2007. **91**(22): p. 224103.
224. Pang, Y., et al., *Hydrides for solid-state batteries: A review.* Materials Today Nano, 2022. **18**: p. 100194.
225. Teprovich, J.A., et al., *Bi-functional $Li_2B_{12}H_{12}$ for energy storage and conversion applications: solid-state electrolyte and luminescent down-conversion dye.* Journal of Materials Chemistry A, 2015. **3**(45): p. 22853-22859.
226. Wu, H., et al., *Structural Behavior of $Li_2B_{10}H_{10}$.* The Journal of Physical Chemistry C, 2015. **119**(12): p. 6481-6487.
227. Kisu, K., et al., *Interfacial stability between $LiBH_4$-based complex hydride solid electrolytes and Li metal anode for all-solid-state Li batteries.* Journal of Power Sources, 2019. **436**: p. 226821.
228. Matsuo, M., et al., *Sodium and magnesium ionic conduction in complex hydrides.* Journal of Alloys and Compounds, 2013. **580**: p. S98-S101.
229. Matsuo, M., et al., *Complex Hydrides with (BH4)− and (NH2)− Anions as New Lithium Fast-Ion Conductors.* Journal of the American Chemical Society, 2009. **131**(45): p. 16389-16391.
230. Tang, W.S., et al., *Unparalleled lithium and sodium superionic conduction in solid electrolytes with large monovalent cage-like anions.* Energy & Environmental Science, 2015. **8**(12): p. 3637-3645.
231. Yamauchi, A., et al., *Preparation and ionic conductivities of $(100-x)(0.75Li_2S\cdot0.25P_2S_5)\cdot xLiBH_4$ glass electrolytes.* Journal of Power Sources, 2013. **244**: p. 707-710.
232. Sakuda, A., et al., *Mechanochemically Prepared $Li_2S–P_2S_5–LiBH_4$ Solid Electrolytes with an Argyrodite Structure.* ACS Omega, 2018. **3**(5): p. 5453-5458.
233. Unemoto, A., et al., *Fast lithium-ionic conduction in a new complex hydride–sulphide crystalline phase.* Chemical Communications, 2016. **52**(3): p. 564-566.
234. Ginnings, D. and T. Phipps, *Temperature-conductance curves of solid salts. Halides of Lithium.* Journal of the American Chemical Society, 1930. **52**(4): p. 1340-1345.
235. Bohnsack, A., *Ternary Chlorides of the Rare-Earth Elements with Lithium, Li_3MCl_6 (M= Tb, Lu, Y, Sc): Synthesis, Crystal Structures, and Ionic Motion.* Journal of Inorganic and General Chemistry, 1997. **623**(7): p. 1067-1073.
236. Wang, C., et al., *Prospects of halide-based all-solid-state batteries: From material design to practical application.* Science Advances, 2022. **8**(36): p. eadc9516.
237. Liu, Z., et al., *High ionic conductivity achieved in $Li_3Y(Br_3Cl_3)$ mixed halide solid electrolyte via promoted diffusion pathways and enhanced grain boundary.* ACS Energy Letters, 2020. **6**(1): p. 298-304.

238. Ohno, S., et al., *How certain are the reported ionic conductivities of thiophosphate-based solid electrolytes? An interlaboratory study.* ACS Energy Letters, 2020. **5**(3): p. 910-915.
239. Maekawa, H., et al., *Halide-stabilized $LiBH_4$, a room-temperature lithium fast-ion conductor.* Journal of the American Chemical Society, 2009. **131**(3): p. 894-895.
240. El kharbachi, A., et al., *Lithium ionic conduction in composites of $Li(BH_4)_{0.75}I_{0.25}$ and amorphous 0.75Li2S·0.25P2S5 for battery applications.* Electrochimica Acta, 2018. **278**: p. 332-339.
241. Minafra, N., et al., *Local Charge Inhomogeneity and Lithium Distribution in the Superionic Argyrodites Li_6PS_5X (X = Cl, Br, I).* Inorganic Chemistry, 2020. **59**(15): p. 11009-11019.
242. Soulié, J.P., et al., *Lithium boro-hydride $LiBH_4$: I. Crystal structure.* Journal of Alloys and Compounds, 2002. **346**(1): p. 200-205.
243. Liu, Z., et al., *High Ionic Conductivity Achieved in $Li_3Y(Br_3Cl_3)$ Mixed Halide Solid Electrolyte via Promoted Diffusion Pathways and Enhanced Grain Boundary.* ACS Energy Letters, 2021. **6**(1): p. 298-304.
244. Bae, J., et al., *Designing 3D nanostructured garnet frameworks for enhancing ionic conductivity and flexibility in composite polymer electrolytes for lithium batteries.* Energy Storage Materials, 2018. **15**: p. 46-52.
245. Wang, X., et al., *Lithium-salt-rich PEO/$Li_{0.3}La_{0.557}TiO_3$ interpenetrating composite electrolyte with three-dimensional ceramic nano-backbone for all-solid-state lithium-ion batteries.* ACS applied materials & interfaces, 2018. **10**(29): p. 24791-24798.
246. Park, M., et al., *A review of conduction phenomena in Li-ion batteries.* Journal of Power Sources, 2010. **195**(24): p. 7904-7929.
247. Wang, Y., et al., *Design principles for solid-state lithium superionic conductors.* Nature materials, 2015. **14**(10): p. 1026-1031.
248. Xu, H., et al., *Y-Doped NASICON-type $LiZr_2(PO_4)_3$ Solid Electrolytes for Lithium-Metal Batteries.* Chemistry of Materials, 2017. **29**(17): p. 7206-7212.
249. Kraft, M.A., et al., *Influence of Lattice Polarizability on the Ionic Conductivity in the Lithium Superionic Argyrodites Li_6PS_5X (X = Cl, Br, I).* Journal of the American Chemical Society, 2017. **139**(31): p. 10909-10918.
250. Kang, J., et al., *Integrated study of first principles calculations and experimental measurements for Li-ionic conductivity in Al-doped solid-state $LiGe_2(PO_4)_3$ electrolyte.* Journal of Power Sources, 2015. **293**: p. 11-16.
251. Jung, Y.S., et al., *Issues and challenges for bulk-type all-solid-state rechargeable lithium batteries using sulfide solid electrolytes.* Israel Journal of Chemistry, 2015. **55**(5): p. 472-485.
252. Hayashi, A., et al., *Improvement of chemical stability of Li_3PS_4 glass electrolytes by adding M_xO_y (M= Fe, Zn, and Bi) nanoparticles.* Journal of Materials Chemistry A, 2013. **1**(21): p. 6320-6326.
253. Goudon, J., et al., *Experimental investigation on lithium borohydride hydrolysis.* International journal of hydrogen energy, 2010. **35**(20): p. 11071-11076.
254. Blanchard, D., et al., *Nanoconfined $LiBH_4$ as a fast lithium ion conductor.* Advanced Functional Materials, 2015. **25**(2): p. 184-192.
255. Auborn, J.J. and D.W. Johnson, *Conductivity of Nasicon ceramic membranes in aqueous solutions.* Solid State Ionics, 1981. **5**: p. 315.

256. Aono, H., et al., *Ionic Conductivity of Solid Electrolytes Based on Lithium Titanium Phosphate.* Journal of The Electrochemical Society, 1990. **137**(4): p. 1023-1027.
257. Yada, C., et al., *A novel all-solid-state thin-film-type lithium-ion battery with in situ prepared positive and negative electrode materials.* Electrochemistry Communications, 2009. **11**(2): p. 413-416.
258. Kühnel, R.-S., D. Reber, and C. Battaglia, *Perspective—Electrochemical Stability of Water-in-Salt Electrolytes.* Journal of The Electrochemical Society, 2020. **167**(7): p. 070544.
259. Richards, W.D., et al., *Interface stability in solid-state batteries.* Chemistry of Materials, 2016. **28**(1): p. 266-273.
260. Sun, Y., et al., *A facile strategy to improve the electrochemical stability of a lithium ion conducting $Li_{10}GeP_2S_{12}$ solid electrolyte.* Solid State Ionics, 2017. **301**: p. 59-63.
261. Schwöbel, A., R. Hausbrand, and W. Jaegermann, *Interface reactions between LiPON and lithium studied by in-situ X-ray photoemission.* Solid State Ionics, 2015. **273**: p. 51-54.
262. Lotsch, B.V. and J. Maier, *Relevance of solid electrolytes for lithium-based batteries: A realistic view.* Journal of Electroceramics, 2017. **38**(2): p. 128-141.
263. Yan, X., et al., *Li/$Li_7La_3Zr_2O_{12}$/$LiFePO_4$ All-Solid-State Battery with Ultrathin Nanoscale Solid Electrolyte.* The Journal of Physical Chemistry C, 2017. **121**(3): p. 1431-1435.
264. Heyne, L., *Fast Ion Transport in Solids*, ed. W.v. Gool. 1973, North Holland,Amsterdam.
265. Van Zeghbroeck, B.V., *Principles of semiconductor devices and heterojunctions*. 2010, Upper Saddle River, N.J.; London: Prentice Hall ; Pearson Education.
266. Keyes, R.W., *Correlation between Mobility and Effective Mass in Semiconductors.* Journal of Applied Physics, 1959. **30**(3): p. 454-454.
267. Han, F., et al., *High electronic conductivity as the origin of lithium dendrite formation within solid electrolytes.* Nature Energy, 2019. **4**(3): p. 187-196.
268. Chen, Y.-T., et al., *Voltammetric Enhancement of Li-Ion Conduction in Al-Doped $Li_{7-x}La_3Zr_2O_{12}$ Solid Electrolyte.* The Journal of Physical Chemistry C, 2017. **121**(29): p. 15565-15573.
269. Yan, G., *Mechanical Behavior of Solid Electrolyte Materials for Lithium-ion Batteries*, in *Energy & Environment*. 2020, Forschungszentrum Jülich GmbH.
270. Ke, X., et al., *Towards rational mechanical design of inorganic solid electrolytes for all-solid-state lithium ion batteries.* Energy Storage Materials, 2020. **26**: p. 313-324.
271. Yan, G., et al., *Anisotropy of the mechanical properties of $Li_{1.3}Al_{0.3}Ti_{1.7}(PO_4)_3$ solid electrolyte material.* Journal of Power Sources, 2019. **437**: p. 226940.
272. McGrogan, F.P., et al., *Compliant Yet Brittle Mechanical Behavior of Li_2S–P_2S_5 Lithium-Ion-Conducting Solid Electrolyte.* Advanced Energy Materials, 2017. **7**(12): p. 1602011.
273. Sakuda, A., et al., *Evaluation of elastic modulus of Li_2S-P_2S_5 glassy solid electrolyte by ultrasonic sound velocity measurement and compression test.* Journal of the Ceramic Society of Japan, 2013. **121**(1419): p. 946-949.
274. Jackman, S.D. and R.A. Cutler, *Effect of microcracking on ionic conductivity in LATP.* Journal of Power Sources, 2012. **218**: p. 65-72.
275. Wang, A.-N., et al., *Mechanical properties of the solid electrolyte Al-substituted $Li_7La_3Zr_2O_{12}$ (LLZO) by utilizing micro-pillar indentation splitting test.* Journal of the European Ceramic Society, 2018. **38**(9): p. 3201-3209.

276. Cho, Y.-H., et al., *Mechanical properties of the solid Li-ion conducting electrolyte: $Li_{0.33}La_{0.57}TiO_3$.* Journal of Materials Science, 2012. **47**(16): p. 5970-5977.
277. Xie, H., et al., *Flexible garnet solid-state electrolyte membranes enabled by tile-and-grout design.* ACS Energy Letters, 2019. **4**(11): p. 2668-2674.
278. Liu, H., et al., *Controlling Dendrite Growth in Solid-State Electrolytes.* ACS Energy Letters, 2020. **5**(3): p. 833-843.
279. Li, Q., et al., *In-situ visualization of lithium plating in all-solid-state lithium-metal battery.* Nano Energy, 2019. **63**: p. 103895.
280. Barsoum, M., *Fundamentals of ceramics*. 2019: CRC press.
281. Birke, P., et al., *Electrolytic Stability Limit and Rapid Lithium Insertion in the Fast-Ion-Conducting $Li_{0.29}La_{0.57}TiO_3$ Perovskite-Type Compound.* Journal of The Electrochemical Society, 1997. **144**(6): p. L167-L169.
282. Hartmann, P., et al., *Degradation of NASICON-type materials in contact with lithium metal: formation of mixed conducting interphases (MCI) on solid electrolytes.* The Journal of Physical Chemistry C, 2013. **117**(41): p. 21064-21074.
283. Li, Y., et al., *Mastering the interface for advanced all-solid-state lithium rechargeable batteries.* Proc Natl Acad Sci U S A, 2016. **113**(47): p. 13313-13317.
284. Cui, Y., et al., *Ionic Conductivity and Stability of the Lithium Aluminum Germanium Phosphate.* ECS Transactions, 2016. **72**(8): p. 139.
285. Chung, H. and B. Kang, *Mechanical and thermal failure induced by contact between a $Li_{1.5}Al_{0.5}Ge_{1.5}(PO_4)_3$ solid electrolyte and Li metal in an all solid-state Li cell.* Chemistry of Materials, 2017. **29**(20): p. 8611-8619.
286. Ma, C., et al., *Interfacial Stability of Li Metal-Solid Electrolyte Elucidated via in Situ Electron Microscopy.* Nano letters, 2016. **16**(11): p. 7030-7036.
287. Wenzel, S., et al., *Direct Observation of the Interfacial Instability of the Fast Ionic Conductor $Li_{10}GeP_2S_{12}$ at the Lithium Metal Anode.* Chemistry of Materials, 2016. **28**(7): p. 2400-2407.
288. Kim, K.H., et al., *Characterization of the interface between $LiCoO_2$ and $Li_7La_3Zr_2O_{12}$ in an all-solid-state rechargeable lithium battery.* Journal of Power Sources, 2011. **196**(2): p. 764-767.
289. Park, K., et al., *Electrochemical Nature of the Cathode Interface for a Solid-State Lithium-Ion Battery: Interface between $LiCoO_2$ and Garnet-$Li_7La_3Zr_2O_{12}$.* Chemistry of Materials, 2016. **28**(21): p. 8051-8059.
290. Miara, L., et al., *About the Compatibility between High Voltage Spinel Cathode Materials and Solid Oxide Electrolytes as a Function of Temperature.* ACS Applied Materials & Interfaces, 2016. **8**(40): p. 26842-26850.
291. Yamamoto, K., et al., *Direct observation of lithium-ion movement around an in situ formed negative electrode / solid state electrolyte interface during initial charge–discharge reaction.* Electrochemistry communications, 2012. **20**: p. 113-116.
292. Jacke, S., et al., *Investigation of the solid-state electrolyte/cathode LiPON/$LiCoO_2$ interface by photoelectron spectroscopy.* Ionics, 2010. **16**(9): p. 769-775.
293. Takada, K., *Interfacial nanoarchitectonics for solid-state lithium batteries.* Langmuir, 2013. **29**(24): p. 7538-7541.
294. Sakuda, A., A. Hayashi, and M. Tatsumisago, *Interfacial Observation between $LiCoO_2$ Electrode and Li_2S−P_2S_5 Solid Electrolytes of All-Solid-State Lithium Secondary Batteries Using Transmission Electron Microscopy.* Chemistry of Materials, 2010. **22**(3): p. 949-956.

295. Takahashi, K., et al., *All-solid-state lithium battery with LiBH4 solid electrolyte.* Journal of Power Sources, 2013. **226**: p. 61-64.
296. Ohta, N., et al., *$LiNbO_3$-coated $LiCoO_2$ as cathode material for all solid-state lithium secondary batteries.* Electrochemistry Communications, 2007. **9**(7): p. 1486-1490.
297. Sakuda, A., et al., *Modification of Interface Between $LiCoO_2$ Electrode and $Li_2S–P_2S_5$ Solid Electrolyte Using $Li_2O–SiO_2$ Glassy Layers.* Journal of The Electrochemical Society, 2009. **156**(1): p. A27.
298. Yubuchi, S., et al., *5V class $LiNi_{0.5}Mn_{1.5}O_4$ positive electrode coated with Li_3PO_4 thin film for all-solid-state batteries using sulfide solid electrolyte.* Solid State Ionics, 2016. **285**: p. 79-82.
299. Ohta, N., et al., *Enhancement of the High-Rate Capability of Solid-State Lithium Batteries by Nanoscale Interfacial Modification.* Advanced Materials, 2006. **18**(17): p. 2226-2229.
300. Seino, Y., T. Ota, and K. Takada, *High rate capabilities of all-solid-state lithium secondary batteries using $Li_4Ti_5O_{12}$-coated $LiNi_{0.8}Co_{0.15}Al_{0.05}O_2$ and a sulfide-based solid electrolyte.* Journal of Power Sources, 2011. **196**(15): p. 6488-6492.
301. Woo, J.H., et al., *Nanoscale Interface Modification of $LiCoO_2$ by Al_2O_3 Atomic Layer Deposition for Solid-State Li Batteries.* Journal of The Electrochemical Society, 2012. **159**(7): p. A1120-A1124.
302. Yada, C., et al., *Dielectric modification of 5V-class cathodes for high-voltage all-solid-state lithium batteries.* Advanced Energy Materials, 2014. **4**(9): p. 1301416.
303. Ito, S., et al., *A rocking chair type all-solid-state lithium ion battery adopting $Li_2O–ZrO_2$ coated $LiNi_{0.8}Co_{0.15}Al_{0.05}O_2$ and a sulfide based electrolyte.* Journal of Power Sources, 2014. **248**: p. 943-950.
304. Dawson, J.A., et al., *Atomic-Scale Influence of Grain Boundaries on Li-Ion Conduction in Solid Electrolytes for All-Solid-State Batteries.* Journal of the American Chemical Society, 2018. **140**(1): p. 362-368.
305. Ban, C.W. and G.M. Choi, *The effect of sintering on the grain boundary conductivity of lithium lanthanum titanates.* Solid State Ionics, 2001. **140**(3): p. 285-292.
306. Yi, E., et al., *Key parameters governing the densification of cubic-$Li_7La_3Zr_2O_{12}$ Li^+ conductors.* Journal of Power Sources, 2017. **352**: p. 156-164.
307. Verkerk, M., B. Middelhuis, and A. Burggraaf, *Effect of grain boundaries on the conductivity of high-purity ZrO_2-Y_2O_3 ceramics.* Solid State Ionics, 1982. **6**(2): p. 159-170.
308. Heitjans, P., et al., *NMR and impedance studies of nanocrystalline and amorphous ion conductors: lithium niobate as a model system.* Faraday Discussions, 2007. **134**: p. 67-82.
309. Sakamoto, J., et al., *Synthesis of nano-scale fast ion conducting cubic $Li_7La_3Zr_2O_{12}$.* Nanotechnology, 2013. **24**(42): p. 424005.
310. Iwaniak, W., et al., *Li Conductivity of Nanocrystalline $Li_4Ti_5O_{12}$ Prepared by a Sol-Gel Method and High-Energy Ball Milling.* Defect and Diffusion Forum, 2009. **289-292**: p. 565-570.
311. Mondal, P., et al., *Enhanced specific grain boundary conductivity in nanocrystalline Y_2O_3-stabilized zirconia.* Solid State Ionics, 1999. **118**(3-4): p. 331-339.
312. Lavik, E., et al., *Nonstoichiometry and Electrical Conductivity of Nanocrystalline CeO_{2-x}.* Journal of Electroceramics, 1997. **1**(1): p. 7-14.
313. Ganapathy, S., et al., *Peeking across Grain Boundaries in a Solid-State Ionic Conductor.* ACS Energy Letters, 2019. **4**(5): p. 1092-1097.

314. Guo, X. and J. Maier, *Grain Boundary Blocking Effect in Zirconia: A Schottky Barrier Analysis.* Journal of The Electrochemical Society, 2001. **148**(3): p. E121.
315. Luo, J., *Interfacial engineering of solid electrolytes.* Journal of Materiomics, 2015. **1**(1): p. 22-32.
316. Ohta, S., Y. Kihira, and T. Asaoka, *Grain Boundary Analysis of the Garnet-Like Oxides $Li_{7+X-Y}La_{3-X}A_XZr_{2-Y}Nb_YO_{12}$ (A = Sr or Ca).* Frontiers in Energy Research, 2016. **4**.
317. Wu, J.-F. and X. Guo, *Origin of the low grain boundary conductivity in lithium ion conducting perovskites: $Li_{3x}La_{0.67-x}TiO_3$.* Physical Chemistry Chemical Physics, 2017. **19**(8): p. 5880-5887.
318. Delaizir, G., et al., *The Stone Age Revisited: Building a Monolithic Inorganic Lithium-Ion Battery.* Advanced Functional Materials, 2012. **22**(10): p. 2140-2147.
319. Baek, S.-W., et al., *Garnet related lithium ion conductor processed by spark plasma sintering for all solid state batteries.* Journal of Power Sources, 2014. **249**: p. 197-206.
320. Kwon, W.J., et al., *Enhanced Li+ conduction in perovskite $Li_{3x}La_{2/3-x}\square_{1/3-2x}TiO_3$ solid-electrolytes via microstructural engineering.* Journal of Materials Chemistry A, 2017. **5**(13): p. 6257-6262.
321. Mei, A., et al., *Role of amorphous boundary layer in enhancing ionic conductivity of lithium–lanthanum–titanate electrolyte.* Electrochimica Acta, 2010. **55**(8): p. 2958-2963.
322. Lu, X., et al., *Increased ionic conductivity of a NASICON lithium ion conductor under the influence of mesoporous materials.* Journal of Alloys and Compounds, 2019. **794**: p. 585-593.
323. Krauskopf, T., et al., *Toward a Fundamental Understanding of the Lithium Metal Anode in Solid-State Batteries- An Electrochemo-Mechanical Study on the Garnet-Type Solid Electrolyte $Li_{6.25}Al_{0.25}La_3Zr_2O_{12}$.* ACS Applied Materials & Interfaces, 2019. **11**(15): p. 14463-14477.
324. Han, F., et al., *Interphase Engineering Enabled All-Ceramic Lithium Battery.* Joule, 2018. **2**(3): p. 497-508.
325. Zhang, Y., et al., *High Capacity All-Solid-State Lithium Battery Using Cathodes with Three-Dimensional Li^+ Conductive Network.* Journal of The Electrochemical Society, 2017. **164**(7): p. A1695-A1702.
326. Tsai, C.-L., et al., *A garnet structure-based all-solid-state Li battery without interface modification: resolving incompatibility issues on positive electrodes.* Sustainable Energy & Fuels, 2019. **3**(1): p. 280-291.
327. Cheng, L., et al., *The origin of high electrolyte–electrode interfacial resistances in lithium cells containing garnet type solid electrolytes.* Physical Chemistry Chemical Physics, 2014. **16**(34): p. 18294-18300.
328. Sharafi, A., et al., *Surface Chemistry Mechanism of Ultra-Low Interfacial Resistance in the Solid-State Electrolyte $Li_7La_3Zr_2O_{12}$.* Chemistry of Materials, 2017. **29**(18): p. 7961-7968.
329. Fu, K.K., et al., *Toward garnet electrolyte-based Li metal batteries: An ultrathin, highly effective, artificial solid-state electrolyte/metallic Li interface.* Sci Adv, 2017. **3**(4): p. e1601659.
330. Kato, T., et al., *In-situ $Li_7La_3Zr_2O_{12}/LiCoO_2$ interface modification for advanced all-solid-state battery.* Journal of Power Sources, 2014. **260**: p. 292-298.
331. Tsai, C.L., et al., *$Li_7La_3Zr_2O_{12}$ Interface Modification for Li Dendrite Prevention.* ACS Appl Mater Interfaces, 2016. **8**(16): p. 10617-26.
332. Han, X., et al., *Negating interfacial impedance in garnet-based solid-state Li metal batteries.* Nature Materials, 2017. **16**(5): p. 572-579.

333. Nagao, M., A. Hayashi, and M. Tatsumisago, *Bulk-type lithium metal secondary battery with indium thin layer at interface between Li electrode and Li_2S-P_2S_5 solid electrolyte.* Electrochemistry, 2012. **80**(10): p. 734-736.
334. Takahashi, K., H. Maekawa, and H. Takamura, *Effects of intermediate layer on interfacial resistance for all-solid-state lithium batteries using lithium borohydride.* Solid State Ionics, 2014. **262**: p. 179-182.
335. Wang, C., et al., *Conformal, Nanoscale ZnO Surface Modification of Garnet-Based Solid-State Electrolyte for Lithium Metal Anodes.* Nano Letters, 2017. **17**(1): p. 565-571.
336. Machida, N., et al., *Electrochemical properties of all-solid-state batteries with ZrO_2-coated $LiNi_{1/3}Mn_{1/3}Co_{1/3}O_2$ as cathode materials.* Solid State Ionics, 2012. **225**: p. 354-358.
337. Liu, T., et al., *Achieving high capacity in bulk-type solid-state lithium ion battery based on $Li_{6.75}La_3Zr_{1.75}Ta_{0.25}O_{12}$ electrolyte: Interfacial resistance.* Journal of Power Sources, 2016. **324**: p. 349-357.
338. Takada, K., et al., *Interfacial phenomena in solid-state lithium battery with sulfide solid electrolyte.* Solid State Ionics, 2012. **225**: p. 594-597.
339. Yada, C., et al., *Dielectric Modification of 5V-Class Cathodes for High-Voltage All-Solid-State Lithium Batteries.* Advanced Energy Materials, 2014. **4**(9): p. 1301416.
340. Xu, X., et al., *Tantalum oxide nanomesh as self-standing one nanometre thick electrolyte.* Energy & Environmental Science, 2011. **4**(9): p. 3509-3512.
341. Okada, K., et al., *Preparation and electrochemical properties of $LiAlO_2$-coated $LiNi_{1/3}Mn_{1/3}Co_{1/3}O_2$ for all-solid-state batteries.* Solid State Ionics, 2014. **255**: p. 120-127.
342. Kim, J., et al., *Enhanced electrochemical performance of surface modified $LiCoO_2$ for all-solid-state lithium batteries.* Ceramics International, 2016. **42**(2): p. 2140-2146.
343. Woo, J.H., et al., *Nanoscale interface modification of $LiCoO_2$ by Al_2O_3 atomic layer deposition for solid-state Li batteries.* Journal of The Electrochemical Society, 2012. **159**(7): p. A1120.
344. Sakuda, A., et al., *All-solid-state lithium secondary batteries using Li_2S–P_2S_5 solid electrolytes and $LiFePO_4$ electrode particles with amorphous surface layer.* Chemistry Letters, 2012. **41**(3): p. 260-261.
345. Li, Y., et al., *Hybrid Polymer/Garnet Electrolyte with a Small Interfacial Resistance for Lithium-Ion Batteries.* Angew Chem Int Ed Engl, 2017. **56**(3): p. 753-756.
346. Fu, K., et al., *Three-dimensional bilayer garnet solid electrolyte based high energy density lithium metal–sulfur batteries.* Energy & Environmental Science, 2017. **10**(7): p. 1568-1575.
347. Liu, B., et al., *Rapid thermal annealing of cathode-garnet interface toward high-temperature solid state batteries.* Nano letters, 2017. **17**(8): p. 4917-4923.
348. Sharafi, A., et al., *Characterizing the Li–$Li_7La_3Zr_2O_{12}$ interface stability and kinetics as a function of temperature and current density.* Journal of Power Sources, 2016. **302**: p. 135-139.
349. Yang, H. and N. Wu, *Ionic conductivity and ion transport mechanisms of solid-state lithium-ion battery electrolytes: A review.* Energy Science & Engineering, 2022. **10**(5): p. 1643-1671.
350. Wakayama H., H. Yonekura, and Y. Kawai, *Three-Dimensional Bicontinuous Nanocomposite from a Self-Assembled Block Copolymer for a High-Capacity All-Solid-State Lithium Battery Cathode.* Chemistry of Materials, 2016. **28**(12): p. 4453-4459.
351. Shiraki, S., et al., *Atomically Well-Ordered Structure at Solid Electrolyte and Electrode Interface Reduces the Interfacial Resistance.* ACS Applied Materials & Interfaces, 2018. **10**(48): p. 41732-41737.

352. Wang, S., et al., *Ultra-fine surface solid-state electrolytes for long cycle life all-solid-state lithium–air batteries.* Journal of Materials Chemistry A, 2018. **6**(43): p. 21248-21254.
353. Koerver, R., et al., *Chemo-mechanical expansion of lithium electrode materials – on the route to mechanically optimized all-solid-state batteries.* Energy & Environmental Science, 2018. **11**(8): p. 2142-2158.
354. Zhang, W., et al., *Interfacial Processes and Influence of Composite Cathode Microstructure Controlling the Performance of All-Solid-State Lithium Batteries.* ACS Applied Materials & Interfaces, 2017. **9**(21): p. 17835-17845.
355. Zhang, W., et al., *(Electro)chemical expansion during cycling: monitoring the pressure changes in operating solid-state lithium batteries.* Journal of Materials Chemistry A, 2017. **5**(20): p. 9929-9936.
356. Koerver, R., et al., *Capacity Fade in Solid-State Batteries: Interphase Formation and Chemomechanical Processes in Nickel-Rich Layered Oxide Cathodes and Lithium Thiophosphate Solid Electrolytes.* Chemistry of Materials, 2017. **29**(13): p. 5574-5582.
357. Bucci, G., et al., *Mechanical instability of electrode-electrolyte interfaces in solid-state batteries.* Physical Review Materials, 2018. **2**(10): p. 105407.
358. Cheng, E.J., A. Sharafi, and J. Sakamoto, *Intergranular Li metal propagation through polycrystalline $Li_{6.25}Al_{0.25}La_3Zr_2O_{12}$ ceramic electrolyte.* Electrochimica Acta, 2017. **223**: p. 85-91.
359. Porz, L., et al., *Mechanism of Lithium Metal Penetration through Inorganic Solid Electrolytes.* Advanced Energy Materials, 2017. **7**(20): p. 1701003.
360. Otoyama, M., et al., *Optical microscopic observation of graphite composite negative electrodes in all-solid-state lithium batteries.* Solid State Ionics, 2018. **323**: p. 123-129.
361. Aguesse, F., et al., *Investigating the Dendritic Growth during Full Cell Cycling of Garnet Electrolyte in Direct Contact with Li Metal.* ACS Applied Materials & Interfaces, 2017. **9**(4): p. 3808-3816.
362. Tsukamoto, R., et al., *In-Situ Cross-Sectional SEM Observations of Li Plating and Stripping on Oxide-Based-Solid-State Electrolytes.* ECS Meeting Abstracts, 2016. **MA2016-02**(53): p. 4116.
363. Randau, S., et al., *Benchmarking the performance of all-solid-state lithium batteries.* Nature Energy, 2020. **5**(3): p. 259-270.
364. Shi, S., et al., *Multi-scale computation methods: Their applications in lithium-ion battery research and development.* Chinese Physics B, 2016. **25**(1): p. 018212.
365. Nolan, A.M., et al., *Computation-Accelerated Design of Materials and Interfaces for All-Solid-State Lithium-Ion Batteries.* Joule, 2018. **2**(10): p. 2016-2046.
366. Science, N. and T. Council, *Materials genome initiative for global competitiveness*. 2011: Executive Office of the President, National Science and Technology Council.
367. Yuan, W.-L., et al., *Materials-Genome Approach to Energetic Materials.* Accounts of Materials Research, 2021. **2**(9): p. 692-696.
368. Curtarolo, S., et al., *AFLOW: An automatic framework for high-throughput materials discovery.* Computational Materials Science, 2012. **58**: p. 218-226.
369. Kirklin, S., et al., *The Open Quantum Materials Database (OQMD): assessing the accuracy of DFT formation energies.* npj Computational Materials, 2015. **1**(1): p. 1-15.

370. Jain, A., et al., *Commentary: The Materials Project: A materials genome approach to accelerating materials innovation.* APL materials, 2013. **1**(1): p. 011002.
371. Henkelman, G., B.P. Uberuaga, and H. Jónsson, *A climbing image nudged elastic band method for finding saddle points and minimum energy paths.* The Journal of chemical physics, 2000. **113**(22): p. 9901-9904.
372. Urban, A., D.-H. Seo, and G. Ceder, *Computational understanding of Li-ion batteries.* npj Computational Materials, 2016. **2**(1): p. 1-13.
373. He, X., Y. Zhu, and Y. Mo, *Origin of fast ion diffusion in super-ionic conductors.* Nature communications, 2017. **8**(1): p. 1-7.
374. Materzanini, G., et al., *High Li-ion conductivity in tetragonal LGPO: A comparative first-principles study against known LISICON and LGPS phases.* Physical Review Materials, 2021. **5**(3): p. 035408.
375. Afandak, A. and H. Eslami, *Ion-Pairing and Electrical Conductivity in the Ionic Liquid 1-n-Butyl-3-methylimidazolium Methylsulfate [Bmim][MeSO4]: Molecular Dynamics Simulation Study.* The Journal of Physical Chemistry B, 2017. **121**(32): p. 7699-7708.
376. France-Lanord, A. and J.C. Grossman, *Correlations from Ion Pairing and the Nernst-Einstein Equation.* Physical Review Letters, 2019. **122**(13): p. 136001.
377. Marcolongo, A. and N. Marzari, *Ionic correlations and failure of Nernst-Einstein relation in solid-state electrolytes.* Physical Review Materials, 2017. **1**(2): p. 025402.
378. Mo, Y., S.P. Ong, and G. Ceder, *First Principles Study of the $Li_{10}GeP_2S_{12}$ Lithium Super Ionic Conductor Material.* Chemistry of Materials, 2012. **24**(1): p. 15-17.
379. Ong, S.P., et al., *Phase stability, electrochemical stability and ionic conductivity of the $Li_{10\pm1}MP_2X_{12}$ (M= Ge, Si, Sn, Al or P, and X= O, S or Se) family of superionic conductors.* Energy & Environmental Science, 2013. **6**(1): p. 148-156.
380. Weber, D.A., et al., *Structural insights and 3D diffusion pathways within the lithium superionic conductor $Li_{10}GeP_2S_{12}$.* Chemistry of Materials, 2016. **28**(16): p. 5905-5915.
381. Xu, M., J. Ding, and E. Ma, *One-dimensional stringlike cooperative migration of lithium ions in an ultrafast ionic conductor.* Applied Physics Letters, 2012. **101**(3): p. 031901.
382. Richards, W.D., et al., *Design of $Li_{1+2x}Zn_{1-x}PS_4$, a new lithium ion conductor.* Energy & Environmental Science, 2016. **9**(10): p. 3272-3278.
383. Richards, W.D., et al., *Design and synthesis of the superionic conductor $Na_{10}SnP_2S_{12}$.* Nature communications, 2016. **7**(1): p. 1-8.
384. Jalem, R., et al., *Concerted migration mechanism in the Li ion dynamics of garnet-type $Li_7La_3Zr_2O_{12}$.* Chemistry of Materials, 2013. **25**(3): p. 425-430.
385. He, X., Y. Zhu, and Y. Mo, *Origin of fast ion diffusion in super-ionic conductors.* Nature Communications, 2017. **8**(1): p. 15893.
386. Kaup, K., et al., *Correlation of Structure and Fast Ion Conductivity in the Solid Solution Series $Li_{1+2x}Zn_{1-x}PS_4$.* Chemistry of Materials, 2018. **30**(3): p. 592-596.
387. Suzuki, N., et al., *Synthesis and Electrochemical Properties of $I\bar{4}$-Type $Li_{1+2x}Zn_{1-x}PS_4$ Solid Electrolyte.* Chemistry of Materials, 2018. **30**(7): p. 2236-2244.
388. Wang, Q., et al., *A New Lithium-Ion Conductor $LiTaSiO_5$: Theoretical Prediction, Materials Synthesis, and Ionic Conductivity.* Advanced Functional Materials, 2019. **29**(37): p. 1904232.
389. Bron, P., et al., *$Li_{10}SnP_2S_{12}$: an affordable lithium superionic conductor.* Journal of the American Chemical Society, 2013. **135**(42): p. 15694-15697.

390. Kato, Y., et al., *High-power all-solid-state batteries using sulfide superionic conductors.* Nature Energy, 2016. **1**(4): p. 16030.
391. Ong, S.P., et al., *Thermal stabilities of delithiated olivine MPO_4 (M=Fe, Mn) cathodes investigated using first principles calculations.* Electrochemistry Communications, 2010. **12**(3): p. 427-430.
392. Zhu, Y., X. He, and Y. Mo, *Origin of outstanding stability in the lithium solid electrolyte materials: insights from thermodynamic analyses based on first-principles calculations.* ACS applied materials & interfaces, 2015. **7**(42): p. 23685-23693.
393. Zhu, Y., X. He, and Y. Mo, *First principles study on electrochemical and chemical stability of solid electrolyte–electrode interfaces in all-solid-state Li-ion batteries.* Journal of Materials Chemistry A, 2016. **4**(9): p. 3253-3266.
394. Benabed, Y., et al., *Assessing the Electrochemical Stability Window of NASICON-Type Solid Electrolytes.* Frontiers in Energy Research, 2021: p. 230.
395. Han, F., et al., *A battery made from a single material.* Advanced materials, 2015. **27**(23): p. 3473-3483.
396. Wenzel, S., et al., *Interfacial reactivity and interphase growth of argyrodite solid electrolytes at lithium metal electrodes.* Solid State Ionics, 2018. **318**: p. 102-112.
397. Zhu, Y., X. He, and Y. Mo, *Strategies based on nitride materials chemistry to stabilize Li metal anode.* Advanced Science, 2017. **4**(8): p. 1600517.
398. Miara, L.J., et al., *First-principles studies on cation dopants and electrolyte| cathode interphases for lithium garnets.* Chemistry of Materials, 2015. **27**(11): p. 4040-4047.
399. Wang, Z., et al., *In situ STEM-EELS observation of nanoscale interfacial phenomena in all-solid-state batteries.* Nano letters, 2016. **16**(6): p. 3760-3767.
400. Fingerle, M., et al., *Reaction and space charge layer formation at the $LiCoO_2$–LiPON interface: insights on defect formation and ion energy level alignment by a combined surface science–simulation approach.* Chemistry of Materials, 2017. **29**(18): p. 7675-7685.
401. Leung, K., et al., *Kinetics-Controlled Degradation Reactions at Crystalline LiPON/Li_xCoO_2 and Crystalline LiPON/Li-Metal Interfaces.* ChemSusChem, 2018. **11**(12): p. 1956-1969.
402. Sakuda, A., A. Hayashi, and M. Tatsumisago, *Interfacial observation between $LiCoO_2$ electrode and Li_2S−P_2S_5 solid electrolytes of all-solid-state lithium secondary batteries using transmission electron microscopy.* Chemistry of Materials, 2010. **22**(3): p. 949-956.
403. Hakari, T., et al., *Structural and Electronic-State Changes of a Sulfide Solid Electrolyte during the Li Deinsertion–Insertion Processes.* Chemistry of Materials, 2017. **29**(11): p. 4768-4774.
404. Koerver, R., et al., *Redox-active cathode interphases in solid-state batteries.* Journal of Materials Chemistry A, 2017. **5**(43): p. 22750-22760.
405. Auvergniot, J., et al., *Interface stability of argyrodite Li_6PS_5Cl toward $LiCoO_2$, $LiNi_{1/3}Co_{1/3}Mn_{1/3}O_2$, and $LiMn_2O_4$ in bulk all-solid-state batteries.* Chemistry of Materials, 2017. **29**(9): p. 3883-3890.
406. Miara, L., et al., *About the compatibility between high voltage spinel cathode materials and solid oxide electrolytes as a function of temperature.* ACS applied materials & interfaces, 2016. **8**(40): p. 26842-26850.
407. Gorai, P., et al., *Devil is in the Defects: Electronic Conductivity in Solid Electrolytes.* Chemistry of Materials, 2021. **33**(18): p. 7484-7498.

408. Shimoda, M., et al., *Controlling Defects to Achieve Reproducibly High Ionic Conductivity in Na_3SbS_4 Solid Electrolytes.* Chemistry of Materials, 2022. **34**(12): p. 5634-5643.
409. Squires, A.G., D.O. Scanlon, and B.J. Morgan, *Native Defects and Their Doping Response in the Lithium Solid Electrolyte Li7La3Zr2O12.* Chemistry of Materials, 2020. **32**(5): p. 1876-1886.
410. Gorai, P., et al., *Defect chemistry of disordered solid-state electrolyte $Li_{10}GeP_2S_{12}$.* Journal of Materials Chemistry A, 2020. **8**(7): p. 3851-3858.
411. Avdeev, M., et al., *Screening of the alkali-metal ion containing materials from the Inorganic Crystal Structure Database (ICSD) for high ionic conductivity pathways using the bond valence method.* Solid State Ionics, 2012. **225**: p. 43-46.
412. Xiao, R., H. Li, and L. Chen, *High-throughput design and optimization of fast lithium ion conductors by the combination of bond-valence method and density functional theory.* Scientific reports, 2015. **5**(1): p. 1-11.
413. Sendek, A.D., et al., *Holistic computational structure screening of more than 12000 candidates for solid lithium-ion conductor materials.* Energy & Environmental Science, 2017. **10**(1): p. 306-320.
414. Wang, X., et al., *Oxysulfide LiAlSO: a lithium superionic conductor from first principles.* Physical Review Letters, 2017. **118**(19): p. 195901.
415. Hautier, G., et al., *Data mined ionic substitutions for the discovery of new compounds.* Inorganic chemistry, 2011. **50**(2): p. 656-663.
416. Zhu, Z., I.-H. Chu, and S.P. Ong, *$Li_3Y(PS_4)_2$ and $Li_5PS_4Cl_2$: New Lithium Superionic Conductors Predicted from Silver Thiophosphates using Efficiently Tiered Ab Initio Molecular Dynamics Simulations.* Chemistry of Materials, 2017. **29**(6): p. 2474-2484.
417. Honrao, S.J., et al., *Discovery of novel Li SSE and anode coatings using interpretable machine learning and high-throughput multi-property screening.* Scientific Reports, 2021. **11**(1): p. 16484.
418. Golov, A. and J. Carrasco, *Enhancing first-principles simulations of complex solid-state ion conductors using topological analysis of procrystal electron density.* npj Computational Materials, 2022. **8**(1): p. 187.
419. Prep, S.S. *8000D Mixer/Mill® - Dual High-Energy Ball Mill*. 2022.
420. Youssef Ben, S., et al., *Synthesis Methods in Solid-State Chemistry*, in *Synthesis Methods and Crystallization*, M. Riadh, Editor. 2020, IntechOpen: Rijeka. p. Ch. 2.
421. Anselmi-Tamburini, U., *Spark Plasma Sintering*, in *Encyclopedia of Materials: Technical Ceramics and Glasses*, M. Pomeroy, Editor. 2021, Elsevier: Oxford. p. 294-310.
422. Yang, Y.F. and M. Qian, *13 - Spark plasma sintering and hot pressing of titanium and titanium alloys*, in *Titanium Powder Metallurgy*, M. Qian and F.H. Froes, Editors. 2015, Butterworth-Heinemann: Boston. p. 219-235.
423. Zhou, M., et al., *Solid Phase Processing of Metal Matrix Composites*, in *Encyclopedia of Materials: Composites*, D. Brabazon, Editor. 2021, Elsevier: Oxford. p. 173-196.
424. Han, X., et al., *Induction of planar Li growth with designed interphases for dendrite-free Li metal anodes.* Energy Storage Materials, 2021. **39**: p. 250-258.
425. Zhu, H., et al. *Spark Plasma Sintering of Lithium Aluminum Germanium Phosphate Solid Electrolyte and its Electrochemical Properties*. Nanomaterials, 2019. **9**.

426. Prakasam, M., et al., *Chapter 9 - Ultrahigh pressure SPS (HP-SPS) as new syntheses and exploration tool in materials science*, in *Spark Plasma Sintering*, G. Cao, et al., Editors. 2019, Elsevier. p. 201-218.
427. Lowell, S., et al., *Characterization of porous solids and powders: surface area, pore size and density*. Vol. 16. 2006: Springer Science & Business Media.
428. Brunauer, S., P.H. Emmett, and E. Teller, *Adsorption of gases in multimolecular layers.* Journal of the American chemical society, 1938. **60**(2): p. 309-319.
429. Borchardt-Ott, W., *Crystallography: an introduction*. 2011: Springer Science & Business Media.
430. Bravais, A., *Mémoire sur les systèmes formés par des points distribués régulièrement sur un plan ou dans l'espace*. 1850: Bachelier.
431. Bragg, W.H. and W.L. Bragg, *The reflection of X-rays by crystals.* Proceedings of the Royal Society of London. Series A, Containing Papers of a Mathematical and Physical Character, 1913. **88**(605): p. 428-438.
432. Krumeich, F. *Bragg's Law of Diffraction*. 2022.
433. Rabiei, M., et al., *Measurement Modulus of Elasticity Related to the Atomic Density of Planes in Unit Cell of Crystal Lattices.* Materials, 2020. **13**(19): p. 4380.
434. Le Bail, A., H. Duroy, and J.L. Fourquet, *Ab-initio structure determination of $LiSbWO_6$ by X-ray powder diffraction.* Materials Research Bulletin, 1988. **23**(3): p. 447-452.
435. Thompson, P., D.E. Cox, and J.B. Hastings, *Rietveld refinement of Debye-Scherrer synchrotron X-ray data from Al_2O_3.* Journal of Applied Crystallography, 1987. **20**(2): p. 79-83.
436. Ford, B.J., Joy, David C. and Bradbury, Savile. *transmission electron microscope*. 2022.
437. *Electron–specimen interactions: processes and detectors*, in *The Principles and Practice of Electron Microscopy*, I.M. Watt, Editor. 1997, Cambridge University, p. 30-58.
438. Egerton, R.F., *Physical Principles of Electron Microscopy: An Introduction to TEM, SEM, and AEM.* Physical Principles of Electron Microscopy, 2005.
439. Bell, D.C., *Transmission Electron Microscopy; Diffraction, Imaging, and Spectrometry C. Barry Carter and David B. Williams (Eds.). Springer International Publishing, Switzerland 2016, 518 pp. ISBN: 978-3-3-319-26649-7.* Microscopy and Microanalysis, 2018. **24**(3): p. 324-324.
440. De Graef, M., *Introduction to Conventional Transmission Electron Microscopy*. 2003, Cambridge: Cambridge University Press.
441. Crispinus, B.T., *Selected Area Diffraction*. 2011: Vertpress.
442. Talebi-Esfandarani, M., et al., *Control of the $LiFePO_4$ electrochemical properties using low-cost iron precursor in a melt process.* Journal of Solid State Electrochemistry, 2016. **20**(12): p. 3481-3490.
443. Wen, C.J., et al., *Thermodynamic and Mass Transport Properties of "LiAl"* Journal of The Electrochemical Society, 1979. **126**(12): p. 2258.
444. Levi, M.D. and D. Aurbach, *Potentiostatic and Galvanostatic Intermittent Titration Techniques*, in *Characterization of Materials*. p. 1-21.
445. Li, J., et al., *Potentiostatic Intermittent Titration Technique for Electrodes Governed by Diffusion and Interfacial Reaction.* The Journal of Physical Chemistry C, 2012. **116**(1): p. 1472-1478.
446. Rousselot, S., *Schéma de L'assemblage D'une Pile Bouton.* LCES, Université de Montréal, 2016.

447. Lacey, M. *Electrochemical Impedance Spectroscopy*. 2022.
448. Macdonald, J.R. and W.B. Johnson, *Fundamentals of Impedance Spectroscopy*, in *Impedance Spectroscopy*. 2005. p. 1-26.
449. Vivier, V. and M.E. Orazem, *Impedance Analysis of Electrochemical Systems.* Chemical Reviews, 2022. **122**(12): p. 11131-11168.
450. Gaberšček, M., *Understanding Li-based battery materials via electrochemical impedance spectroscopy.* Nature Communications, 2021. **12**(1): p. 6513.
451. Sensing, S. *How Does a "Micro Fuel Cell" Oxygen Sensor Work?* 2022.
452. Levitt, M.H., *Spin dynamics: basics of nuclear magnetic resonance*. 2013: John Wiley & Sons.
453. Jacobsen, N.E., *NMR spectroscopy explained: simplified theory, applications and examples for organic chemistry and structural biology*. 2007: John Wiley & Sons.
454. *Nuclear Magnetic Resonance. Website: https://chem.libretexts.org/@go/page/1797*
455. SCHURKO, R., *Introduction to Solid State NMR.* Florida State University, 2022.
456. *Elementary Quantum Chemistry*, in *A Chemist's Guide to Density Functional Theory*. 2001. p. 3-18.
457. Schrödinger, E., *Collected papers on wave mechanics*. Vol. 302. 2003: American Mathematical Soc.
458. Sutcliffe, B.T., *The Born-Oppenheimer Approximation*, in *Methods in Computational Molecular Physics*, S. Wilson and G.H.F. Diercksen, Editors. 1992, Springer US: Boston, MA. p. 19-46.
459. Hohenberg, P. and W. Kohn, *Inhomogeneous Electron Gas.* Physical Review, 1964. **136**(3B): p. B864-B871.
460. Kohn, W. and L.J. Sham, *Self-Consistent Equations Including Exchange and Correlation Effects.* Physical Review, 1965. **140**(4A): p. A1133-A1138.
461. Perdew, J.P., K. Burke, and M. Ernzerhof, *Generalized Gradient Approximation Made Simple.* Physical Review Letters, 1996. **77**(18): p. 3865-3868.
462. Becke, A.D., *A new mixing of Hartree–Fock and local density-functional theories.* The Journal of Chemical Physics, 1993. **98**(2): p. 1372-1377.
463. Heyd, J., G.E. Scuseria, and M. Ernzerhof, *Hybrid functionals based on a screened Coulomb potential.* The Journal of Chemical Physics, 2003. **118**(18): p. 8207-8215.
464. Heyd, J., G.E. Scuseria, and M. Ernzerhof, *Erratum: "Hybrid functionals based on a screened Coulomb potential" [J. Chem. Phys. 118, 8207 (2003)].* The Journal of Chemical Physics, 2006. **124**(21): p. 219906.
465. Chelikowsky, J.R., *1.01 - Electrons in Semiconductors: Empirical and ab initio Pseudopotential Theories*, in *Comprehensive Semiconductor Science and Technology*, P. Bhattacharya, R. Fornari, and H. Kamimura, Editors. 2011, Elsevier: Amsterdam. p. 1-41.
466. Zhou, F., et al., *First-principles prediction of redox potentials in transition-metal compounds with LDA+U.* Physical Review B, 2004. **70**(23): p. 235121.
467. Sarah, A.T., et al., *The DFT+U: Approaches, Accuracy, and Applications*, in *Density Functional Calculations*, Y. Gang, Editor. 2018, IntechOpen: Rijeka. p. Ch. 1.
468. Cococcioni, M., *Correlated Electrons: From Models to Materials Modeling and Simulation.* Correlated Electrons: From Models to Materials Modeling and Simulation, 2012. **2**.
469. Chadi, D.J. and M.L. Cohen, *Special Points in the Brillouin Zone.* Physical Review B, 1973. **8**(12): p. 5747-5753.

470. Gonze, X., et al., *First-principles computation of material properties: the ABINIT software project.* Computational Materials Science, 2002. **25**(3): p. 478-492.
471. José, M.S., et al., *The SIESTA method for ab initio order-N materials simulation.* Journal of Physics: Condensed Matter, 2002. **14**(11): p. 2745.
472. Hafner, J., *Ab-initio simulations of materials using VASP: Density-functional theory and beyond.* Journal of computational chemistry, 2008. **29**(13): p. 2044-2078.
473. Ong, S.P., et al., *Python Materials Genomics (pymatgen): A robust, open-source python library for materials analysis.* Computational Materials Science, 2013. **68**: p. 314-319.
474. McQuarrie, D.A., *Statistical Mechanics.* University Science Books: Sausalito, 2000.
475. Chu, I.-H., et al., *Insights into the Performance Limits of the $Li_7P_3S_{11}$ Superionic Conductor: A Combined First-Principles and Experimental Study.* ACS Applied Materials & Interfaces, 2016. **8**(12): p. 7843-7853.
476. Broberg, D., et al., *PyCDT: A Python toolkit for modeling point defects in semiconductors and insulators.* Computer Physics Communications, 2018. **226**: p. 165-179.
477. Broberg, D., *Point Defect Engineering of Energy Materials from First-Principles Calculations*. 2019, UC Berkeley.
478. Park, J.S., et al., *Point defect engineering in thin-film solar cells.* Nature Reviews Materials, 2018. **3**(7): p. 194-210.
479. Freysoldt, C., J. Neugebauer, and C.G. Van de Walle, *Fully Ab Initio Finite-Size Corrections for Charged-Defect Supercell Calculations.* Physical Review Letters, 2009. **102**(1): p. 016402.
480. Freysoldt, C., J. Neugebauer, and C.G. Van de Walle, *Electrostatic interactions between charged defects in supercells.* physica status solidi (b), 2011. **248**(5): p. 1067-1076.
481. Kumagai, Y. and F. Oba, *Electrostatics-based finite-size corrections for first-principles point defect calculations.* Physical Review B, 2014. **89**(19): p. 195205.
482. Aurbach, D., et al., *A short review of failure mechanisms of lithium metal and lithiated graphite anodes in liquid electrolyte solutions.* Solid State Ionics, 2002. **148**(3): p. 405-416.
483. Lin, D., Y. Liu, and Y. Cui, *Reviving the lithium metal anode for high-energy batteries.* Nature Nanotechnology, 2017. **12**(3): p. 194-206.
484. Winter, M. and J.O. Besenhard, *Wiederaufladbare Batterien.* Chemie in unserer Zeit, 1999. **33**(6): p. 320-332.
485. Orsini, F., et al., *In situ Scanning Electron Microscopy (SEM) observation of interfaces within plastic lithium batteries.* Journal of Power Sources, 1998. **76**(1): p. 19-29.
486. Muramatsu, H., et al., *Structural change of Li_2S–P_2S_5 sulfide solid electrolytes in the atmosphere.* Solid State Ionics, 2011. **182**(1): p. 116-119.
487. Weber, D.A., et al., *Structural Insights and 3D Diffusion Pathways within the Lithium Superionic Conductor $Li_{10}GeP_2S_{12}$.* Chemistry of Materials, 2016. **28**(16): p. 5905-5915.
488. Zhang, Q., et al., *Sulfide-Based Solid-State Electrolytes: Synthesis, Stability, and Potential for All-Solid-State Batteries.* Advanced Materials, 2019. **31**(44): p. 1901131.
489. Zhang, Z., et al., *Synthesis and characterization of argyrodite solid electrolytes for all-solid-state Li-ion batteries.* Journal of Alloys and Compounds, 2018. **747**: p. 227-235.
490. Chen, S., et al., *Sulfide solid electrolytes for all-solid-state lithium batteries: Structure, conductivity, stability and application.* Energy Storage Materials, 2018. **14**: p. 58-74.
491. Tian, Y., et al., *Compatibility issues between electrodes and electrolytes in solid-state batteries.* Energy & Environmental Science, 2017. **10**(5): p. 1150-1166.

492. Schwietert, T.K., et al., *Clarifying the relationship between redox activity and electrochemical stability in solid electrolytes.* Nature Materials, 2020.
493. Chung, H. and B. Kang, *Mechanical and Thermal Failure Induced by Contact between a $Li_{1.5}Al_{0.5}Ge_{1.5}(PO_4)_3$ Solid Electrolyte and Li Metal in an All Solid-State Li Cell.* Chemistry of Materials, 2017. **29**(20): p. 8611-8619.
494. Cui, Y., et al., *Ionic Conductivity and Stability of the Lithium Aluminum Germanium Phosphate.* ECS Transactions, 2016. **72**(8): p. 139-146.
495. Bard, A.J. and L.R. Faulkner, *Electrochemical methods and applications*. 2000, New York; London: Wiley-Interscience.
496. Knauth, P., *Inorganic solid Li ion conductors: An overview.* Solid State Ionics, 2009. **180**(14): p. 911-916.
497. Wenzel, S., et al., *Interphase formation on lithium solid electrolytes—An in situ approach to study interfacial reactions by photoelectron spectroscopy.* Solid State Ionics, 2015. **278**: p. 98-105.
498. Alpen, U., et al., *Ionic conductivity of $Li_{14}ZnGeO_{44}$ (LISICON).* Electrochimica Acta, 1978. **23**(12): p. 1395-1397.
499. Ong, S.P., et al., *Phase stability, electrochemical stability and ionic conductivity of the $Li_{10\pm1}MP_2X_{12}$ (M = Ge, Si, Sn, Al or P, and X = O, S or Se) family of superionic conductors.* Energy & Environmental Science, 2013. **6**(1): p. 148-156.
500. Feng, J.K., et al., *All solid state lithium ion rechargeable batteries using NASICON structured electrolyte.* Materials Technology, 2013. **28**(5): p. 276-279.
501. Connell, J.G., et al., *Kinetic versus Thermodynamic Stability of LLZO in Contact with Lithium Metal.* Chemistry of Materials, 2020. **32**(23): p. 10207-10215.
502. Xu, X., et al., *High lithium ion conductivity glass-ceramics in $Li_2O–Al_2O_3–TiO_2–P_2O_5$ from nanoscaled glassy powders by mechanical milling.* Solid State Ionics, 2006. **177**(26): p. 2611-2615.
503. Birke, P., et al., *A first approach to a monolithic all solid state inorganic lithium battery.* Solid State Ionics, 1999. **118**(1): p. 149-157.
504. Shi, X., et al., *Fabrication and electrochemical properties of LATP/PVDF composite electrolytes for rechargeable lithium-ion battery.* Solid State Ionics, 2018. **325**: p. 112-119.
505. Liang, X., et al., *Preparation and performance study of a PVDF–LATP ceramic composite polymer electrolyte membrane for solid-state batteries.* RSC Advances, 2018. **8**(71): p. 40498-40504.
506. Plummer, W.B., *Moisture Content of Carbon Blacks.* Rubber Chemistry and Technology, 1930. **3**(2): p. 185-189.
507. Liu, L., et al., *Water adsorption on carbon - A review.* Advances in Colloid and Interface Science, 2017. **250**: p. 64-78.
508. Dewey, C.S., P.K. Lefforge, and G.L. Cabot, *Moisture sorption by Carbon Black.* Industrial & Engineering Chemistry, 1932. **24**(9): p. 1045-1050.
509. Vetter, K.J. and D. Berndt, *Stromdichte- und pH-Abhängigkeit des elektrochemischen Auf- und Abbaus von Oxydschichten auf Pt, Pd und Au.* Zeitschrift für Elektrochemie, Berichte der Bunsengesellschaft für physikalische Chemie, 1958. **62**(3): p. 378-386.

510. Jiang, P., et al., *Room-Temperature Reaction of Oxygen with Gold: An In situ Ambient-Pressure X-ray Photoelectron Spectroscopy Investigation.* Journal of the American Chemical Society, 2010. **132**(9): p. 2858-2859.
511. Ong, S.P., et al., *Li−Fe−P−O2 Phase Diagram from First Principles Calculations.* Chemistry of Materials, 2008. **20**(5): p. 1798-1807.
512. Jain, A., et al., *Commentary: The Materials Project: A materials genome approach to accelerating materials innovation.* APL Materials, 2013. **1**(1): p. 011002.
513. Blöchl, P.E., *Projector augmented-wave method.* Physical Review B, 1994. **50**(24): p. 17953-17979.
514. Kresse, G. and J. Furthmüller, *Efficient iterative schemes for ab initio total-energy calculations using a plane-wave basis set.* Physical Review B, 1996. **54**(16): p. 11169-11186.
515. Fu, J., *Fast Li+ Ion Conduction in Li_2O-Al_2O_3-TiO_2-SiO_2-P_2O_2 Glass-Ceramics.* Journal of the American Ceramic Society, 1997. **80**(7): p. 1901-1903.
516. M. Holzapfel, G.W., G. Nuspl, S. Busl, *Phase-Pure Lithium Aluminium Titanium Phosphate And Method For Its Production And Use*. 2012, Sued-Chemie AG: USA.
517. Foran, G., et al., *The Impact of Absorbed Solvent on the Performance of Solid Polymer Electrolytes for Use in Solid-State Lithium Batteries.* iScience, 2020. **23**(10): p. 101597.
518. Mankovsky, D., et al., *Water content in solid polymer electrolytes: the lost knowledge.* Chemical Communications, 2020. **56**(70): p. 10167-10170.
519. Sun, Q., et al., *Decomposition failure of $Li_{1.5}Al_{0.5}Ge_{1.5}(PO_4)_3$ solid electrolytes induced by electric field: A multi-scenario study using Scanning Probe Microscopy-based techniques.* Journal of Power Sources, 2020. **471**: p. 228468.
520. Paolella, A., et al., *Understanding the Reactivity of a Thin $Li_{1.5}Al_{0.5}Ge_{1.5}(PO_4)_3$ Solid-State Electrolyte toward Metallic Lithium Anode.* Advanced Energy Materials, 2020. **10**(32): p. 2001497.
521. Xiao, Y., et al., *Computational Screening of Cathode Coatings for Solid-State Batteries.* Joule, 2019. **3**(5): p. 1252-1275.
522. Aboulaich, A., et al., *A New Approach to Develop Safe All-Inorganic Monolithic Li-Ion Batteries.* Advanced Energy Materials, 2011. **1**(2): p. 179-183.
523. Wen, C.J., *Thermodynamic and Mass Transport Properties of "LiAl".* Journal of The Electrochemical Society, 1979. **126**(12): p. 2258.
524. Wen, C.J., et al., *Thermodynamic and Mass Transport.* Journal of The Electrochemical Society, 1979. **126**(12): p. 2258-2266.
525. Zhang, W., et al., *Molecularly Tunable Polyanions for Single-Ion Conductors and Poly(solvate ionic liquids).* Chemistry of Materials, 2021. **33**(2): p. 524-534.
526. Delmas, C., A. Nadiri, and J.L. Soubeyroux, *The nasicon-type titanium phosphates $ATi_2(PO_4)_3$ (A=Li, Na) as electrode materials.* Solid State Ionics, 1988. **28-30**: p. 419-423.
527. Hartmann, P., et al., *Degradation of NASICON-Type Materials in Contact with Lithium Metal: Formation of Mixed Conducting Interphases (MCI) on Solid Electrolytes.* Journal of Physical Chemistry C, 2013. **117**(41): p. 21064-21074.
528. Inozemtseva, A.I., et al., *In Situ XPS Studies of Solid Electrolyte Electroreduction Through Graphene Electrode.* Journal of The Electrochemical Society, 2020. **167**(11): p. 110533.
529. Dilshad, N., et al., *Amines as dual function ligands in the two-phase synthesis of stable $Au_xCu_{(1-x)}$ binary nanoalloys.* Journal of Materials Chemistry, 2012. **22**(21): p. 10514-10524.

530. Wang, J., et al., *Hybrid solid electrolyte enabled dendrite-free Li anodes for high-performance quasi-solid-state lithium-oxygen batteries.* National Science Review, 2020. **8**(2).
531. Méry, A., et al., *A Critical Review for an Accurate Electrochemical Stability Window Measurement of Solid Polymer and Composite Electrolytes.* Materials (Basel), 2021. **14**(14).
532. Kumaravel, V., J. Bartlett, and S.C. Pillai, *Solid Electrolytes for High-Temperature Stable Batteries and Supercapacitors.* Advanced Energy Materials, 2021. **11**(3): p. 2002869.
533. Feng, X., et al., *Thermal runaway mechanism of lithium ion battery for electric vehicles: A review.* Energy Storage Materials, 2018. **10**: p. 246-267.
534. Wu, Y., et al., *Progress in thermal stability of all-solid-state-Li-ion-batteries.* InfoMat, 2021. **3**(8): p. 827-853.
535. Liu, K., et al., *Materials for lithium-ion battery safety. Sci Adv 4 (6): eaas9820*. 2018.
536. Hayamizu, K., *Temperature Dependence of Self-Diffusion Coefficients of Ions and Solvents in Ethylene Carbonate, Propylene Carbonate, and Diethyl Carbonate Single Solutions and Ethylene Carbonate + Diethyl Carbonate Binary Solutions of LiPF6 Studied by NMR.* Journal of Chemical & Engineering Data, 2012. **57**(7): p. 2012-2017.
537. Kurzweil, P. and K. Brandt, *Chapter 3 - Overview of Rechargeable Lithium Battery Systems*, in *Electrochemical Power Sources: Fundamentals, Systems, and Applications*, J. Garche and K. Brandt, Editors. 2019, Elsevier. p. 47-82.
538. Kurzweil, P. and J. Garche, *2 - Overview of batteries for future automobiles*, in *Lead-Acid Batteries for Future Automobiles*, J. Garche, et al., Editors. 2017, Elsevier: Amsterdam. p. 27-96.
539. Zugmann, S., et al., *Measurement of transference numbers for lithium ion electrolytes via four different methods, a comparative study.* Electrochimica Acta, 2011. **56**(11): p. 3926-3933.
540. Kalhoff, J., et al., *Safer Electrolytes for Lithium-Ion Batteries: State of the Art and Perspectives.* ChemSusChem, 2015. **8**(13): p. 2154-2175.
541. McMeeking, R.M., et al., *Metal Electrode Surfaces Can Roughen Despite the Constraint of a Stiff Electrolyte.* Journal of The Electrochemical Society, 2019. **166**(6): p. A984-A995.
542. Murugan, R., V. Thangadurai, and W. Weppner, *Fast Lithium Ion Conduction in Garnet-Type $Li_7La_3Zr_2O_{12}$.* Angewandte Chemie International Edition, 2007. **46**(41): p. 7778-7781.
543. Salimkhani, H., A. Yurum, and S.A. Gursel, *A glance at the influence of different dopant elements on $Li_7La_3Zr_2O_{12}$ garnets.* Ionics, 2021. **27**(9): p. 3673-3698.
544. Raju, M.M., et al., *Crystal Structure and Preparation of $Li_7La_3Zr_2O_{12}$ (LLZO) Solid-State Electrolyte and Doping Impacts on the Conductivity: An Overview.* Electrochem, 2021. **2**(3): p. 390-414.
545. Rangasamy, E., et al., *The effect of 24c-site (A) cation substitution on the tetragonal–cubic phase transition in $Li_{7-x}La_{3-x}A_xZr_2O_{12}$ garnet-based ceramic electrolyte.* Journal of Power Sources, 2013. **230**: p. 261-266.
546. Jin, Y. and P.J. McGinn, *Al-doped $Li_7La_3Zr_2O_{12}$ synthesized by a polymerized complex method.* Journal of Power Sources, 2011. **196**(20): p. 8683-8687.
547. Allen, J.L., et al., *Effect of substitution (Ta, Al, Ga) on the conductivity of $Li_7La_3Zr_2O_{12}$.* Journal of Power Sources, 2012. **206**: p. 315-319.
548. Buannic, L., et al., *Dual Substitution Strategy to Enhance Li^+ Ionic Conductivity in $Li_7La_3Zr_2O_{12}$ Solid Electrolyte.* Chemistry of Materials, 2017. **29**(4): p. 1769-1778.

549. Ramakumar, S., et al., *Structure and Li+ dynamics of Sb-doped $Li_7La_3Zr_2O_{12}$ fast lithium ion conductors.* Physical Chemistry Chemical Physics, 2013. **15**(27): p. 11327-11338.
550. Sakamoto, J., et al., *Synthesis of nano-scale fast ion conducting cubic $Li_7La_3Zr_2O_{12}$.* Nanotechnology, 2013. **24**(42): p. 424005.
551. Wu, J.-F., et al., *Gallium-Doped $Li_7La_3Zr_2O_{12}$ Garnet-Type Electrolytes with High Lithium-Ion Conductivity.* ACS Applied Materials & Interfaces, 2017. **9**(2): p. 1542-1552.
552. Hanc, E., W. Zając, and J. Molenda, *Synthesis procedure and effect of Nd, Ca and Nb doping on structure and electrical conductivity of $Li_7La_3Zr_2O_{12}$ garnets.* Solid State Ionics, 2014. **262**: p. 617-621.
553. Shao, C., et al., *Enhanced ionic conductivity of titanium doped $Li_7La_3Zr_2O_{12}$ solid electrolyte.* Electrochimica Acta, 2017. **225**: p. 345-349.
554. Liu, X., et al., *High lithium ionic conductivity in the garnet-type oxide $Li_{7-2x}La_3Zr_{2-x}Mo_xO_{12}$ (x=0-0.3) ceramics by sol-gel method.* Journal of the American Ceramic Society, 2017. **100**(4): p. 1527-1533.
555. Song, S., et al., *Crystal structure, migration mechanism and electrochemical performance of Cr-stabilized garnet.* Solid State Ionics, 2014. **268**: p. 135-139.
556. Song, S., et al., *Gd-doped $Li_7La_3Zr_2O_{12}$ garnet-type solid electrolytes for all-solid-state Li-Ion batteries.* Electrochimica Acta, 2018. **270**: p. 501-508.
557. Murugan, R., S. Ramakumar, and N. Janani, *High conductive yttrium doped $Li_7La_3Zr_2O_{12}$ cubic lithium garnet.* Electrochemistry Communications, 2011. **13**(12): p. 1373-1375.
558. Hitz, G.T., E.D. Wachsman, and V. Thangadurai, *Highly Li-Stuffed Garnet-Type $Li_{7+x}La_3Zr_{2-x}Y_xO_{12}$.* Journal of The Electrochemical Society, 2013. **160**(8): p. A1248-A1255.
559. Jiang, Y., et al., *Investigation of Mg^{2+}, Sc^{3+} and Zn^{2+} doping effects on densification and ionic conductivity of low-temperature sintered $Li_7La_3Zr_2O_{12}$ garnets.* Solid State Ionics, 2017. **300**: p. 73-77.
560. Yang, T., et al., *The synergistic effect of dual substitution of Al and Sb on structure and ionic conductivity of $Li_7La_3Zr_2O_{12}$ ceramic.* Ceramics International, 2018. **44**(2): p. 1538-1544.
561. Chen, X., et al., *Synthesis of Ta and Ca doped $Li_7La_3Zr_2O_{12}$ solid-state electrolyte via simple solution method and its application in suppressing shuttle effect of Li-S battery.* Journal of Alloys and Compounds, 2018. **744**: p. 386-394.
562. Li, Y., et al., *Effect of Al-Mo codoping on the structure and ionic conductivity of sol-gel derived $Li_7La_3Zr_2O_{12}$ ceramics.* Ionics, 2018. **24**(11): p. 3305-3315.
563. Shen, L., et al., *Preparation and characterization of Ga and Sr co-doped $Li_7La_3Zr_2O_{12}$ garnet-type solid electrolyte.* Solid State Ionics, 2019. **339**: p. 114992.
564. Liu, X., et al., *Improving the room temperature ionic conductivity of Al-$Li_7La_3Zr_2O_{12}$ ceramics by Ba and Y or Ba and W co-doping.* Ceramics International, 2019. **45**(10): p. 13488-13495.
565. Li, X., et al., *Rational design of strontium antimony co-doped $Li_7La_3Zr_2O_{12}$ electrolyte membrane for solid-state lithium batteries.* Journal of Alloys and Compounds, 2019. **794**: p. 347-357.
566. Wagner, R., et al., *Fast Li-Ion-Conducting Garnet-Related $Li_{7-3x}Fe_xLa_3Zr_2O_{12}$ with Uncommon $I\bar{4}3d$ Structure.* Chemistry of Materials, 2016. **28**(16): p. 5943-5951.
567. Samson, A.J., et al., *A bird's-eye view of Li-stuffed garnet-type $Li_7La_3Zr_2O_{12}$ ceramic electrolytes for advanced all-solid-state Li batteries.* Energy & Environmental Science, 2019. **12**(10): p. 2957-2975.

568. Hofstetter, K., et al., *Present understanding of the stability of Li-stuffed garnets with moisture, carbon dioxide, and metallic lithium.* Journal of Power Sources, 2018. **390**: p. 297-312.
569. Wang, C., et al., *Garnet-Type Solid-State Electrolytes: Materials, Interfaces, and Batteries.* Chemical Reviews, 2020. **120**(10): p. 4257-4300.
570. Kotobuki, M., et al., *Compatibility of $Li_7La_3Zr_2O_{12}$ Solid Electrolyte to All-Solid-State Battery Using Li Metal Anode.* Journal of The Electrochemical Society, 2010. **157**(10): p. A1076.
571. Ma, C., et al., *Interfacial Stability of Li Metal–Solid Electrolyte Elucidated via in Situ Electron Microscopy.* Nano Letters, 2016. **16**(11): p. 7030-7036.
572. Jonderian, A. and E. McCalla, *The role of metal substitutions in the development of Li batteries, part II: solid electrolytes.* Materials Advances, 2021. **2**(9): p. 2846-2875.
573. Dogan, F., et al., *Solid State NMR Studies of Li_2MnO_3 and Li-Rich Cathode Materials: Proton Insertion, Local Structure, and Voltage Fade*. Journal of The Electrochemical Society, 2014. **162**(1), A235–A243.
574. Jalem, R., et al., *Experimental and first-principles DFT study on the electrochemical reactivity of garnet-type solid electrolytes with carbon.* Journal of Materials Chemistry A, 2016. **4**(37): p. 14371-14379.
575. Fang, Z., et al., *Systematic study and effective improvement of voltammetry for accurate electrochemical window measurement of solid electrolytes.* Electrochimica Acta, 2022. **414**: p. 140210.
576. Zallocco, V.M., et al., *Electrochemical stability of a NASICON solid electrolyte from the lithium aluminum germanium phosphate (LAGP) series.* Solid State Ionics, 2022. **378**: p. 115888.
577. Méry, A., et al., *A Critical Review for an Accurate Electrochemical Stability Window Measurement of Solid Polymer and Composite Electrolytes.* Materials, 2021. **14**(14): p. 3840.
578. Wen, C.J., et al., *Use of electrochemical methods to determine chemical-diffusion coefficients in alloys: application to 'LiAl'.* International Metals Reviews, 1981. **26**(1): p. 253-268.
579. Tsai, C.-L., et al., *High conductivity of mixed phase Al-substituted $Li_7La_3Zr_2O_{12}$.* Journal of Electroceramics, 2015. **35**(1): p. 25-32.
580. Thompson, T., et al., *Electrochemical Window of the Li-Ion Solid Electrolyte $Li_7La_3Zr_2O_{12}$.* ACS Energy Letters, 2017. **2**(2): p. 462-468.
581. Brugge, R.H., J.A. Kilner, and A. Aguadero, *Germanium as a donor dopant in garnet electrolytes.* Solid State Ionics, 2019. **337**: p. 154-160.
582. Smetaczek, S., et al., *Investigating the electrochemical stability of $Li_7La_3Zr_2O_{12}$ solid electrolytes using field stress experiments.* Journal of Materials Chemistry A, 2021. **9**(27): p. 15226-15237.
583. Wang, R.M., et al., *Enhanced Electrochemical Performance of Al- and Nb-Codoped LLZO Ceramic Powder and Its Composite Solid Electrolyte.* Acs Applied Energy Materials, 2021. **4**(12): p. 13912-13921.
584. Ma, K., et al., *Synthesis, Structure, Transport Properties, Electrochemical Stability Window, and Lithium Plating/Stripping of Mg and Nb Codoped $Li_7La_3Zr_2O_{12}$ Garnet-Type Solid Electrolytes.* The Journal of Physical Chemistry C, 2022. **126**(18): p. 7828-7840.
585. Jonderian, A., et al., *Suite of High-Throughput Experiments for Screening Solid Electrolytes for Li Batteries.* Journal of The Electrochemical Society, 2022. **169**(5): p. 050504.

586. Binninger, T., et al., *Comparison of computational methods for the electrochemical stability window of solid-state electrolyte materials.* Journal of Materials Chemistry A, 2020. **8**(3): p. 1347-1359.
587. Aguesse, F., et al., *Investigating the Dendritic Growth during Full Cell Cycling of Garnet Electrolyte in Direct Contact with Li Metal.* Acs Applied Materials & Interfaces, 2017. **9**(4): p. 3808-3816.
588. Kulova, T.L., et al., *A study of lithium insertion into electrodes with thin gold films.* Russian Journal of Electrochemistry, 2010. **46**(8): p. 877-881.
589. Bach, P., et al., *Lithiation and Delithiation Mechanisms of Gold Thin Film Model Anodes for Lithium Ion Batteries: Electrochemical Characterization.* Electrochimica Acta, 2015. **164**: p. 81-89.
590. Renner, F.U., et al., *Gold model anodes for Li-ion batteries: Single crystalline systems studied by in situ X-ray diffraction.* Electrochimica Acta, 2008. **53**(21): p. 6064-6069.
591. Yang, G., et al., *Lithium Plating and Stripping on Carbon Nanotube Sponge.* Nano Letters, 2019. **19**(1): p. 494-499.
592. Dong, B., et al., *Halogenation of $Li_7La_3Zr_2O_{12}$ solid electrolytes: a combined solid-state NMR, computational and electrochemical study.* Journal of Materials Chemistry A, 2022. **10**(20): p. 11172-11185.
593. Foran, G., et al., *NMR Study of Lithium Transport in Liquid–Ceramic Hybrid Solid Composite Electrolytes.* ACS Applied Materials & Interfaces, 2022. **14**(38): p. 43226-43236.
594. Buckeridge, J., et al., *Determination of the Nitrogen Vacancy as a Shallow Compensating Center in GaN Doped with Divalent Metals.* Physical Review Letters, 2015. **114**(1): p. 016405.
595. Meyer, J., *Resolving the controversy.* Nature Materials, 2018. **17**(3): p. 210-211.
596. Qi, B., S. Ólafsson, and H.P. Gíslason, *Vacancy defect-induced d0 ferromagnetism in undoped ZnO nanostructures: Controversial origin and challenges.* Progress in Materials Science, 2017. **90**: p. 45-74.
597. Miara, L.J., et al., *First-Principles Studies on Cation Dopants and Electrolyte|Cathode Interphases for Lithium Garnets.* Chemistry of Materials, 2015. **27**(11): p. 4040-4047.
598. Medasani, B., et al., *Predicting defect behavior in B2 intermetallics by merging ab initio modeling and machine learning.* npj Computational Materials, 2016. **2**(1): p. 1.
599. Canepa, P., et al., *Role of Point Defects in Spinel Mg Chalcogenide Conductors.* Chemistry of Materials, 2017. **29**(22): p. 9657-9667.
600. Gorai, P., et al., *Devil is in the Defects: Electronic Conductivity in Solid Electrolytes.* Chemistry of Materials, 2021.
601. Swift, M.W., et al., *Predicting low-impedance interfaces for solid-state batteries.* Current Opinion in Solid State and Materials Science, 2022. **26**(3): p. 100990.
602. Dudney, N.J.A.W., William C%A Nanda, Jagjit, *Handbook of Solid State Batteries*. Handbook of Solid State Batteries.
603. Kratzer, E.G.S.a.M.C., *Trends in Charged Defect Behavior*, in *Charged Semiconductor Defects: Structure, Thermodynamics and Diffusion*. 2009, Springer London: London. p. 63-72.
604. Jones, R.O. and O. Gunnarsson, *The density functional formalism, its applications and prospects.* Reviews of Modern Physics, 1989. **61**(3): p. 689-746.
605. Freysoldt, C., et al., *First-principles calculations for point defects in solids.* Reviews of Modern Physics, 2014. **86**(1): p. 253-305.

606. Zhang, S.B. and J.E. Northrup, *Chemical potential dependence of defect formation energies in GaAs: Application to Ga self-diffusion.* Physical Review Letters, 1991. **67**(17): p. 2339-2342.
607. Komsa, H.-P., T.T. Rantala, and A. Pasquarello, *Finite-size supercell correction schemes for charged defect calculations.* Physical Review B, 2012. **86**(4): p. 045112.
608. Sun, R., et al., *Intrinsic stoichiometry and oxygen-induced p-type conductivity of pyrite FeS_2.* Physical Review B, 2011. **84**(3): p. 035212.
609. Zając, W., M. Tarach, and A. Trenczek-Zając, *Towards control over redox behaviour and ionic conductivity in $LiTi_2(PO_4)_3$ fast lithium-ion conductor.* Acta Materialia, 2017. **140**: p. 417-423.
610. Harbach, F. and F. Fischer, *Raman Spectra and Optical Absorption Edge of Li_3PO_4 Single Crystals.* physica status solidi (b), 1974. **66**(1): p. 237-245.
611. Dahliah, D., G.-M. Rignanese, and G. Hautier, *Defect compensation in the p-type transparent oxide Ba_2BiTaO_6.* Journal of Materials Chemistry C, 2020. **8**(27): p. 9352-9357.
612. Scanlon, D.O. and G.W. Watson, *On the possibility of p-type SnO_2.* Journal of Materials Chemistry, 2012. **22**(48): p. 25236-25245.
613. Robertson, J. and S.J. Clark, *Limits to doping in oxides.* Physical Review B, 2011. **83**(7): p. 075205.
614. Yang, J.-H., et al., *Self-regulation of charged defect compensation and formation energy pinning in semiconductors.* Scientific Reports, 2015. **5**(1): p. 16977.
615. Walsh, A. and A. Zunger, *Instilling defect tolerance in new compounds.* Nature Materials, 2017. **16**(10): p. 964-967.
616. Zunger, A., *Practical doping principles.* Applied Physics Letters, 2003. **83**(1): p. 57-59.
617. Miller, S.A., et al., *Empirical modeling of dopability in diamond-like semiconductors.* npj Computational Materials, 2018. **4**(1): p. 71.
618. Goyal, A., et al., *On the Dopability of Semiconductors and Governing Material Properties.* Chemistry of Materials, 2020. **32**(11): p. 4467-4480.
619. Brunin, G., et al., *Transparent conducting materials discovery using high-throughput computing.* npj Computational Materials, 2019. **5**(1): p. 63.
620. Woods-Robinson, R., et al., *Wide Band Gap Chalcogenide Semiconductors.* Chemical Reviews, 2020. **120**(9): p. 4007-4055.
621. Woods-Robinson, R., et al., *Assessing High-Throughput Descriptors for Prediction of Transparent Conductors.* Chemistry of Materials, 2018. **30**(22): p. 8375-8389.
622. Wei, S.-H. and S.B. Zhang, *Chemical trends of defect formation and doping limit in II-VI semiconductors: The case of CdTe.* Physical Review B, 2002. **66**(15): p. 155211.
623. Hautier, G., *Finding the needle in the haystack: Materials discovery and design through computational ab initio high-throughput screening.* Computational Materials Science, 2019. **163**: p. 108-116.
624. Peng, H., et al., *Convergence of density and hybrid functional defect calculations for compound semiconductors.* Physical Review B, 2013. **88**(11): p. 115201.
625. Danny Broberg, K.B., Shivani Srivastava, Diana Dahliah, Benjamin A. D. Williamson, Leigh Weston, David O. Scanlon, Gian-Marco Rignanese, Shyam Dwaraknath, Joel Varley, Kristin Persson, Mark Asta, and Geoffrroy Hautier, *High-throughput calculations of charged point defect properties with semi-local density functional theory - performance benchmarks for materials screening applications.* Under revision, 2023.

626. Haneef, H.F., A.M. Zeidell, and O.D. Jurchescu, *Charge carrier traps in organic semiconductors: a review on the underlying physics and impact on electronic devices.* Journal of Materials Chemistry C, 2020. **8**(3): p. 759-787.
627. Lischka, K., *Deep level defects in narrow gap semiconductors.* Physica Status Solidi B, Basic Research, 1986. **133**(1): p. 17-46.
628. Chen, L., et al., *Electrochemical Stability Window of Polymeric Electrolytes.* Chemistry of Materials, 2019. **31**(12): p. 4598-4604.
629. Pandian, S., et al., *Electrochemical stability of ether based salt-in-polymer based electrolytes: Computational investigation of the effect of substitution and the type of salt.* Journal of Power Sources, 2018. **393**: p. 204-210.
630. Ong, S.P., et al., *Electrochemical Windows of Room-Temperature Ionic Liquids from Molecular Dynamics and Density Functional Theory Calculations.* Chemistry of Materials, 2011. **23**(11): p. 2979-2986.
631. Lu, Z. and F. Ciucci, *Metal Borohydrides as Electrolytes for Solid-State Li, Na, Mg, and Ca Batteries: A First-Principles Study.* Chemistry of Materials, 2017. **29**(21): p. 9308-9319.
632. Walsh, A., et al., *Self-Regulation Mechanism for Charged Point Defects in Hybrid Halide Perovskites.* Angewandte Chemie International Edition, 2015. **54**(6): p. 1791-1794.
633. Rangasamy, E., J. Wolfenstine, and J. Sakamoto, *The role of Al and Li concentration on the formation of cubic garnet solid electrolyte of nominal composition $Li_7La_3Zr_2O_{12}$.* Solid State Ionics, 2012. **206**: p. 28-32.
634. Minami, K., et al., *Lithium ion conductivity of the Li_2S–P_2S_5 glass-based electrolytes prepared by the melt quenching method.* Solid State Ionics, 2007. **178**(11): p. 837-841.
635. Hautier, G., et al., *Accuracy of density functional theory in predicting formation energies of ternary oxides from binary oxides and its implication on phase stability.* Physical Review B, 2012. **85**(15): p. 155208.
636. Wang, L., T. Maxisch, and G. Ceder, *Oxidation energies of transition metal oxides within the GGA+U framework.* Physical Review B, 2006. **73**(19): p. 195107.
637. Benabed, Y., et al., *Assessing the Electrochemical Stability Window of NASICON-Type Solid Electrolytes.* Frontiers in Energy Research, 2021. **9**(230).
638. Zhang, N., et al., *Structural, Electrochemical, and Thermal Properties of Nickel-Rich $LiNi_xMn_yCo_zO_2$ Materials.* Chemistry of Materials, 2018. **30**(24): p. 8852-8860.
639. Ozawa, K., *Lithium-ion rechargeable batteries with $LiCoO_2$ and carbon electrodes: the $LiCoO_2$/C system.* Solid State Ionics, 1994. **69**(3): p. 212-221.
640. Liang, G., et al., *Developing high-voltage spinel $LiNi_{0.5}Mn_{1.5}O_4$ cathodes for high-energy-density lithium-ion batteries: current achievements and future prospects.* Journal of Materials Chemistry A, 2020. **8**(31): p. 15373-15398.
641. Tolganbek, N., et al., *Current state of high voltage olivine structured $LiMPO_4$ cathode materials for energy storage applications: A review.* Journal of Alloys and Compounds, 2021. **882**: p. 160774.
642. Hautier, G., et al., *Phosphates as Lithium-Ion Battery Cathodes: An Evaluation Based on High-Throughput ab Initio Calculations.* Chemistry of Materials, 2011. **23**(15): p. 3495-3508.
643. He, B., et al., *High-throughput screening platform for solid electrolytes combining hierarchical ion-transport prediction algorithms.* Scientific Data, 2020. **7**(1): p. 151.

644. Xiao, R., H. Li, and L. Chen, *Candidate structures for inorganic lithium solid-state electrolytes identified by high-throughput bond-valence calculations.* Journal of Materiomics, 2015. **1**(4): p. 325-332.
645. Satpati, A., G.R. Kandregula, and K. Ramanujam, *Machine learning enabled high-throughput screening of inorganic solid electrolytes for regulating dendritic growth in lithium metal anodes.* New Journal of Chemistry, 2022. **46**(29): p. 14227-14238.
646. Su, Y., et al., *LiPON thin films with high nitrogen content for application in lithium batteries and electrochromic devices prepared by RF magnetron sputtering.* Solid State Ionics, 2015. **282**: p. 63-69.
647. Inaguma, Y., et al., *T. Uchida, M. Ikuta and M. Wakihara.* Solid State Commun, 1993. **86**: p. 689-93.
648. Deiseroth, H.-J., et al., *Li_7PS_6 and Li_6PS_5X (X: Cl, Br, I): Possible Three-dimensional Diffusion Pathways for Lithium Ions and Temperature Dependence of the Ionic Conductivity by Impedance Measurements.* Zeitschrift für anorganische und allgemeine Chemie, 2011. **637**(10): p. 1287-1294.
649. Shin, B.R., et al., *Comparative Study of TiS_2/Li-In All-Solid-State Lithium Batteries Using Glass-Ceramic Li_3PS_4 and $Li_{10}GeP_2S_{12}$ Solid Electrolytes.* Electrochimica Acta, 2014. **146**: p. 395-402.
650. Zhao, E., et al., *Pechini synthesis of high ionic conductivity $Li_{1.3}Al_{0.3}Ti_{1.7}(PO_4)_3$ solid electrolytes: The effect of dispersant.* Journal of Alloys and Compounds, 2016. **680**: p. 646-653.
651. Pershina, S.V., et al., *Glass-ceramics in $Li_{1+x}Al_xGe_{2-x}(PO_4)_3$ system: The effect of Al_2O_3 addition on microstructure, structure and electrical properties.* Journal of Alloys and Compounds, 2020. **835**: p. 155281.
652. Moos, R. and K.H. Härdtl, *Electronic transport properties of $Sr_{1-x}La_xTiO_3$ ceramics.* Journal of Applied Physics, 1996. **80**(1): p. 393-400.
653. Newman, D.S., et al., *The ionic hall effect in the solid electrolyte $C_5H_6NAg_5I_6$.* Electrochimica Acta, 1977. **22**(8): p. 811-814.